Measurement of vector Boson polarisation in WZ production at the LHC with the ATLAS detector

Angela Maria Burger

Communauté
UNIVERSITÉ Grenoble Alpes

THÈSE

Pour obtenir le grade de

DOCTEUR DE LA COMMUNAUTÉ UNIVERSITÉ GRENOBLE ALPES

Spécialité : Physique Subatomique et Astroparticules

Arrêté ministériel : 25 mai 2016

Présentée par

Angela Maria BURGER

Thèse dirigée par **Emmanuel SAUVAN**

préparée au sein du **Laboratoire d'Annecy de Physique de Particules**
dans **l'École doctorale de physique de Grenoble**

Mesure de la polarisation de bosons vecteurs lors de leur production par paire WZ au LHC avec le détecteur ATLAS

Measurement of Vector Boson polarisation in WZ production at the LHC with the ATLAS detector

Thèse soutenue publiquement le **3 juillet 2018**,
devant le jury composé de :

Claude CHARLOT
Directeur de Recherche, Laboratoire Leprince-Ringet, Rapporteur
Elzbieta RICHTER-WAS
Professeur, Jagiellonian University, Marian Smoluchowski Institute of Physics, Rapporteur
Pascal PRALAVORIO
Directeur de Recherche, Centre de Physique des Particules de Marseille, Examinateur
Jan KRETZSCHMAR
Lecturer, University of Liverpool, Examinateur
Giovanni LAMANNA
Directeur de Recherche, Laboratoire d'Annecy de Physique des Particules, Président

Contents

Chapter 1

Introduction

Within the scope of this thesis, the measurement of the cross section of the associate production of a W and a Z decaying fully leptonically and the measurement of the boson polarisation are presented. For the measurement, proton-proton collision data from the ATLAS experiment at the Large Hadron Collider at a center-of-mass energy of $\sqrt{s} = 13$ TeV from 2015 and 2016 with an integrated luminosity of 36.1 fb^{-1} are analyzed. The production of WZ diboson events contains a diagram with the coupling vertex WWZ. Its coupling strength is given by the Electroweak sector of the Standard Model and the Electroweak Symmmetry Breaking mechanism, any deviation could hint for new physics in these sectors. The WZ channel is furthermore the only diboson channel uniquely sensitive to the WWZ vertex and a measurement of the WZ cross section therefore can be used to constrain it. The knowledge of the WZ cross section is also very important for Standard Model measurements and searches for new physics beyond the Standard Model for which WZ events constitute an important background. Precise knowledge of the WZ cross section will improve the precision on these measurements due to a smaller uncertainty on the background estimation.

Diboson measurements involving W and Z bosons are performed in several channels: WW, WZ and ZZ. While the production cross section is the largest for WW, the measurement suffers from irreducible background from $t\bar{t}$ events whose production cross section is several times larger than the signal cross section. Measurements of the WW cross section were for example done with ATLAS data at $\sqrt{s} = 8$ TeV in association with no [1] and one [2] hadronic jet and at 13 TeV [3]. Using data from the CMS experiments, results for the WW cross section were obtained with 19.4 fb^{-1} of $\sqrt{s} = 8$ TeV data using events containing zero or one hadronic jets [4], and with 2.3 fb^{-1} of $\sqrt{s} = 13$ TeV data separately for zero or one hadronic jet in the event [5]. The ZZ channel, on the other hand, has the cleanest signal, producing four isolated, high-energetic leptons with a well-defined invariant mass and has therefore the most favorable signal-to-background ratio among the diboson channels. However, the production cross section is the lowest, the ATLAS measurement at $\sqrt{s} = 13$ TeV yielded only about 1000 signal events with 36 fb^{-1} [6]. Further measurements of the ZZ cross section were performed at $\sqrt{s} = 8$ [7] with 20.3 fb^{-1} of data and at 13 TeV with 3.2 fb^{-1} of 2015 data [8] using data from the ATLAS experiment and at $\sqrt{s} = 8$ TeV [9] and 13 TeV [10] using 19.6 fb^{-1} and 35.9 fb^{-1} of CMS data, respectively. Among the diboson channels, WZ is a good trade-off between signal-to-background ratio and number of expected events: while its production cross section is smaller than WW, the WZ signal is a few times larger than the expected background yield.

Only leptonic decays of the bosons to electrons and muons are taken into account. Leptons can be identified and measured with a higher precision, the precision of the final results is therefore expected to be larger if only leptons are considered as signal. A good signal-to-background ratio is expected due to the clean leptonic signal topology.

Measurements of the WZ cross section taking into account fully leptonic decays to electrons and muons of the two bosons were done at a collision center-of-mass energy of $\sqrt{s} = 7$ [11] and 8 TeV [12] with the ATLAS experiment and by CMS using 7 and 8 TeV data [13] and with 13 TeV data [14]. At $\sqrt{s} = 13$ TeV, a paper with WZ cross-section measurements has been published by the ATLAS collaboration with 3.2 fb^{-1} of 2015 data [15] and a conference note has been released with measurements on 3.2 fb^{-1} of 2015 data and 13.3 fb^{-1} of 2016 data [16] including the extraction of limits on anomalous triple gauge couplings. Cross sections and coupling strengths have been found to be well compatible with Standard Model predictions. The ATLAS measurement at $\sqrt{s} = 8$ TeV [12] is up to now the most precise measurement with a precision of 4.2%.
WZ measurements were also performed using the semi-leptonic decay channel to profit from the larger dataset due to the larger hadronic decay cross section of the W and Z bosons. These measurements consider both WW and WZ diboson final states: WW/WZ cross section measurements in the semi-leptonic decay channel were performed on 20.2 fb^{-1} of ATLAS data [17] and with 19.3 fb^{-1} of CMS data [18] both at $\sqrt{s} = 8$ TeV. However, a less favorable signal-to-background ratio limit the precision of the measurement, measurements in the leptonic channels up to now yielded more precise cross section results. However, boosted topologies can be exploited to improve the sensitivity to the WZ and WW cross section at high WZ invariant masses where non-standard couplings are expected to impact the quantity of WZ production most, should they exist. Up to date, no deviations from Standard Model couplings and cross sections have been found with the semi-leptonic topologies.

Whereas a measurement of the diboson couplings is also sensitive to new physics occurring at energies beyond the reach of the LHC, direct searches for WZ diboson resonances are sensitive to resonances at lower energies which can be produced by proton-proton collisions at the LHC. WZ resonances are predicted in various theoretical models for beyond the Standard Model extensions, for example in theories with extra dimensions, for example [19] and extended Higgs models [20]. Searches with 13 TeV data have been performed by CMS [21] and ATLAS [22], no excesses have been found.

The scattering cross section of W and Z bosons was also measured within the scope of [12] and using 36.1 fb^{-1} of $\sqrt{s} = 13$ TeV data [23], however, details will not be discussed in this thesis. The scattering of W and Z, enhanced in the signal topology of associated production of W and Z bosons with two hadronic jets, is sensitive to four-boson couplings $WWZZ$. Vector boson scattering is an important test of Standard Model gauge couplings and electroweak symmetry breaking: the scattering of two longitudinally polarised gauge bosons mediated by the Higgs boson cancels divergences in the scattering of two longitudinally polarised gauge bosons. Any deviations from the gauge couplings as predicted in the Standard Model would modify or alter this fragile cancellation and could lead to an increase of WZ cross section. The measurement of the fraction of longitudinally polarised bosons in the WZ system is therefore a good probe physics beyond the Standard Model. In fact, some extensions to the Standard Model predict a larger fraction of longitudinally polarised bosons in pair-produced bosons, as has been studied for WW diboson events in [24].

Within the scope of this thesis, the fractions of longitudinally and transversely polarised bosons within the WZ signal are measured inclusively over the boson momentum and pseudorapidity. This is the first measurement of the boson polarisation in WZ events and the first boson polarisation measurement in pair-produced events in hadronic collisions. Boson polarisation in single W boson production has been measured with ATLAS [25] and CMS data [26] at $\sqrt{s} = 7$ TeV and the angular coefficients in the Z boson decay were also measured both by ATLAS [27] and CMS [28] with $\sqrt{s} = 8$ TeV data, however, no measurement has yet been performed on the diboson system using data from hadronic collisions. However, using data from electron-positron collisions provided by the LEP collider, two measurements on the W polarisation in W^+W^- events have been reported: by the L3 collaboration [29] and the OPAL collaboration [30]. These measurements were performed at center-of-mass energies of $\sqrt{s} = 183 - 209$ GeV on the semileptonic decay of the W^+W^- pair, where one of the W bosons decays leptonically to one lepton and one neutrino and the other hadronically into two quarks.

While the polarisation of single W and Z polarisation is presented in bins of boson momentum and pseudorapidity, the WZ polarisation measurement will be fully inclusive, a measurement differential in momentum and rapidity is not feasible due to the low cross section of WZ production.

All results rely on the reconstruction of the final states consisting of electrons and muon and their identification. Electrons and their identification therefore play an important role in this analysis. The electron identification efficiency and its modelling will be studied in this thesis and correction factors will be derived to correct the simulated electron identification efficiencies to the electron identification efficiency measured in 2015 and 2016 data. These correction factors are used in all ATLAS analyses whose signature contain electrons. The uncertainty on this correction factor is one of the main systematic uncertainties in the WZ diboson cross section measurement relying on fully leptonic decays of the bosons. Studies on a possible improvement of the standard method to calculate the electron identification efficiency are also presented.

The contribution to the WZ measurement within the framework of this thesis include studies on the WZ lepton selection optimization, the extraction of the reducible background with the Matrix Method and the polarisation measurement. The electron identification efficiency measurement was also part of the work done.

Chapter 2

Elements of the Standard Model of particle physics

Within the scope of this thesis, the cross section and properties of WZ pair production are measured. This process is predicted and described by the Standard Model of particle physics, the theoretical model of elementary particle dynamics. Data of proton-proton collisions have been analyzed and the measurement result is compared to the predictions given by the Standard Model. In the following section, fundamental concepts of the theoretical modeling of WZ production in a hadron collider are introduced. In Section 2.1, a short introduction of the Standard Model theory is given. Hard scattering and underlying processes happening at hadron colliders are discussed in Section 2.2.

2.1 The Electroweak theory and the Standard Model

2.1.1 The Standard Model

2.1.1.1 The Standard Model as Gauge Theory

The Standard Model (SM) is expressed in the framework of Quantum Field Theory. Quantum field theory is based on the principles of quantum mechanics and relativity. Requiring the theory to be lorentz invariant ensures that fundamental laws of physics, like momentum and energy conservation and the invariance of the speed of light, are valid in all reference frames.

In Quantum Field Theory, interactions are mediated by the exchange of particles, the bosons. Interactions are modelled as rotations in a complex space with some conserved quantity associated with that space. Any rotation of a field ϕ can be expressed as follows [31]:

$$\phi^{'} = \exp(i\theta(x))\phi, \tag{2.1}$$

where $\theta(x)$ is the phase shift at some space-time point x. Elementary particle dynamics has to describe localized interactions and therefore, local phase transformations. The Standard Model is a gauge theory, its Lagrangian has to be invariant under gauge transformations. This is demonstrated in the following by means of the Lagrangian of Quantum Electrodynamics (QED) which describes a spin-$\frac{1}{2}$ particle with mass m, for example an electron. A local gauge transformation, as in equation (2.1), introduces an extra term in the Lagrangian:

$$\mathcal{L} = i\hbar c\bar{\psi}\gamma^{\mu}\partial_{\mu}\psi - \mathrm{m}c^2\bar{\psi}\psi, \tag{2.2}$$

such that the QED Lagrangian becomes

$$\mathcal{L} \rightarrow \mathcal{L} - \hbar c(\partial_\mu \theta)\bar{\psi}\gamma^\mu\psi. \tag{2.3}$$

In order to conserve invariance under local gauge transformation, a field A_μ, corresponding to the photon, is introduced. The phase transformation of this new field compensates the phase shift of the electron in the Lagrangian in equation (2.3)

$$\mathrm{A}_\mu \rightarrow \mathrm{A}_\mu + \partial_\mu \frac{-\hbar c}{q}\theta(\mathrm{x}). \tag{2.4}$$

Introducing also the term of the free, massless field A_μ of the electromagnetic potential, a spin-1 field described by the Proca equation, the full QED Lagrangian can be written as

$$\mathcal{L} = -\frac{1}{16\pi}F^{\mu\nu}F_{\mu\nu} + [i\hbar c\bar{\psi}\gamma^\mu\partial_\mu\psi - mc^2\bar{\psi}\psi] + \hbar c\bar{\psi}\gamma^\mu\psi\mathrm{A}_\mu, \tag{2.5}$$

where

$$F^{\mu\nu} = (\partial^\mu A^\nu - \partial^\nu A^\mu). \tag{2.6}$$

It is convenient for the following to introduce the covariant derivative

$$\mathcal{D}_\mu \equiv \partial_\mu - i\mathrm{A}_\mu, \tag{2.7}$$

and to replace the simple derivative in equation (2.2) by this covariant derivative in order to make it invariant under local gauge transformation.

An essential concept of quantum field theory is renormalizability. The SM theory contains terms which are divergent in integration over the momentum space, however, the renormalization process allows to absorb these divergent parts of the integral in physical parameters like masses or couplings, which then, as a consequence become energy or scale dependent. All renormalization methods introduce a scale μ_R, the renormalization scale. To obtain a prediction on a quantity, for instance a cross section, μ_R may be chosen to be equal to the typical energy scale at which the interaction takes place. If all orders of perturbation theory are included in the calculation, the dependence of the observable on the renormalization scale cancels [32].

2.1.1.2 Matter particles and fields

Essentially, all elementary particles can be assigned to two groups: matter and force particles. An overview scheme of all particles in the Standard Model is given in Figure 2.1.

Matter particles are the building blocks of matter. All quarks and leptons, which are fermions, belong to this group. Protons and neutrons are made of quarks. Together with electrons they form neutral atoms. Quarks and leptons are arranged in three "generations" each consisting of one quark with positive charge $\frac{2}{3}e$ and one with negative charge $-\frac{1}{3}e$, a negatively charged lepton l with charge $-e$, where e is the elementary charge, and the corresponding neutral neutrino ν_l. Note that, according to the solution of the Dirac equation for spin-$\frac{1}{2}$ particles, each elementary matter particle has a corresponding anti-particle. This anti-particle has the same mass as its counterpart but with opposite charge-like quantum numbers. In Table 2.1 and 2.2, the fundamental properties of the quarks and leptons[1] are given.

[1]Note that in the SM, neutrinos are massless. However, the measurement of neutrino oscillation gives experimental proof for non-zero neutrino masses.

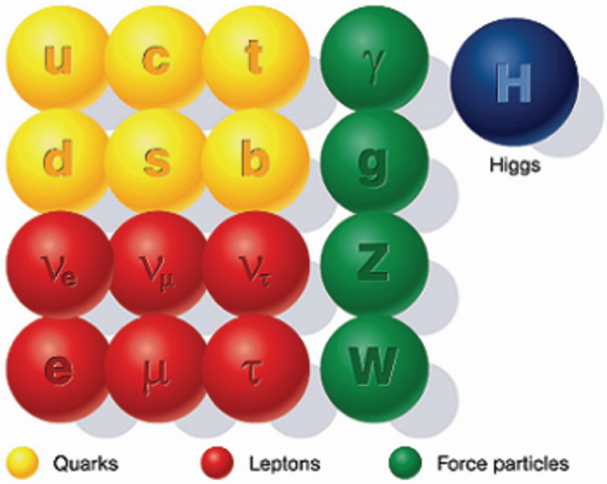

Figure 2.1 – *Overview over all known particles in the Standard Model. Details are given in the text.*

Generation	Flavour	Charge [e]	Mass [MeV]
1st	up (u)	+2/3	$2.2^{+0.6}_{-0.4}$
	down (d)	-1/3	$4.7^{+0.5}_{-0.4}$
2nd	charm (c)	+2/3	$(1.28 \pm 0.03) \cdot 10^3$
	strange (s)	-1/3	96^{+8}_{-4}
3rd	top (t)	+2/3	$(173.1 \pm 0.6) \cdot 10^3$
	bottom (b)	-1/3	$(4.18^{+0.04}_{-0.03}) \cdot 10^3$

Table 2.1 – *Quarks and their properties. Data extracted from [33], the masses are given in the $\overline{MS}$ scheme (given at the scale of the quarks' mass $\bar{m}(\mu_R^2 = \bar{m}^2)$, except for the u, d and s quarks where the scale 2 GeV is used).*

In quantum field theory, interactions are mediated by exchange particles with integer spin. In Section 2.1.1.1, the photon, the exchange particle of quantum-electrodynamics, a massless, neutral spin-1 particle, has already been introduced. The heavy charged W^+ and W^- and the neutral Z bosons mediate the weak interaction which is responsible for particle decays. Massless spin-1 gluons convey the strong force, an attractive force between quarks keeping them together in hadrons. The scalar Higgs field provides the weak bosons and the fermions with mass through the Electroweak Symmetry Breaking and Higgs mechanism. Some fundamental properties of the interaction mediating particles are listed in Table 2.3.

Generation	Flavour	Charge [e]	Mass [MeV]
1st	e (electron)	-1	$0.5109989461 \pm 0.0000000031$
	ν_e	0	≈ 0
2nd	μ (muon)	-1	$105.6583745 \pm 0.0000024$
	ν_μ	0	≈ 0
3rd	τ (tau)	-1	1776.86 ± 0.12
	ν_τ	0	≈ 0

Table 2.2 – *Leptons and their properties. Based on [33].*

Boson	Mediated Force	Charge [e]	Spin	Mass [GeV]	Couples to
photon (γ)	electromagnetic	0	1	0	all electrically charged particles
$W^{\pm}$	weak	± 1	1	80.385 ± 0.015	all quarks and leptons, itself, Z-boson, photon, Higgs
Z-boson	weak	0	1	91.1876 ± 0.0021	all quarks and leptons, W-boson, Higgs
gluon	strong	0	1	0	all quarks, itself
Higgs	-	0	0	125.09 ± 0.24	all massive particles, itself

Table 2.3 – *Standard Model bosons and their properties. From [33].*

2.1.2 The Electroweak theory

All particles carrying weak charge, for instance all quarks and leptons, can participate in a weak interaction. They behave as doublets under the weak interaction: leptons can be arranged in the following "isospin" doublets

$$\begin{pmatrix} e \\ \nu_e \end{pmatrix}, \begin{pmatrix} \mu \\ \nu_\mu \end{pmatrix}, \begin{pmatrix} \tau \\ \nu_\tau \end{pmatrix},$$

and quarks as following:

$$\begin{pmatrix} u \\ d' \end{pmatrix}, \begin{pmatrix} c \\ s' \end{pmatrix}, \begin{pmatrix} t \\ b' \end{pmatrix}.$$

Note that while lepton flavour is conserved[2] and there is no interaction connecting the leptons of different generations, the quark flavour is not. The states d', s' and b' are linear combination of d, s and b quarks, the flavour mixing is given by the Kobayashi-Maskawa Matrix (CKM-Matrix).

It has been shown by C. Wu in her famous experiment [34], that the weak interaction is parity-violating and connects only the left-handed states of the weak doublets, right handed states are singlets under the weak interaction.

Mathematically, a weak interaction can be expressed as a rotation in the $SU(2)_L$ weak isospin space with the Pauli-matrices τ being the generators of the SU(2) space [31]:

$$\psi \rightarrow \exp(-iq\tau \circ \lambda(\mathbf{x})/(\hbar c))\psi, \tag{2.8}$$

where q is a coupling constant and $\lambda(\mathbf{x})$ is a local phase transformation. The weak interaction only couples to left-handed chiral states, denoted by the "L" as for example in the notation of the symmetry group $SU(2)_L$.

Following the scheme introduced in section 2.1.1.1, three new massless fields, $\mathbf{W}_\mu = (W^1_\mu, W^2_\mu, W^3_\mu)$, are introduced, they compensates any local phase transformation in the weak interaction as shown by Yang and Mills [35].

[2] The observation of neutrino oscillation indicates that there is a lepton flavour violation. However, this is not yet included in the Standard Model.

The coupling strengths of weak and electromagnetic interaction become equal at some energy, hence, they manifest as a single electroweak interaction. The underlying symmetry of the electroweak interaction is $SU(2)_L \times U(1)_Y$, where Y, the hypercharge, is given by

$$Y = 2(Q - T_3). \tag{2.9}$$

Q is the electric charge, the conserved quantity due to gauge invariance in QED, and T_3 is the third component of the weak isospin, the conserved quantity of the weak interaction [31]. The hypercharge Y is the conserved quantity in the $U(1)_Y$ symmetry group with the mediator B_μ, a neutral, massless gauge field. At low energy, this symmetry is broken, resulting in the generation of the observable mass eigenstates of the electroweak interaction, $W^\pm$, Z and the photon γ [36].

The first two components of the $\mathbf{W}_\mu$ fields mix to create the two charged bosons $W^\pm$ by a simple basis transformation of the $SU(2)_L$ basis, the Pauli matrices, $\tau_\pm = \frac{1}{2}(\tau_1 - i\tau_2)$. The fields in this new basis are [32]

$$W_\mu^\pm = \frac{1}{\sqrt{2}}(W_\mu^1 \mp iW_\mu^2). \tag{2.10}$$

The B_μ field of the $U(1)_Y$ symmetry group and the W_μ^3 field of $SU(2)_L$ mix to create the observable mass eigenstates, the Z and the photon A_μ:

$$\mathrm{A}_\mu = \mathrm{B}_\mu \cos(\theta_\mathrm{W}) + \mathrm{W}_\mu^3 \sin(\theta_\mathrm{W}), \tag{2.11}$$

$$\mathrm{Z}_\mu = -\mathrm{B}_\mu \sin(\theta_\mathrm{W}) + \mathrm{W}_\mu^3 \cos(\theta_\mathrm{W}). \tag{2.12}$$

The angle θ_W is the weak mixing angle which was determined experimentally as $\theta_W = 28.75°$.
This angle $\sin(\theta_\mathrm{W})$ can be expressed in terms of the $SU(2)_L$ and $U(1)_Y$ gauge fields coupling strengths, $\mathrm{g_W}$ and g', respectively,

$$\sin(\theta_\mathrm{W}) = \frac{g'}{\sqrt{\mathrm{g_W^2} + g'^2}}. \tag{2.13}$$

The electroweak Lagrangian is given by

$$\begin{aligned} \mathcal{L} = &-\frac{1}{4}\mathrm{W}^i_{\mu\nu}\mathrm{W}_i^{\mu\nu} - \frac{1}{4}\mathrm{B}_{\mu\nu}\mathrm{B}^{\mu\nu} + \\ &\bar{\psi}_\mathrm{L}(i\gamma^\mu\partial_\mu - \mathrm{g_W}\frac{\tau_i}{2}\gamma^\mu\mathrm{W}_\mu^i - \mathrm{g'}\frac{\mathrm{Y}}{2}\gamma^\mu\mathrm{B}_\mu)\psi_\mathrm{L} + \\ &\bar{\psi}_\mathrm{R}(i\gamma^\mu\partial_\mu - \mathrm{g'}\frac{\mathrm{Y}}{2}\gamma^\mu\mathrm{B}_\mu)\psi_\mathrm{R}. \end{aligned} \tag{2.14}$$

where $\mathrm{W}_{\mu\nu}$ and $\mathrm{B}_{\mu\nu}$ are the field strength tensors of $SU(2)_L$ and $U(1)_Y$ respectively. The first and the second term in the first line represent the free gauge fields. Note that the $\mathrm{W}_i^{\mu\nu}$ do not commute and $SU(2)_L$ is a non-Abelian group, therefore the weak bosons also interact with themselves, the term $W^{\mu\nu}$ in case of $SU(2)_L$ is defined as

$$W_i^{\mu\nu} = (\partial^\mu W_i^\nu - \partial^\nu W_i^\mu) - g_W(W^\mu \times W^\nu)_i. \tag{2.15}$$

The field strength tensor $\mathrm{B}_{\mu\nu}$ is defined as in equation (2.6).

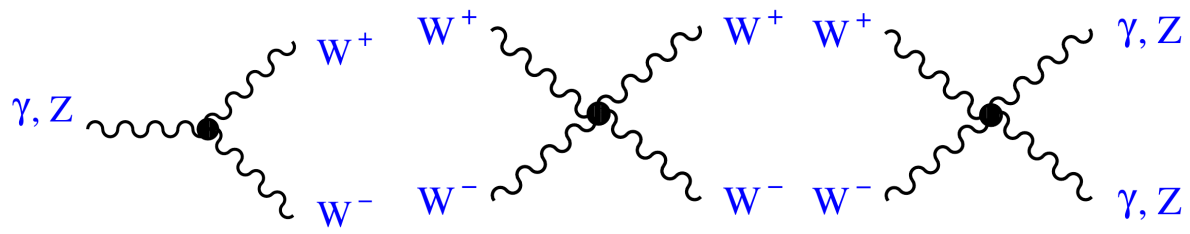

Figure 2.2 – *Triple and quartic gauge coupling vertices. From [37].*

2.1.3 Gauge couplings

The non-Abelian nature of $SU(2)_L \times U(1)_Y$ was already discussed in Section 2.1.2. The Lagrangian of the free electroweak boson fields in equation (2.14) contains triple (TGC) and quartic gauge couplings (QGC) as a consequence of this non-Abelian nature. The possible coupling vertices are illustrated in Figure 2.2.

Note that always two W bosons are coupled in the vertex, self-coupling of neutral gauge bosons are forbidden in the Standard Model [37]. The strengths of the TGCs and QGCs are fully specified by the Standard Model and any deviation will manifest itself in a change of the boson pair production cross section. Measuring boson pair production therefore is a stringent test of the Standard Model and the $SU(2)_L \times U(1)_Y$ structure of the electroweak interaction.

2.1.4 Electroweak Symmetry Breaking

Until now, the electroweak Lagrangian in equation (2.14) describes massless fields. However, masses are measured for the $W^{\pm}$ and the Z boson. But adding mass terms in equation (2.14) spoils local gauge invariance. Instead of adding mass terms in the Lagrangian, another approach is chosen, a redefinition of the vacuum ground state [31]. The basic idea is to add a scalar field $\phi(x)$ which couples to the gauge bosons [38],

$$\phi = \begin{pmatrix} \phi^+(x) \\ \phi^0(x) \end{pmatrix}. \tag{2.16}$$

This scalar potential is chosen such that it has a continuous symmetry and creates a ground state with non-zero vacuum expectation value

$$V(\phi) = \mu^2 |\phi^\dagger \phi| + \lambda (\phi^\dagger \phi)^2. \tag{2.17}$$

The potential introduces an additional term in the Lagrangian of equation (2.14)

$$\mathcal{L}_s = (D^\mu \phi)^\dagger (D_\mu \phi) - V(\phi), \tag{2.18}$$

with $V(\phi)$ having the form of equation (2.17). For a value $\mu^2 < 0$, the potential has a non-zero, degenerate ground state with a rotational, continuous symmetry, but the lowest-energy ground state does not share the symmetry of the Lagrangian. By choosing one ground state, the symmetry is broken. This is referred to as "Spontaneous Symmetry Breaking". An illustration of the potential in equation (2.17) is given in Figure 2.3 and is often referred to as "Mexican hat" potential due to its shape.

Inevitably, the vacuum ground state will take the state with the lowest energy, however, it is degenerate. The system will therefore choose one specific ground state, the symmetry is broken [31].
The ground state ϕ_0 of the Lagrangian is chosen such that electromagnetism described by

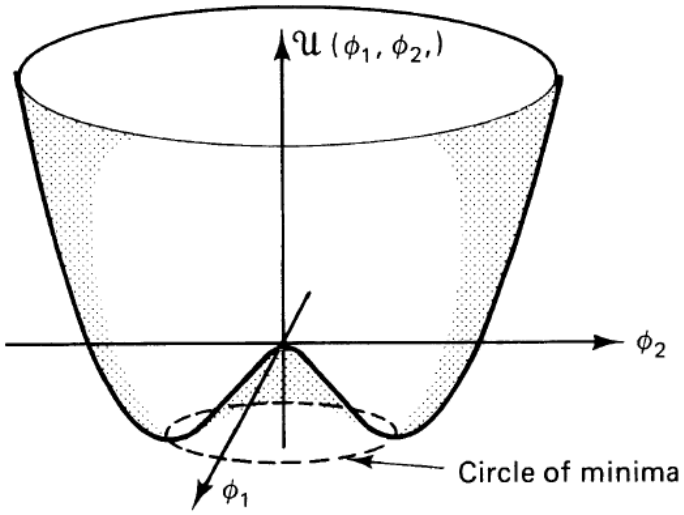

Figure 2.3 – *Illustration of the Higgs potential given in equation (2.17). From [31].*

the $U(1)_{\text{QED}}$ subgroup is unbroken and represents the ground state of the vacuum and any interaction conserves the electric charge [38]

$$\phi_0 = \frac{1}{\sqrt{2}} \begin{pmatrix} 0 \\ v + h \end{pmatrix}. \tag{2.19}$$

The symmetry group $SU(2)_L \times U(1)_Y$ gets broken down to $U(1)_{QED}$, which generates the $W^{\pm}$ and the Z boson. Latter acquire a mass while the photon remains massless. According to the Goldstone theorem, in a system with a Lagrangian with continuous symmetry and a ground state with broken symmetry, massless spin 0 particles exist. In the process of electroweak symmetry breaking, therefore three massless Goldstone modes are created [37].

Interactions are small fluctuations around a ground state. Note that, until now, the ground state, the vacuum, was defined to be at zero potential [31]. With interactions taking place in a vacuum with non-zero expectation value and with local gauge invariance still valid, the three Goldstone modes are "absorbed" by the massless gauge bosons. A massless gauge boson has two degrees of freedom corresponding to two transverse polarisation modes. The degrees of freedom of the Goldstone modes become the longitudinal polarisation of the Gauge bosons, hence, they acquire mass [37].

This mechanism to give masses to the gauge bosons has been proposed by P. Higgs [39, 40], F. Englert and R. Brout [41] and by G. Guralnik, C. Hagen, and T. Kibble [42, 43]. The particle associated with the scalar field has been found by the ATLAS and CMS collaborations in 2012 using proton-proton collision data at a center-of-mass energy of $\sqrt{s} = 8$ TeV [44, 45].

2.1.5 Quantum Chromodynamics

Processes of strong interaction are described in the color space $SU(3)_C$. Local gauge transformations are expressed in a similar way as in the $SU(2)$ weak interaction, only that the basis of the $SU(3)_C$ algebra are the eight Gell-Mann matrices which give rise to eight massless spin-1 gauge fields, the gluons, the mediating bosons of quantum chromodynamics (QCD). "Color" takes in QCD the role of "charge". There are three different charges, denoted "red", "green" and "blue". The $SU(3)_C$ algebra is, like $SU(2)_L$, non-abelian, gluons

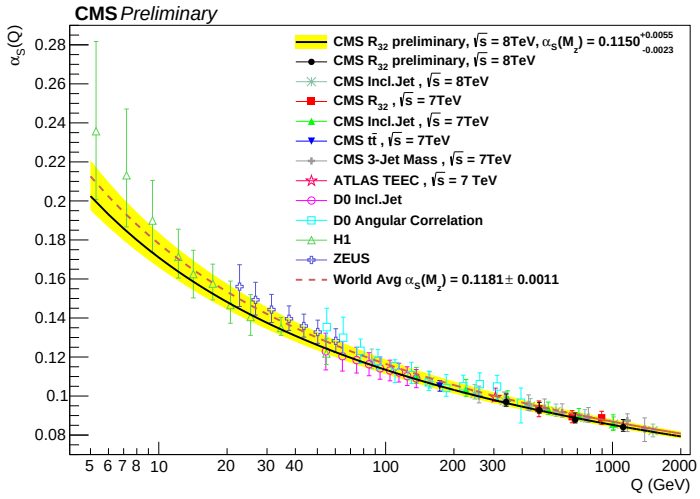

Figure 2.4 – *Measurements of the strong coupling constant as a function of energy scale performed by analyses of experimental data of CMS, ATLAS, D0, H1 and Zeus and the world average. From [46].*

therefore carry themselves "color-charge" and are able to couple to each other. In fact, gluon carry two colors, a color and an anti-color. In an interaction, for instance with a quark, the gluon exchanges the color (anti-color) of the quark with their anti-color (color), therefore, color is conserved in strong interaction. The strong interaction is flavor conserving and couples with the same strength to all flavour states.

Quarks form color-singlet or color-neutral states, consisting either of one quark and one anti-quark (mesons) with one color and the corresponding anti-color, or three quarks with the three different color- or anti-color states (baryons). States with net color charge do not exist as free particles in nature, the mesons or baryons are kept in bound color-singlet states. This is called "confinement".

Due to vacuum polarisation, gluons propagators can generate a quark-anti-quark pair which annihilates again to a gluon. This "screens" the color charge. However, gluons couple to themselves and gluon loops can occur in the propagator. These "camouflage" the color charge. Calculations in quantum chromodynamics show that latter effect is larger which leads to an increasing strong coupling constant with increasing distances and decreasing coupling with decreasing distance and larger momentum transfer. This effect is called "asymptotic freedom": the larger the distance between two quarks, the stronger the coupling between them. The "running" of the strong coupling α_S behaves according to equation (2.20) for six quark flavours [36]

$$\alpha_S = \frac{\alpha_S(\mu^2)}{1 + \frac{7}{4\pi}\alpha_S(\mu^2) ln(\frac{q^2}{\mu^2})}, \tag{2.20}$$

where q is the momentum transfer in the interaction and μ^2 is a renormalization scale. The coupling α_S becomes very large at low energy, however, the perturbative expansion leading to equation (2.20) is not valid up to arbitrary low energies.

Measurements of α_S done by the experiments CMS, ATLAS, D0, H1 and Zeus at different energy scales and the world average in Figure 2.4 confirm the running of the strong coupling.

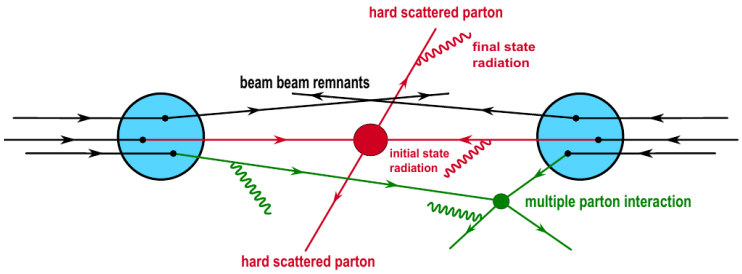

Figure 2.5 – *Illustration of a hard-scattering event in a proton-proton collider. From [47].*

2.2 Event topology in a proton-proton collider and its modelling

2.2.1 The structure of the proton

Within the scope of this thesis, data from proton-proton collisions are analyzed. In a hard proton-proton collision event, one constituent from each colliding proton scatters inelastically, as illustrated in Figure 2.5.

The cross section of a process with a given production mechanism depends consequently on the structure and parton content of the proton. Theoretical predictions therefore rely on the knowledge of the proton structure. The latter is parameterized with the parton distribution function (PDF). The PDF function $f_{q/p}(x_q, Q^2)$ describes the probability to find a parton q in the proton with a fraction x_q of the proton longitudinal momentum.

In principle, the proton consists of two up-quarks and one down-quark (valence quarks) and gluons. Small energy fluctuations can generate and annihilate quark-anti-quark pairs (sea quarks), as long as they have low momenta or this happens at a short time-scale in order not to violate energy conservation [48]. The larger the scattering energy, the more heavy quarks within the proton can be probed.

The PDF is therefore dependent on the energy Q at which the proton is probed: the parton taking part in the inelastic scattering can radiate another particle or can even be produced by the splitting of another particle. It depends on the energy of the scattering particle whether this collinear radiation can be resolved [48].

In principle, the PDF describes the low-energy contribution of the proton-proton collision: everything which cannot be treated in the framework of perturbative calculation of the scattering, like soft collinear gluon radiation off the initial state quark, is absorbed in the PDF in analogy to the renormalization procedure described in Section 2.1.1.1 [49]. A cut-off has to be defined separating the low-energy part of the scattering process from the high-energy part. The introduction of this cut-off makes the PDF dependent on the factorization scale μ_F. Note that the dependence on the scale μ_F cancels if the scattering process were evaluated at all orders.

However, as the perturbative calculation is only calculated in finite order, the cross section result is dependent on μ_F. The dependence is the stronger, the lower the perturbative order. Therefore, a theory uncertainty on the factorization scale dependence of the cross section has to be estimated. This factorization scale is chosen according to the typical energy scales of the hard process examined.

The parton distribution functions are non-perturbative and cannot be determined from theory but are obtained through a fit to data. A PDF can be measured at an arbitrary energy scale and converted to another energy scale [49]. Figure 2.6 shows the CT10 PDF [50]

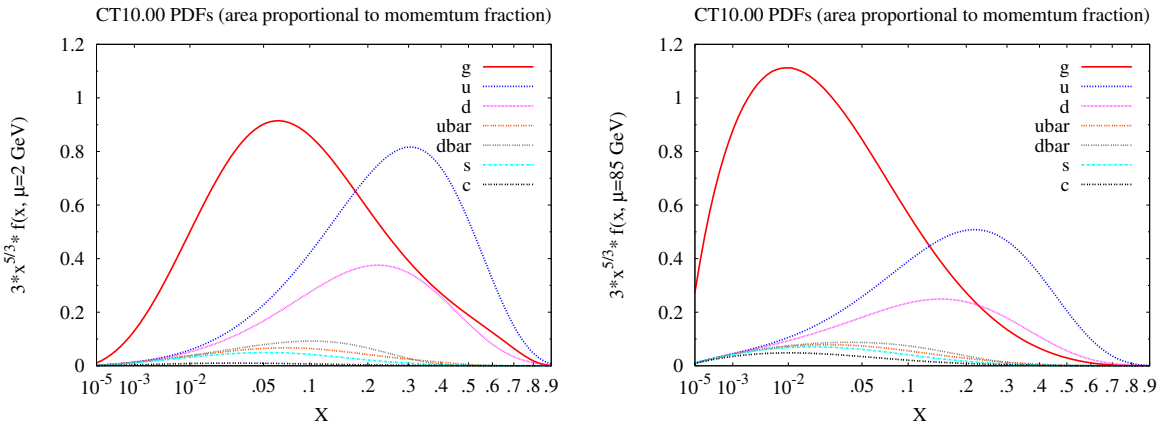

Figure 2.6 – *The PDF set CT10 [50] of the proton at a scale $\mu_F = 2\,GeV$ (left) and at $\mu_F = 85$ GeV (right). The energy scale $\mu_F = 85$ GeV corresponds to the energy range relevant for this work. From [50].*

at two different energy scales: on the left, the PDF of the proton probed at low energy $\mu_F = 2$ GeV, on the right the same PDF at $\mu_F = 85$ GeV which corresponds to the energy scale relevant for this work.

From Figure 2.6, the most general features of a PDF can be recognized: The gluon PDF and the sea quark PDFs are large for low momentum transfer and the valence quark distributions peak at about $x = \frac{1}{3}$. At $x \approx 1$, the PDF decreases, the probability is small to find a proton with one parton carrying all the energy of the proton [48].

2.2.2 Hard-scattering processes at the Large Hadron collider

At energies probed in high-energy proton-proton collisions, the proton constituents, the partons, quarks and gluons, behave as quasi-free particles in the proton due to the asymptotic freedom in QCD: the higher the energy or the smaller the distances the partons are probed at, the smaller the coupling between them. Therefore, the cross section can be assumed as the incoherent sum of all partonic cross sections and the factorization theorem can be applied. The factorization theorem describes the separation of the scattering theory in a high- and a low-energetic part: the internal structure of the proton (PDF) which can only be described using low-energy physics and the partonic cross section $\sigma(q_a q_b \to X)$ which can be treated using perturbation theory. This perturbative calculation is truncated at a certain order in the strong coupling constant which provokes a dependence on a renormalization scale μ_R as already introduced in Section 2.1.5.

According to the factorization theorem, the cross section of an event $\sigma(p_A p_B \to X)$ can be determined by weighting the perturbative partonic cross section $\sigma(q_a q_b \to X)$ with the non-perturbative PDF evaluated at a scale μ_F, $f_{q/p}(x_q, \mu_F^2)$ [49].

The production cross section of a final state X in a proton-proton collider can therefore be written as

$$\sigma(p_A p_B \to X) = \int dx_a dx_b f_{a/A}(x_a, \mu_F^2) f_{b/B}(x_b, \mu_F^2) \sigma(x_a x_b s, \mu_R^2). \tag{2.21}$$

Each constituent of the protons A and B carries a fraction $x_q, q \in \{a, b\}$ of the proton longitudinal momentum. The quantities in equation (2.21) are illustrated in Figure 2.7.

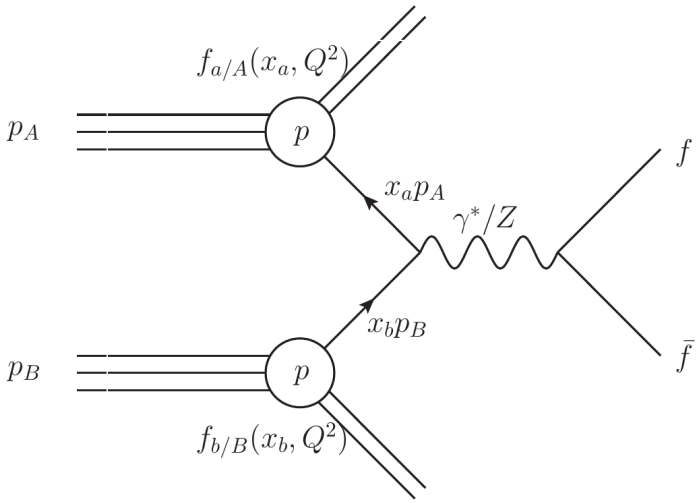

Figure 2.7 – *Illustration of the quantities in equation (2.21) to describe the hard scattering cross section yielding the final state $\sigma(pp \to X)$. From [51].*

2.2.3 Soft processes at hadron colliders

Soft processes occur alongside the hard scattering in a hadron collider. The hard scattering final state described in equation (2.21), may undergo emissions of softer radiation of photons, quarks and gluons. The simulation of the hard-scattering event is therefore interfaced with another MC simulating these softer emissions, the parton shower. Possible double counting of parton emissions from the parton shower MC and the MC modelling the hard-scattering process have to be taken into account in simulations at higher order from next-to-leading order on. Different implementations of the particle splitting process and the treatment of the double-counting give rise to different MC models for the parton-shower, see for example [52, 53]. Possible mis-modelling of the parton-shower process may be estimated by comparing the results obtained with different parton shower models.

The coloured final states from the hard-scattering event and the parton shower have to form color-neutral states as only those are observed in nature. This process is called hadronization. QCD dictates that whereas at high energy, the quarks can be assumed as free particles, at low energy transfer or long distances, the partons are governed by confinement: the potential energy between quarks and anti-quarks increases with their distance and new quark-anti-quark pairs are created out of this energy. If the kinetic energy of the resulting quark-anti-quark pairs is low enough, bound color-neutral states are formed [31]. The hadronization process is illustrated in Figure 2.8 and gives rise to emission of several colorless hadrons in the direction of the original quark denominated as "hadron jet".

Two main approaches are used to model this process: the cluster model [54] applied in the `Herwig` and `Sherpa` Monte Carlo simulations and the string model [55] used to simulate the hadronization process in `Pythia`.
All processes happening in the hard collision of the two protons and which are not associated to the hard interaction final state, are summarized in the topology of the "underlying event". Besides the hard interaction between two partons, semi-hard parton-parton scattering or multiple interactions of the partons in the protons may occur. The debris which is the left-over of the protons after the hard interaction, called "beam-beam remnants", and initial and final state radiation not associated to the hard-scattering event are also elements of the underlying event. The underlying event is therefore a consequence of the

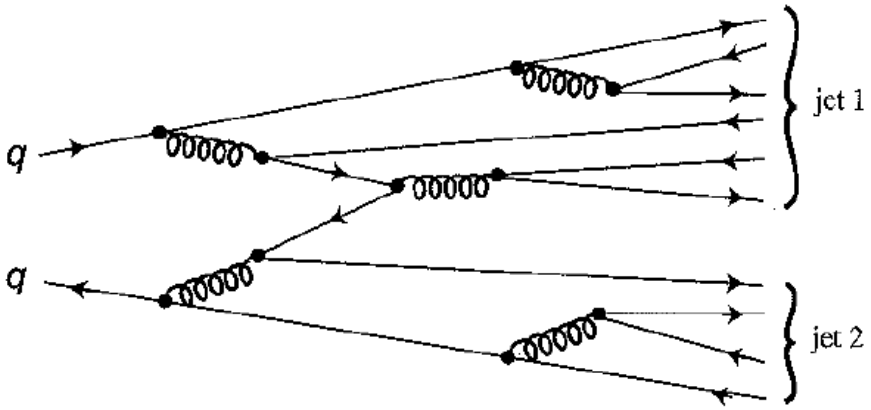

Figure 2.8 – *Illustration of the hadronization process. From [31].*

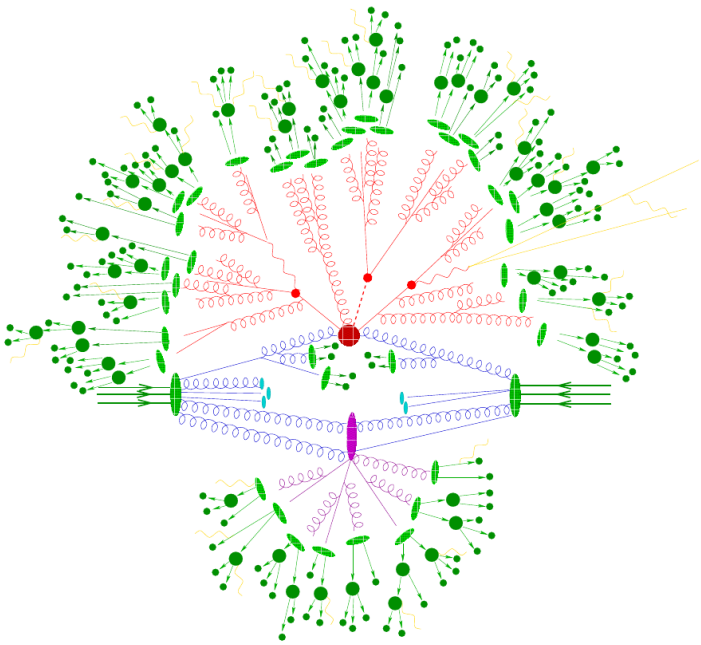

Figure 2.9 – *In the horizontal plane, the incoming initial protons are shown whereas two of their partons undergo a hard collision, illustrated as the red blob, the parton showers and hard final states resulting from the hard interaction are likewise painted red. Initial state radiation is marked as blue and a secondary semi-hard interaction with all its final states particles is illustrated in purple. The resulting color-neutral states and their decays are indicated in green, photons are indicated yellow. From [52].*

complex structure of the proton as composite particle [56].

Figure 2.9 illustrates all processes associated to a proton-proton collision, including the hard parton-parton interaction, initial- and final state radiation, another possible semi-hard interaction and all parton showers and hadronization.

Chapter 3

WZ diboson production in proton-proton collisions and vector boson polarisation

In this thesis, the cross section measurement of WZ diboson production is presented and the polarisation of W and Z vector bosons in WZ events will be estimated. This will be a first measurement of the boson polarisation pair-produced events using events from hadronic collisions. The following chapter provides an overview on the theoretical framework of WZ production in Section 3.2 and their polarisation in Section 3.3. A motivation for the choice of the WZ diboson channel is given in Section 3.1.

3.1 WZ production in the context of diboson processes

The properties of W and Z bosons and their couplings are strongly connected to the Electroweak Symmetry breaking mechanism. Any measurement on these bosons is a probe of this mechanism. Three diboson channels of the associated production of W and/or Z boson exist: WW, WZ and ZZ diboson production. Their measured total cross sections at $\sqrt{s}$ = 7, 8 and 13 TeV are compared in Figure 3.1 and set into the context of other ATLAS cross-section measurements.

Only fully leptonic decays of diboson events are considered, the most precise measurements on diboson production cross sections have been done on these decays with data from hadronic collisions: they reach a higher signal-to-background ratio and the measurement of leptons is more precise than that of hadronic jets. The ZZ decay to two lepton pairs with a well-defined dilepton invariant mass provides a clear signal in the detector. This channel reaches the highest signal-to-background ratio among the diboson channels, however, also the lowest cross section. WZ production has a cross section which is about three times higher than the ZZ cross section at $\sqrt{s}$ =13 TeV and the background contamination in the selected WZ events can still be kept at a reasonable level. WW production has the highest cross section among the diboson channels, however, the process cannot be distinguished easily from $t\bar{t}$ events which also decay to a W pair. $t\bar{t}$ events have a much higher cross section than WW events. Moreover, the reconstruction of the full event kinematics is not possible due to two neutrinos in the final state.

The production channel via the tri-boson vertex WWZ makes the WZ channel also an interesting probe for new physics: it allows to exclusively probe the WWZ vertex coupling strength.

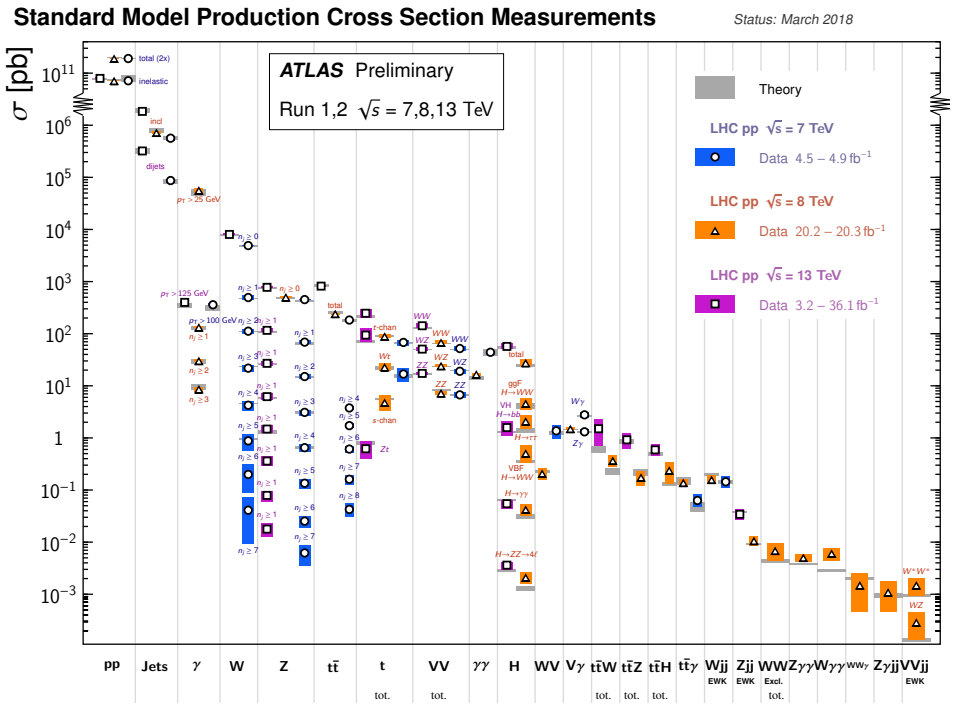

Figure 3.1 – *Results of selected total cross-section measurements using ATLAS data at a center-of-mass energy of $\sqrt{s}$ = 7, 8 and 13 TeV. All diboson measurements performed at these energies are indicated on this summary plot. From [57].*

3.2 WZ production and higher-order effects

Measuring the WZ production cross section and its properties directly probes the WWZ vertex which is given by the non-abelian structure of the Standard Model gauge theory and the Electroweak Symmetry Breaking mechanism. Precise knowledge of this coupling strength is a test of the Standard Model and allows to probe potential new physics. Knowledge of the production processes and limitations of the theory predictions are therefore of major importance. In the following, processes leading to the production of a WZ boson pair in a proton-proton collision are presented and higher-order corrections and theory uncertainties are depicted.

3.2.1 WZ production at leading order (LO)

At leading order, three diagrams contribute to the production of a WZ pair: the t- and u-channel (the scattering of a quark (q) and an anti-quark ($\bar{q}$)), shown in Figure 3.2 left and center, and the s-channel (quark-anti-quark annihilation), illustrated in Figure 3.2 on the right. The latter contains the triple-gauge vertex WWZ. The production of W^+Z at leading order mainly occurs via the scattering or the annihilation of a $u\bar{d}$ quark pair and via a $d\bar{u}$ quark pair to produce a W^-Z boson pair. At the LHC, a proton-proton collider, the cross section for W^+Z production is about 30% larger [58] than for W^-Z as the u-valence-quark density in the proton is larger than the d-valence quark density while the $\bar{u}$ and $\bar{d}$ contents in the proton are approximately the same [59].

W and Z bosons can undergo decays into quarks and leptons, whereas in this thesis, only leptonic decays to either electrons e or muons μ are considered. The Z decays leptonically into two same-flavour, opposite charged leptons ($Z \to \ell^+\ell^-$) and the W to one

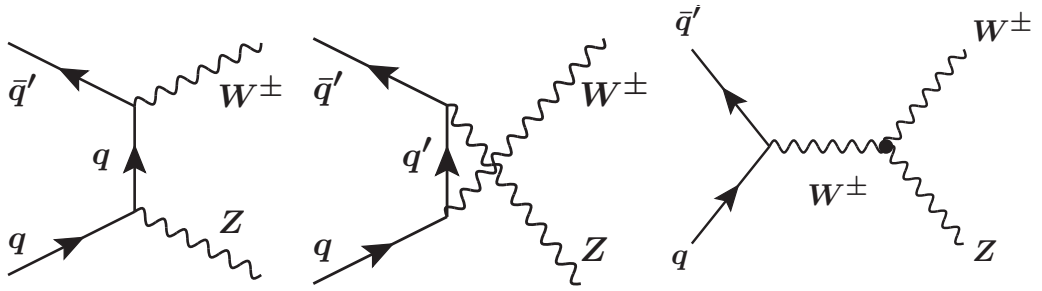

Figure 3.2 – *WZ production processes in a hadron collider: t-channel (left) and u-channel (center) quark-anti-quark scattering and s-channel quark-anti-quark annihilation (right).*

lepton and the corresponding (anti-)neutrino ($W \to \ell\nu_\ell$) giving rise to 4 different final states: $e\nu_e ee$, $\mu\nu_\mu\mu\mu$, $e\nu_e\mu\mu$ and $\mu\nu_\mu ee$, denoted as eee, $\mu\mu\mu$, $e\mu\mu$ and μee in the following, whereas the first position denotes the lepton from the W decay. The cross section for each of these channels is equal if the selection cuts are the same for electrons and muons. Interference effects occur in the eee and $\mu\mu\mu$-channels due to identical particles in the final state, however, they are at the per mille level as stated in [60].

One of the most characteristic features of WZ production at LO is a strong suppression of WZ events with scattering angles $\cos(\theta) = 0.1$ in W^-Z and $\cos(\theta) = -0.1$ in W^+Z events, where θ is the angle of the Z-boson with the quark direction in the WZ rest-frame. Therefore, the theory predicts a gap, the so-called approximate radiation zero, at central rapidity ($\cos(\theta) = \pm 0.1$) at leading order.

The concept of polarisation and helicity will be introduced later in Section 3.3.1, however it shall be mentioned here, that the approximate zero is a consequence of the cancellation of the dominant helicity state at a certain scattering angle: The WZ production cross section receives dominant contribution from t- and u- channel diagrams. Only these diagrams contribute to a production of a boson pair with the helicity combination left- and right transverse helicity which is the dominant helicity state. However, the production of this state is suppressed for scattering angles $\cos(\theta) = 0.1$ for W^-Z and $\cos(\theta) = -0.1$ for W^+Z. At energies relevant for WZ production at the LHC, only contributions for longitudinal-longitudinal and left- and right transverse polarised boson pairs contribute, all other states are strongly suppressed. Therefore, at $\cos(\theta) = \pm 0.1$, only boson pairs contribute where both bosons are longitudinally polarised [61].

3.2.2 Higher-order contributions and corrections to WZ production

3.2.2.1 Higher-order QCD corrections

It has been shown, for example in [58, 62], that the leading order cross section prediction does not provide a realistic description of the WZ production cross section and its properties. Higher-order calculations include new diagrams and topologies which have large contributions to the cross section, the WZ production cross section would be strongly underestimated by neglecting them. A deficit in the predicted cross section with respect to the measurement result could lead to a mis-interpretation of the results as new physics effect, in addition, higher-order corrections mostly contribute strongly in regions of phase space where new physics is expected, should it exist in this measurement channel.

At higher order, the full leading-order effects are included as well as additional virtual contributions from loops and real radiation of quarks or gluons. The next-to leading order prediction contains virtual contributions from one gluon loop (final state: $q\bar{q}' \to WZ$) and real emission processes. Real emissions processes imply the radiation of a gluon from an initial state quark resulting in the final state $q\bar{q}' \to WZg$, and gluon-quark induced vector-boson production in association with one quark where the second vector-boson is either radiated from the final state quark or the vector boson, the corresponding final state is $qg \to WZq'$. Latter process mostly proceeds as follows: a W or Z boson with high transverse momentum recoils against a quark with large transverse momentum. In most cases the quark or also the boson radiates a soft and collinear boson. This topology contains a boson with high transverse momentum and a quark with a collinear boson. The bosons are therefore produced centrally and dilute the approximate zero and deform the boson transverse momentum spectrum, especially at large transverse momentum. These topologies have a sizable contribution to the WZ production process.

Present state-of-the art theory predictions, for instance [59, 62], are NNLO accurate and contain, besides all NLO calculations, two-loops virtual corrections to the final state $q\bar{q}' \to WZ$, one-loop virtual corrections to the NLO diagrams and two parton emissions. The calculations provided in [59] further contain off-shell effects and spin-correlations, non-resonant, single-resonant and double-resonant components. Therefore, a calculation of fully differential distributions and fiducial cross sections can also be provided.

In [62], the center-of-mass energy dependent predicted inclusive cross sections are compared at leading order, next-to-leading order and next-to-next-to leading order. At $\sqrt{s} = 13$ TeV, the NLO calculation increases the W^+Z cross section by $\frac{\sigma_{NLO}}{\sigma_{LO}} = 79.0\%$ and the W^-Z cross section by $\frac{\sigma_{NLO}}{\sigma_{LO}} = 83.1\%$ with respect to LO. Going from NLO to NNLO further increases the cross section by $\frac{\sigma_{NNLO}}{\sigma_{NLO}} = 10.9\%$ and 11.0% for W^+Z and W^-Z, respectively. Figure 3.3 compares the inclusive cross section as a function of the center-of-mass energy $\sqrt{s}$ for leading order, next to leading order and next-to-next-to leading order. The diagrams entering at NNLO show a sizeable contribution with respect to NLO, the theoretical uncertainties, which estimate the contribution of missing higher-order diagrams, underestimate the NNLO contribution. However, all partonic production channels are now included at NNLO and a convergence of the perturbative series is visible, the theory uncertainty on the NNLO cross section is expected to estimate correctly the contribution of higher-order contributions. This is also supported by the comparison of the NNLO prediction with the experimental results of the WZ total cross section done at $\sqrt{s} = 8$ TeV [12, 62] and at $\sqrt{s} = 13$ TeV [15]: a good agreement of the NNLO prediction with the experimental results is observed. Figure 3.3 also indicates that going from LO to NLO yields large corrections. These are a consequence of the cancellation of the dominant helicity state at one specific region of phase space (approximate zero) at LO and of the contribution of the diagram $qg \to WZq'$ as explained above.

3.2.2.2 Electroweak corrections

Electroweak corrections at NLO precision to the WZ production cross section have been assessed for example in [63–66]. They include next-to-leading order effects taking into account virtual one-loop photon corrections and real emissions of one photon, $q\bar{q} \to WZ\gamma$, denoted quark-induced EW processes in the following. More recent calculations [65, 66] take also photon-quark-induced processes into account: $q\gamma \to WZq'$. A family of new WZ production diagrams contribute where the W is either radiated from the initial-state (anti-

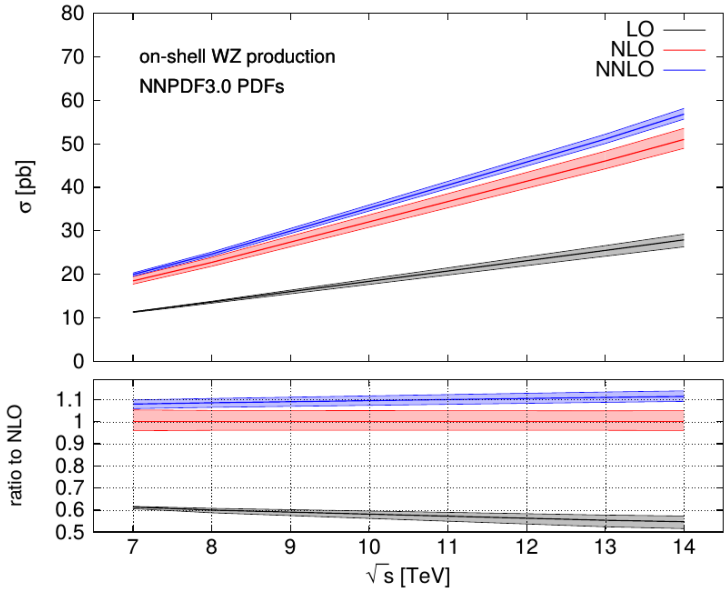

Figure 3.3 – *Comparison of next-to-leading order inclusive cross section with leading order and next-to-next-to leading order as a function of the center-of-mass-energy $\sqrt{s}$. The ratio-plot shows the cross sections normalized to next-to-leading order. The theory bands include the impact of scale variations which are explained in section 3.2.3. From [62].*

)quark or photon, from the final-state (anti-) quark or from the final-state Z. Two examples of these new diagrams can be seen in Figure 3.4. The calculations performed in [66] include also off-shell effects for LHC collisions at a center-of-mass energy of $\sqrt{s} = 13$ TeV.

Two processes contribute to the EW corrections, however with a different sign: quark-induced processes and photon-quark induced processes. Photon-quark induced processes always increase the cross section in the entire phase-space, while quark-induced processes in overall decrease the cross section. Photon-quark induced processes only partly compensate the quark-induced processes.

The amount of EW correction depends on the kinematic region and are sizeable in particular in regions with high partonic center-of-mass energy [64]. The effect of the electroweak correction on the total cross section is small as most WZ events are produced with a low diboson invariant mass. Quark-induced EW processes cause negative corrections of about -5% at low boson transverse momentum p_{T}, these rise to about -25% at a boson p_{T} of 600 GeV in the measurement phase space. Virtual quark-induced processes contribute mostly to this large negative correction at high boson p_{T}. Photon-quark induced processes partly compensate these corrections, they amount to 15-25% at a boson p_{T} of 600 GeV, depending on the W-charge and the boson [66].

In [66], corrections to the total cross section from electroweak correction were estimated to -1.3% for W^+Z and to -1.1% for W^-Z[1]. Cuts on the kinematic regions of phase space impact the magnitude of the electroweak corrections as radiative tails of the boson kinematic distributions are reduced. In a phase space close to the measurement phase of this analysis, corrections to the inclusive cross section amount to about -4%. These

[1]Calculations were done for the WZ decay to the final states $\mu^+\mu^- e^\pm \nu_e$ and $\mu^+\mu^-\mu^\pm\nu_\mu$. Electroweak corrections to leptons before any QED final state radiation have been derived ("Born leptons"). Final state radiation is combined with the closest lepton if it is within a cone of $\Delta R_{\ell,\gamma} < 0.1$ around the lepton.

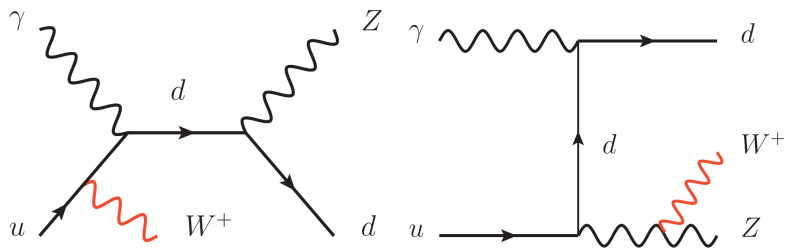

Figure 3.4 – *Two examples for photon-quark induced processes. From [65].*

electroweak corrections are not included in simulations and are therefore not implemented in the analysis and not applied on the predictions yet.

3.2.3 Theory uncertainties

Due to missing higher-orders, the theory predictions have a limited precision. The theory uncertainty considers parametric uncertainties, such as the experimental precision on W and Z masses, the uncertainty on the PDF and the impact of missing higher-order diagrams. The uncertainty on the W and Z masses have a negligible impact, it affects the predicted cross section by less than 0.2% and can therefore, according to [65], be safely neglected.
The parton density is obtained by fitting experimental data and has a limited precision due to the uncertainty on the fit. One way to estimate the impact of this uncertainty on the predicted cross section is to calculate the cross section using several different PDF sets, obtained using different methods and data, and to compare the results.

Another way to estimate the uncertainty due to the limited knowledge of the PDF is to use the uncertainties of the fit with which the PDF has been obtained. Some of the fit parameters are correlated, the covariance matrix of the fit is diagonalized and the physical quantity of interest is recalculated by varying the PDF in the direction of one eigenvector by the square root of the corresponding eigenvalue [67–69]. The PDF uncertainty on the physical quantity of interest Q is then calculated by

$$\Delta Q = \sqrt{\frac{1}{2}\sum_i (Q(E_i^+) - Q(E_i^-))^2}, \tag{3.1}$$

where $E_i^{\pm}$ are the PDF sets obtained with the variations in the direction of the eigenvector.

A dependence on an energy scale due to renormalization procedures remains in the theoretical calculations as they only account for diagrams up to next-to-next-to leading order or even next-to leading order only, see Section 2.1.1.1. This scale dependence can be used to estimate the impact of truncated missing higher-order diagrams. The standard procedure is to vary these renormalization scales.

Two scales are introduced: one scale is introduced by factorization (factorization scale μ_{F}) and one by renormalization (renormalization scale μ_{R}) as defined in Sections 2.2.1 and 2.2.2, respectively. The value of the central scales μ_0 implemented can differ depending on the simulation. The standard choice for the scale variations is $\frac{1}{2}\mu_0 \leq \mu_R = \mu_F \leq 2\mu_0$ whereas μ_{F} and μ_{R} are varied independently. The higher the perturbative order of the cross section calculation, the lower the scale uncertainty: The scale uncertainty on the total cross section was estimated to be 5% at NLO and 2% at NNLO [62].

3.2.4 Prediction for the WZ cross section

Higher-order corrections to WZ production and the precision of current state-of-the-art calculations have already been discussed in Section 3.2.2.1. Predictions of WZ productions are NNLO accurate in QCD and cross sections are provided by the MATRIX code [59]. As these calculation also contain off-shell and spin-correlation effects, non-resonant, single and double-resonant components, differential cross sections as well as cross sections in restricted phase spaces can be extracted. A restricted phase space can for example be the phase space in which the measurement is performed defined by the acceptance of the detector and the selection criteria of the measurement. In this analysis, the cross section of WZ production in the phase space defined by the detector acceptance contains only fully leptonic decays of the bosons to electrons, muons and/or tau-leptons and is denoted as "fiducial" cross section. The fiducial phase space will be defined later in Section 7.1.1, the fiducial cross section will be anticipated here. Note that the fiducial cross section is defined with respect to the decay to one fully leptonic decay channel, the total cross section is defined by the WZ production cross section with decays to all possible final states to hadrons and leptons. The different orders of magnitude of total and fiducial cross sections is therefore partly attributed to the small branching ratios of the fully leptonic decay channels.

The only restriction in the definition of the total phase space is a resonant Z in the final state with an invariant mass m_Z in $66 < m_Z < 116$ GeV.

NNLO predictions for WZ production in the total phase space yield:

$$\sigma^{\text{tot.PS}}_{W^\pm Z,\,\text{MATRIX}} = 49.6 \pm 0.06\,(\text{stat.})^{+1.1}_{-1.0}\,(\text{scale})\ \text{pb}. \tag{3.2}$$

In the fiducial phase space, the cross section is calculated as

$$\sigma^{\text{fid.PS}}_{W^\pm Z,\,\text{MATRIX}} = 64.0 \pm 0.02\,(\text{stat.})^{+1.5}_{-1.3}\,(\text{scale})\ \text{fb}. \tag{3.3}$$

The uncertainties contain statistical uncertainties on the Monte Carlo sample and uncertainties from QCD scale variations. The nominal renormalization and factorization scales were fixed to $(m_Z + m_W)/2$ in MATRIX, where m_Z and m_W are the masses of the Z and the W bosons, respectively. The cross section is calculated using particles before the simulation of the detector response. Note that the calculation contains no electroweak corrections.

Figure 3.5 shows the NNLO prediction provided by MATRIX in comparison with the WZ cross-section measurements at $\sqrt{s}$ =7, 8 and 13 TeV on ATLAS data. For comparison, the plot also displays the prediction at NLO. Good agreement is observed for ATLAS measurements and the NNLO prediction by MATRIX.

MATRIX can only provide distributions at generator level, it includes no detector simulation. To compare to data distributions measured with the detector, other MC samples are necessary which are interfaced to the GEANT4 ATLAS detector simulation [70]. Four complementary samples simulating WZ boson pair production and their leptonic decay are available, however, only at NLO precision in QCD.

The baseline model used to predict the signal process is based on the Powheg Box simulation [71] for the matrix element modelling at NLO precision in QCD. It is interfaced with the Pythia8 [72] parton shower model. Dynamic renormalization and factorization QCD scales are implemented equal to $m_{WZ}/2$, where m_{WZ} is the invariant mass of the WZ system.

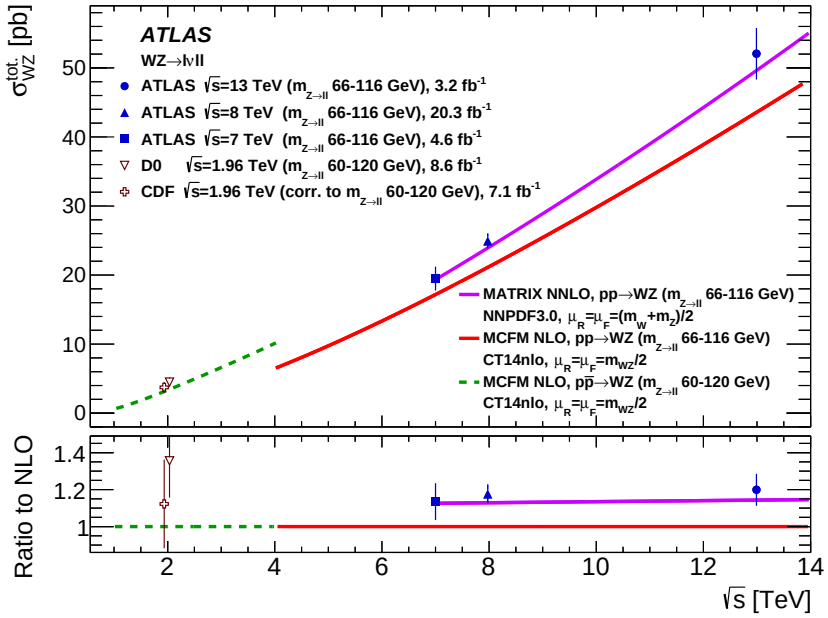

Figure 3.5 – *Comparison of the total cross section calculcated at NLO precision in QCD and the recent NNLO predictions by MATRIX with the WZ cross-section measurements at $\sqrt{s} = 7$, 8 and 13 TeV with ATLAS data. From [15].*

Process	Generators	order in QCD	PDF	k-factor
$WZ \to \ell\nu\ell\ell$	Powheg+Pythia8	NLO	NLO CT10	1.18
$WZ \to \ell\nu\ell\ell$	Powheg+Herwig	NLO	NLO CT10	1.18
$WZ \to \ell\nu\ell\ell$	Sherpa 2.2.2	$WZ + q$: NLO, $WZ + 3q$: LO	NNLO NNPDF30	1.0
$WZ \to \ell\nu\ell\ell$	MC@NLO	NLO	NLO CT10	1.18
$WZ \to \ell\nu\ell\ell$	MATRIX	NNLO	NNPDF3.0nnlo	-

Table 3.1 – *Summary of signal MC simulations. Based on [82].*

To estimate the uncertainty due to the modelling of the parton shower, Powheg is alternatively interfaced with the Herwig [73] parton shower model. A global rescaling factor of 1.18 to correct the prediction of the WZ Powheg+Pythia8 and Powheg+Herwig MC from NLO to NNLO, denoted k-factor, has been derived based on the prediction provided by MATRIX in the fiducial phase space of the ATLAS analysis.

An alternative prediction by Sherpa 2.2.2 [74–81] is available at NLO precision in QCD for WZ plus one parton and at LO for WZ in association with up to three partons. The event can contain still more partons in the final state but these arise from the parton shower. The Sherpa model is therefore able to provide a more reliable prediction for events with up to three hadronic jets, while the Powheg+Pythia8 prediction at NLO is only reliable for up to one hadronic jet, especially for differential distribution as a function of the number of jets.

A further MC simulation, MC@NLO, is available [53]. This simulation uses the Herwig parton shower model.

Table 3.1 provides an overview of all signal simulations and their most important features.

3.3 Vector boson polarisation

Recently, an increased interest of theorists in angular variables, which are sensitive to polarisation, has been noted, for example in [24, 83–85]. New physics affecting the triple gauge vertex present in WZ diboson production would affect distributions sensitive to large partonic center-of-mass energy, but could also be observed through a modification of the vector boson polarisation and angular variables. Vector boson scattering (VBS) mediated by the Higgs cancels the divergence of the VBS cross section with energy caused by the scattering of two longitudinal bosons. A measurement of the scattering of longitudinal bosons would therefore be very sensitive to new physics [24]. Due to lack of statistics, latter process is out of reach, but these examples clearly motivate to start looking into polarisation of W and Z bosons. Within the scope of this thesis, the first polarisation measurement of the bosons in pair-produced events in hadronic collisions will be performed, the theoretical framework will be presented in the following.

3.3.1 Polarisation of spin 1 particles

Helicity is defined as the projection of the particle's spin $\vec{s}$ on its momentum $\vec{p}$, $\vec{s}\cdot\vec{p}$. Is the spin aligned with the momentum, the particle is transversely polarised. A particle with spin parallel to its momentum is defined as right-handed, denominated with the index "R" in the following, a particle with spin anti-parallel to its direction of motion as left-handed transversely polarised, marked with the index "L". Three spin eigenstates exist for spin 1 particles: $0, \pm 1\hbar$, therefore, for massive bosons, a third polarisation state is possible, the longitudinal polarisation corresponding to helicity zero, denoted with the index "0" in the following. Note that the helicity is not lorentz invariant for massive particles but dependent on the reference frame of the measurement: if a particle is slower than the speed of light, a reference frame R_f faster than the particle's reference frame exists. Going to the reference frame R_f, the helicity would flip as the particle's direction of motion changes in the frame R_f. Massless spin 1 particles, like the photon, can only take transverse polarisation states.

In the Standard Model, the mass terms from W and Z bosons come from the Electroweak Symmetry Breaking mechanism. Without EWSB, W and Z bosons were massless and would only exist in transversely polarised states. In EWSB, three degrees of freedom enter through the three Goldstone bosons appearing due to the nature of the vacuum ground state. These degrees of freedom are absorbed by the three vector bosons and become their longitudinal polarised component and the bosons acquire a mass. The existence of the longitudinal component in vector boson polarisation is therefore directly related to the EWSB mechanism.

The polarisation vectors are defined as follows, according to [86]:

$$\begin{aligned} \epsilon_\mu(\pm 1) &= \frac{1}{\sqrt{2}}(0; \pm 1, -i, 0), \\ \epsilon_\mu(0) &= (0; 0, 0, 1). \end{aligned} \tag{3.4}$$

3.3.2 The reference frame for the polarisation measurement

Variables sensitive to polarisation effects are necessary to extract polarisation information on the bosons. Angular variables have been shown to be very sensitive to polarisation.

The variable which is used to discriminate between the different polarisation states in the measurement presented in this thesis is the cosine of the angle θ^*. The angle θ^* is the decay angle of one of the leptons ℓ_{pol} from the W (Z) boson decay in the restframe of the

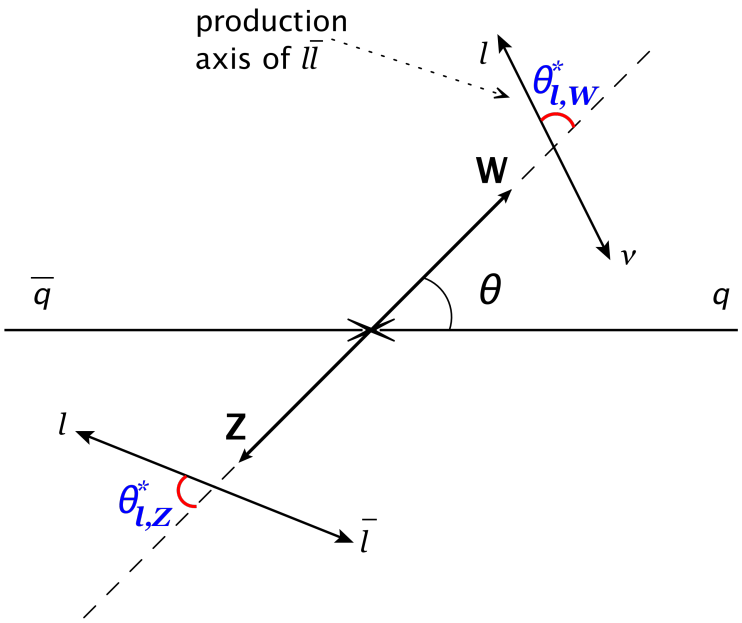

Figure 3.6 – *Illustration of the angular variables used as a discriminant in the polarisation measurement. The angle θ^* is the angle between the lepton in the restframe of the boson with respect to the boson boost in the WZ restframe. To measure the W polarisation, the decay angle between the charged lepton and the W boost in the WZ restframe is used, in case of a Z polarisation measurement, the angle is measured with respect to the negative lepton from the Z decay. From [82].*

W (Z) boson with respect to the W (Z) boson boost in the WZ restframe. In case of a Z boson polarisation measurement, the angle is defined with respect to the negatively charged lepton of the Z decay and in case of a W boson polarisation measurement, with respect to the charged lepton of the W decay. In Figure 3.6, the angles $\theta^*_{\ell,W}$ and $\theta^*_{\ell,Z}$ in the WZ system relevant for the polarisation measurements are illustrated. The azimuthal angle ϕ is defined as the angle around the W or Z boson axis, it is not drawn in Figure 3.6.

The definition of the WZ and the W restframes require the knowledge of the neutrino longitudinal momentum. This quantity is not accessible in the detector as the neutrino does not leave any signal in the detector. Only the transverse component of the neutrino momentum can be assessed using momentum conservation in the transverse plane as will be detailed later in Section 4.3.4. Using the charged lepton from the W decay and the missing transverse energy from the neutrino and imposing the W mass, the neutrino longitudinal momentum can be extracted by solving the resulting quadratic equation. In case of two solutions, the solution for the neutrino longitudinal momentum with the smaller absolute value is used. It has been checked that this procedure does not introduce any bias.

To avoid the reconstruction of the longitudinal neutrino momentum, the variable $\cos(\theta^*_{2D})$ is introduced: All lepton and boson momenta are projected in the transverse plane. The angle θ^*_{2D} is defined as the angle between the transverse momentum of the leptons in the transverse W restframe and the W boost in the transverse plane with respect to the transverse WZ boost. It has been introduced in the W polarisation measurement with $\sqrt{s} = 7$ TeV ATLAS data [25].

The discriminating power and the properties of the $\cos(\theta^*)$ distribution of the different polarisation states can be intuitively derived using considerations on angular momentum conservation. The case is easier for W bosons, as the W couples exclusively to left-handed

leptons and right-handed anti-leptons, it will be shortly illustrated for the W^- polarisation: If the W^- is right-handed, angular momentum conservation dictates that most of its momentum is transferred to the right-handed anti-neutrino. This anti-neutrino is therefore emitted collinearly to the W boson according to momentum conservation. In the restframe of the W boson, its decay products are emitted back-to-back in an angle of 180° relative to each other. The angle θ^* between the lepton and the boson boost will therefore be close to 180°, $\cos(\theta^*)$ close to -1. If the W^- is left-handed, the left-handed lepton ℓ^- will get most of its momentum and the angle $\cos(\theta^*)$ between the lepton direction and the boson boost will be small, $\cos(\theta^*)$ will have values close to 1.

In case of W^- polarisation, the template representing left-handed polarisation states will therefore be accumulated around $\cos(\theta^*) = 1$, for right-handed polarisation, the values of $\cos(\theta^*)$ will be accumulated around -1. Using the same argumentation, it can be verified that longitudinal bosons give their momentum in similar fractions to their decay products, θ^* therefore will be close to 90° and $\cos(\theta^*)$ will have values around zero.

In principle, the same arguments can be applied to intuitively derive the shape of the polarisation templates in case of the Z, however, it has to be considered, that the Z couples to both, left- and right-handed leptons, however, with a preference.

Using this simple argumentation, it becomes clear that the polarisation can be assessed using the variable $\cos(\theta^*)$. In the following sections, the analytic form of the angular distributions of the pure polarisation states will be derived.

3.3.3 The spin-density matrix

The complete polarisation properties of the boson are given by the spin-density matrix. The spin-density matrix is a 3x3 matrix with the diagonal elements related to the pure polarisation states. The interference between the polarisation states is given by the off-diagonal elements. A set of helicity cross sections σ^α can be defined according to [86, 87], which are related to linear combinations of the helicity density matrix elements $H_{mm'}$. The helicity cross sections σ^α relevant for this thesis are defined as following, for details see for instance [87]:

$$\begin{aligned} \sigma^{\mathrm{U+L}} &\sim H_{00} + H_{++} + H_{--}, \\ \sigma^{\mathrm{L}} &\sim H_{00}, \\ \sigma^{\mathrm{P}} &\sim H_{++} - H_{--}, \end{aligned} \tag{3.5}$$

where σ^{L} is the cross section for the longitudinal polarisation state of the gauge bosons, σ^{P} the difference between left- and right handed transverse polarisation cross sections and $\sigma^{\mathrm{U+L}}$ is the production cross section, denoted as unpolarised cross section. The other helicity cross sections, which are not shown here, are interference cross sections between the polarisation states.

The angular dependence of the cross section can be expressed as a sum over the nine helicity cross sections σ^α multiplied by harmonic polynomials $g_i(\theta^*, \phi)$:

$$\frac{d\sigma}{dp_{\mathrm{T}}^2 dy d\cos(\theta^*) d\phi} = \sum_{i=1}^{9} g_i(\theta^*, \phi) \frac{3}{16\pi} \frac{d\sigma^i}{dp_T^2 dy}. \tag{3.6}$$

The harmonic polynomials are dependent on the angles θ^* and ϕ spanned by the lepton from the boson decay in the boson restframe and the boson boost in the WZ restframe.

These angles have already been defined in Section 3.3.2. Equation (3.6) can be rewritten specifying the harmonic polynomials and defining angular coefficients A_i:

$$\begin{aligned}\frac{d\sigma}{dp_{\mathrm{T}}^2 dy d\cos(\theta^*) d\phi} = \\ \frac{3}{16\pi}\frac{d\sigma^{\mathrm{U+L}}}{dp_{\mathrm{T}}^2 dy}\Big[\\ (1+\cos^2(\theta^*)) + \frac{1}{2}A_0(1-3\cos^2(\theta^*) + A_1\sin(2\theta^*)\cos(\phi) + \frac{1}{2}A_2\sin^2(\theta^*)\cos(2\phi) + \\ A_3\sin(\theta^*)\cos(\phi) + A_4\cos(\theta^*) + A_5\sin^2(\theta^*)\sin(2\phi) + \\ A_6\sin(2\theta^*)\sin(\phi) + A_7\sin(\theta^*)\sin(\phi)\Big].\end{aligned} \tag{3.7}$$

The unpolarised cross section has been factored out on the right-hand side of equation 3.7. The components A_i, $i \in \{0, 1, ..., 7\}$, are therefore proportional to the ratios between the helicity cross sections σ^{α} and the unpolarised cross sections $\sigma^{\mathrm{U+L}}$. The components A_i relevant here are related to the helicity cross sections as follows:

$$\begin{aligned}A_0 &= \frac{2d\sigma^{\mathrm{L}}}{d\sigma^{\mathrm{U+L}}}, \\ A_4 &= \frac{2d\sigma^{\mathrm{P}}}{d\sigma^{\mathrm{U+L}}}.\end{aligned} \tag{3.8}$$

The coefficients A_i are a function of the rapidity and the transverse momentum of the boson and all decay angles have been factorized in equation (3.7). The A_i coefficients are therefore independent of the decay kinematics and are only dependent on the dynamics of the WZ production [27]. Assuming symmetry in the azimuthal angle ϕ, one obtains by integrating over ϕ:

$$\frac{d\sigma}{d\cos(\theta^*)dp_{\mathrm{T}}^2 dy} = \frac{3}{8}\frac{\sigma^{\mathrm{U+L}}}{dp_{\mathrm{T}}^2 dy}\big[(1+\cos^2(\theta^*)) + A_0\frac{1}{2}(1-3\cos^2(\theta^*)) + A_4\cos(\theta^*)\big], \tag{3.9}$$

3.3.4 Analytical expression for vector boson polarisation

From equations (3.5) and (3.8), it is obvious that the coefficients A_0 and A_4 are related to the pure polarisation states of the boson, namely left- (f_L) and right transverse (f_R) and longitudinal (f_0) polarisation as follows in case of the W boson [25]:

$$\begin{aligned}f_0 &= \frac{1}{2}A_0, \\ f_L - f_R &= \mp\frac{A_4}{2}.\end{aligned} \tag{3.10}$$

Note that the coefficients A_i and therefore also $f_i, i \in \{0, L, R\}$ are dependent on the boson transverse momentum p_{T} and rapidity y.
The angular distribution of the W-boson can therefore be expressed in terms of the pure polarisation states cross section using equation (3.9):

$$\frac{1}{\sigma^{\mathrm{U+L}}}\frac{d\sigma}{d\cos(\theta^*)} = \frac{3}{8}f_L(1\mp\cos(\theta^*))^2) + \frac{3}{8}f_R(1\pm\cos(\theta^*))^2 + \frac{3}{4}f_0\sin^2(\theta^*), \tag{3.11}$$

where the upper sign is for W^+ and the lower sign for W^- polarisation. The fractions $f_i, i \in \{0, L, R\}$ are pure polarisation cross sections normalized by the unpolarised cross sections, therefore, they sum up to one:

$$f_L + f_R + f_0 = 1 \tag{3.12}$$

The corresponding equation for the Z boson is equivalent, however, the Z coupling to right- and left-handed fermions has to be considered [85], whereas W-bosons only couple to left-handed fermions:

$$\begin{aligned}\frac{1}{\sigma^{\mathrm{U+L}}}\frac{d\sigma}{d\cos(\theta^*)} = \frac{3}{8}f_L(1+\cos(\theta^*)^2 - 2\cdot\frac{2\cdot c_v c_a}{c_v^2+c_a^2}\cos(\theta^*)) + \frac{3}{8}f_R(1+\cos(\theta^*)^2 \\ +2\cdot\frac{2\cdot c_v c_a}{c_v^2+c_a^2}\cos(\theta^*)) + \frac{3}{4}f_0\sin^2(\theta^*),\end{aligned} \tag{3.13}$$

where $c_v = -\frac{1}{2} + 2\sin^2(\theta_W)$ is the vector and $c_a = -\frac{1}{2}$ is the axial vector coupling of the Z boson to leptons and θ_W the weak mixing angle. The factor $\frac{2\cdot c_v c_a}{c_v^2+c_a^2}$ will be denoted as C_W in the following.

From equations (3.11) and (3.13), it becomes clear that each polarisation is associated with a specific angular distribution of the decay lepton. The $\cos(\theta^*)$-distribution can therefore be fit with the functions given in equations (3.11) and (3.13) given that the system is symmetric in the azimuthal angle ϕ.

Examples of the distributions of $\cos(\theta^*)$ are given in Figure 3.7: the $\cos(\theta^*)$ distribution of polarised bosons and their sum are shown.

However, fiducial cuts destroy the symmetry in ϕ and equations (3.11) and (3.13) do not describe the $\cos(\theta^*)$ distribution in data where fiducial cuts are applied. Models which describe the behaviour of polarised bosons have to be created.

3.3.5 Generation of MC samples with bosons in a single polarisation state

The expressions derived in Section 3.3.4 can now be used to generate samples of purely polarised bosons to have a model of their properties. The Powheg+Pythia8 sample introduced in Section 3.2.4 containing all possible polarisation states are reweighted such that all information on the polarisation of one of the bosons is removed and that the sample generates a flat $\cos(\theta^*)$ distribution for either the Z or W reference lepton. For this, the polarisation fractions in the sample have to be known. Further weighting of this sample by a polynomial, the components proportional to f_i, with $i \in \{0, L, R\}$, of equations (3.11) or (3.13) for instance, will then cause the $\cos(\theta^*_W)$ or $\cos(\theta^*_Z)$ distribution of the reweigthed MC sample to take the shape of that polynomial.

To determine the polarisation in the MC model in an unbiased way, the leptons have to be correctly assigned to the mother boson. To reconstruct the WZ pair and to assign the leptons to the mother bosons, truth information available in the MC sample is used.

An analytic fit of equation (3.11) or (3.13) generated with the $\cos(\theta^*_{W(Z)})$ distribution of the MC sample is performed. Examples of this analytic fit are shown in Figure 3.7 for the W^+ and the W^- on the top and for the Z in association with a W^+ and a W^- on the bottom. Note that the polarisation fractions are extracted as a function of p_{T} and the rapidity. The fits illustrated here are inclusive over p_{T} and the rapidity. The polarisation is

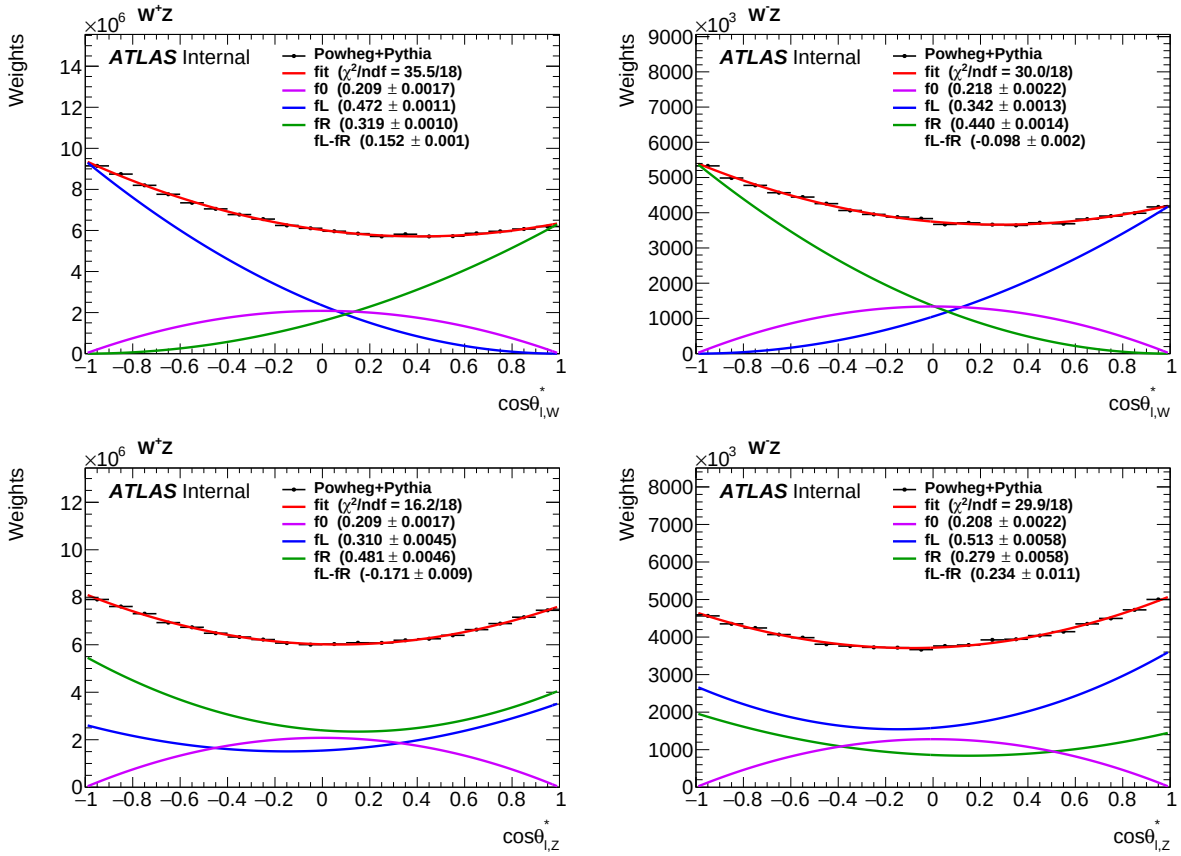

Figure 3.7 – *Analytic fit to the* $\cos(\theta^*)$ *distribution in MC in the total phase-space using equation (3.11)(equation (3.13)) to describe the* $\cos(\theta^*)$ *distribution in* W *(top) (*Z*, bottom). On the left, the fit is shown for* W^+ *or* Z *polarisation in* W^+Z *events. On the right, the same is shown for* W^-Z *events. From [82].*

dependent on the production mode of the boson, which in turn depends on p_{T}. Figure 3.8 illustrates the dependence of the extracted polarisation fractions in the MC on p_{T} and the rapidity for some examples.

By weighting the events with the inverse of equation (3.11), information on the W polarisation is removed, weighting by the inverse of equation (3.13) removes information on the Z polarisation from the MC sample. Weighting then by the polynomials of equation (3.11) or equation (3.13) proportional to f_i, with $i \in \{0, L, R\}$, then creates MC samples representing one polarisation state. The weights to create samples containing polarised W bosons are given by equation (3.14):

$$w_{0,\mathrm{L,R}} = \frac{\frac{1}{\sigma^{\mathrm{U+L}}_{W^\pm Z}} \frac{d\sigma_{W^\pm Z}}{d\cos\theta^*_{\ell,W}}|_{0,\mathrm{L,R}}}{\frac{3}{8} f_{\mathrm{L}}(1 \mp \cos\theta^*_{\ell,W})^2 + \frac{3}{8} f_{\mathrm{R}}(1 \pm \cos\theta^*_{\ell,W})^2 + \frac{3}{4} f_0 \sin^2\theta^*_{\ell,W}}, \tag{3.14}$$

where

$$\begin{aligned}
\frac{1}{\sigma^{\mathrm{U+L}}_{W^\pm Z}} \frac{d\sigma_{W^\pm Z}}{d\cos\theta^*_{\ell,W}}|_0 &= \frac{3}{4}\sin^2\theta^*_{\ell,W}, \\
\frac{1}{\sigma^{\mathrm{U+L}}_{W^\pm Z}} \frac{d\sigma_{W^\pm Z}}{d\cos\theta^*_{\ell,W}}|_{\mathrm{L}} &= \frac{3}{8}(1 \mp \cos\theta^*_{\ell,W})^2, \\
\frac{1}{\sigma^{\mathrm{U+L}}_{W^\pm Z}} \frac{d\sigma_{W^\pm Z}}{d\cos\theta^*_{\ell,W}}|_{\mathrm{R}} &= \frac{3}{8}(1 \pm \cos\theta^*_{\ell,W})^2.
\end{aligned} \tag{3.15}$$

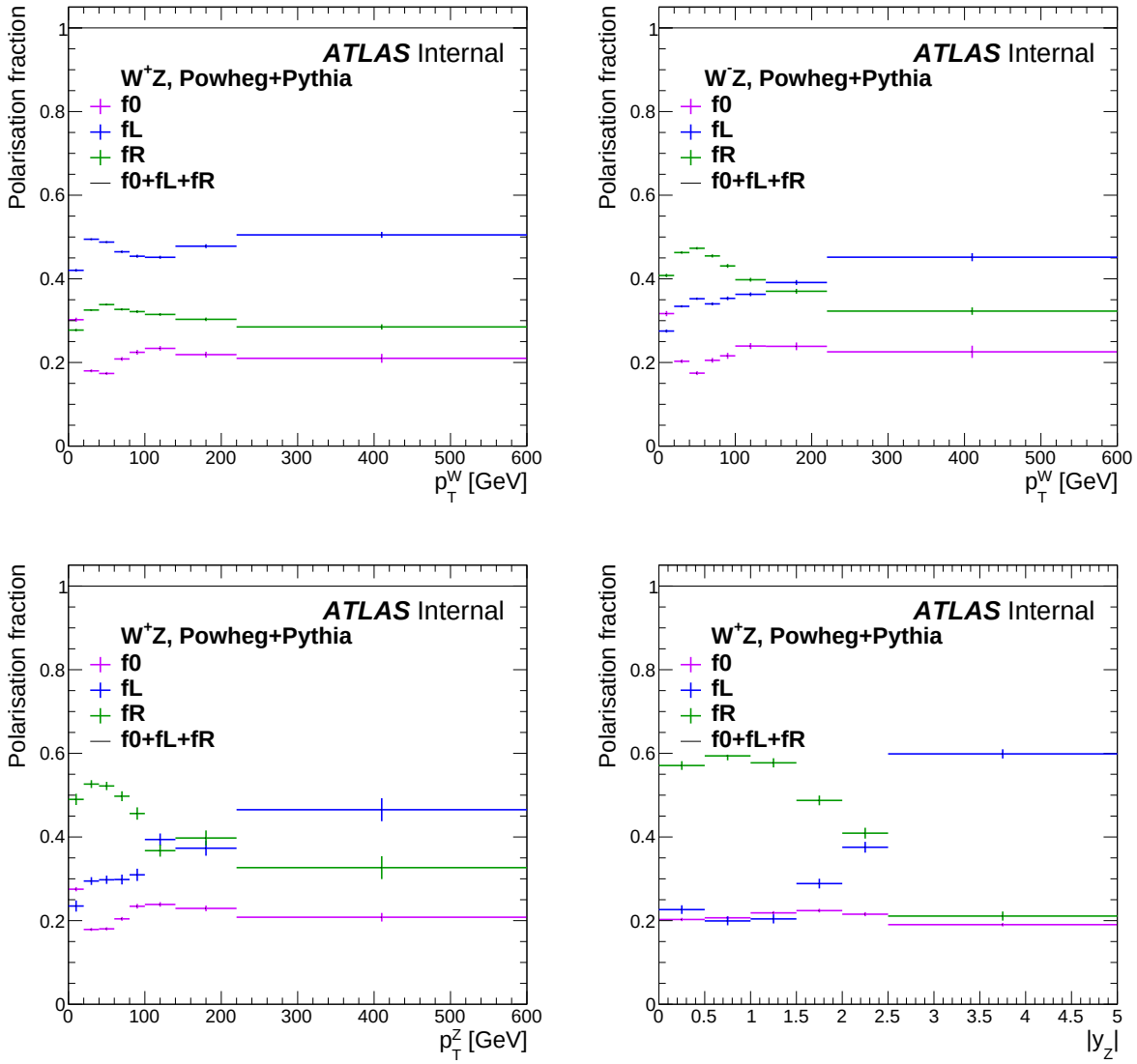

Figure 3.8 – *Examples of the dependence of the polarisation fractions on the boson p_{T} and the boson rapidity. In the top row, the polarisation fractions as a function of p_{T} in the total phase-space are shown for W^+ (left) and W^- (right) bosons. In the bottom row, the polarisation of Z in W^+Z events as a function of the p_{T} of the Z boson is shown on the left and as a function of the Z rapidity on the right. From [82].*

To create samples containing Z bosons with a single polarisation state, the weights defined by equation (3.16) are applied:

$$w_{0,\mathrm{L,R}} = \frac{\frac{1}{\sigma^{\mathrm{U+L}}_{W^\pm Z}} \frac{d\sigma_{W^\pm Z}}{d\cos\theta^*_{\ell,Z}}\big|_{0,\mathrm{L,R}}}{\frac{3}{8}f_{\mathrm{L}}(1+2C_W\cos\theta^*_{\ell,Z}+\cos^2\theta^*_{\ell,Z}) + \frac{3}{8}f_{\mathrm{R}}(1+\cos^2\theta^*_{\ell,Z}-2C_W\cos\theta^*_{\ell,Z}) + \frac{3}{4}f_0\sin^2\theta^*_{\ell,Z}}, \tag{3.16}$$

where

$$\begin{aligned}
\frac{1}{\sigma^{\mathrm{U+L}}_{W^\pm Z}}\frac{d\sigma_{W^\pm Z}}{d\cos\theta^*_{\ell,Z}}|_0 &= \frac{3}{4}\sin^2\theta^*_{\ell,Z},\\
\frac{1}{\sigma^{\mathrm{U+L}}_{W^\pm Z}}\frac{d\sigma_{W^\pm Z}}{d\cos\theta^*_{\ell,Z}}|_{\mathrm{L}} &= \frac{3}{8}(1+2C_W\cos\theta^*_{\ell,Z}+\cos^2\theta^*_{\ell,Z}),\\
\frac{1}{\sigma^{\mathrm{U+L}}_{W^\pm Z}}\frac{d\sigma_{W^\pm Z}}{d\cos\theta^*_{\ell,Z}}|_{\mathrm{R}} &= \frac{3}{8}(1+\cos^2\theta^*_{\ell,Z}-2C_W\cos\theta^*_{\ell,Z}).
\end{aligned} \tag{3.17}$$

Note that the weak mixing angle enters here through the expression C_W in equation (3.16). In the denominator of equation (3.16), the weak mixing angle implemented internally in the simulation has to be applied. To reweight to a single polarisation state, the weak mixing angle corresponding most to the data is applied in the numerator of equation (3.16).

The advantage of this reweighting method is that any kinematic variable can be extracted from the polarised boson sample and its distribution will also represent the properties of the polarised boson. Cuts on the phase space and the event reconstruction can be propagated to the distributions without affecting its polarisation state.

3.4 Impact of anomalous triple gauge couplings on WZ differential cross sections and polarisation

The WZ production mode via the Triple Gauge Vertex WWZ (Figure 3.2, right) is especially sensitive to new physics. There are two standard parametrizations for anomalous triple gauge vertices (aTGCs): the effective Lagrangian and the effective field theory (EFT).

The WWZ vertex is parametrized as following by the effective Lagrangian (for instance: [58]):

$$\mathcal{L} = ig_{WWV}[g_1^Z(W^+_{\mu\nu}W^{-\nu} - W^{+\mu}W^-_{\mu\nu})V^\nu + \kappa^Z W^+_\mu W^-_\nu V^{\mu\nu} + \frac{\lambda^Z}{m_W^2}W^{+\nu}_\mu W^{-\rho}_\nu V^{-\mu}_\rho], \tag{3.18}$$

For the three coupling parameters of the WWZ vertex in equation (3.18), in the Standard Model $\kappa = g_1^Z = 1$ and $\lambda^Z = 0$ applies. Deviations from the Standard Model are expressed in terms of $\Delta g_1^Z := g_1^Z - 1$, $\Delta\kappa^Z := \kappa^Z - 1$ and λ^Z.

The Effective Field Theory [88] is another approach to parametrize aTGCs. A linear combination of higher-dimensional operators is added to the four-dimensional operators of the Standard Model. ATGCs are described by dimension six operators.

$$\mathcal{L} = \mathcal{L}_{SM} + \sum_{d=5}^{\inf}\frac{1}{\Lambda^{d-4}}\sum_i c_i\mathcal{O}_i^{(d)}, \tag{3.19}$$

with the couplings relevant for WWZ aTGCs:

$$\begin{aligned}
\mathcal{O}_{WWW} &= \frac{c_{WWW}}{\Lambda^2}Tr[W_{\mu\nu}W^{\nu\rho}W^\mu_\rho],\\
\mathcal{O}_W &= \frac{c_W}{\Lambda^2}(D_\mu\Phi)^\dagger W^{\mu\nu}(D_\nu\Phi),\\
\mathcal{O}_B &= \frac{c_B}{\Lambda^2}(D_\mu\Phi)B^{\mu\nu}(D_\nu\Phi).
\end{aligned} \tag{3.20}$$

The dimensionless coefficients $c_i, i \in \{WWW, W, B\}$ are called Wilson coefficients and parametrize the coupling strength of the new physics to the SM particles. The EFT is a low-energy-approximation of phenomena happening at higher energy scales, the constant Λ in equation (3.19) denotes the scale at which the heavier new physics appears, for example as a massive new particle with the mass being Λ. The EFT approach is valid only for energies below Λ. It is more in use today as it is also sensitive to Higgs couplings.

The EFT and Effective Lagrangian are equivalent approaches and EFT Wilson coefficients are related to the Effective Lagrangian couplings as follows:

$$\begin{aligned} g_1^Z &= 1 + c_W \frac{m_Z^2}{2\Lambda^2}, \\ \kappa^Z &= 1 + (c_W - c_B \tan^2(\theta_W)) \frac{m_W^2}{2\Lambda^2}, \\ \lambda^Z &= c_{WWW} \frac{3g^2 m_W^2}{2\Lambda^2}, \end{aligned} \tag{3.21}$$

Variables sensitive to partonic center-of-mass energy are used to measure aTGCs because effects from aTGCs grow with energy. Examples for such variables are for example the boson transverse momentum or the diboson transverse invariant mass. Differential distributions of these variables are extracted and using the tails of these distributions, limits on aTGCs are set. Using leptonically decaying WZ events produced in proton-proton collisions, limits on aTGCs have been extracted for example in [12, 16] using the diboson transverse invariant mass. However, this is not discussed here in further detail as it is out of the scope of this thesis.

Polarisation and angular variables are also sensitive to aTGCs and generally to anomalous boson couplings as new physics in boson couplings might modify the polarisation state of the bosons. In Higgsless models, for instance, the balance between the scattering of two longitudinal bosons and the scattering diagrams mediated by the Higgs is destroyed, causing an amplitude increase of the longitudinal boson helicity amplitude with energy [24]. These models are of course not feasible any more after the discovery of the Higgs [44, 45]. however, they show that deviations from the SM can indeed change the helicity fractions of the bosons.

In the SM, the W and Z bosons in WZ events are primarily opposite-transversely polarised $\mathcal{M}(\pm, \mp)$, longitudinal polarisation is subdominant. All other polarisation states are strongly suppressed at LHC energies: for instance the helicity amplitude $\mathcal{M}(\pm, \pm)$ is forbidden for massless bosons in the SM and scale with $\frac{m_W^2}{E^2}$ in case of massive bosons [58][2]. However, the aTGC couplings λ^Z, g_1^Z and κ^Z contribute to this helicity state [61]. These also can produce the other helicity states suppressed or subdominant in the SM, namely $\mathcal{M}(0, \pm)$ and $\mathcal{M}(0, 0)$. The transverse-transverse polarisation state is not affected by aTGCs because it contains no triple gauge vertex.
Longitudinal-longitudinal diboson states are already present in the SM at LO, though they constitutes a subdominant contribution. $\mathcal{M}(0, 0)$ would for example receive contributions proportional to g_1^Z which would scale like $\frac{E^2}{M_W^2}$ [58]. As $\mathcal{M}(0, 0)$ is sizeable in the SM and can also receive input from BSM, it is very sensitive to BSM due to the interference SM-BSM, the deviations from the SM enter linearly in the Wilson coefficients [83].
The amplitudes $\mathcal{M}(\pm, \pm)$ and $\mathcal{M}(0, \pm)$ are not present in the SM at leading order, therefore, no interference is present between SM and BSM. BSM physics enters through these

[2]Note that a LO, it is strongly suppressed but at higher order, diagrams with gluon radiation in the final state can contribute to the amplitude $\mathcal{M}(\pm, \pm)$ as the gluon can carry away an arbitrary polarisation [83].

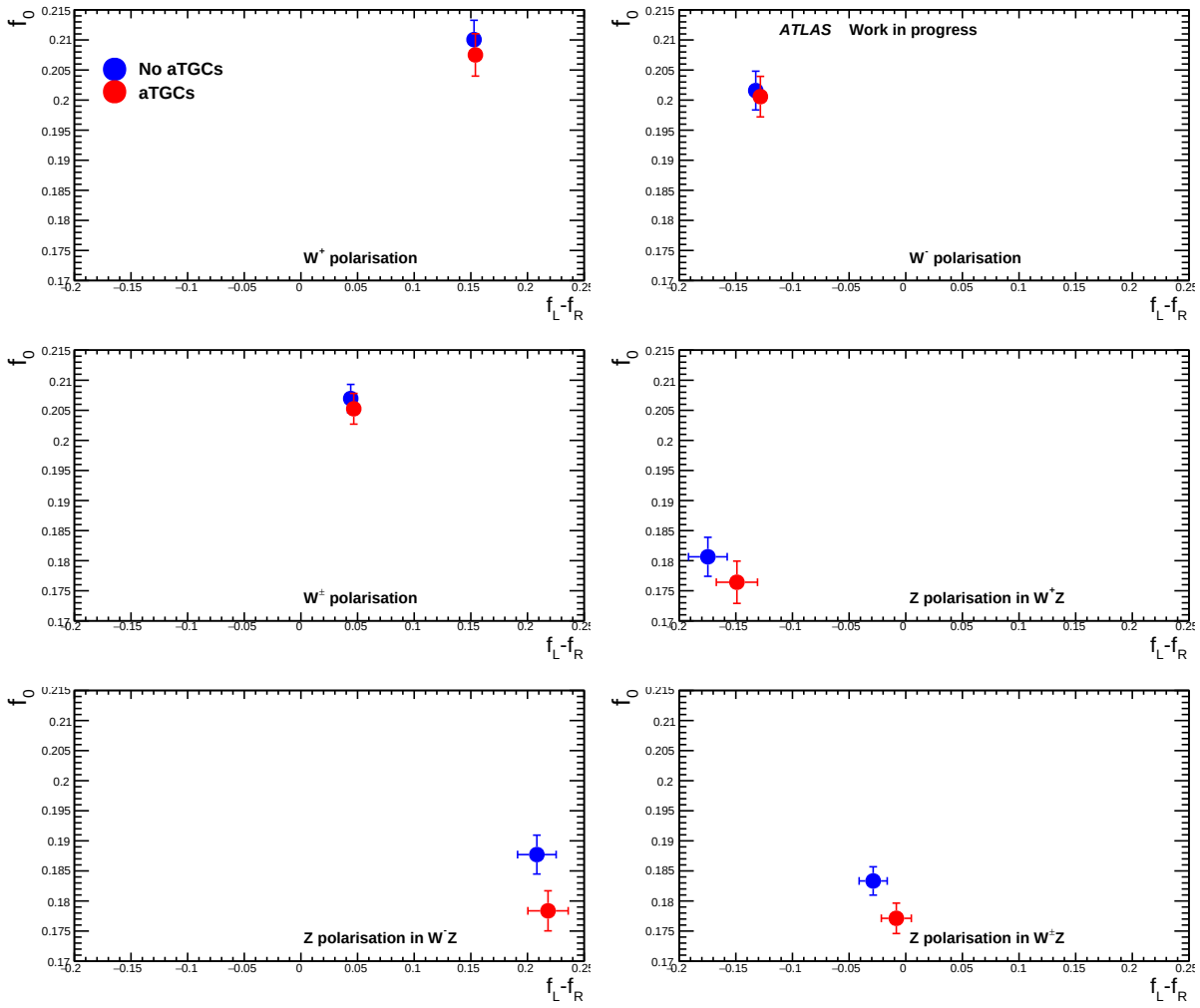

Figure 3.9 – *Impact of non-zero aTGCs on the polarisation fractions for all boson polarisation measurements in the diboson system. Both predictions, for zero and non-zero aTGCs have been produced with* MC@NLO*. The value of the aTGCs have been chosen according to the limits obtained at 13 TeV in [16]. The aTGCs were set to* $\Delta g_1^Z = 0.032$, $\Delta\kappa_1^Z = 0.24$ *and* $\lambda^Z = -0.016$. *The uncertainties contain only statistical uncertainties on the MC sample.*

amplitudes only with $c_i^2, i \in \{WWW, W, B\}$, which would make them difficult to detect. The amplitude $\mathcal{M}(0,0)$ is small, using the events with $\mathcal{M}(\pm,\mp)$ which are dominant would be of advantage, however, they receive no contribution from aTGCs, no interference with BSM physics is present in these states. This is only true if integrating over the azimuthal angle ϕ. Studies [83, 84] have shown that distribution of the angle ϕ can be used to resurrect this interference, making also the $\mathcal{M}(\pm,\mp)$ helicity amplitude sensitive to BSM physics.

The impact on aTGCs on polarisation is exemplified in Figure 3.9 for one specific set of aTGCs. Weights to simulate events with aTGCs are available for MC@NLO. The aTGCs parameters have been set to $\Delta g_1^Z = 0.032$, $\Delta\kappa_1^Z = 0.24$ and $\lambda^Z = 0.014$ in the following. The impact of aTGCs on the polarisation fraction f_0 and the transverse polarisation difference $f_L - f_R$ is clearly visible. However, to be sensitive in the measurement, a higher collision center-of-mass energy is necessary or a larger statistics of parton-parton collisions with high partonic center-of-mass energy. A cut on for example the boson p_{T} could help to increase the sensitivity on aTGCs in polarisation measurements.

Chapter 4

The Large Hadron Collider and the ATLAS detector

4.1 The Large Hadron Collider

4.1.1 The LHC machine

With its circumference of 26.7 km, the Large Hadron Collider (LHC) is currently the world's largest particle accelerator and collider. The synchrotron is situated at CERN (European Organization for Nuclear Research) in Geneva, about 100 m below the surface. Protons are collided at unprecedented energy, currently at a center-of-mass energy of $\sqrt{s} = 13\,\text{TeV}$, but also a part of experimental time is dedicated to lead ion collisions. At each of the four collision points, one experiment is situated to measure the products of the collisions. Two multi-purpose detectors, ATLAS and CMS, are designed to collect high luminosity data and are located diametrically opposite to each other in the ring. Two specialized low-luminosity experiments take data at the two remaining crossing points: ALICE, optimized for measuring heavy ion collisions and LHCb, specialized on b-physics and measurements of CP-violation.

In the LHC, two proton beams travel at nearly the speed of light in opposite directions. Dipole magnets keep the protons on their circular path. As the two counter-rotating beams have the same charge, an oppositely poled magnetic field has to be imposed on them. The protons travel therefore in two separated beam pipes but these are contained within the same yoke. The cross section of these dipole magnet is shown in Figure 4.1.

The high proton energy requires a 8 T dipole field to direct the protons on their circular path making necessary a high electrical current of about 12000 A in the electromagnets. This can only be achieved by making use of superconducting technology. For this reason, Niobium-titanium filaments embedded in the dipoles are cooled to a temperature of 1.9 Kelvin.

Besides dipoles, sets of quadrupole magnets are installed around the accelerator to focus the beam. Smaller corrections to the proton trajectory are done using sextupole and octopole magnets.

The protons are accelerated using radio-frequency (RF) cavities operating at a frequency of 400 MHz [90]. Protons are collided in bunches, each bunch contains about 10^{11} protons. The protons have to pass through a chain of pre-accelerators before being injected in the LHC. At the beginning of the chain, protons are extracted from Hydrogen atoms and

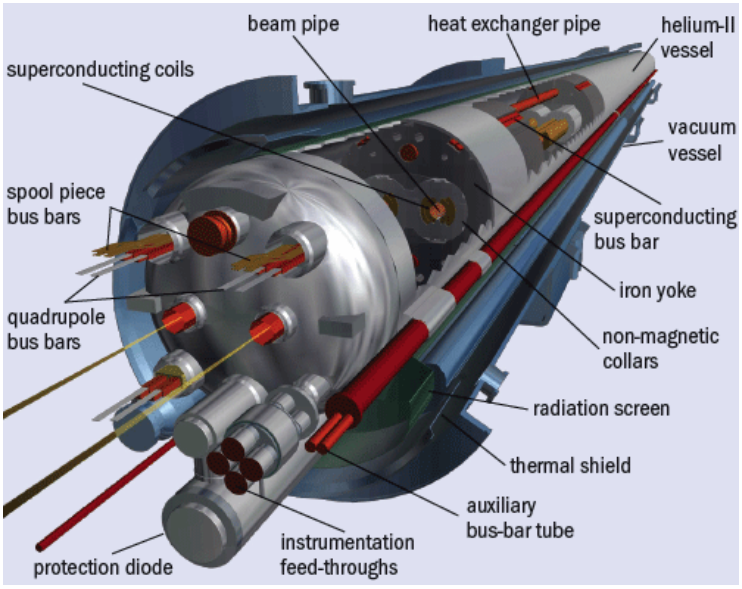

Figure 4.1 – *Cross section of a LHC dipole. From [89].*

accelerated in a linear accelerator (LINAC2) to 50 MeV. At this energy, they are injected in the four superposed rings of the PS Booster where the energy is increased to 1.4 GeV. The next element in the accelerator chain, the PS (Proton Synchrotron), a synchrotron with a diameter of 628 m, accelerates the protons to 26 GeV. It also defines the longitudinal bunch structure by consecutive splitting of the bunches and the bunch spacing. In the SPS (Super Proton Synchrotron), an accelerator with a diameter of 7 km, the energy is further increased to 450 GeV. From the SPS, the protons are injected in the LHC. A schematic illustration of the CERN accelerator facilities and the LHC accelerator chain is shown in Figure 4.2.

After the LHC is completely filled, the magnetic field is ramped up to 8 T and the RF cavities accelerate the protons to an energy of 6.5 TeV each.
More technichal details on the LHC machine can be found in [90].

The LHC was started in 2008, first collisions took place in 2009. The data of Run1 was collected in 2010-2013, at first at $\sqrt{s} = 7$ TeV and later at 8 TeV. This period was followed by a long shut-down (LS1) in 2013-2014, and in 2015, the LHC restarted again at a higher center-of-mass energy of $\sqrt{s} = 13$ TeV. The data relevant for this thesis was collected in 2015 and 2016 at this energy.

4.1.2 LHC collision parameters and Luminosity

After the long shut-down LS1, the first part of 2015 data was collected with a bunch-spacing of 50 ns to re-establish operation [92]. This data was not used in this analysis, the data-taking relevant for this thesis started with the operation at a bunch-spacing of 25 ns and extended until the end of 2016. While in 2015, the focus was mainly laid on machine operation, 2016 was a data production year.
The amount of collected data can be expressed in terms of "integrated luminosity", which is the instantaneous luminosity integrated over the data taking time. The instantaneous luminosity L is a proportionality factor which relates the cross section of a certain process σ to the events N produced per second

$$\frac{dN}{dt} = L \cdot \sigma. \tag{4.1}$$

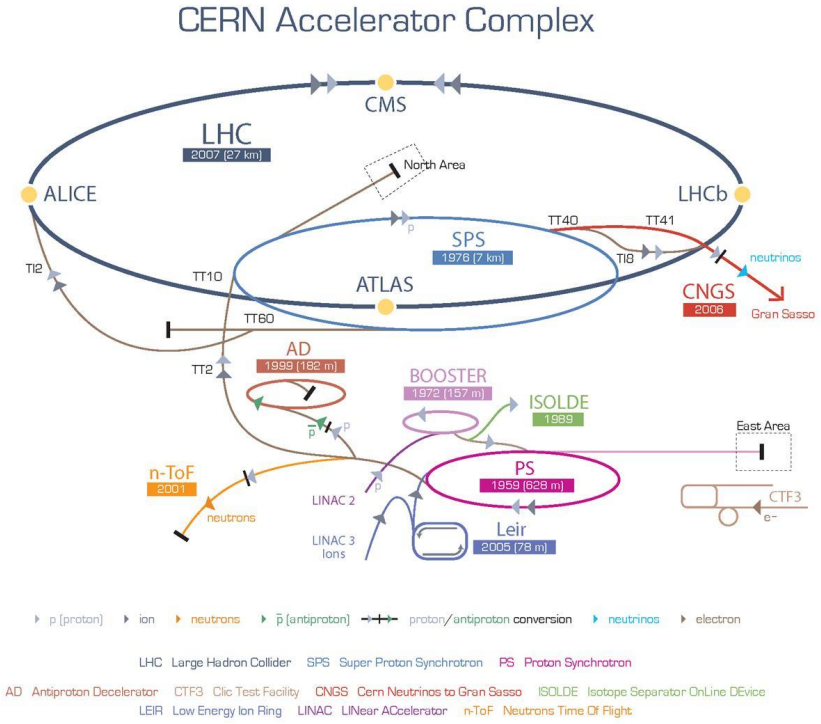

Figure 4.2 – *The Large Hadron Collider LHC (top, dark blue) with its pre-accelerators and affiliated experiments. From [91].*

The instantaneous luminosity is related to the LHC accelerator operation parameters as follows [90]:

$$L = \frac{N_b^2 \cdot n_b \cdot f_{\text{rev}} \cdot \gamma}{4\pi\epsilon_n\beta^*} \cdot F, \tag{4.2}$$

where N_b is the number of particles per bunch, n_b the number of bunches per beam, f_{rev} is the revolution frequency and γ the relativistic γ factor. ϵ_n is the normalized transverse beam emittance and related to the transverse size of the beam. The envelope of the beam is given by the β-function, β^* is the value of the β-function at the collision point and is related to the longitudinal dimension of the beam. The more focused the beam, the higher the probability for a collision. F is a geometric factor which also includes the angles at which the beams are collided.
The parameters of equation (4.2) in a standard proton-proton run in 2015 and 2016 are given in Table 4.1. The integrated luminosity $\mathcal{L}$ of 2015 and 2016 data recorded by ATLAS amounts to $\mathcal{L} = 36.1\ \text{fb}^{-1}$.

4.1.3 Pile-up at hadron colliders

It is important to note that any hard process in the LHC does not happen isolated: protons collide in bunches in the LHC, bunch crossings happen every 25 ns and several hard interactions occur per bunch crossing. Figure 4.3 displays the number of interactions per bunch crossing in 2015 and 2016 in the LHC and shows that in average about 24 collisions happened per bunch crossing.

Interactions affecting the collision of interest because they happen in its vicinity and within a short time interval around the collision are referred to as “pile-up”. There are several sources of pile-up [95], for example interactions from protons with the LHC colli-

	2015	2016
Beam energy [TeV]	6.5	6.5
Protons per bunch (average at start of collision), 10^{11}	1.1	1.1
Maximum number of bunches	2244	2076
Bunch spacing [ns]	25	25
Transverse normalized emittance (μm)	3.5	3.4
Half crossing angle (μrad)	145	185
β^* [m]	0.8	0.4
Maximum peak luminosity (10^{34} cm^{-2}s^{-1})	0.51	1.4
Total integrated luminosity (delivered by LHC) [fb^{-1}]	4.2	40

Table 4.1 – *LHC beam parameters in 2015 and 2016 [92, 93].*

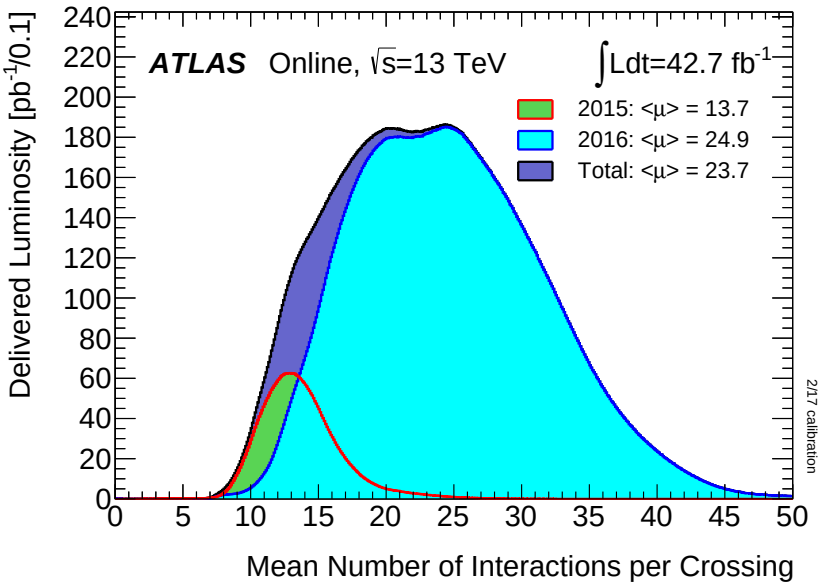

Figure 4.3 – *Mean number of interactions per bunch crossing at the LHC in 2015 and 2016 collisions. From [94].*

mators ("beam halo events") or residual gas in the LHC beam pipes ("beam gas events") and effects from the gas in the detector cavern ("cavern background"), whereas the most important pile-up components are in-time pile-up and out-of-time pile-up. In-time pile-up denominates hard collision events which happen within the same bunch crossing besides the collision of interest. Their energy deposit might alter the detector signal of the collision event of interest. Out-of-time pile-up describes a similar phenomena but the additional collisions happen temporarily close to the collision of interest, for example during one of the previous or following bunch crossings. The response time of the ATLAS subdetectors is larger than the time between two collisions, therefore energy deposits from these out-of-time pile-up events also might affect the signal of the collision of interest.
Pile-up is included in MC event simulations, the simulation uses either a phenomenological approach to estimate the pile-up or a data-driven approach based on special "zero-bias" LHC runs. In this analysis, the PYTHIA8 model [72] provides the modelling of the pile-up. The pile-up distribution in the simulation might differ from the one in data. The pile-up profile in simulation is reweighted such that it matches the data profile.

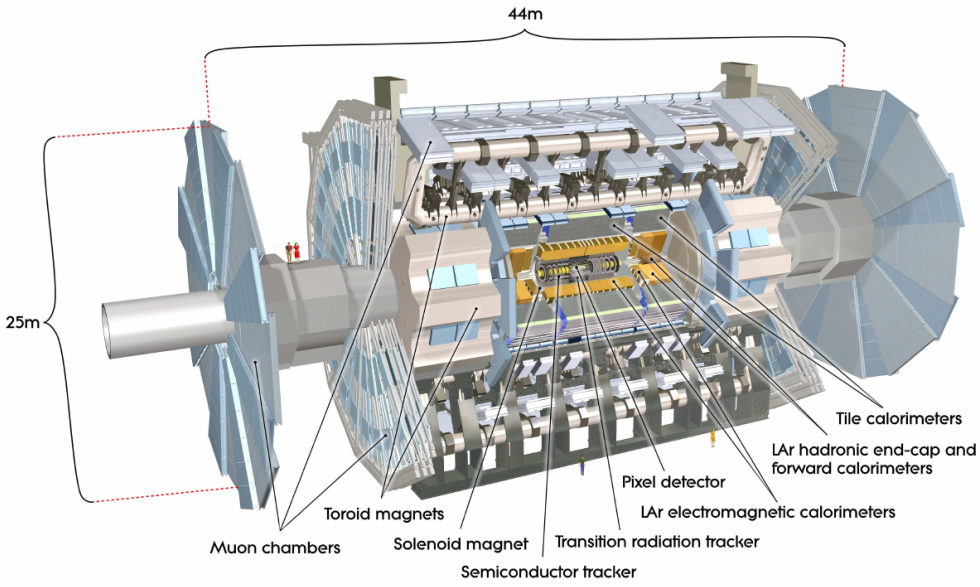

Figure 4.4 – *Cut-away view of the ATLAS detector. From [96].*

4.2 The ATLAS detector

All collision events analysed in the scope of this thesis were obtained with the ATLAS ("A Toroidal LHC ApparatuS") detector during the proton-proton collision operating mode of the LHC in 2015 and 2016.
ATLAS was designed as a multi-purpose detector with a broad physics program from Standard Model precision measurement to new physics searches including many confirmed or potential final states and processes. Particles issuing from inelastic hadron-hadron collisions are identified, energy, momenta and charge of all hadronic jets, leptons and photons are measured. Using momentum conservation in the plane transverse to the beam axis allows to access information about particles that leave the experiment undetected.
ATLAS, illustrated in Figure 4.4, is situated at one of the four collision points at the LHC and is the largest in size of the four experiments: the cylindrically-shaped detector measures 44m in length and 25m in diameter and weights about 7000 tons.
At the center of the detector, the particle collisions take place. ATLAS covers nearly the complete solid angle around the collision point and is forward-backward symmetric. It consists of several subdetectors which are arranged in layers around the collision point. Each subdetector provides complementary information about the particle and all pieces of information are combined to get the whole picture of the event.
ATLAS is divided in three main sub-systems: The inner detector with Pixel detectors, Silicon Microstrip Trackers (SCT) and Transistion-Radiation-Trackers (TRT) (Section 4.2.2), the Calorimeters which are divided into Electromagnetic Calorimeters (Section 4.2.3) and Hadronic Calorimeters (Section 4.2.4) and the Muon detectors (Section 4.2.5). The inner detector and the muon detectors are immersed in a magnetic field. A trigger (Section 4.2.6) preselects potentially interesting events and rejects the rest. In the following, more details on these subsystems are given.

4.2.1 The ATLAS coordinate system

To begin the description of the ATLAS detector, the coordinate system to describe any position in the detector is introduced. Its origin is situated at the collision point. The

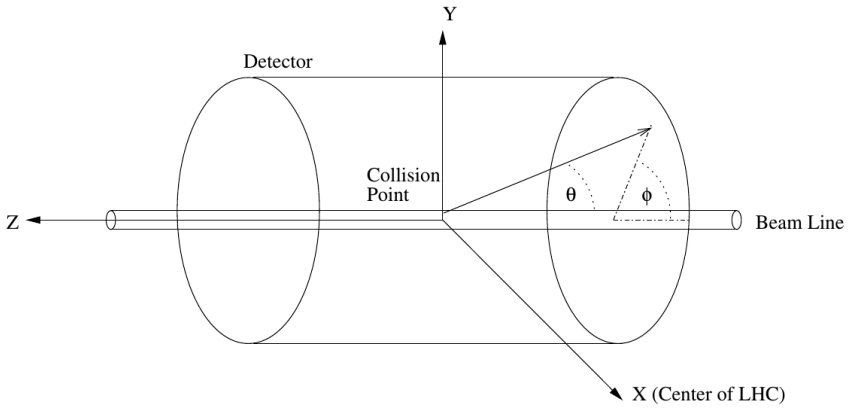

Figure 4.5 – *The ATLAS detector coordinate system. From [51].*

x-axis points from the collision point to the center of the LHC and the y-axis points upwards, the x-y plane is therefore transverse to the beam direction. The z-axis is parallel to the beam axis, its direction points such that the axes form a Cartesian right-handed coordinate system. The detector has a cylindrical form, it is therefore convenient to also introduce coordinates in a cylindrical and spherical coordinate system. An azimuthal angle ϕ is defined as the angle around the z-axis, it hence measures an angle in the x-y plane, the transverse plane. The polar angle θ is defined as the angle with the beam axis. In practice, the pseudorapidity is used instead of the angle θ. The pseudorapidity is defined as $\eta = -ln(\tan(\frac{\theta}{2}))$ for massless objects, for massive objects, the definition $\eta = \frac{1}{2}ln(\frac{E+p_z}{E-p_z})$ is used, whereas E is the energy and p_z the longitudinal momentum of the particle. Any distance ΔR between two objects can be described in the pseudorapidity-azimuthal angle-space as $\Delta R = \sqrt{\Delta\eta^2 + \Delta\phi^2}$. The ATLAS coordinate system with the angles θ and ϕ is illustrated in Figure 4.5.

4.2.2 The ATLAS Inner Detector

The inner detector (ID) detects charged particles and reconstructs their tracks. Using pattern recognition, the track can be extrapolated back to the interaction point and therefore, charged particles can be assigned an interaction point. Momentum measurement of charged particles can be performed by means of the effect of the magnetic field on the track and the identification of b-hadrons and τ-lepton decays is made possible by the reconstruction of displaced vertices. Precise tracking detectors with high granularity are necessary to resolve the on average 25 vertices per bunch crossing, to identify displaced vertices and to do precision physics. The required momentum resolution of the tracks was set to $\frac{\sigma_{p_T}}{p_T} = 0.05\% p_T[\text{GeV}] \bigoplus 1\%$.
The inner detector consists of 3 independent subsystems: the pixel detector, the silicon microstrip detector (SCT) and the transition radiation tracker (TRT), a schematic view of the ID is shown in Figure 4.6.

The entire inner detector is immersed in a magnetic field of 2 T making possible momentum measurements and the identification of the sign of the charge by measuring the bending radius and direction of the charged particle in the magnetic field.
The pixel detector is placed closest to the beam pipe. The innermost layer, the Insertable B-Layer, is 3.3 cm away from the collision point, it was newly installed in 2014 [97]. The pixel detector is arranged in 4 layers around the beam pipe in the barrel and in two disks perpendicular to the beam pipe in each end-cap ensuring tracking up to $|\eta| = 2.5$. The identical pixels of size 50×400 μm^2 are segmented in the R-ϕ and z-plane. Oxygenated

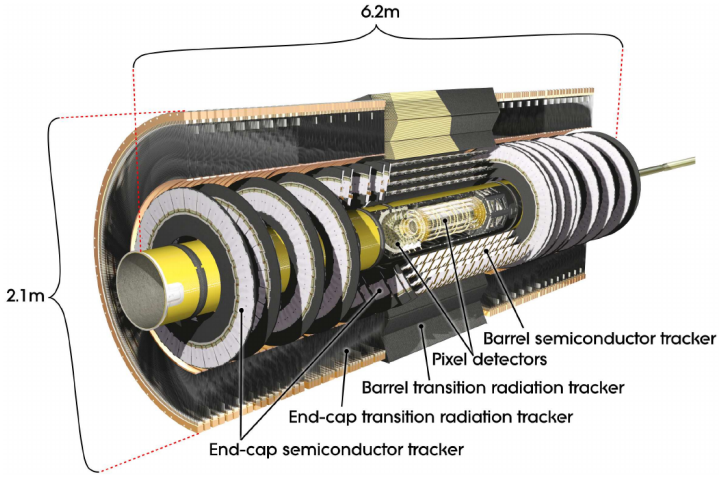

Figure 4.6 – *Schematic view of the ATLAS inner detector. From [96].*

n-type silicon wavers are used, the readout pixels are on the n^+ doped side of the detector. A bias voltage of initially 150V is applied which can be increased to compensate for the higher noise due to ageing caused by the high radiation level. Pixel, as well as SCT detectors are kept at a temperature of -5 to -10C to suppress noise.
The SCT detectors are arranged the same way as the pixel detectors in 4 coaxial layers in the barrel and 9 disk layers in each end cap but each of them consist of two layers of strips which are rotated by 40 mrad relatively to each other to allow measuring two space points in each set of strips. Like the pixel detector, the SCT also covers pseudorapidity regions up to $|\eta| = 2.5$. A bias voltage of 150V is applied to the p and n doped silicon, it can be increased depending on the ageing. Pixel and SCT can resolve discrete space points.
The TRT consists of straw tubes as cathodes of a diameter of 4 mm, tungsten wires of a diameter of 31 μm coated with gold are stretched in the center of each of the tubes serving as anodes. 73 layers of straw tubes are located in the barrel and 160 layers in each endcap. A potential difference of 1530 V is applied between cathode and anode, resulting into a charge multiplication (gain) of 2.5×10^4. The TRT is kept at room temperature and its tubes are filled with a gas-mixture of Xenon, CO_2 and O_2. The TRT provides additional tracking information up to a pseudorapidity of $|\eta| = 2.0$ only in the R-ϕ-plane but with average 36 hits per track, a large number of tracking points are available. Due to that and to the large measured track length, the TRT also contributes to the momentum measurement. The tubes are interleaved with polypropylene fibers which serve as transition radiation material. Crossing electrons provoke the production of transition radiation photons. This is used for electron identification and discrimination from photons and hadrons [96].

4.2.3 The Electromagnetic Calorimeter

Through electro-magnetic interactions with the detector material of the electromagnetic calorimeter ECAL, information about the energy, position and identity of the particle can be extracted. The ATLAS ECAL is a sampling calorimeter whose absorber material are lead plates and whose active material is liquid Argon (LAr). Electromagnetic interaction of photons and electrons[1] generates secondary particles through pair production and bremsstrahlung, respectively, which interact with the ECAL absorber material lead. A cascade of particles, a shower, is produced up to the point where the electrons or photons have too little energy to produce secondary particles and loose the remaining energy through

[1]Meaning, here and in the following: electrons and positrons

collisions with atoms (electrons) or Compton scattering and photoeffect (photons). The shower shape itself (width, length, location of maximum) provides important information about the identity of the particle. Lead has a short radiation length[2], allowing for a compact construction of the ECAL. In the active material, LAr, the argon atoms are ionized by the charged particles in the shower, the charge drifts to the readout electrodes situated in gaps between the absorber due to the high voltage applied at the electrodes. The signal has a triangular shape whose peak is proportional to the energy loss of the particle. The ATLAS ECAL achieves an energy resolution of $\frac{\sigma_E}{E} = \frac{10\%}{\sqrt{E[\mathrm{GeV}]}} \bigoplus 0.7\%$ which was verified with test-beam data. Liquid argon is well suited as active medium due to its ionization yield and its radiation hardness.

To reduce dead material from cryogenics the solenoid and the ECAL share the same cryogenic vessel. The accordion shaped ECAL is symmetric in ϕ and consists of copper with absorber lead plates attached to them. The whole construction is situated in a tank of liquid argon.

Its cylindrical shape is divided in 4 subsystems, illustrated in Figure 4.7: EMB (electro-magnetic barrel calorimeter), covering the range $|\eta| < 1.475$, the EMEC (electro-magnetic end-cap), covering the range $1.37 < |\eta| < 3.2$, the HEC (hadronic end-cap calorimeter) and the FCAL (Forward calorimeter). The HEC is part of the hadronic calorimeter and is discussed in the next section, and the FCAL covers the very forward region from $3.1 < |\eta| < 4.9$. Both HEC and FCAL are also based on LAr as active material and lead as absorber material.

The LAr barrel is composed of two identical half-barrels, separated by a small gap at z=0. The two end-caps, completing the cylinder, consist each of two coaxial wheels ($1.375 < |\eta| < 2.5$ and $2.5 < |\eta| < 3.2$). The region $1.37 < |\eta| < 1.52$ is called "crack"-region or transition region as the transition between the EMB and the EMEC is located there. The particles have to cross more material in that region.

The calorimeter depth is about 22 radiation length in the barrel and 24 radiation length in the end-cap. Especially important for precision measurements is the EMB and the EMEC up to $|\eta| < 2.5$. They consist of 3 layers, fine granularity in $|\eta|$ of the first layer makes accurate position measurements possible. In the $\eta \times \phi$ space, a granularity of $0.025/8 \times 0.1$ for $|\eta| < 1.4$ is given for the first layer. The granularity in η is lower in the transition region, and decreases with increasing $|\eta|$ from $0.025/8 \times 0.1$ for $1.5 < |\eta| < 1.8$ to 0.025×0.1 for $2.4 < |\eta| < 2.5$.

The largest energy deposit happens in the 2nd calorimeter layer while the 3rd layer captures the shower tail and is therefore less segmented. The segmentation of the second calorimeter layer amounts to 0.025×0.025 for $|\eta| < 2.5$ and of the third layer to 0.050×0.025 for $|\eta| < 1.35$ and $1.5 < |\eta| < 2.5$.

For $|\eta| < 1.8$, a presampling layer measures the energy loss in front of the ECAL. Its granularity is 0.025×0.1 in the $\eta \times \phi$ space.

Coarser granularity is sufficient for the outer η-regions $|\eta| > 2.5$ to reconstruct jets and missing transverse energy ([96], [98]).

4.2.4 The Hadronic Calorimeter

The hadronic calorimeter consists of 3 parts: The Tile-Calorimeter in the barrel region, the HEC (Hadronic end-cap) and the Forward Calorimeter FCAL spanning to the very forward region close to the beam-pipe as shown in Figure 4.7. The Tile-Cal is located behind the

[2]The length of the particle path after it has lost $\frac{1}{e}$ of its original energy.

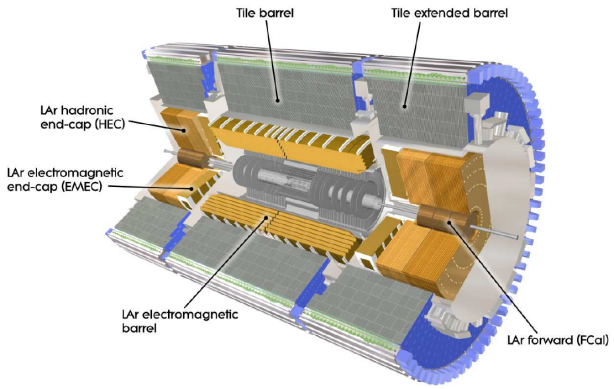

Figure 4.7 – *Cut-away view of the ATLAS Electromagnetic and Hadronic calorimeters. From [96].*

ECAL, further away from the beam-axis and is divided into two parts: the barrel ($|\eta| < 1.0$) and the extended barrel ($0.5 < |\eta| < 1.7$). Like all calorimeters in ATLAS, it is a sampling calorimeter: its absorber is steel and scintillator tiles are used as active material. Hadronic interactions with the absorber material produce cascades of particles, the resulting showers are usually larger than electromagnetic showers. Information on shower shapes are used to discriminate and identify particles. The Tile-Cal is segmented into 3 layers and 64 modules of alternating steel-scintillator tile layers with a size of $\Delta\phi \approx 0.1$ extending radially and normal to the beam line. Its size is 7.4 λ_{INT}[3]. At the tile edges, the readout system is located consisting of wave-length shifting fibers which themselves are read-out by photo-multiplier tubes. In the gap region between the barrels, special modules of steel-scintillator sandwiches ensure that the energy is partially read out in the crack region.

The HEC ensures the hadronic particle detection in the region $1.5 < |\eta| < 3.2$ and therefore overlaps with the Tile-Cal at its edges. Two independent wheels join the the end-cap region directly behind the end-cal ECAL in each end-cap and share the same LAr cryostat with latter. It is a sampling calorimeter with copper as absorber and liquid argon as active material. Each end-cap consists of two wheels, a front wheel with 24 copper plates and a coarser sampled rear wheel with 16 copper plates. Hadronic barrel and end-cap calorimeters are required to achieve an energy resolution of $\frac{\sigma_E}{E} = \frac{50\%}{\sqrt{E[\text{GeV}]}} \bigoplus 3\%$.

The FCAL, extending the ATLAS coverage to very forward regions ($3.1 < |\eta| < 4.9$), allowing to measure particles encompassing very low angles with the beam axis, comprises an electromagnetic and a hadronic calorimeter. Its first layer, a copper/LAr sampling calorimeter is optimized for electro-magnetic measurements, while the 2nd and the 3rd layer are optimized for hadronic measurements. As the FCAL is set back a little bit with respect to the ECAL front face by about 1.2m, the calorimeter has to be kept more compact and contain the hadronic showers despite the smaller space available. Therefore, tungsten is used as an absorber material. Liquid argon is the active material and it shares the same cryogenic vessel as the HEC ([96], [98]).

4.2.5 The Muon Detectors

The muon system is located outside of the calorimeters and is therefore the outermost detector layer. It comprises four different detector types for measurements on muons: Two precision measurement detector systems and two detector types with fast and precise time

[3] λ_{INT}: nuclear interaction length, mean path a hadronic particle travels in the medium before an inelastic collision with a nucleus of the medium happens.

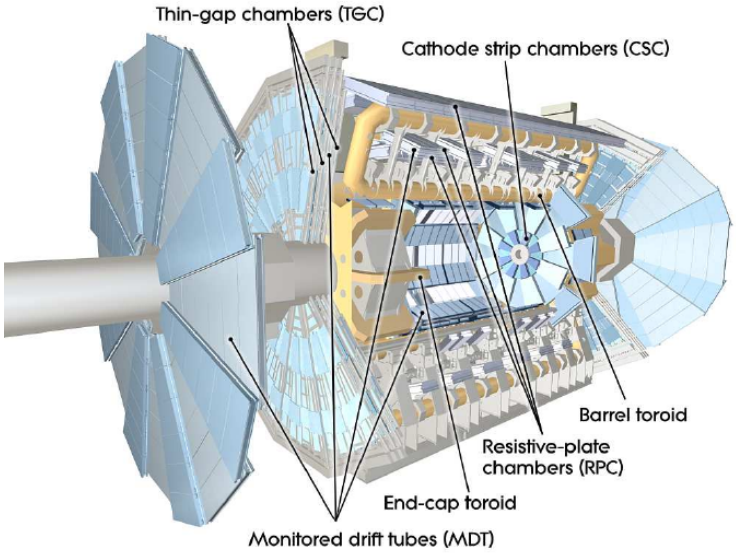

Figure 4.8 – *Cut-away view of the ATLAS muons system. From [96].*

response mainly used for triggering. The layout of the ATLAS muon system can be seen in Figure 4.8.

All detectors are gaseous chambers based on ionization of the contained gas, the resulting electrons from ionization drift to a positively charged cathode. Momentum measurement is performed by means of a magnetic field bending the trajectory of the charged muon. The barrel toroid generates the magnetic field in the pseudorapidity region $|\eta| < 1.4$. It consists of eight coils which are arranged radially and symmetrically around the beam axis. The endcap toroid is located at both ends of the barrel toroid and is rotated with respect to the latter by 22.5 deg. It generates the magnetic field in the region $1.6 < |\eta| < 2.7$. A combination of barrel and end-cap fields provides the magnetic field for the transition region at $1.4 < |\eta| < 1.6$. The magnetic field generated by the superconducting magnets is largely perpendicular to the incoming particles' trajectory.

Precision measurement is carried out by Monitored Drift tubes (MDT). However, in the region $2.0 < |\eta| < 2.7$, the first muon detector layer has been replaced by Cathode Strip Chambers (CSC) whose time resolution and rate capability is higher which is necessary for the forward region. These two detector types cover the region up to $|\eta|$ =2.7 and provide momentum measurement and accurate measurement of the coordinate in the bending plane (η): for MDTs, a resolution in η of 35 μm and for the CSCs, 40μm is obtained. CSCs also can measure the coordinate in the non-bending plane, ϕ, with a coarser resolution of 5 mm.

MDTs consist of tubes with a diameter of 29.970 mm arranged in 3 layers filled with Argon and CO_2. A tungsten-rhenium wire is spanned in each tube which has an electrical potential of 3080V with respect to the tube walls. Passing muons ionize the gas in the tubes and the electrons are collected by the wire anode. The tube setup allows for high mechanical stability and precision whereas a long pulse length resulting from the drifting time difference of the charges closest and furthest away from the wire is a disadvantage. Furthermore, MDTs can read out only one track per chamber in order to guarantee a non-ambiguous assignment of the ϕ-coordinate measured by one of the trigger chambers. For uncorrelated tracks, this effect is negligible in that region whereas for correlated muon tracks, issuing for example of the decay of a particle into two muons, information from the tracker is also used for the combination of η and ϕ coordinates.

At high η, in the region $2.0 < |\eta| < 2.7$, where the muon rate is higher and the tracking

system is only partly present, CSC precision measurement chambers are used in the first endcap-layer. CSC multiwire proportional chambers are beneficial here also due to their faster time response. Each chamber contains four planes of CSCs which deliver each one measurement of the η and of the ϕ coordinate. These chambers are arranged in two disks of each eight chambers, eight small and eight large chambers. In each chamber, parallel wires are arranged in the radial direction serving as anodes. The two cathodes are segmented, one in stripes parallel to the wires and one in stripes perpendicular to the wires. Therefore, two coordinates of the track, η and ϕ, can be determined. The position of the track is determined by measuring the relative signal strength arriving at each cathodes, interpolating yields the maximum which corresponds to the center of the track. Cathodes perpendicular to the wires measure the η-coordinate, the cathodes parallel to the wires measure the ϕ-coordinate. The spacing of latter is larger, a lower resolution is therefore archived for the ϕ-coordinate. If more than one track hits a chamber, the measurement of the pulse-height resolve ambiguities of the coordinate assignment.

The trigger chambers fulfil the following purposes:

- provide trigger information for muons and their approximate transverse momentum
- identify bunch-crossing
- measure the muon coordinate in the azimuthal direction (ϕ-plane) and therefore complement the MDT measurement in the η-direction

Trigger information is provided up to $|\eta|$ =2.4 in the full ϕ-range. The transition region between the barrel and the end-cap toroid is masked. Two different chamber types are installed: Resistive plate chambers (RPC), installed in the barrel ($|\eta|$ <1.05) in three layers concentric around the beam axis, two situated before and after the MDT middle layer and one close to the outer MDT layer. In the end-cap, 4 layers of Thin Gap Chambers (TGC) are mounted ($1.05 \leq |\eta| \leq 2.4$): one in front and two behind the second MDT wheel, the 4th layer is implemented before the innermost tracking layer. In order to suppress background, a signal has to be registered by more than one trigger layer and has to coincide in η and in ϕ separately.

Triggering on transverse momentum is achieved by measuring the deviation from a straight line of the track measured between two trigger chambers. The straight line is defined by the interpolation between the interaction point and a reference trigger layer which is the second layer in the barrel or the first layer in the end-cap. The low-p_T trigger in the barrel uses the two inner RPC trigger chambers whereas the high-p_T-trigger processes the signal of the inner and outer RPC chambers. To identify bunch-crossings and to meet the requirements of a trigger system, a fast response is necessary. Signal from both RPC and TGC chambers have a spread of 15-25 ns. The muon momentum p increases with respect to its transverse momentum p_T the higher $|\eta|$ giving rise to a smaller track curvature. To ensure similar p_T-resolution at high $|\eta|$, the granularity in the end-cap trigger system is $|\eta|$-dependent.

RPCs consist of parallel resistive plates with a gap filled with gas in between. An electric field is applied between the resistive plates. Particles traversing the gas gap provoke an electron avalanche, the signal is read out via capacitive coupling by strips which are segmented in η and ϕ-direction and attached to the outer side of the resistive plates.

The TGC consists of anode wires, parallel to each other and of cathodes arranged in strips which are orthogonal to the wires. The relative distance of the wires (1.8 mm) is larger than the distance of the cathodes to the wires (1.4 mm). The wires measure the

η-coordinate while the azimuthal coordinate is measured by the strips. The multi-wire-proportional chambers are operated in quasi-saturated mode with a gain of $3{\times}10^5$ in a gas-mixture of CO_2 and n-C_5H_{12}. The granularity of the TGCs is η-dependent.

4.2.6 The Trigger System

Limits to data reconstruction and storage amount and rate are given by the bandwidth of the computing resources. In order to adapt to the resources available, the event rate of about 40 MHz in the ATLAS detector has to be reduced by putting an event preselection system in place [99, 100]. The trigger is the decision algorithm that rejects an event or stores it for offline analyses.

It faces several challenges: the high instantaneous luminosity, whereas the event rate increases linearly with the instantaneous luminosity, the pile-up causing additional occupancy in the detector and the low rate of important physics events compared to the huge rate of uninteresting background events. This, and the limited computing resources, set the following requirements: the trigger system has to decide in a very short timescale which events are potentially interesting and reduce the event rate to an amount which can be handled by the computing resources. It has to reject as many uninteresting background events as possible while keeping potentially interesting events.

The trigger consists of two stages: a hardware based level 1 trigger (L1) and a software based higher level trigger (HLT), each of them can make a decision. The L1 trigger defines regions of interest (ROI) based on coarse-grained detector information from the muon and calorimeter systems within 2.5 ns and manages to reduce the event rate from 40 MHz to about 100 kHz. Muon, electromagnetic cluster, jet or τ candidate objects can be identified within a ROI, but also the geometrical association between objects (angles, momentum sum, invariant mass) and track information can be probed.

The ROI defined by the L1 trigger is passed on to the HLT which is able to reconstruct the full event based on the full granularity of the detector. Using this information, the HLT decides whether or not to write the event to storage and reduces the event rate further to 1 kHz. Also, multi-object triggers, for example di-electron or di-muon triggers, are available.

4.3 Reconstruction of particles with the ATLAS detector

Given the signal in the detector, information about the identity of the object and its momentum and energy is extracted. A reconstruction algorithm is run over the detector signals creating a sample of candidates of a certain object. Identification criteria are applied to identify objects out of the sample of possible candidates while rejecting candidate objects wrongly associated to the sample. Varying tightness of the identification criteria meet the requirement for different analyses for either high-quality objects or a high quantity of objects. Further requirements on the isolation can be applied to some objects to further increase the purity of the object sample.

Several types of objects are defined according to the particles introduced in Section 2.1.1.2: electrons, muons, taus, photons and hadronic jets. Weakly interacting particles like neutrinos are reconstructed as missing energy in the event. To analyse leptonic decays of WZ pairs, essentially three different types of objects are of interest: electrons, muons and missing transverse energy. Hadronic jets are an important input to missing transverse energy

reconstruction. These physics objects are defined in the following.

4.3.1 Electron reconstruction and identification

Charged particles, like electrons, leave a trace in the tracker and electromagnetically interacting objects an energy deposit in the electromagnetic calorimeter. Electrons are expected to mainly generate dense showers which do not leak too much into the hadronic calorimeter. Electron reconstruction therefore relies on signal in the tracking detector and the electromagnetic calorimeter. Signal in the hadronic calorimeter is used to discriminate against hadrons. Information from tracker and ECAL are combined by track-cluster matching.

In a first step, a sliding-window algorithm sweeps the calorimeter signal output for energy deposits in windows of size 3×5 units whereas one unit corresponds to a size of 0.025×0.025 in (η, ϕ). Energy deposits from electrons in the ECAL are expected to yield "towers" which span through all calorimeter layers. These towers are required to have a minimum energy deposit of 2.5 GeV and are denominated as electron cluster "seeds". If a seed is found, clusters are constructed from energy deposits in nearby calorimeter cells.

A pattern recognition algorithm searches for signature in the tracker compatible with the pion hypothesis of energy loss in the detector from interactions with the detector material. This pattern recognition algorithm is applied on track seeds with at least three hits in different silicon detector layers and attempts to build tracks with at least seven hits. If this is failing and the track is possibly compatible with a EM cluster seed, because it falls within a region of $\Delta R < 0.3$ around the barycentre of an EM cluster, the pattern recognition algorithm is repeated but this time based on the electron hypothesis. This pattern recognition algorithm allows for a larger energy loss of the track due to Bremsstrahlung at each intersection point with the detector material [101]. The track pattern is fit using a χ^2 approach assuming either the pion or the electron hypothesis, depending on which pattern recognition algorithm was applied to build the track.

The resulting signatures in the two sub-detectors are combined in the following. A first match is performed by extrapolating the track in the calorimeter middle layer and its extrapolated position is compared to the position of the cluster barycentres. Energy loss by bremsstrahlung is taken into account and at least four hits in the silicon detector are required. Loosely matched tracks are refit considering energy losses and then once again applying stricter conditions. It is possible that several tracks can be associated to the same cluster. In that case, attention is given to the track-cluster distance ΔR and the number of pixel hits. A big importance is also laid on a hit in the first silicon layer.

The direction in η and ϕ is determined using track information. The cluster energy is reconstructed out of the energy deposited in the cluster associated with the electron, the estimated energy in front of the calorimeter and in the hadronic calorimeter and is corrected by energy deposit leaking outside the cluster. The such-obtained energy is assigned as the electron energy and the energy together with the corresponding track give information about the 4-momentum of the electron. Further requirements on the distance to the primary vertex reduces the contamination from electrons from photon conversion and from the decay of heavier particles.

The energy scale for electrons was estimated with a precision of less than one per mil in the barrel and a few per mil in the endcap. Details on the electron calibration using $Z \to ee$ events can be found in [102].

Identification criteria are applied to further reduce the contamination from non-electron objects. A multivariate discriminant is created from shower shape variables, track variables, quality of track-cluster matching and energy leakage in the hadronic calorimeter [103]. Variables which enter the discriminant are for example, to name a few:

- E_{ratio} is defined as the difference between the largest and the second largest energy deposit in the EM calorimeter cells divided by the total energy deposit in the cluster. E_{ratio} is calculated using only energy deposits in the first (strip) layer.
- $\Delta\eta_1$ concerns the track-cluster matching and is defined as the difference of the cluster position in the calorimeter strip layer and the extrapolated track.
- F_{side} is defined in the first (strip) calorimeter layer and counts the energy outside the three central strips of the shower around the maximum value but within seven strips.
- Wstot is the total lateral shower width in the strip layer of the EM calorimeter.
- eProbHT is a likelihood variable based on the probability that a hit in the TRT is a high-threshold hit.
- The hadronic leakage, R_{had}, is the ratio of the transverse energy E_{T} in the hadronic calorimeter to E_{T} of the electromagnetic cluster. In the region $|\eta| < 0.8$ or $|\eta| > 1.37$, only the energy in the first layer of the hadronic calorimeter enters the calculation of R_{had}.
- Ws3 is a measure for the EM shower width in the calorimeter and considers the three strips around the strip with maximal energy deposit and is given in strip cell units. Note that this variable is not in the Run 2 identification menu, it is however used later for the measurement of the electron identification efficiency.

A likelihood is calculated from the discriminant input variables, a selection requirement on the likelihood determines whether the object is more likely an electron or not. Three different levels of tightness are defined: `Loose`, `Medium` and `Tight`. These categories are inclusive: `Tight` is contained in `Medium` which is contained in `Loose`. The tighter the identification selection, the more efficient the background rejection, but at the expense of signal efficiency. The electron identification efficiency for `Loose` is the highest (about 95%), whereas `Tight` is designed to meet the requirements of an analysis needing very high quality electrons and high background rejection at the expense of identification efficiency (around 80%).

Shower shapes are expected to vary with the electron p_{T} and the amount of material in the electron's path. The identification criteria are therefore a function of electron energy and pseudorapidity. Furthermore, some shower shape distributions are sensitive to the amount of pile-up. To reduce the sensitivity of the menu to pile-up conditions, the identification menu is loosened as a function of the number of primary vertices.

Electrons can also be produced as secondary particles through the decay of heavy-flavour quarks. Though these are real electrons, they are considered as non-prompt or "fake electrons". They produce non-isolated electrons in contrast to boson decays, for instance W and Z decays, which produce isolated electrons. Therefore, to further increase the purity of the signal sample, isolation criteria are applied. Two isolation variables are defined: the calorimetric and the track isolation.

Calorimetric isolation $E_{\mathrm{T}}^{\mathrm{cone0.2}}$ is the energy calculated from the sum of transverse energies of the topological clusters in a cone of $\Delta R < 0.2$ around the cluster associated to the electron candidate. The transverse energy of the electron itself within a cluster of size $\Delta\eta \times \Delta\phi = 0.125 \times 0.175$ around the cluster barycentre is subtracted. The calorimetric isolation variable is corrected for energy leakage out of the cluster and for energy deposit of pile-up and underlying events.

The track isolation variable $p_{\mathrm{T}}^{\mathrm{varcone0.2}}$ is defined as the sum of transverse momenta of all tracks in a cone of $\Delta R = \min(0.2, 10\ \mathrm{GeV}/E_{\mathrm{T}})$ around the track of the candidate electron. Only tracks fulfilling basic requirements on the track quality are taken into account, the electron track itself is excluded.

Several working points are defined, providing either a constant isolation selection efficiency (denoted `Loose`, `Tight` Isolation), or an efficiency which is a well-defined function of the electron p_{T} (`Gradient` working points). Alternatively, a constant cut value on the isolation variable is applied (`FixedCut` working points).

Some of the variables in the identification or isolation menu are not expected to be well modelled by MC simulation. However, the selection efficiency has to be reproduced by MC simulation. The calculated MC electron efficiency is therefore corrected by a scale factor to account for the different data and MC electron efficiencies. Simulated events are reweighted by this scale factor. Scale factors are multiplicative and a scale factor is applied for each selected lepton in the event.

A Tag and Probe method is implemented to measure reconstruction, identification, trigger and isolation selection efficiency in data. This Tag and Probe method exploits the well-defined event topology of either the $Z \to ee$ or the $J/\Psi \to ee$ decay using either the invariant mass of the Z or the J/Ψ or isolation properties. Scale factors are given with a precision of a few percent at low E_{T} and better than 1% at high E_{T}. A detailed description of the measurement of the electron identification efficiency using the Tag and Probe method is given in Section 5.

More information about the electron reconstruction, identification and isolation in Run 2 can be found in [101].

4.3.2 Muon reconstruction and identification

Muons leave a signal in the Muon Spectrometer (MS), the inner detector (ID) and the calorimeters. To reconstruct a muon, especially signals from the MS and the ID are evaluated. In regions not covered by the MS, energy loss properties in the calorimeters also help to detect muons. In regions where no information of the ID is available, muon reconstruction can be also performed using only MS information.

Tracks in the inner detector are reconstructed by means of a pattern recognition algorithm like the one for electrons described in Section 4.3.1. Algorithms search for hits in the muon chambers aligned on a trajectory. Segments are constructed by fitting these hits to a combined pattern. Based on these segments, a combinatorial search is performed to combine and fit segments from different layers to form muon track candidates taking into account hit multiplicity and fit quality. Muon track candidates are built from at least two matching segments. In the barrel-endcap transition region, only one high-quality segment with information on both η and ϕ coordinates is sufficient. If the assignment of segments to tracks is ambiguous, the best assignment is chosen. Alternatively, segments can be shared between tracks, if certain conditions are fulfilled. Finally, a global χ^2 fit is performed through the hits forming a track candidate. Hits causing a large χ^2 can be removed from

the track, a new fit is then performed. An algorithm searches for hits lying on the muon trajectory not yet included.

Information from the subdetectors are then combined. Different types of muons are defined differing by the subdetector information considered.

- Combined muons (CB): Reconstructed tracks in the ID and MS are matched by means of a combined fit through all hits in ID and MS. To improve the fit quality, hits can be removed or added. Usually, the patterns are matched starting from tracks from the MS, which are extrapolated to the ID, however, the extrapolation can also be performed starting with ID tracks.

- Segment tagged muons (ST): tracks in the ID are extrapolated to the MS and combined with at least one track segment.

- Calorimeter-tagged muons (CT): An ID track is extrapolated to a calorimeter signal compatible with a signal from a minimum-ionizing particle.

- Extrapolated muons: In regions where no information of the ID is available, MS muon trajectories are extrapolated to the beam line. If the extrapolated track is compatible with an interaction point taking into account its energy loss, a muon can be reconstructed. Minimal requirements on the track quality in the MS have to be fulfilled.

For central muons, the momentum resolution was found to be 2.3%, for forward muons with $|\eta| > 2.2$, the resolution was measured to 2.9% in the momentum range in question. The momentum scale is known with a precision of 0.05%.

An identification algorithm is then run over the muon candidate sample. The analyzer can choose between three levels of tightness, `Loose`, `Medium` and `Tight` and one menu optimized for high-p_{T} muons, with stricter or looser cuts on several variables: the ratio of compatibility between charge and momentum measurements in the ID and MS considering their uncertainties, the relative difference between MS and ID p_{T} measurement with respect to the combined track p_{T} and requirements on the χ^2 of the fit. Requirements on the number of hits and maximum number of holes in the tracks in ID and MS are set depending on the detector region.

As in the case of electrons, isolation selection criteria can be applied on top of the identification selection. Track- and calorimeter based variables are defined in a similar way than for electrons with the difference that the cone size for the muon track isolation variable, $p_T^{\mathrm{varcone30}}$, includes track momenta within a cone of $\Delta R = \min(0.3, 10\ \mathrm{GeV}/p_{\mathrm{T}})$ around the muon instead of a cone size of $\Delta R = 0.2$ as for the electron counterpart. The isolation selection criteria follow the same concept as for electrons.

Identification efficiencies in data and MC are measured using a Tag and Probe method similar to the one for electrons exploiting the distinct topology of $Z \to \mu\mu$ or $J/\Psi \to \mu\mu$ decays. Scale factors are measured with a precision of a few percent.

More information on muon reconstruction and the identification and isolation working points in Run 2 can be found in [104].

4.3.3 Hadronic jet reconstruction

Jets are reconstructed from signal in the calorimeters. Topological clusters are built from topologically connected calorimeter cells containing a signal which is significantly above a noise threshold [105]. Clusters of energy deposit are combined using the anti-kt algorithm [106] with a radius parameter of $R = 0.4$. The distances and the transverse momenta of the clusters are inputs to the clustering algorithm. Topological clusters are merged to a jet if the quantity d_{ij} is smaller than the quantity d_{iB} which are defined as:

$$\begin{aligned} d_{ij} &= \min(k_{ti}^{-2}, k_{tj}^{-2})\frac{\Delta_{ij}^2}{R^2}, \\ d_{iB} &= k_{ti}^{-2}, \end{aligned} \tag{4.3}$$

where Δ_{ij} is defined as $\Delta_{ij}^2 = (y_i - y_j)^2 + (\phi_i - \phi_j)^2$ and k_{ti} denotes the transverse momentum of cluster i, ϕ_i its azimuthal angle and y_i its rapidity.

This algorithm starts from the most energetic cluster, combines first the largest energy deposits to the jets within a radius of R, before adding the softer particles in a top to bottom approach sorted by their transverse momentum. Softer particles are first clustered to harder particles rather then clustering among themselves. It is therefore the clusters with the largest energy deposit that determine the position and shape of the jet, soft particles have little influence. The clustering algorithm is therefore infrared and collinear safe and produces jets with a fixed cone opening angle.

To reduce the dependency on pile-up, jets are not seeded from the pre-sampling layers and clusters are only added to the jet if the signal in the cluster exceeds a threshold. During the reconstruction process, the cluster energy is measured at the electromagnetic scale.

In several steps, the jet energy which is measured at the electromagnetic scale during reconstruction, is calibrated to the jet energy scale. The direction of the jet is first corrected such that it points to the hard-scattering vertex. The jet energy is corrected for the energy deposit from pile-up in two steps: at first a factor proportional to the area of the jet is subtracted from the reconstructed jet energy, the proportionality factor is calculated from the median p_{T} density of the jets in the event. The correction of the remaining pile-up dependence is determined with MC.

The jet is then calibrated to the jet energy scale. This calibration is based on a Gaussian fit of the energy ratio $\frac{E^{\mathrm{reco}}}{E^{\mathrm{truth}}}$ being the ratio of the simulated jet energy in MC of reconstructed and truth jets, respectively. The inverse of the mean of the Gaussian is the calibration factor from the electromagnetic scale to the jet energy scale.

The so-called Global Sequential Calibration corrects effects from different calorimeter responses due to fluctuations of the jet particle composition and the energy distribution within the jet. Finally, a residual in situ calibration to jets in data correct for different energy responses in MC and data. This correction is derived using the recoil against a well-defined and well-calibrated object such as Z bosons or photons. A similar method using the p_{T} balance in dijet events is also used to derive a residual calibration for jets in the region $|\eta| > 0.8$ by calculating the balance of the probe jet with a well-calibrated central jet.

The jet energy calibration is more precise for central jets $|\eta| < 1.2$ with transverse momenta of $20 < p_{\mathrm{T}} < 500$ GeV with a precision of more than 1% and less precise for central jets with $p_{\mathrm{T}} = 20$ GeV with a precision of 4.5%.

More details about jet reconstruction and energy calibration can be found in [105, 107].

To discriminate a jet from the hard interaction of interest from jets originating from pile-up, additional information from inner detector tracks can be used [108]. A cut on a

multivariate discriminant called jet-vertex-tagger (JVT) aims to reject jets from pile-up. It is based on the combination of several variables relying on the association of jets to tracks and on the association of tracks to primary vertices. Input tracks to this algorithm are required to have a transverse momentum of at least 500 MeV and are assigned to jet clusters using a ghost association technique [106]: ghost tracks are defined with the track's 4-momentum but infinitesimal magnitude which help to assign the tracks to the jet cluster.

4.3.4 Missing transverse energy and neutrino reconstruction

Particles interacting very weakly with matter can be detected indirectly by summing the momenta of all objects in the event and restoring transverse momentum balance: momentum conservation implies that as the transverse momentum before the collision is zero, it has to be zero after the collision as well. The imbalance of transverse momentum is denoted as "missing transverse energy", E_{T}^{miss}, and is associated with neutrinos in a Standard Model analysis. E_{T}^{miss} measurement relies on reconstructed, calibrated objects ("hard term") and on contributions from tracks associated to the event vertex but not to any object ("soft term"). Only tracks are considered in the soft term, neglecting not assigned energy deposits in the calorimeters.

Objects contributing to the hard term are electrons, photons, tau leptons, jets and muons. E_{T}^{miss} is calculated from the negative vectorial sum of all objects from each object class and the soft term, separately for the x and y coordinates in the transverse plane.

Objects included in the calculation of E_{T}^{miss} must meet certain requirements on object quality and identification and be matched to the hard-scattering vertex of the event. To suppress pile-up effects, tracks attributed to the soft term must issue from the hard-scattering vertex as well. Furthermore, overlap removal of tracks attributed to the soft term close to other objects avoids double-counting.

Mis-measurement of the E_{T}^{miss} could issue from limited detector acceptance and coverage and the fact that calorimetric energy deposits are not considered in the soft term. A detailed description on the E_{T}^{miss} measurement is given in [109].

Chapter 5

Electron identification efficiency measurement using the probe isolation distribution in the framework of a $Z \to ee$ Tag and Probe method

Many analyses, for example cross section measurements like the WZ cross section measurement presented in this thesis, rely on an accurate estimation of the efficiency of electron identification and its modeling in MC simulations. Electrons are identified using three identification criteria called `Loose`, `Medium` and `Tight`, defined in Section 4.3.1.

The electron identification efficiency is the probability that a real (genuine) electron[1] is identified given it is reconstructed,

$$\epsilon = \frac{\mathrm{N}_{\text{pass ID}}}{\mathrm{N}_{\text{pass ID}} + \mathrm{N}_{\text{fail ID}}}, \tag{5.1}$$

whereas $\mathrm{N}_{\text{pass ID}}$ are the number of real electrons passing the identification criteria and $\mathrm{N}_{\text{fail ID}}$ is the number of real electrons which fail the identification cut.

As the electron identification efficiency is difficult to model, the approach is to calculate the identification efficiency in data and simulation and derive a correction factor in order to correct for an imperfect modelling in MC simulations. This correction factor, the ID scale factor SF, is the ratio of the identification efficiency in data, ϵ_{Data}, and MC, ϵ_{MC},

$$SF = \frac{\epsilon_{\text{Data}}}{\epsilon_{\text{MC}}}. \tag{5.2}$$

A Tag and Probe method based on the $Z \to ee$ decay topology is used to select a pure and unbiased sample of real electrons. Remaining background from fake electrons (i.e. electrons from the decay of heavy quarks, misidentified jets or photons) is estimated by means of the probe isolation distribution ("Z_{iso}" method). This method is based on the assumption that electrons from a $Z \to ee$ decay are isolated in contrast to electrons from jets for example. It is therefore possible to define regions dominated by signal and by background.

The electron identification scale factors were measured with the Z_{iso} method and another $Z \to ee$ Tag and Probe method called the Z_{mass} method [103], which uses the invariant

[1] In the following, genuine electrons are denoted as "real" electrons.

mass of the electron pair to discriminate between signal and background. A combination of the SF results obtained with these two measurements has been provided to the ATLAS collaboration for 2015 and 2016 analyses. Furthermore, the Z_{iso} method was integrated in the official framework of the working group.

As the efficiency is dependent on the electron energy and the detector region, the measurement is performed in total in 200 bins in E_{T} and η ranging from an electron energy E_{T} of 15 GeV to an energy of 200 GeV for a rapidity region of $-2.47 < \eta < 2.47$. For a documentation of the 2015 measurement with a bunch-spacing of 25 ns, see [101]. A description on the basic concepts of the $Z \to ee$ Tag and Probe method is given in Section 5.1, the event selection is presented in Section 5.2 and information on the treatment of the background is given in Section 5.3. The treatment of the uncertainties is discussed in Section 5.4, the results are shown in Section 5.5 and in Section 5.6, studies on an improvement of the method are presented.

5.1 The Tag and Probe method on the $Z \to ee$ decay

For the identification efficiency measurement, a pure and unbiased electron sample selected from data is necessary. The $Z \to ee$ Tag and Probe method makes use of the topology of the decay of a Z-boson to two electrons with a well-defined value of the di-electron invariant mass. In the framework of a Tag and Probe method, strict quality and identification criteria are applied on one of the two electrons, called the tag. The other electron of the $Z \to ee$ decay, the probe, is then identified by means of this tag electron and the invariant mass of the tag and the probe, which should yield an invariant mass close to the Z-mass. Furthermore, tag and probe electron should have opposite charge. In order not to bias the identification efficiency measurement, no identification criteria is applied to the probe electron by default. The probe electron is only required to be a reconstructed electron. The electron identification efficiency is therefore measured on top of the reconstruction efficiency, reconstructed electrons are given as input to the measurement. All combinations of tag and probe electrons are considered, in particular, it is possible that a tag electron can be a probe if there is another electron in the event passing the tag selection and any probe can be a tag, assumed it meets the tag criteria. If only one tag and probe pair from each event were allowed, a bias would be introduced as mainly electrons meeting the stricter tag criteria would not be considered in the measurement. An illustration of the Tag and Probe methodology is given in Figure 5.1

5.2 Event selection

Only reconstructed electrons are considered in this measurement. The LAr, Tile and SCT (silicon microstrip tracker) subdetectors have to be fully functional, the full event information must be available and the event must pass the Good Run List. The event must fire a single-lepton trigger, either `HLT_e24_lhmedium_L1EM20VH or HLT_e60_lhmedium` for 2015 data or `HLT_e24_lhmedium_nod0_L1EM20VH` or `HLT_e60_lhmedium_nod0` for 2016 data. The event has to contain at least one primary vertex and at least two tracks have to be assigned to that vertex. Furthermore, the event has to contain at least two electrons. Object quality criteria on the electromagnetic calorimeter cluster of the tag and the probe electron have to be fulfilled and a jet veto is applied to the probe electrons, discarding all probes reconstructed within a radius of ΔR <0.4 from an AntiKt4 jet with a transverse

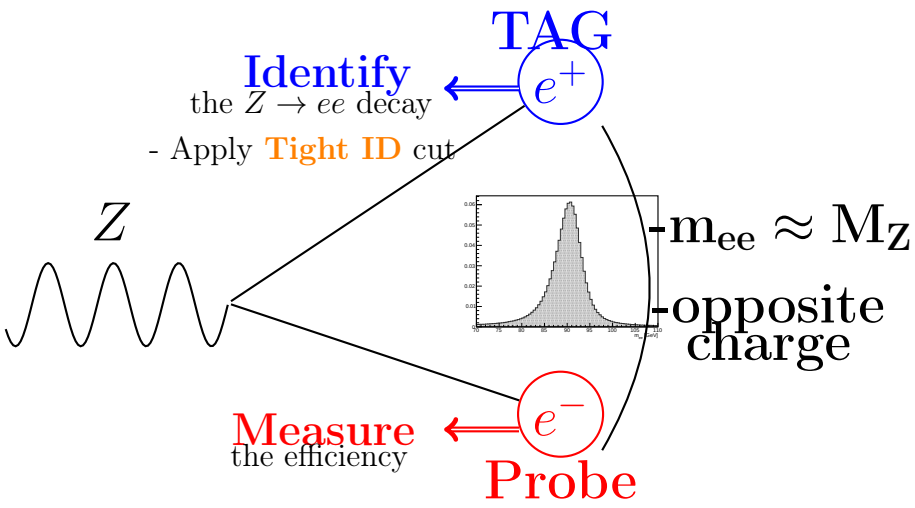

Figure 5.1 – *Illustration of the Tag and Probe method.*

Event in *Good Run List*	
Event fires single-lepton trigger	
Number of vertices ≥ 1	
≥ 2 tracks assigned to the vertex	
≥ 2 electrons in event	
Object quality criteria on ECAL cluster of tag and probe electron	
Reject probe electrons within ΔR <0.4 to AntiKt4 jet with $E_{\mathrm{T}} > 20$ GeV	
Tag	**Probe**
$E_{\mathrm{T}} > 25$ GeV	$E_{\mathrm{T}} \geq 15$ GeV
$-2.47 \leq \eta \leq 2.47$	$-2.47 \leq \eta \leq 2.47$
Not in $1.37 \leq \lvert\eta\rvert \leq 1.52$	-
Match to trigger	-
Pass `Tight` ID (LH)	Electron reconstruction successful
$75 \leq m_{ee} \leq 105$ GeV	
Tag & probe have opposite charge	
For MC events: successful truth matching for tag & probe electrons	

Table 5.1 – *Summary of the event selection cuts for the Z_{Iso} Tag & Probe analysis.*

energy E_{T} larger than 20 GeV. The phase space of the measurement is defined in the central region of the detector, thus for a pseudorapidity of $-2.47 \leq \eta \leq 2.47$, and an energy of $E_{\mathrm{T}} \geq 15$ GeV. The energy E_{T} of the tag electron must not go below 25 GeV and additionally to the pseudorapidity cut of $-2.47 \leq \eta \leq 2.47$, the barrel-endcap transition region $1.37 \leq |\eta| \leq 1.52$ is excluded. Also, the tag electron is required to be successfully matched to the fired single-lepton trigger and must satisfy the criteria of the `Tight` likelihood-based identification menu. The tag and probe electron pair must be oppositely charged and their invariant mass must be within a window of $75 \leq m_{ee} \leq 105$ GeV. In case of a MC sample, the reconstructed tag and probe electron must correspond to the two truth electrons from the Z-boson decay in the event which is checked using truth-matching. All selection cuts are summarized in Table 5.1.

5.3 Evaluation and subtraction of fake-electron background

Background to this measurement is composed of fake electrons, objects mis-identified as electrons and non-isolated electrons which can be electrons reconstructed within jets. To estimate the background, a data-driven technique is used: data events are used to model the background. Templates are constructed selecting probe electrons equally charged as the tag electron which fail cuts on shower shapes or loose identification criteria. These templates are constructed such that they represent the shape of the isolation distribution of the fake-electron background. As the $Z \to ee$ decay yields isolated electrons, the background should be well separable from the signal in the isolation distribution. The background enriched region is used to scale the background template to data. The scaling procedure is described in Section 5.3.3 and the construction of the templates is explained in Section 5.3.2. The discriminating variable, used to separate signal from background, is defined in Section 5.3.1.

5.3.1 The probe isolation distribution as discriminating variable

The energy in the isolation cone around the electron, $E_{\text{T}}^{cone,r}$, is calculated by summing up all the transverse momenta of the topological clusters, $E_{\text{T,topocluster}}$ [110], whose center of gravity[2] is lying within a distance $\Delta R = r$ to the center of gravity of the topological cluster assigned to the electron. The electron transverse energy E_{T}^{el}, defined as all the transverse energy within a window of fixed size of $\Delta\eta \times \Delta\phi = 0.125 \times 0.175$, around the center of the cluster assigned to the electron is subtracted:

$$E_{\text{T}}^{cone,r} = \left(\sum_{i(\text{topoclusters}) \in \Delta R < r} E_{\text{T,topocluster}} \right) - E_{\text{T}}^{\text{el}}. \tag{5.3}$$

An illustration of the definition of the calorimetric energy within an isolation cone is shown in Figure 5.2. For this measurement, the isolation cone radius r is 0.3.

The distribution of this variable is peaked around zero for isolated electrons whereas for non-isolated electrons, the calorimetric isolation takes values larger than zero. This can be exploited to define a signal and a background dominated region. Note that negative values of $E_{\text{T}}^{cone,r}$ are caused by corrections of the pile-up and the underlying event [101]: In the calculation of $E_{\text{T}}^{cone,r}$, a fixed amount of energy is subtracted from the energy in the cone. This subtraction energy is obtained from the calculation of a median energy density of the jets in the event and multiplied to the cone area excluding the area assigned to the central electron [111].

5.3.2 Background template construction

Background is estimated by constructing a template which represents the shape of the isolation distribution of background electrons. This template models the shape only, subsequently, the template has to be scaled to data to also represent the number of background events.

To construct the background template, probe electrons are selected by inverting cuts. Three different background templates are defined either by inverting cuts on shower shape

[2] Sum of cell position with respect to the ATLAS coordinate system weighted by the energy collected in the cell and divided by the energy sum in all the cells in the topological cluster [110].

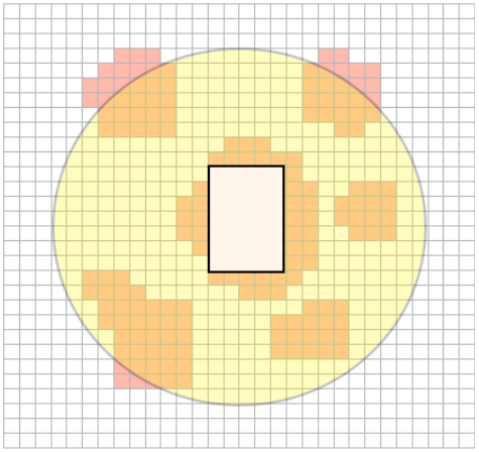

Figure 5.2 – *Illustration of the calorimetric isolation within an isolation cone with radius r around the electron $E_T^{cone,r}$. The cone is indicated by the yellowish circle, the topological clusters included in the calculation of $E_T^{cone,r}$ are illustrated in red. The energy in a fixed window size of $\Delta\eta \times \Delta\phi = 0.125 \times 0.175$ around the center of the cluster assigned to the electron, is subtracted. Latter is indicated by the white rectangle in the center of the cone. From [111].*

variables and/or on track-cluster-matching variables or by requiring the electron to fail the loose cut-based identification selection. Variables included in the background selection are mostly also contained in the identification menu definition. Furthermore, to avoid statistical overlap between the data signal electrons and the template electrons, only probe electrons having the same charge as the tag electron are selected. The resulting sample is dominated by fake electrons which are supposed to have the same isolation properties as the background events in the measurement and therefore model their isolation distribution shape.

The Z_{iso} method scale factor results are very sensitive to the background template definition, on the one hand due to the correlation between the isolation and identification variables and on the other hand due to the bias introduced by badly reconstructed real electrons which pass the background selection. This contribution is estimated and subtracted after the construction of the template. Three template definitions are used to model the background in this measurement, their discrepancy is used to estimate the systematic uncertainty introduced due to the modelling of the background. Studies within the scope of [103] have proven that these templates model well the background shape.

The three templates are defined as follows:

- "Template H2HANCE": Cuts on at least two of the following four variables, defined in Section 4.3.1, have to fail: E_{ratio}, $\Delta\eta_1$, F_{side} and `Ws3`. The definition of the cuts on these variables depends on E_{T} and η.

- "Template 1": The probe electron has to fail the cuts on the variables `Wstot` AND `eProbHT`, defined in Section 4.3.1. The definition of this template is dependent on E_{T} and η as shape biases were observed in studies within the scope of [103] or the variables are not defined for some (E_{T}, η) bins. For instance, no TRT information is available for $|\eta| > 2.0$, however, signal from the TRT is necessary for `eProbHT`. For these cases, the template is either constructed selecting probe electrons with the same charge as the tag electron without any further selection or the template shape

E_T bins [GeV]	10< E_T <20	20< E_T <25	25< E_T <40	40< E_T <60	E_T >60
Barrel	same-sign only		same-sign and Template1		
EndCap	same-sign only	same-sign and Template1			
$\|\eta\| > 2.01$	same as bin 1.81< $\|\eta\|$ <2.01				
Crack-region	same-sign only				

Table 5.2 – *Definition of Template 1 as a function of E_T and η. In some bins, variables included in the "Template 1" background selection are not defined or Template 1 does not describe the shape of the background well enough. In these cases, the template is either constructed using same-sign tag and probe events without any further selection or taken from another bin.*

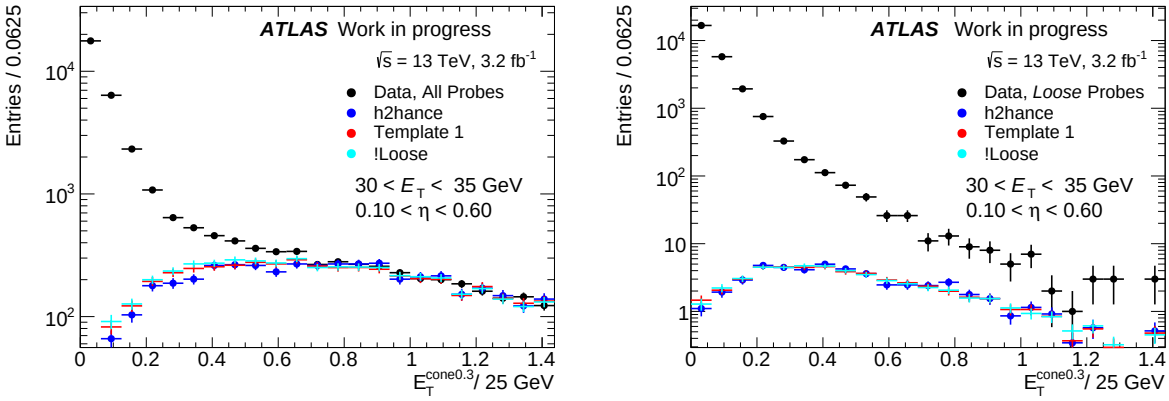

Figure 5.3 – *Comparison of the three background templates "H2HANCE" (blue), "Template 1" (red) and "!LOOSE" (light blue) for 3.2 fb^{-1} of $\sqrt{s} = 13$ TeV data recorded in 2015. An example for the background template for reconstructed electrons for one bin in E_T and η is shown on the left, the corresponding background template for `Loose` probe electrons is shown on the right. All templates are scaled to data, represented by the black dots. The procedure to scale the templates will be explained later in Section 5.3.3.*

is assumed to be the same as in another η-bin. The (E_T, η)-dependent definition of this template is listed in Table 5.2.

- "!LOOSE": Fail the cut-based loose identification menu.

A comparison between the three background templates is shown in Figure 5.3.

The likelihood identification menus contain a cut on the hadronic leakage, R_{had}, which is strongly correlated to the isolation as topological clusters also contains energy deposits in the hadronic calorimeter [103]. The shape of the probe isolation therefore changes by applying an identification cut on the background. This has to be considered in the construction of the background template for the electron candidate sample passing the identification selection by applying a cut on R_{had}, otherwise the requirement that the template shape reproduces the background shape is not given any more. Figure 5.4 illustrates the impact of the R_{had} cut on the shape of the isolation distribution of fake electrons.

Before scaling the template, the contribution of real electrons passing the background selection has to be estimated and subtracted. The shape of the isolation distribution is different for real and fake electrons, therefore a shape bias would be introduced in the template were this contribution not treated correctly. This so-called real electron contamination is estimated by applying the background selection on a $Z \to ee$ MC. The

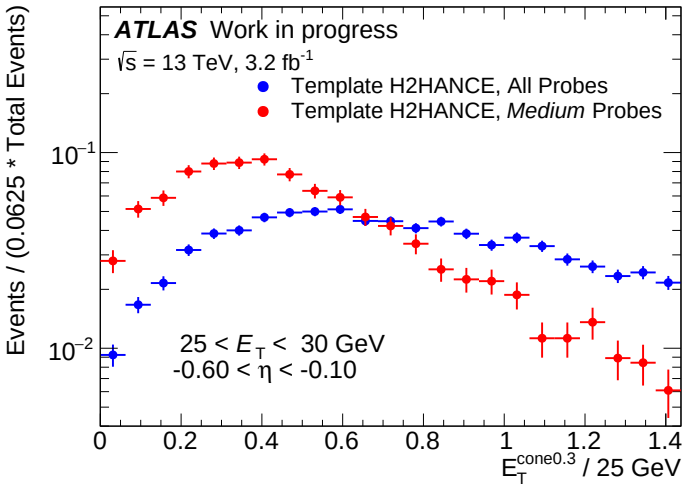

Figure 5.4 – *Example of the impact of the hadronic leakage cut on the shape of the background template, in this case Template* H2HANCE. *Note that the templates are scaled to the same integral for a better comparison.*

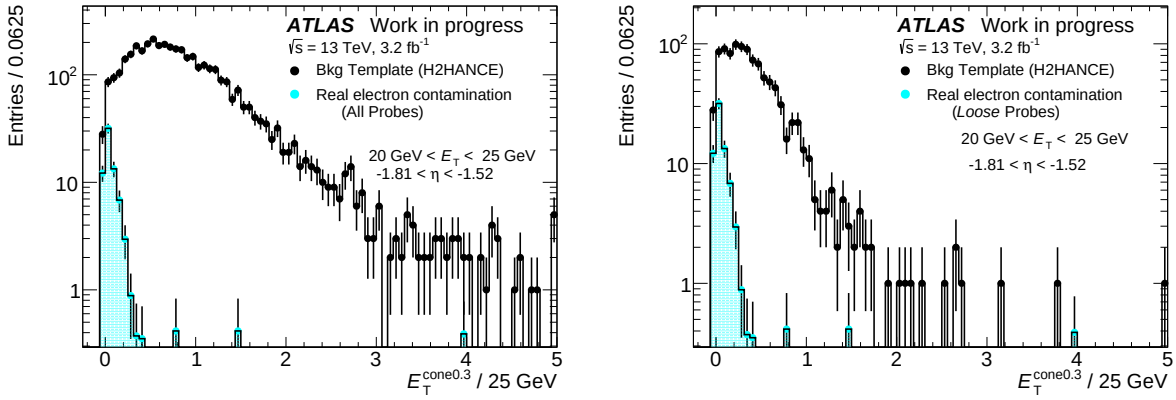

Figure 5.5 – *Visualization of the contribution of the real electron contamination to the background template for one bin in* (E_{T}, η) *for all probes (left) and for* `Loose` *probes (right). The distortion of the template shape especially in the signal region can be clearly seen.*

number of probe electrons in data and MC is compared by selecting an event sample containing tag and probe electrons passing both a `Tight` likelihood selection and whose invariant mass is found within a window of $80 < m_{ee} < 100$ GeV in order to reduce background from fake electrons in the data distribution. The number of selected events in data is compared with the number of selected events in MC and the ratio of data to MC events is the resulting scaling factor to scale the number of probes in the $Z \to ee$ MC sample to the number of probes in data.

The scaled real electron contamination contribution is then subtracted from the background template. Figure 5.5 illustrates the real electron contamination of the background model for one bin in (E_{T}, η) for all probes (left) and for `Loose` probes (right). It is clearly visible that the real electron contamination is accumulated around the peak region of the isolation distribution like the selected real electron signal events. Its contribution varies, it is in most cases below 5% but in the barrel-endcap transition region, the so-called crack-region, and for the forward detector region it can be as high as 40-60%.

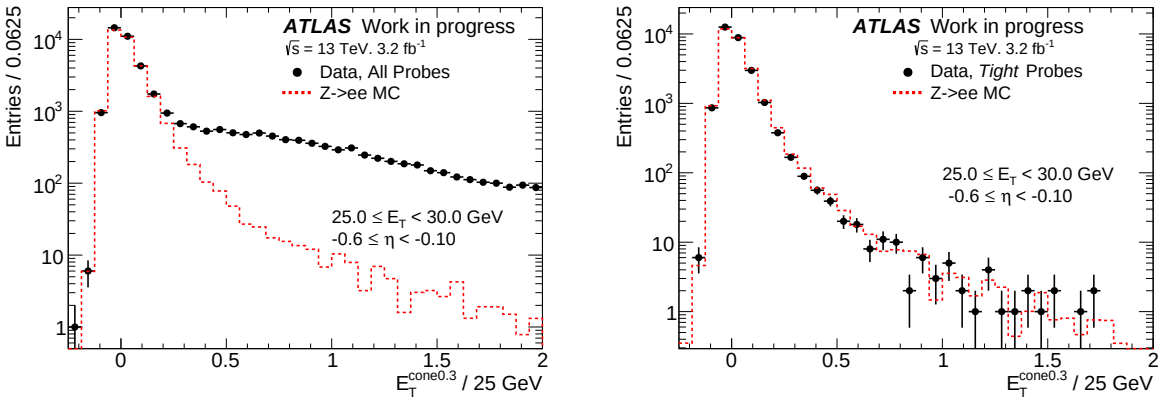

Figure 5.6 – *Comparison of the probe isolation distribution in data (black dots) and in a $Z \to ee$ MC simulation (red dotted lines). The isolation distribution is shown for reconstructed probes (left) and* `Tight` *probes (right) for one bin in E_{T} and η. The difference between data and MC corresponds to the fake electron background.*

5.3.3 Background evaluation and subtraction procedure

Due to the way the discriminating variable is constructed, it is possible to define a signal and a background-dominated region and use latter to scale the background template to data. The fake background is visualized in Figure 5.6 by means of the comparison of the isolation distribution of selected data events with a $Z \to ee$ MC simulation whereas the discrepancy is caused by fake electron background.

The number of events in the background template selection for which $E_{\text{T}}^{cone,r}/25\,\text{GeV} > 0.5$ applies is scaled to the number of data events in the same region defined by this isolation cut. Note that no shape information enters in the scaling procedure, the scaling is only based on counting the number of events in a selected sample. In the original scaling procedure described in [103], the contribution from real $Z \to ee$ electrons in the tail region of the probe isolation distribution, defined by $E_{\text{T}}^{cone,r}/25\,\text{GeV} > 0.5$, was neglected. The procedure was modified and now also the number of real electrons in the probe isolation distribution tail are considered. While these are negligible for the reconstructed electrons where there are much more background events in the probe isolation distribution tail than signal events (see Figure 5.6, left), it has a visible effect on the distribution of electrons passing the identification selection: the identification cut significantly reduces the number of background events (see Figure 5.6, right). Thus, first the number of real electron events is estimated by means of a $Z \to ee$ MC and scaled accordingly to data like the real electron contamination (see Section 5.3.2). The obtained number of real electron events in the distribution tail is then subtracted from the data event number in the tail region before scaling the background model to data. In Figure 5.7 and Figure 5.8, examples of the scaled background templates (blue shaded area), the $Z \to ee$ MC isolation distribution (red dotted lines) and their sum (purple line), which should yield the data (black dots), are shown. The distribution is shown for reconstructed (left) and reconstructed+identified (right) electrons for both scaling procedures: Figure 5.8 shows an example of the data, MC probe isolation distribution in a $Z \to ee$ MC and the estimated background if assuming that there are no real electrons in the isolation distribution tail and Figure 5.7 illustrates the agreement to data if the real electrons in the tail are considered when scaling the background template. As the latter procedure yields a better agreement with data, for 2016 scale factors, exclusively this scaling procedure was used while for 2015 scale factors

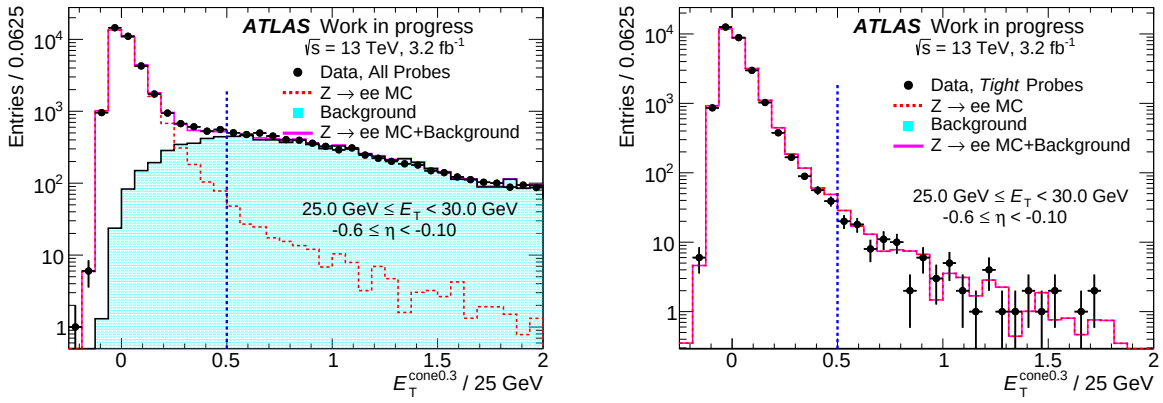

Figure 5.7 – *Example of the probe isolation distribution of the selected data events (black dots) and the scaled background template representing the isolation distribution of fake electrons (blue shaded area). The $Z \rightarrow ee$ MC simulation is plotted with red dots and the sum of MC and scaled background template is represented by the purple distribution which should match the data. The background template in this figure was scaled to data in the tail region $E_{\mathrm{T}}^{cone,r}/25\,GeV > 0.5$ (indicated by the vertical blue dotted line), real electrons in the tail of the isolation distribution were considered. The agreement to data is good for both reconstructed electrons (left) and* `Tight` *probes (right).*

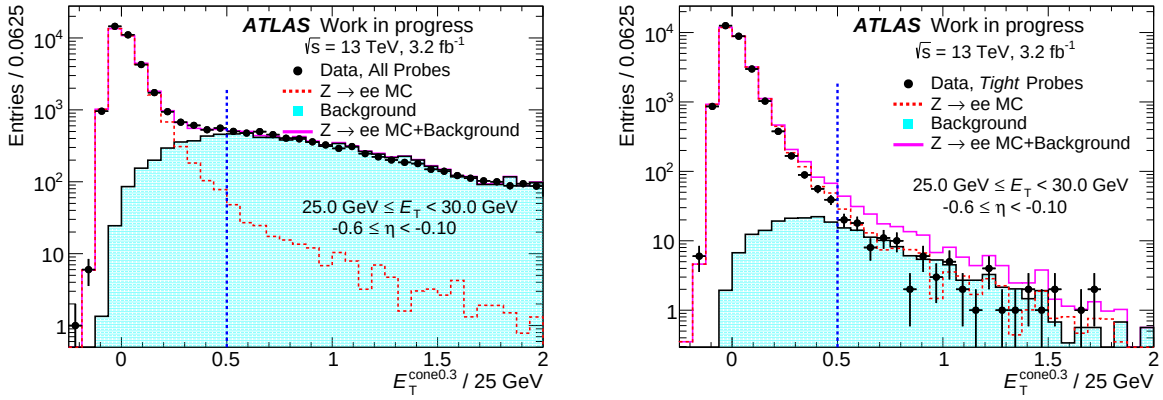

Figure 5.8 – *Example of the probe isolation distribution of the selected data events (black dots) and the scaled background template representing the isolation distribution of fake electrons (blue shaded area). The $Z \rightarrow ee$ MC simulation is plotted with red dots and the sum of MC and scaled background template is represented by the purple distribution which should match the data. The background template in this figure was scaled to data in the tail region $E_{\mathrm{T}}^{cone,r}/25\,GeV > 0.5$ (indicated by the vertical blue dotted line), assuming no real electrons in the distribution tail. The agreement to data is good for reconstructed electrons (left), but discrepancies are observed for* `Tight` *probes (right) where the background is overestimated.*

both approaches were applied and used in the estimation of the systematic uncertainty (see Section 5.4.2).

The impact of this improved scaling procedure is illustrated in Figure 5.9 for three different E_{T}-bins. The scale factor results obtained with the assumption that there is only background in the distribution tail is compared to the results obtained when considering

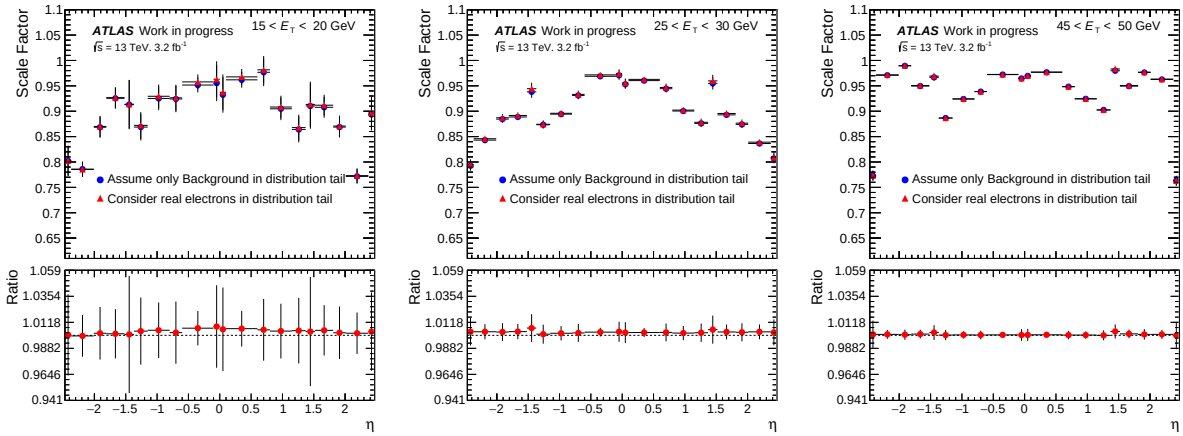

Figure 5.9 – *Comparison of the scale factor results obtained with the two different scaling procedures. Results obtained assuming only background in the tail region are marked with blue dots and the red dots represent the scale factor results obtained considering the real electrons in the tail region of the probe isolation distribution. These scale factor results were obtained with the efficiency calculation with* `Tight` *probe electrons. The uncertainties on the contain statistical uncertainties only, uncertainties on the ratio considers the statistical uncertainties on the blue dots from the upper panel. Note that the statistical uncertainties on the scale factor results for the different options are completely correlated.*

real electrons in the probe isolation distribution tail.

From Figure 5.9, it is already visible that the impact of this improved background scaling procedure on the scale factor result is small.

5.4 Computation of the uncertainties on the efficiencies and scale factors

5.4.1 Computation of the statistical uncertainty

To evaluate the statistical uncertainty on the electron identification efficiency $\epsilon = \frac{N_{\text{Numerator}}}{N_{\text{Denominator}}}$, the fact that the numerator (= number of reconstructed events passing the identification selection, N_{pass}) is a subset of the denominator (= number of reconstructed events passing and failing the identification criterion, N_0), has to be taken into account. Therefore, the denominator, N_0, has to be decomposed into statistically independent samples, $N_0 = N_{\text{pass}} + N_{\text{fail}}$, whereas N_{fail} is the number of events which fail the identification criterion. Using this, the efficiency calculation can be written as follows:

$$\epsilon = \frac{N_{\text{pass}}}{N_{\text{pass}} + N_{\text{fail}}} = \frac{N_{\text{pass}}}{N_0}, \tag{5.4}$$

N_{pass} and N_{fail} are disjoint sets as the outcome of the identification selection is either pass of fail. Applying standard Gaussian error propagation of uncorrelated quantities on equation (5.4) yields

$$\Delta\epsilon^2_{\text{stat.}} = \frac{(1-2\epsilon)\Delta N^2_{\text{pass}} + \epsilon^2 \Delta N^2_0}{N^2_0}, \tag{5.5}$$

where ΔN_{pass} and ΔN_0 are the statistical uncertainties on the numerator and the denominator, respectively, being $\sqrt{N_{\text{p}}}$ and $\sqrt{N_0}$ for unweighted events, as the case for data, and $\sqrt{\sum_i w_i^2}$, where w_i are the event weights, if dealing with weighted events as in MC.

While with equation (5.5), the statistical uncertainty on the MC efficiency can be calculated, the background template scaling and subtraction has to be accounted for in the calculation of the uncertainty on the data efficiency. A comparison of the number of events in the background template tail, $N_{\text{temp},c}$, with the number of probes in the tail region of the data isolation distribution yields the background template scale factor as described in Section 5.3.3:

$$SF_{\text{bkg}} = \frac{N_{\text{bkg},c}}{N_{\text{temp},c}}, \tag{5.6}$$

where $N_{\text{bkg},c}$ is $N_{\text{data},c}$, the number of probes in the data probe isolation distribution tail, if signal $Z \to ee$ events in the tail region are neglected and $N_{\text{data},c} - N_{\text{MC},c}$ if taking into account real $Z \to ee$ events in the tail. Latter is estimated by means of a $Z \to ee$ MC sample and $N_{\text{MC},c}$ is the predicted number of MC $Z \to ee$ in the tail region.

Note that the data probes are required to be oppositely charged as the tag electron, while all the probes passing the template selection are equally charged as the tag electron. Data samples and background template samples are therefore statistically independent.

In the following, the index "c" denotes the tail region of the isolation distributions, which is defined as $E_{\text{T}}^{cone,r}/25\ \text{GeV} > a$ where r, the opening angle of the isolation cone, is either 0.3 or 0.4 and $a \in \{0.4, 0.5, 0.6\}$. The index s denotes the peak region, $E_{\text{T}}^{cone,r}/25\ \text{GeV} < a$.

For the efficiency measurement, only the probes in the peak region were considered, consistently in the measurement of the MC efficiency and of the data efficiency. Therefore, only the statistical uncertainty on the background events in the probe isolation distribution's peak region are of interest:

$$N_{\text{bkg},s} = \frac{N_{\text{bkg},c}}{N_{\text{temp},c}} \cdot N_{\text{temp},s} = SF_{\text{bkg}} \cdot N_{\text{temp},s}. \tag{5.7}$$

The statistical uncertainty on equation (5.7) is calculated, using Gaussian error propagation on the statistically uncorrelated samples, as

$$\Delta N_{\text{bkg,s}} = \left(N_{\text{temp,s}} \cdot \frac{N_{\text{data,c}}^2}{N_{\text{temp,c}}^2} \cdot \left(1 + \frac{N_{\text{temp,s}}}{N_{\text{data,c}}} + \frac{N_{\text{temp,s}}}{N_{\text{temp,c}}} \right) \right)^{1/2}, \tag{5.8}$$

if $N_{\text{bkg,c}} = N_{\text{data,c}}$ and real $Z \to ee$ in the tail region are neglected and as

$$\Delta N_{\text{bkg,s}} = \left(N_{\text{temp,s}} \cdot \frac{(N_{\text{data,c}} - N_{\text{MC,c}})^2}{N_{\text{temp,c}}^2} \cdot \left(1 + \frac{N_{\text{temp,s}} \cdot (N_{\text{data,c}} + (\Delta N_{\text{MC,c}})^2)}{(N_{\text{data,c}} - N_{\text{MC,c}})^2} + \frac{N_{\text{temp,s}}}{N_{\text{temp,c}}} \right) \right)^{1/2}, \tag{5.9}$$

if $N_{\text{bkg,c}} = N_{\text{data,c}} - N_{\text{MC,c}}$. The statistical uncertainty on the MC events in the control region, $\Delta N_{\text{MC,c}}$, corresponds to the square root of the sum of squared event weights w_i, $\sqrt{\sum_i w_i^2}$.

The signal $Z \to ee$ events in data in the probe isolation distribution peak, N_{sig}, is calculated as the number of selected data events in the peak region with the the estimated

background events subtracted, $N_{\text{sig}} = N_{\text{data,s}} - N_{\text{bkg,s}}$. Its statistical uncertainty can be written as

$$\Delta N_{\text{sig}} = \sqrt{(\Delta N_{\text{data,s}})^2 + (\Delta N_{\text{bkg,s}})^2}. \tag{5.10}$$

The statistical uncertainty is evaluated separately for identified probes and reconstructed probes N_{pass} and N_0 and the results are plugged in equation (5.5) to obtain the statistical uncertainty on the data efficiency.

The selected samples for the different systematic variations are strongly statistically correlated. Therefore, to evaluate the combined statistical uncertainty on the measurement, the arithmetic mean of the statistical uncertainty is calculated, treating all the individual statistical uncertainties as 100% correlated:

$$\sigma^2_{\text{stat.}} = \frac{1}{N^2}(\sum_{i}^{N} \sigma_{i,\text{stat.}})^2, \tag{5.11}$$

whereas N is the number of systematic variations.

A detailed description of the treatment of the statistical uncertainty on efficiency measurements can be found in [112].

5.4.2 Computation of the systematic uncertainty

To estimate the systematic uncertainty on the scale factor and efficiency results, analysis parameters and selection cuts are varied. The application of a different background template out of the three templates defined in Section 5.3.2 is an example for such a variation. The scale factor is then recalculated with the new analysis parameter or selection cut. In total, the impact of seven sources of systematic uncertainty is investigated. All combinations of parameters are considered and an individual scale factor calculation is performed for each parameter set. At the end, a distribution of scale factors, which is assumed to be Gaussian, is obtained and the arithmetic mean and the standard deviation of the distribution of individual results yield the central scale factor result and the systematic uncertainty. Therefore, there is no baseline measurement to obtain the central scale factor value but all variations are treated as variations of the same measurement and are treated with equal importance. Figure 5.10 shows an example of this scale factor distribution for one bin in E_{T} and η.

In the following section, the analysis parameter and selection cut variations used to estimate the systematic uncertainty are discussed.

5.4.2.1 Variation of the cut on the invariant mass of tag and probe electron

Apart from the tag and probe invariant mass window cut of $75 < m_{ee} < 105$ GeV, tag and probe pairs with an invariant mass within the windows $70 < m_{ee} < 110$ GeV and $80 < m_{ee} < 100$ GeV are alternatively selected. By loosening the invariant mass window cut, more tag and probe pairs which lost some of their energy radiating off bremsstrahlung are selected and this causes lower-quality electrons to enter the selection. Looser invariant mass cuts result in lower identification efficiencies. Furthermore, widening the invariant mass window increases the fraction of background, a variation of the tag and probe invariant mass cut therefore also tests the stability of the background subtraction.

Figure 5.11 shows the impact of a variation of the tag and probe invariant mass cut on the scale factor. Tightening the cut increases the scale factor. Electrons which lost energy

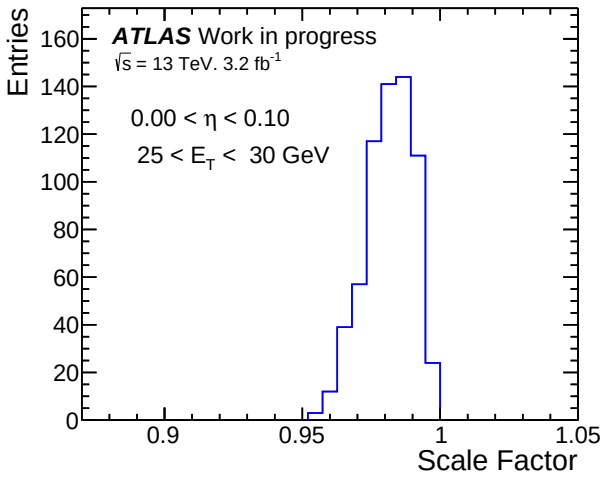

Figure 5.10 – *Scale factor distribution resulting from the individual scale factor measurement for each parameter set. The scale factor result is the arithmetic mean of this distribution and the systematic uncertainty is the standard deviation.*

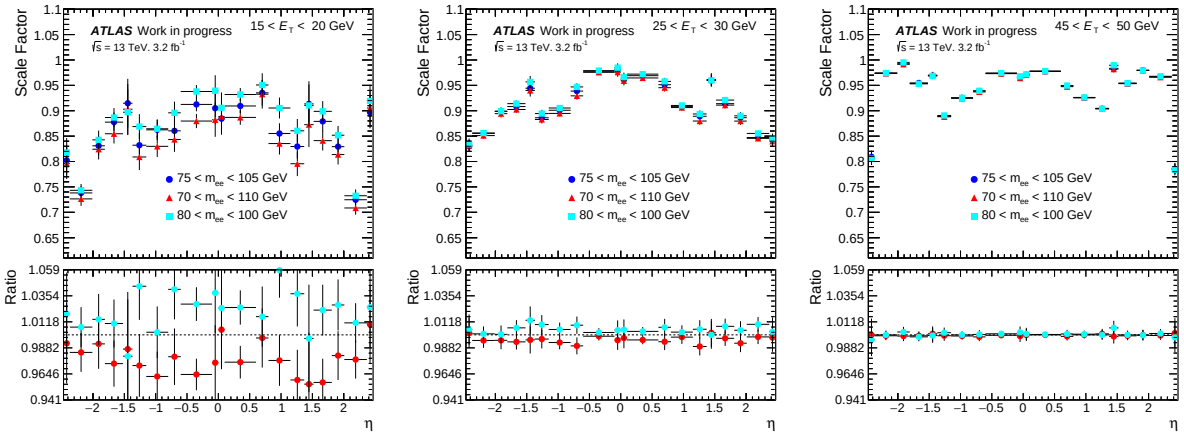

Figure 5.11 – *Impact of a tag and probe pair invariant mass cut variation on the scale factor as a function of η for three different bins in E_{T}. The scale factor results for the three different invariant mass window cuts for a* `Tight` *selection are shown in the plot. The ratio plot shows the ratio between the up and down variation with respect to the central variation in the color consistent with the upper plot. Only statistical uncertainties are shown, the uncertainties on the ratio considers the uncertainties on the dark blue dots from the upper panel.*

due to bremsstrahlung are likely to be less well modeled, the scale factor moves away from one. The impact on the scale factor is highest for low electron transverse energy E_{T} and decreases with higher E_{T}. It is in most cases below 3% but it can be as high as 6%.

5.4.2.2 Variation of the tag electron selection

The tag requirement is varied slightly: in addition to the `Tight` likelihood requirement, the tag must also pass the isolation criterion $E_{\mathrm{T}}^{cone,r}/25$ GeV <0.3. This way, the uncertainty on the scale factor result due to the tag selection and the event quality is estimated. The scale factor result should not depend much on the tag selection and the effect is indeed

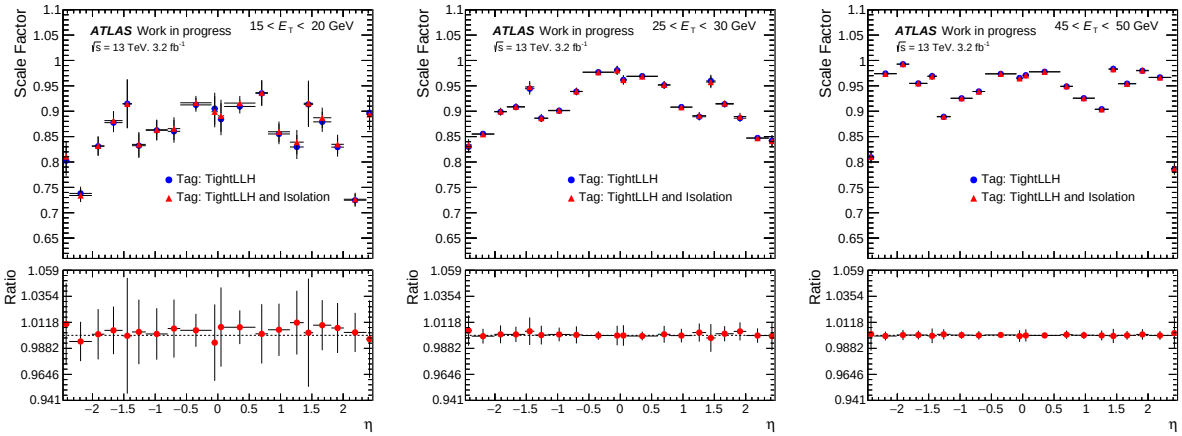

Figure 5.12 – *Impact of a variation of the Tag selection shown for the* `Tight` *scale factor as a function of* η *for three different bins in* E_{T}*. Only statistical uncertainties are shown on the plot. The ratio plot visualizes the change of the scale factor if applying an isolation criterion in addition to the* `Tight` *selection with respect to a tag selection without an additional isolation criterion. The uncertainties on the ratio considers statistical uncertainties on the blue dots from the upper panel.*

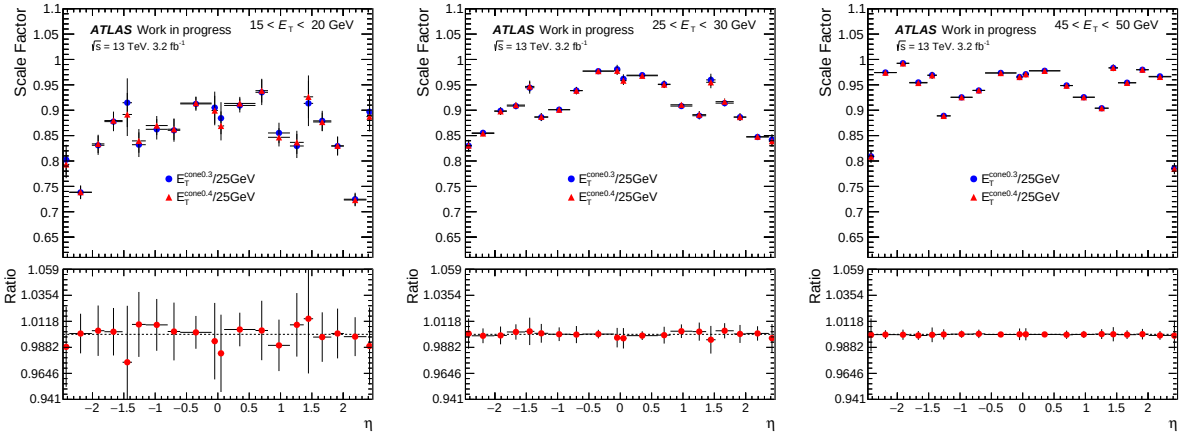

Figure 5.13 – *Effect of the change of the size of the isolation cone in the definition of the probe isolation as a function of* η *for three different* E_T*-bins. The ratio plot shows the ratio with respect to a cone size of* $r = 0.3$*. Uncertainties on the scale factors contain statistical uncertainties only, the ratio panel contains statistical uncertainties on the blue dots.*

below 1% which is exemplified in Figure 5.12.

5.4.2.3 Variation of the discriminating variable

An alternative cone size in which the energy around the electron is collected is used to calculate the probe isolation $E_{\text{T}}^{cone,r}$. Apart from a cone size of $r = 0.3$, a cone size of $r = 0.4$ is applied. The uncertainty due to energy leakage out of the isolation cone is estimated. The effect of this variation is visualized in Figure 5.13 for the scale factor for a `Tight` selection and is in most cases well below 1%.

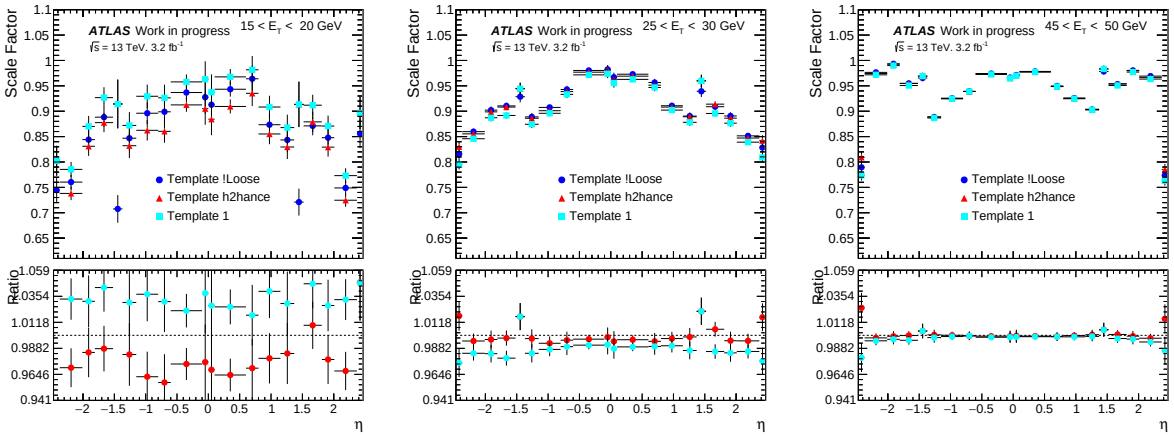

Figure 5.14 – *Impact of the background model variation on the* `Tight` *identification efficiency scale factor as a function of* η *for three different bins in* E_{T}*. The different background templates have been described in Section 5.3.2. The ratio on the lower panel on the plots is taken with respect to the Template* !LOOSE*. Uncertainties contain statistical uncertainties, the ratio panel contains statistical uncertainties on the dark blue dots from the upper panel.*

5.4.2.4 Variation of the background template selection

Three different background template selections are applied to model the background shape. These selections have been described in Section 5.3.2. This approach allows to estimate the uncertainty introduced by the modelling the background shape. How the background template model influences the scale factor result for a `Tight` selection is shown in Figure 5.14. The variation of the background template has the highest contribution to the scale factor systematic uncertainty. The impact of this variation is around 3-5% for the lowest E_{T}-bin. A mis-modelling of the background template could therefore introduce a large bias in the scale factor measurement.

5.4.2.5 Variation of the scaling of the real electron contamination

The $Z \to ee$ MC distribution is scaled to data by comparing the number of `Tight` probes in MC and data which pass together with the corresponding tag electron an invariant mass window cut of $80 < m_{ee} < 100$ GeV. Furthermore, the probe has to be oppositely charged as the tag electron (see Section 5.3.2). The so-obtained MC-to-data scaling factor is used to scale the real electron contamination of the background template. However, the real electron contamination is selected by requiring the probe to be equally charged as the tag electron. In principle, in a $Z \to ee$ MC, the production of a Z boson and its decay to two electrons should be simulated along with pile-up and underlying event, therefore, two oppositely charged electrons should be contained in a $Z \to ee$ MC event. Furthermore, truth-matching to the tag and the probe MC electron is applied. Thus, the only reason for charge-misidentification should be from electrons which underwent bremsstrahlung and subsequent pair-production of the photon and from very high-energetic electrons whose track in the inner detector is very straight and the direction of the bending cannot be determined reliably. Dealing with electrons from a Z boson decay, the contribution of latter component should not be very high. The effect of bremsstrahlung is higher, the more matter the electron traverses the detector. Whereas in data, besides bremsstrahlung, incorrect track-cluster matching is also an issue. The validity of the MC-to-data scaling factor for same-sign tag and probe pairs therefore has to be checked and corrected for possible

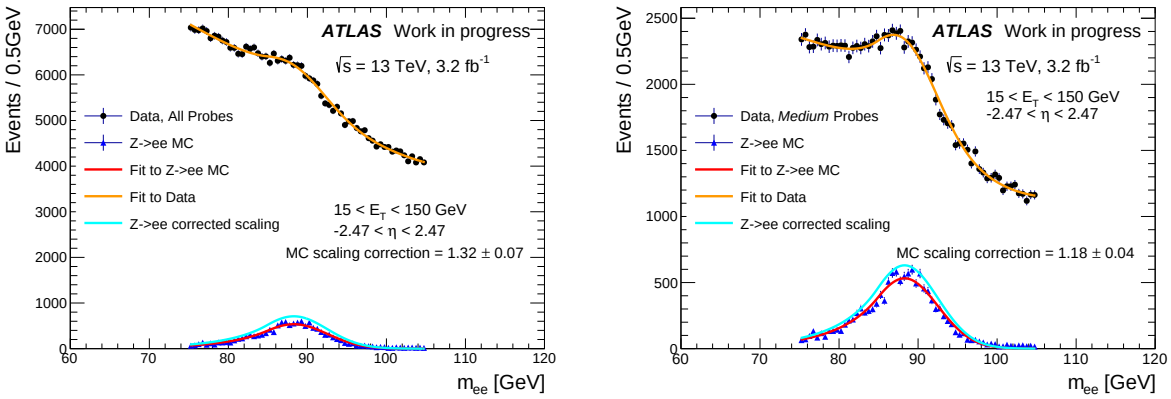

Figure 5.15 – *Examples of a fit to the invariant mass of tag and reconstructed (left) and* `Medium` *(right) template probe electrons with a transverse probe energy E_{T} of $15 < E_{\text{T}} < 150$ GeV and a pseudorapidity η within $-2.47 < \eta < 2.47$. A sum of a 3rd-order polynomial and a Crystal-ball function (orange line) is fitted to data (black dots) and a Crystal-Ball function (red line) is fitted to the $Z \to ee$ MC real electron contamination distribution (blue triangles). A Crystal-Ball function with the corrected normalization is represented by the light blue line.*

mis-modelling of the charge-misidentification in MC. The invariant mass distributions of the same-sign tag and probe pairs passing the background selection in data and MC are compared to estimate this effect.

In MC, the invariant mass distribution of the same-sign tag and probe pairs is accumulated around the Z-boson mass whereas in data, the invariant mass of the tag and the probe electron passing the template selection should be an exponentially shaped curve. Real electron-contamination contained in the template form a peak at the Z-mass. A Crystal-Ball function was fitted to the tag and probe invariant mass distribution of real electron contamination events in MC. The invariant mass distribution of the background template probe and the corresponding tag in data is fitted with the sum of a 3rd-order polynomial and a Crystal-Ball function whereas all fit parameters of the Crystal-Ball function were fixed to the values obtained with the real electron contamination distribution fit except for the normalization. Examples of the fit are shown in Figure 5.15. The normalization parameters of the Crystal-Ball functions are extracted from the MC and data fit results and compared. The ratio of the normalization parameters is an estimate of the uncertainty of applying the MC-to-data scale factor derived using oppositely charged tag and probe pairs to same-sign tag and probe pairs. It gives also a rough estimate on the effect of the charge mis-identification mis-modelling. A correction was estimated on the templates for all and identified probes inclusively over all bins in E_{T} and η. The correction is the same for all working points. This correction was estimated to $\pm 30\%$ for all and identified probes. This up and down variation has a maximal effect of about 0.5-1% on the scale factor result but can be higher in the barrel-endcap transition region and in the endcaps as can be extracted from Figure 5.16. The effect on the scale factor result due to this variation is higher for η bins with a higher fraction of real electron contamination: for the crack-region and for the most forward η-bin.

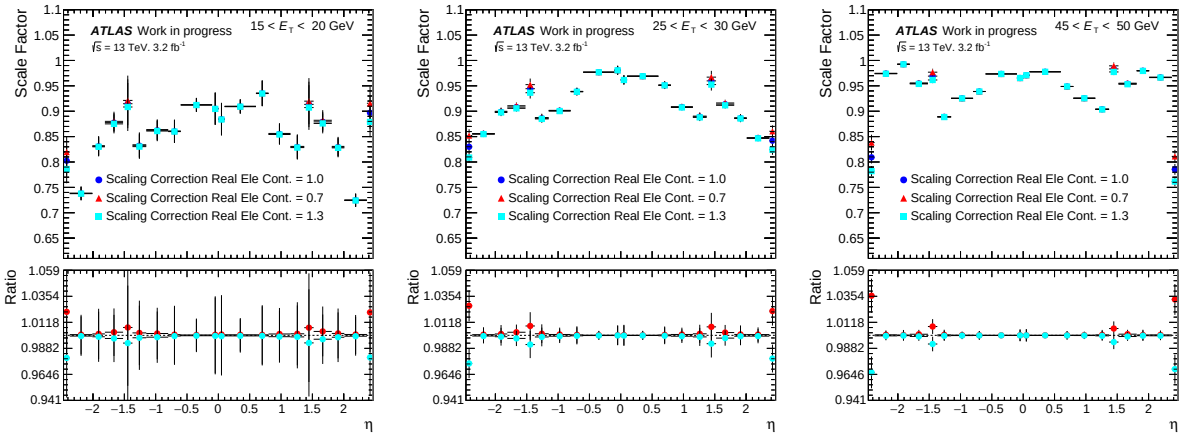

Figure 5.16 – *Impact of a variation of the real electron contamination of the background template by ±30%. Statistical uncertainties are shown on the scale factors. The ratio shown below is taken with respect to the central variation which is the nominal MC-to-data scaling factor, the uncertainties on the ratio consider the statistical uncertainties on the dark blue dots.*

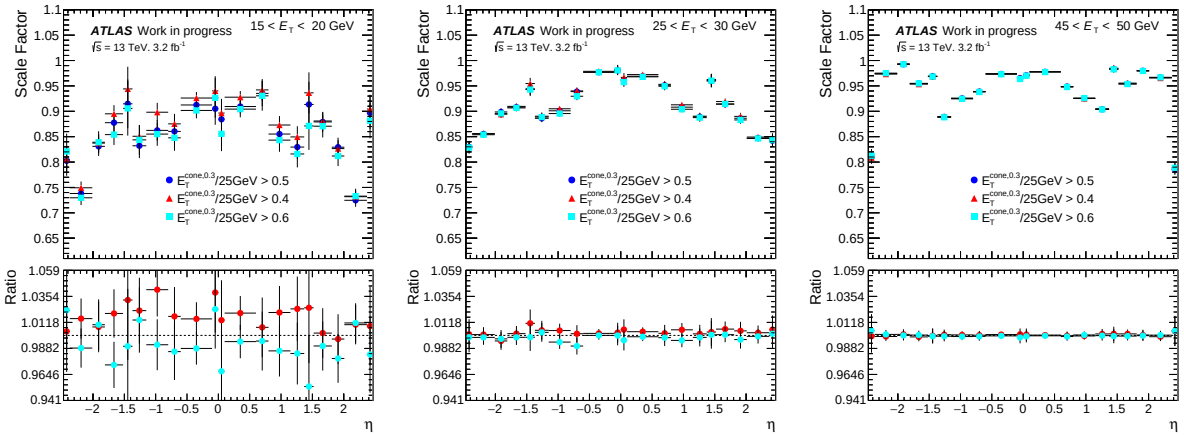

Figure 5.17 – *Effect of a variation of the probe isolation cut. The ratio plot shows the ratio with respect to the central variation,* $E_{\mathrm{T}}^{\mathrm{cone},r}/25\ GeV = 0.5$.

5.4.2.6 Variation of the background template scaling region

The electrons in the tail region of the probe electron isolation distribution are not considered in the calculation of the scale factor. Therefore, it is obvious to probe the impact of this probe isolation cut by varying the definitions of tail and signal region. Apart from the cut at $E_{\mathrm{T}}^{\mathrm{cone},r}/25\ \mathrm{GeV} = 0.5$ dividing the probe isolation into a signal and a tail region, cuts at $E_{\mathrm{T}}^{\mathrm{cone},r}/25\ \mathrm{GeV} = 0.4$ and $E_{\mathrm{T}}^{\mathrm{cone},r}/25\ \mathrm{GeV} = 0.6$ are applied alternatively. The up and down variations yield a difference of up to 3-4% with respect to the central variation which can be seen by means of Figure 5.17 for the `Tight` selection. The impact of this systematic decreases with the electron transverse energy.

5.4.2.7 Variation of the scaling procedure

As described in Section 5.3.3, the background template is scaled to the tail region of the data probe isolation distribution, defined as $E_{\mathrm{T}}^{\mathrm{cone},r}/25\ \mathrm{GeV} > a$ whereas $r = 0.3$ or 0.4 and $a \in \{0.4, 0.5, 0.6\}$. The scaling of the template can be derived neglecting real electrons in this tail region or taking this contribution into account. These two possible

Systematic	15< E_{T} < 20 GeV		45< E_{T} < 50 GeV	
	`Loose`	`Tight`	`Loose`	`Tight`
m_{ee} cut [%]	5.8	5.9	0.48	0.63
Tag selection [%]	1.2	1.2	0.37	0.20
$E_{\text{T}}^{\text{cone},r}$ size [%]	2.5	2.5	0.11	0.12
Background template [%]	26.9	29.3	2.9	2.5
Real electron contamination [%]	2.3	2.1	4.3	3.6
Signal, Control region definition [%]	3.7	4.6	0.42	0.43
Scaling procedure [%]	1.1	0.80	0.32	0.35

Table 5.3 – *Relative impact of the systematic variations on the scale factor compared to a reference variation for two bins in E_{T} for the `Loose` and `Tight` identification menus. If two systematic variations of a parameter exist, one of them is chosen as reference, in case of three systematic variation, the variation giving the most central scale factor is chosen as reference. These value correspond to values in the ratio plots of Figures 5.9- 5.17. Note that the largest impact of a variation among all η bins in that E_{T} bin is displayed. Therefore, the impact shown in the table might be large as it is can also be the impact of the systematic in the transition or the end-cap region, as in the case of the background template uncertainty.*

scaling procedures have already been described in detail in Section 5.3.3. For 2016 data however, real electron contribution in the isolation distribution tail is always considered in the calculation of the background template scaling factor. The presence of real electrons in the distribution tail is not negligible any more compared to the background for identified electrons, and therefore has an impact on the background contribution in the signal region. Still, distribution tails are often subject to mis-modelling. This mis-modelling could be estimated this way. However, the order of magnitude of the impact of this systematic uncertainty is below 1% and small compared to other uncertainties. It can therefore be safely neglected in 2016 scale factor calculation. The order of magnitude of this variation can be extracted from Figure 5.9.

Table 5.3 provides a summary of the impact of the various systematic uncertainties.

The procedure to evaluate the systematic uncertainties should be improved because of following reasons:

- All variations are treated as individual measurements and enter with the same weight in the final result. This is also true for extreme results.
- It is always assumed that the true value for the scale factor lies in between the scale factor results for the various variations, this might not be necessarily true.
- This procedure of taking the mean and the standard deviation is based on the assumption that the scale factor results are normally distributed. This is true for most cases with exception of some problematic η-regions, for instance the crack-region.
- If too many meaningless variations enter the systematic uncertainty calculation, the systematic uncertainty could be artificially reduced. However, all variations have a visible effect on the final scale factor result.
- The systematic uncertainty calculation based on variations in the measurement procedures and definitions rather than the impact on systematic sources could lead to a

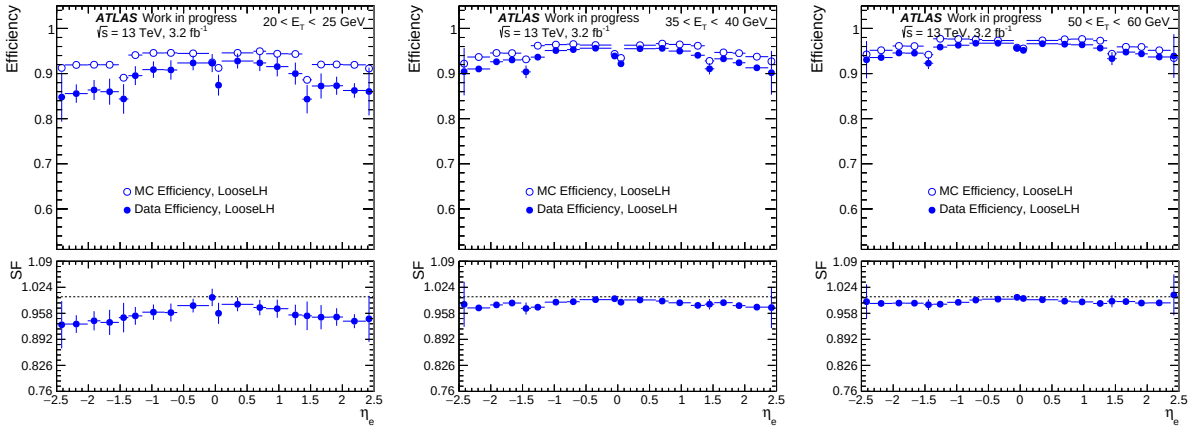

Figure 5.18 – *Data (full dots) and MC (open dots) identification efficiencies as a function of η for three different bins in E_{T} for the* `Loose` *working point. The ratio data to MC efficiency, the scale factor, is shown in the ratio plot. The uncertainties contain statistical and systematic uncertainties.*

double-counting of systematic effects.

Therefore, it has been decided that for future measurements, one baseline variation will be chosen and the contribution of the systematic sources will be evaluated by taking the difference between the baseline result and the result of one extreme variation. Furthermore, it is planned to not any more vary the analysis parameters but to relate the systematic uncertainty to systematic sources like the impact of electron p_{T} and energy mis-modelling for instance.

5.5 Results

In this section, some results for the electron identification efficiencies and the corresponding scale factors are presented. Electron identification scale factors have been calculated for 2015 and 2016 data with a bunch-spacing of 25 ns and a center-of-mass energy $\sqrt{s} = 13\,\mathrm{TeV}$ and provided to the ATLAS collaboration for data analyses with 2015 and 2016 data. Note that only scale factors and not efficiencies are provided and recommended to be used in analyses as the efficiencies are dependent on the event topology. The dependence on the event topology cancels if taking the ratio between data and MC efficiencies, thus, the idea is to correct the selection efficiencies in MC obtained in the individual analyses with the scale factor. The scale factors can be applied to an electron under the condition that the electron is separated from the closest jet by a distance of $\Delta R > 0.4$.
Following results were obtained with the full 2015 25 ns data set ($\mathcal{L} = 3.2\,\mathrm{fb}^{-1}$) and a MC which includes the simulation of 2015 pile-up conditions. These results were also used as a pre-estimate for the scale factors for 2016 data along with several correction considering the change in pile-up conditions and the new gas in the transition-radiation detector (TRT). The latter corrections are not taken into account here.

In Figure 5.18, Figure 5.19 and Figure 5.20, examples for MC (empty dots) and data (filled dots) efficiencies are shown as a function of η for three different E_{T}-bins. The ratio-plot visualizes the scale factor. Figure 5.18 displays some results for the `Loose` identification menu, Figure 5.19 for `Medium` and Figure 5.20 for the `Tight` menu.

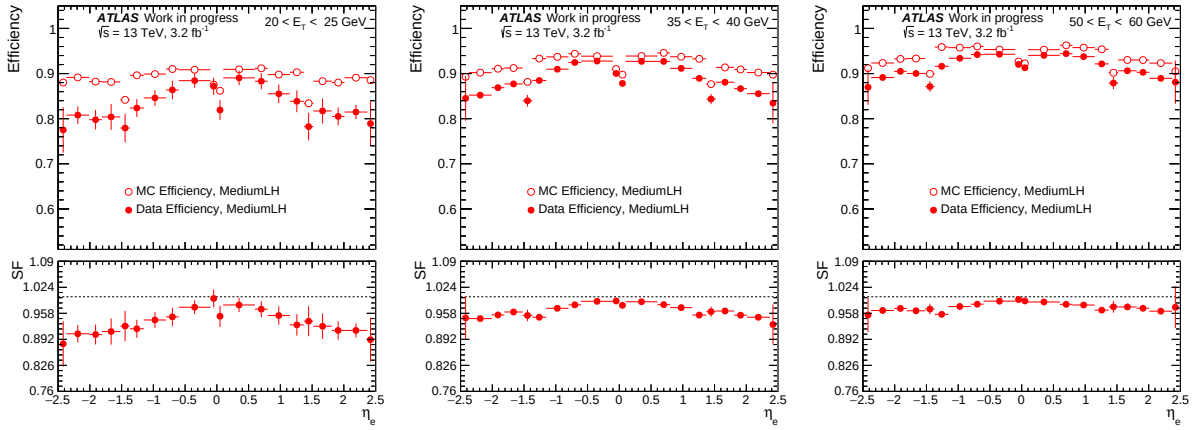

Figure 5.19 – *Data (full dots) and MC (open dots) identification efficiencies as a function of η for three different bins in E_{T} for the* `Medium` *working point. The ratio data to MC efficiency, the scale factor, is shown in the ratio plot. The uncertainties contain statistical and systematic uncertainties.*

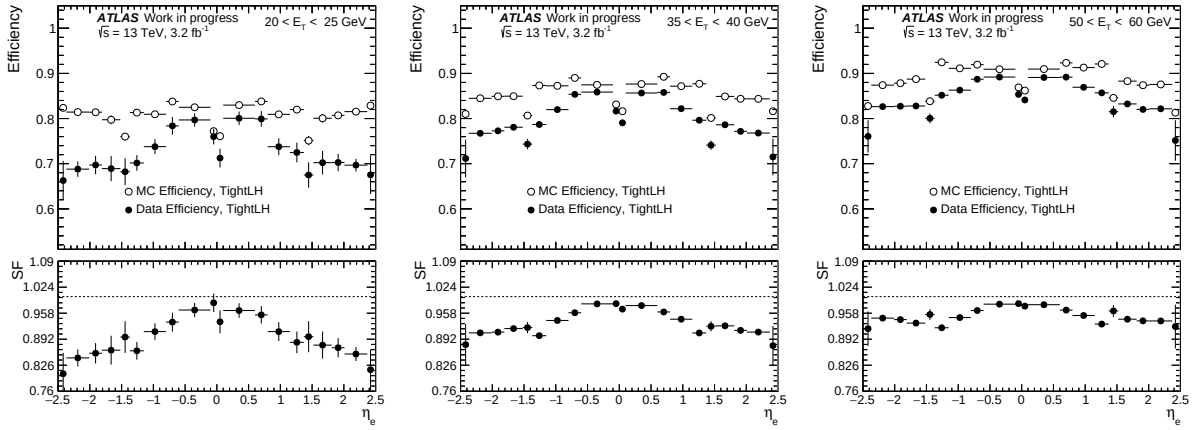

Figure 5.20 – *Data (full dots) and MC (open dots) identification efficiencies as a function of η for three different bins in E_{T} for the* `Tight` *working point. The ratio data to MC efficiency, the scale factor, is shown in the ratio plot. The uncertainties contain statistical and systematic uncertainties.*

To create the identification menus, simulated distributions of the discriminating variables of real and fake electron background are used as input. A multivariate analysis method generates several cut chains to decide whether the electron is a signal or a fake electron. The criteria and cuts are tightened with increasing menu tightness. In some cases, the data distribution of the discriminating variable is shifted with respect to the MC distribution. A shift of the distribution of real electrons towards the MC distribution simulating the discriminating variable in question for fake electron causes more real electron to be declared as background with respect to MC, thus resulting in a lower identification efficiency for data. The interaction of the radiation with the detector is higher in the transition region between the barrel and the endcap due to the higher amount of matter in the detector. This affects the identification efficiency as the signature of real electrons is less different from the signature of fake electrons in that region.

Figure 5.21 shows the relative statistical and total uncertainties on the scale factors obtained with the Z_{iso} method as a function of η for four bins in E_{T}. The uncertainties decrease with increasing E_{T}: while the precision is around 3-5% for $15 < E_{\text{T}} < 20$ GeV, it is around 1% for $25 < E_{\text{T}} < 30$ GeV and decreases to sub-percent level for higher electron

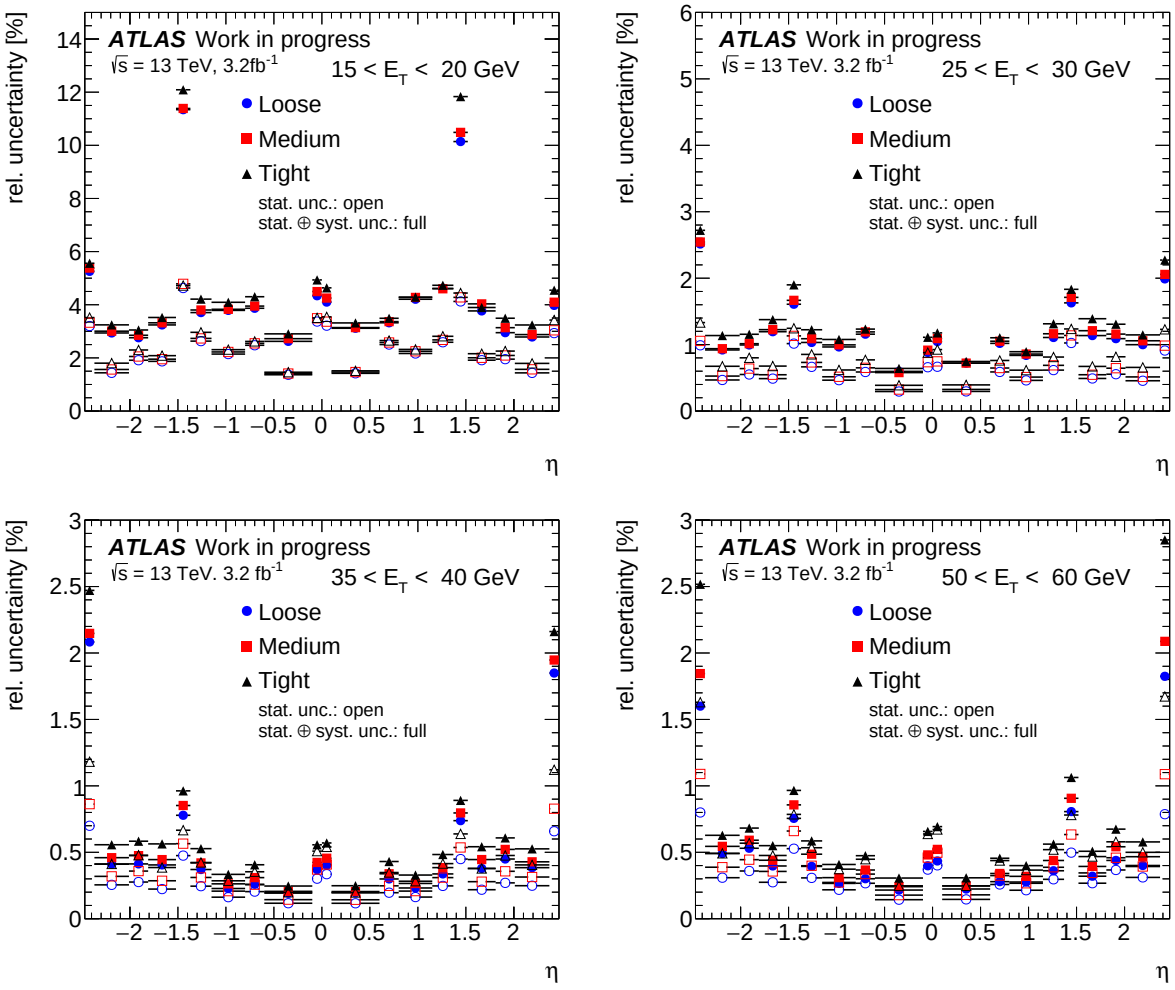

Figure 5.21 – *Relative uncertainties on the scale factor results. The open dots show the statistical uncertainty, the full dots the total uncertainty consisting of statistical and systematic uncertainties. Blue dots represent uncertainties on scale factors for the* `Loose` *menu, red* `Medium` *and black* `Tight` *scale factor uncertainties. Note that the range of the ordinate differs in the plots.*

E_{T}. The precision is lower in the crack-region and at high $|\eta|$.

Two complementary methods are used to obtain the scale factors applied to electrons in ATLAS data: the Z_{mass}, which uses the tag and probe invariant mass as a discriminating variable, and the Z_{iso} method which was discussed in detail above. At low E_{T}, the two methods show a discrepancy: the Z_{mass} method always yields systematically higher scale factor results as the Z_{Iso} method. Different effects were evaluated (see Section 5.4.2), but none of them seems to be responsible for this discrepancy. However, at high E_{T}, they are perfectly in agreement as indicated in Figure 5.22.

The results from the Z_{mass} and the Z_{iso} methods are combined to obtain the scale factors correcting the electron identification efficiency in simulations in ATLAS analyses. The behaviour of the efficiencies and scale factors of that combination as a function of η for a E_{T}-range $15 < E_{\mathrm{T}} < 80\,\mathrm{GeV}$ is presented in Figure 5.23 and as a function of E_{T} for $-2.47 < \eta < 2.47$ in Figure 5.24. Note that another Tag and Probe method on the $J/\Psi \rightarrow ee$ decay is used to obtain efficiencies and scale factors for electron transverse energies of $7 < E_{\mathrm{T}} < 20$ GeV, for details, see [101].

Figure 5.24 clearly shows that the efficiency is larger with increasing E_{T}. Fake elec-

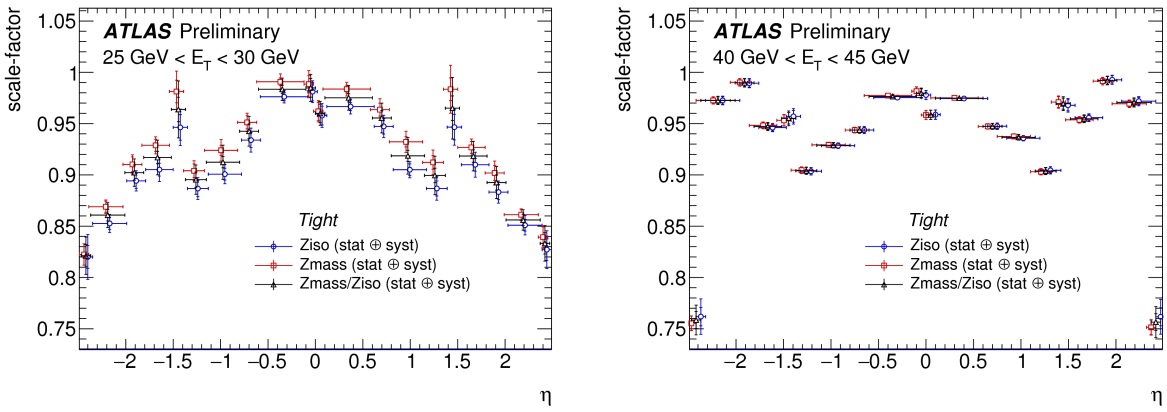

Figure 5.22 – *Comparison of electron identification scale factors obtained with the Z_{mass} and Z_{iso} method in one bin at low E_{T} and in one bin at high E_{T} and their combination. From [101].*

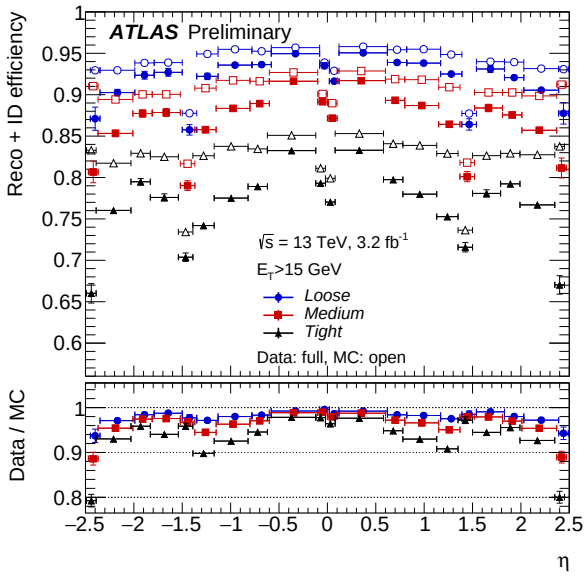

Figure 5.23 – *Illustration of the η-dependence of the data (full dots) and MC (open dots) efficiencies inclusive in E_T for the working points* `Loose` *(blue),* `Medium` *(red) and* `Tight` *(black). The ratio plots show the scale factors. Inner error bars show the statistical uncertainty, outer error bars show the total uncertainty. Note that the data efficiencies in this plot are obtained by applying the scale factors to the MC efficiencies. From [101].*

tron background coming from low-energetic hadrons, electron from decaying b-hadrons and misidentified photons is larger at lower E_{T} and stricter cuts need to be used by the menus. This results in lower identification efficiencies.

5.6 Studies on improvements of the method: Application of a Template Fit in the Z_{iso} method

Variations of the background model drive the resulting scale factor approximately 2-3% up or down (see Figure 5.14). This is the largest contribution to the systematic uncertainty.

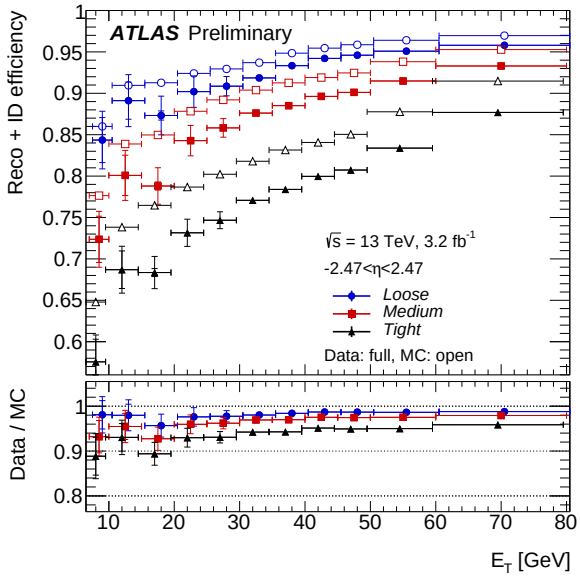

Figure 5.24 – *Illustration of the E_T-dependence of the data (full dots) and MC (open dots) efficiencies inclusive in η for the working points* `Loose` *(blue),* `Medium` *(red) and* `Tight` *(black). The ratio plots show the scale factors. Inner error bars show the statistical uncertainty, outer error bars show the total uncertainty. Note that the data efficiencies in this plot are obtained by applying the scale factors to the MC efficiencies. From [101].*

It is therefore desirable to reduce this systematic component, to assess the goodness of the background models and to potentially improve or replace them.

A probe isolation cut is applied on the Z_{iso} method. However, the electron isolation is correlated to some variables used in the construction of the identification menu. This can introduce a bias in the electron identification efficiency measurement, it is therefore preferable to avoid this isolation cut.

The scaling of the background template was up to now done using a cut-and-count procedure. To scale the background model, shape information of the templates can be considered by implementing a template fit of the signal and background models to data.

5.6.1 The model

In the Z_{iso} method, three templates are used to describe the data probe isolation distribution: The signal isolation distribution, h_{signal}, modelled by the $Z \to ee$ MC, the data-driven background template, h_{bkgmod}, as described in Section 5.3, and the real electron contamination h_{cont} (see Section 5.3.2), also modelled by a $Z \to ee$ MC, which has to be subtracted from the background template.

The peak of the isolation distribution, representing low energies in the isolation cone around the electron, can constrain the scaling of the signal template, the distribution tail constrains the background template. However, there is no means to constrain the real electron contamination, this components differs according to the detector region. This component is fixed at the moment and not included in the fit: As the sample of real electron contamination of background consists of real electrons, they have the same isolation properties than the signal and one would risk to compensate for mis-modelling of the signal. In principle, the scaling factor of the real electron contamination should have the same value as the scaling factor of the signal distribution as both are taken from the same MC, although, a

difference could issue due to the charge-misidentification mis-modelling. One could think about including a small correction factor to the nominal scaling of the MC to data in the fit of the real electron contamination which one could constrain to the interval [0.7,1.3]. This was already motivated and explained in detail in Section 5.3.
Therefore, the data distribution is modelled as following:

$$h_{\text{data}} = a \cdot h_{\text{signal}} - b \cdot (h_{\text{bkgmod}} - a \cdot c \cdot h_{\text{cont}}), \tag{5.12}$$

where a is the MC scaling factor to scale h_{signal} to data which is free in the fit, b is the factor to scale the background template, which is also left floating in the fit and c is a correction factor, correcting for deviations from the $Z \rightarrow ee$ MC scaling (factor a). All factors a, b and c are positive. For first studies of this new Z_{iso} method, the factor $a \times c$ to scale the real electron contamination is fixed to the nominal $Z \rightarrow ee$ MC-to-data scaling applied in the cut-and-count method. The real electron contamination is therefore excluded from the fit. In most cases the real electron contamination does not exceed a few percent of the background template, the effect therefore is expected to be minor: a variation of the real electron contamination of 30% impacts the overall scale factor result by up to 0.5% as shown in Figure 5.16.
The fit model reduces to:

$$h_{\text{data}} = a \cdot h_{\text{signal}} - b \cdot h_{\text{bkgmod\_corr}}, \tag{5.13}$$

whereas $h_{\text{bkgmod\_corr}}$ is the background model corrected for the real electron contamination. For first studies, a binned fit to data is performed. In order to reduce the dependence of the scale factor result on possible $Z \rightarrow ee$ signal mis-modelling, only the number of background events is extracted from the fit. The number of probe electrons entering the efficiency calculation, N_{signal}, is therefore the difference between the amount of data and the amount of background:

$$N_{\text{signal}} = \int h_{\text{data}} - b \cdot \int h_{\text{bkgmod\_corr}}. \tag{5.14}$$

Note that for first studies, systematic variations are not considered yet. Potential sources of systematic uncertainty have to be identified and some might be different from the systematics applied to the cut-and-count method listed in Section 5.4.2 due to the change of the measurement procedure.

5.6.2 Validation of the method

In order to check the viability of the template fit method and the compatibility of its results with the cut-and-count method, the method is validated at first. The cut-and-count method, introduced in Sections 5.1-5.5, corresponds to a two-bin fit, a bin where the background is scaled and a bin used for the measurement. Therefore, results obtained with a two-bin fit should correspond to results from the cut-and-count method. Figure 5.25 shows comparisons between the cut-and-count Z_{iso} method and the two-bin fit in four different E_{T} bins as a function of η for the `Tight` working point. Note that all systematic parameters are fixed to a specific set of variables and no systematic variations are performed. No uncertainties are displayed on the plots, the scale factor calculation is performed on the same sample of events. Furthermore, besides the different approach to scale the background template, the template fit and the cut-and-count method are in principle the same, the systematic uncertainties are therefore also expected to be strongly correlated.

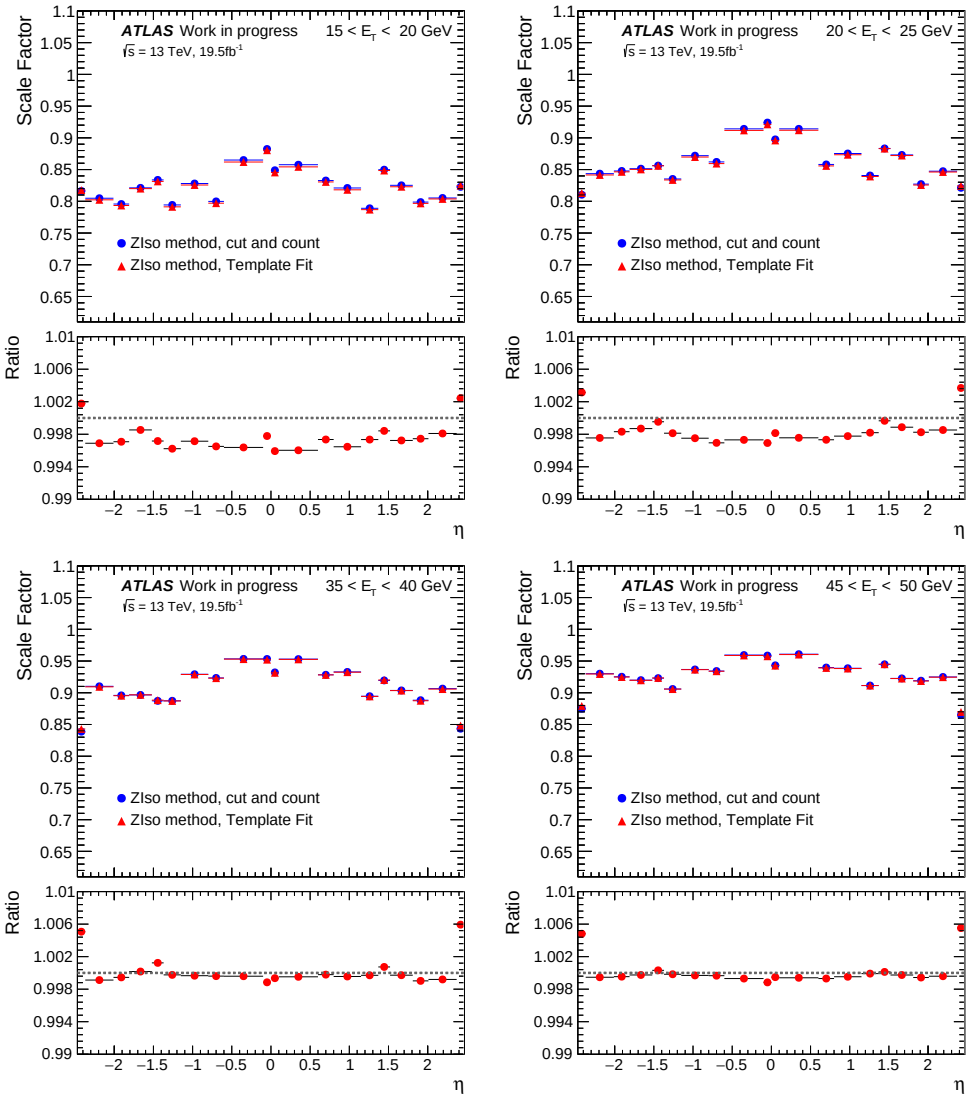

Figure 5.25 – *Comparison of the scale factor results for the* `Tight` *working point obtained with the cut-and-count Z_{iso} method and the Z_{iso} template fit method for a fit of the model to data in two bins.*

The two methods agree well, especially at high E_{T}. However, there are some discrepancies at sub-percent level which are largest in the lowest E_{T} bin: for $15 < E_{\text{T}} < 20$ GeV, where the discrepancies are largest, the two methods agree within 0.4%. There are two main differences between the methods:

- The way the signal and background models are scaled to data: the template fit method is based on a fit and returns a results which minimizes the χ^2 in the signal *and* background dominated regions. It takes into account event yields and shapes. The scaling of the background distribution in the cut-and-count method is only based on event counting in the background dominated tail region of the probe isolation distribution. The signal-dominated peak region, which includes the largest fraction of the selected events, is not taken into account in the estimation of the background template scale.

- The probe isolation cut which is applied only for the cut-and-count method. The template fit Z_{iso} method takes into account all values of the probe isolation.

A two-bin template fit should largely eliminate differences issuing from point one, however, some small discrepancies could still remain from the fact that the template fit also considers background and $Z \to ee$ MC events in the peak of the probe isolation distribution to obtain the background template scaling.

Figure 5.26 compares the cut-and-count Z_{iso} method results with the template fit Z_{iso} method results. A cut on the probe isolation has been applied in the template fit method at a value of $E_{\text{T}}^{\text{cone,r}}/25$ GeV <0.5 corresponding to the isolation cut applied to the cut-and-count method. The cut on the probe isolation is applied to the template fit method by only counting electrons with $E_{\text{T}}^{\text{cone,r}}/25$ GeV <0.5 after the fit has been performed. The differences are largely eliminated now and negligible differences of less than 0.1-0.2% remain. Note that the cut on the probe isolation introduces a bias in the scale factors due to the correlation between the isolation and some variables in the electron ID menu, R_{had} for instance. Therefore, the electron ID efficiency slightly depends on the electron isolation and therefore, the electron ID efficiency might be different for $E_{\text{T}}^{\text{cone,r}} <0.5$ and $E_{\text{T}}^{\text{cone,r}} >0.5$. Due to this isolation cut, only scale factors can be directly compared, the efficiencies are expected to be different by construction: the efficiency for isolated electrons is different than for non-isolated electrons. This effect should cancel in the ratio, which is the scale factor, if the isolation variable is well modelled for reconstructed and identified electrons. In the calculation of the MC efficiency, the only difference between the two methods is the application of the probe isolation cut.

For the remaining discrepancies, differences in the background template scaling method and region could be responsible. In fact, the rather large discrepancies of about 0.5% between the methods at high $|\eta|$ issue from a shift between data and $Z \to ee$ MC probe isolation distribution: the template fit averages the background scale factor over the whole region while the cut and count method only takes into account a part of the distribution for the scaling which could result into a larger dependence on bin migrations.
At low E_{T}, the discrepancies are largest, the background yield is larger or comparable with the expected signal yield at low E_{T}, at high E_{T}, signal events dominate the event yield. Consequently, small differences in background yield between the methods have a higher impact on the data efficiency results at low E_{T}.

Concluding the validation studies, the template fit method and the cut-and-count method yield consistent results if a template fit is applied on two bins which correspond to the signal and background dominated regions of the cut-and-count method. The application of a probe isolation cut in the cut-and-count method which is not present in the template fit method is mainly responsible for the differences between the cut-and-count method and the two-bin template fit. Remaining differences are negligible and are intrinsic to the method: they are caused by the different background template scaling regions. All differences are therefore well understood and the compatibility of the methods is proven.

5.6.3 Studies on the modelling of the probe isolation

Too fine binning of the histograms in a binned fit could highlight possible $Z \to ee$ MC signal mis-modelling which would result into a too large systematic due to MC mis-modelling. On the other hand, if the binning is too coarse, information on the template shape is lost and therefore their discriminating power. Figure 5.27 shows examples of the Template fit with histogram binnings of 4, 5, 7 and 9 in the range $E_{\text{T}}^{cone,r} \in [-0.25, 5.0]$. The bin widths are variable and smaller at low isolation values preferably populated by real electrons whereas the tails where less statistics is expected are divided in less bins with larger width.

The optimal binning is chosen with the intention to mask possible shape mis-descriptions

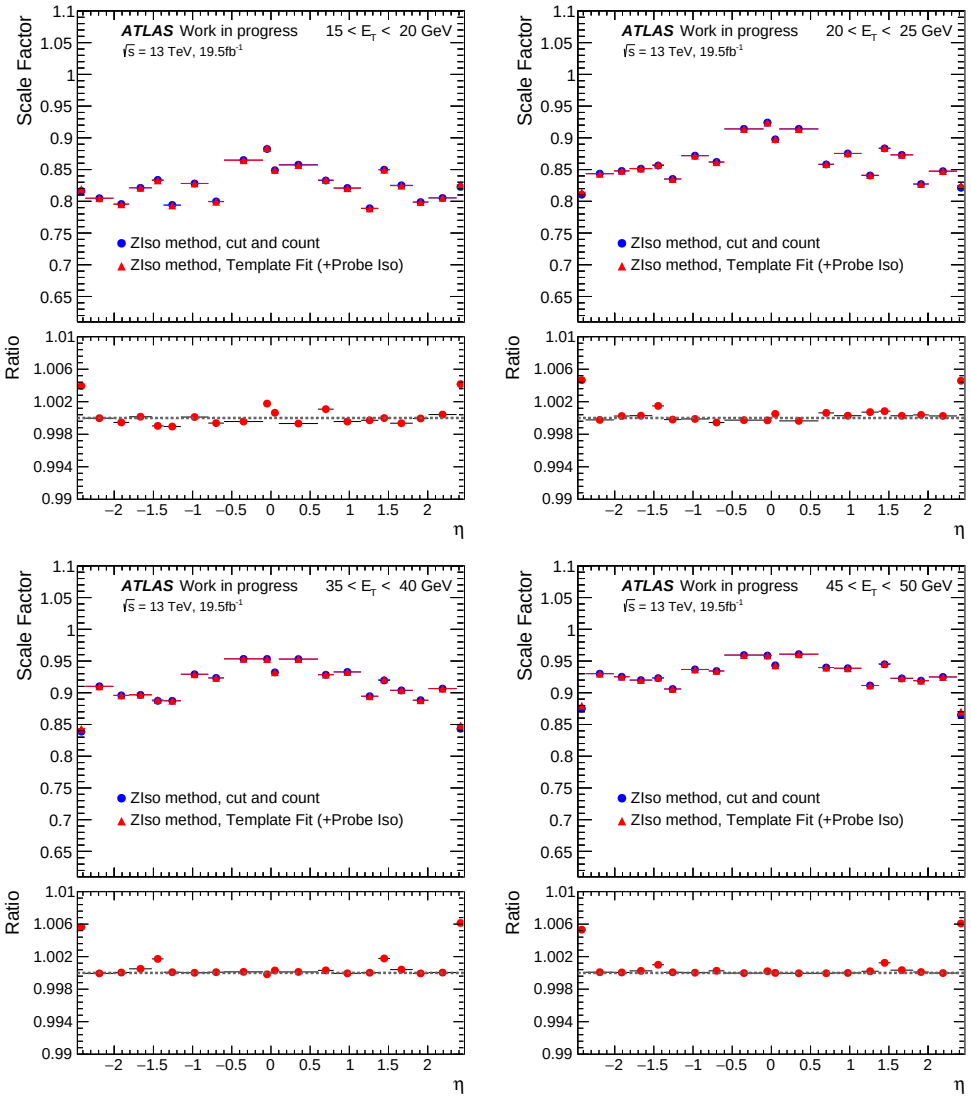

Figure 5.26 – *Comparison of the* `Tight` *scale factor results for four* E_{T} *bins as a function of* η *for the cut-and-count* Z_{iso} *method and the template fit* Z_{iso} *method with a probe isolation cut at* $E_T^{cone,r} < 0.5$ *applied.*

of the $Z \to ee$ signal MC. In the following, the shape of the $Z \to ee$ MC is compared to data by choosing a configuration with low expected background: a `Tight` identification criteria is chosen for the probe electron, the invariant mass of the tag and probe pair, m_{ee}, is required to be in a tight window around the Z mass ($80 < m_{ee} < 100\,\text{GeV}$) and the tag is required to be isolated in addition to passing the `Tight` identification criteria. The distributions of Data and MC probe isolation values are scaled to the same integral. Three examples for the probe isolation distribution obtained with this configuration are shown in Figure 5.28 for the 9-bin option.

An estimator is defined to quantify the agreement between the shape of the probe isolation distribution in the $Z \to ee$ signal MC and in data:

$$\frac{\chi^2}{\text{ndf}} = \frac{1}{\text{ndf}} \cdot \sum_i \left(\frac{d_i - m_i}{\Delta d_i^{stat.}}\right)^2, \tag{5.15}$$

where ndf is the number of bins, d_i and m_i are the bin contents in the probe isolation bin i of the data and MC distribution respectively and $\Delta d_i^{stat.}$ is the statistical uncertainty on

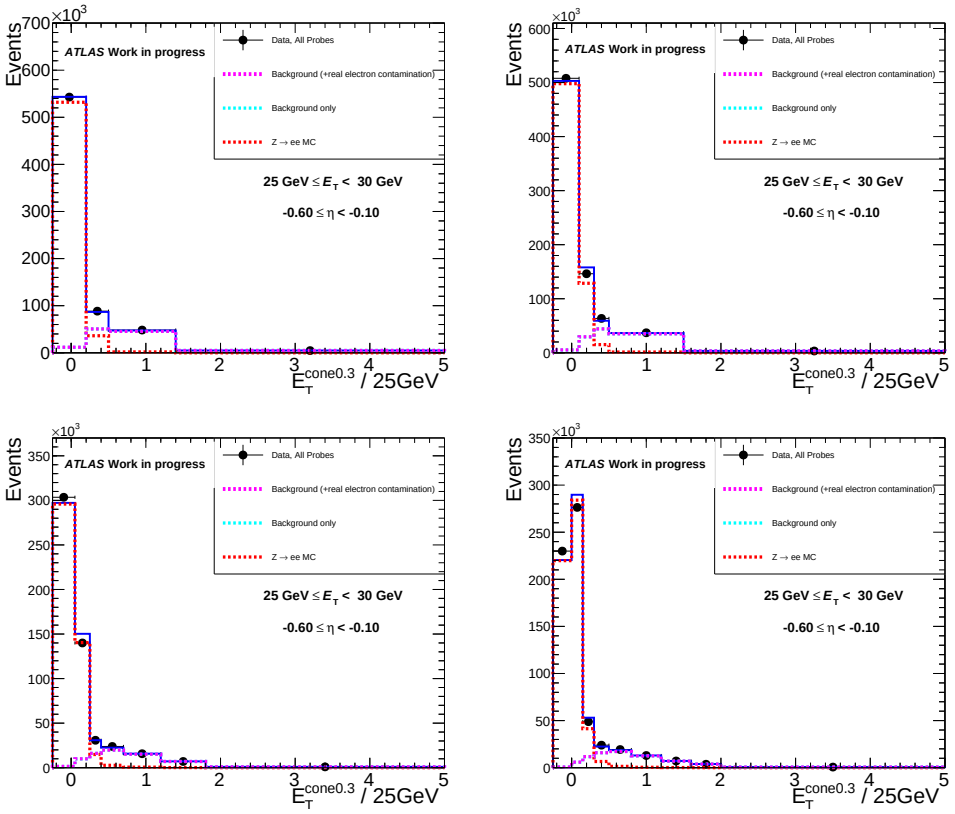

Figure 5.27 – *Example of a template fit for the* (E_{T}, η) *bin* $25 < E_{\mathrm{T}} < 30\ GeV$ *and* $-0.60 < \eta < -0.10$ *to 4 bins (top, left), 5 bins (top, right), 7 bins (bottom, left) and 9 bins (bottom, right) in the interval* $E_{\mathrm{T}}^{cone,r} \in [-0.25, 5.0]$.

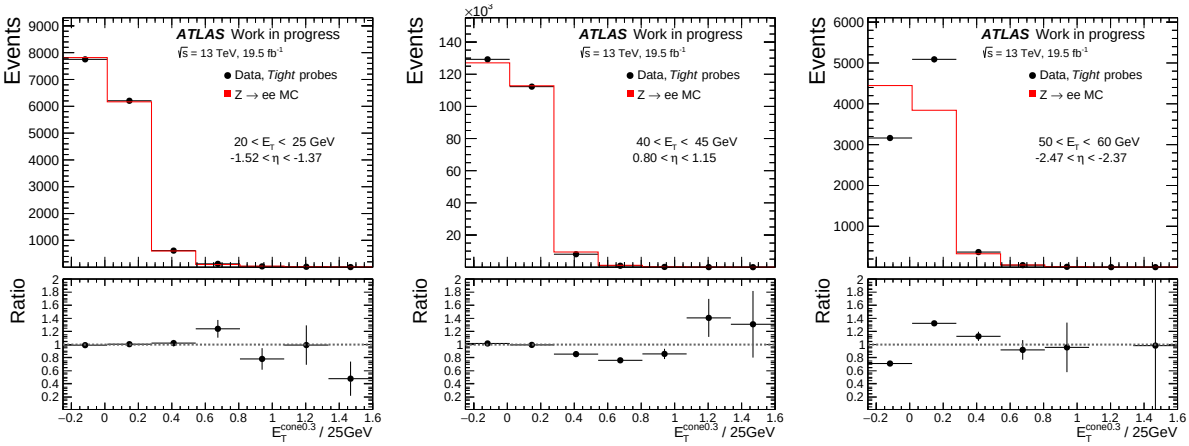

Figure 5.28 – *Examples for the probe isolation distribution obtained for* `Tight` *probes and* `Tight` *and isolated tag electrons. The invariant mass of tag and probe electrons* m_{ee} *is required to be within* $80 < m_{ee} < 100\ GeV$. *The probe isolation distribution is divided into nine bins. Here only the range* $-0.25 < E_T^{cone0.3}/25\ GeV < 1.6$ *is shown.*

the bin i in data. Some examples of the $\frac{\chi^2}{\text{ndf}}$ values are shown in Figure 5.29 for 3 bins in E_{T} as a function of η. Note that the $\frac{\chi^2}{\text{ndf}}$ values are high as only the statistical uncertainties on the data are considered in the calculation of the $\frac{\chi^2}{\text{ndf}}$ estimator.

In general and for all binning options, an increase of the $\frac{\chi^2}{\text{ndf}}$ value at high $|\eta|$ and in the central region at $0.1 < |\eta| < 0.6$ is observed in all E_{T} bins. It seems that the description of

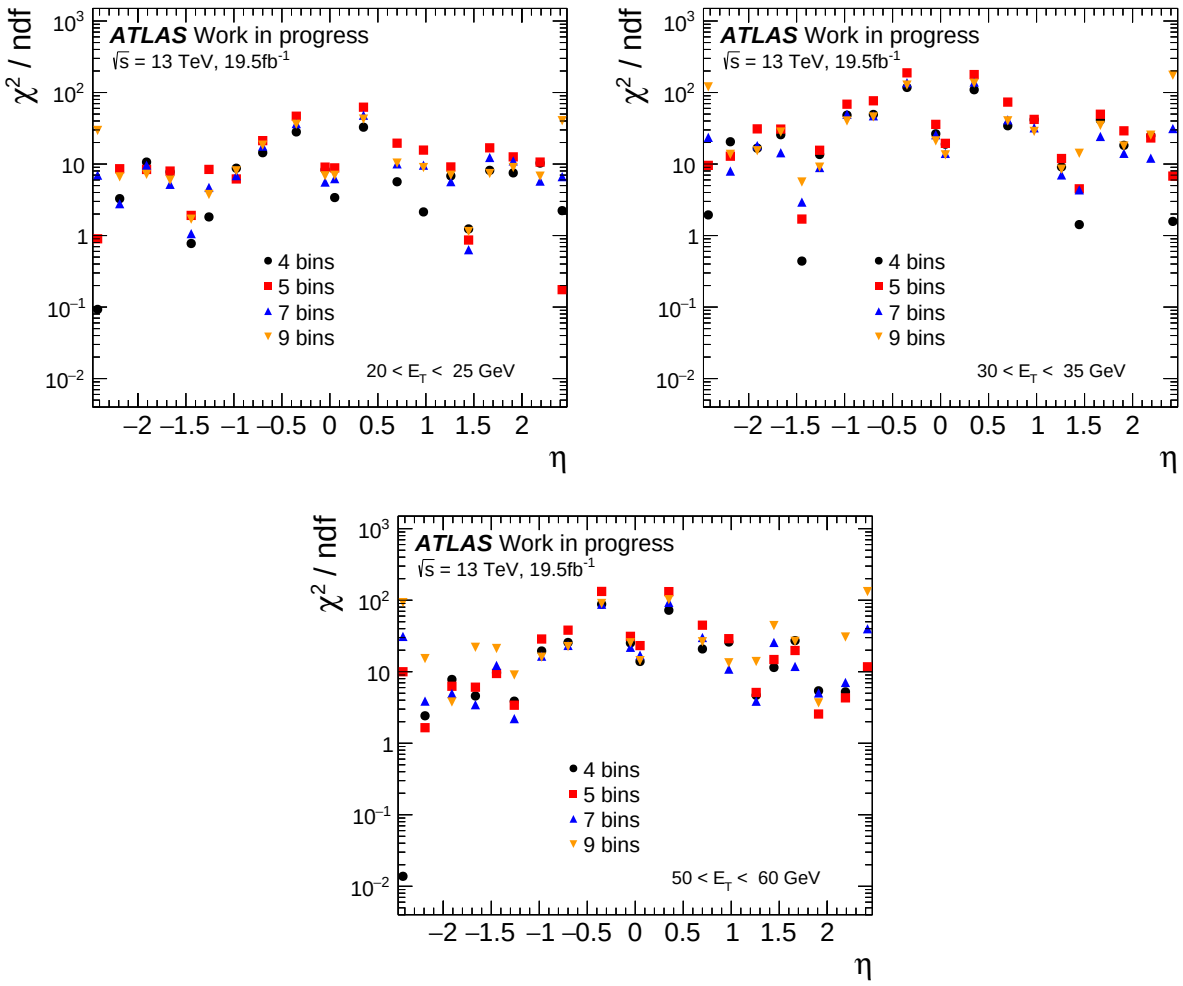

Figure 5.29 – *Examples of the* $\frac{\chi^2}{\text{ndf}}$ *values of a comparison between the* $Z \to ee$ *signal MC and data isolation distribution scaled to the same integral of* `Tight` *electrons for 3 bins in* E_{T} *as a function of* η.

the electron isolation is poor in those regions. Furthermore, the MC modelling gets worse at high E_{T}.

The highest $\frac{\chi^2}{\text{ndf}}$ value and therefore lowest agreement between data and MC is observed for the five-bin option. The nine-bin option seems to highlight especially the mis-description in the forward detector which, on the other hand, seems to be better captured by the five-bin option. The best MC description of the data are provided by the four-bin and seven-bin options. However, the MC-data agreement gets worse for high E_{T} in case of four bins. To summarize, a division of the isolation distribution in four or seven bins provides the best MC-data agreement and mask best shape mis-descriptions of the MC model. However, some central bins in $|\eta|$ and the forward $|\eta|$ region are generally badly described by MC. At high values of $|\eta|$, there is a shift between data and MC isolation distribution that increases the $\frac{\chi^2}{\text{ndf}}$. This shift can be clearly seen on the right plot of Figure 5.28.

A morphing technique could be applied to consider the MC mis-modelling: a new $Z \to ee$ signal distribution can be created out of a linear interpolation between two distributions. That way, shifts in the electron isolation distribution and possible shape distortions can be corrected. An additional uncertainty can be derived to account for the mis-modelling of the signal component in the fit.

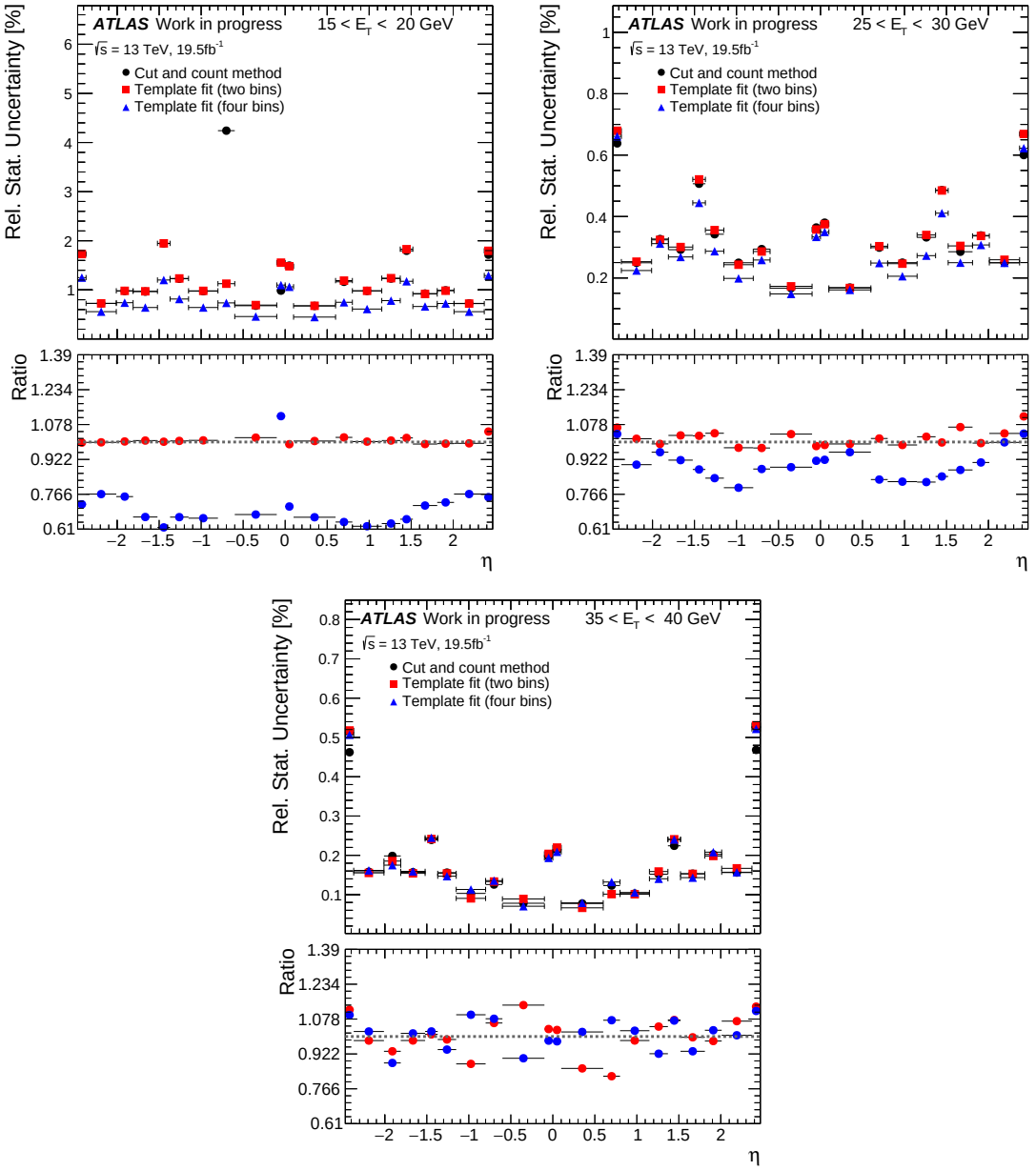

Figure 5.30 – *Relative statistical uncertainties on the data electron identification efficiency results for three bins in E_{T} as a function of η for the Z_{iso} template fit to two bins (red squares) and to four bins (blue triangles). For comparison, the statistical uncertainty on the cut-and-count Z_{iso} method results (black dots) are shown. The ratio plot shows the ratio of the template fit and cut-and-count Z_{iso} method statistical uncertainties.*

5.6.4 Statistical uncertainty

Statistical uncertainties in the Z_{iso} template fit results are obtained with toy experiments. Statistical uncertainties on data as well as on the MC $Z \to ee$ signal template and the background template are taken into account.

Figure 5.30 shows the statistical uncertainty on the data electron identification efficiency obtained with the template fit to two and four bins and on the cut-and-count Z_{iso} method in three bins in E_{T} as a function of η. The ratio plot compares the statistical uncertainties on the template fit results with those on the cut-and-count method.

The uncertainty on the template fit results obtained with two bins is in agreement with the statistical uncertainty on the results of the cut-and-count method. This corresponds to a closure test of the statistical uncertainty calculation with the template fit. A higher statistical precision is obtained with the template fit method on four bins at low E_{T}: the precision is up to 40% better for $15 < E_{\text{T}} < 20$ GeV. In case of the cut and count method and in principle also in case of the template fit to two bins, only information on the event yields are available. In the template fit to four bins, shape information also helps to scale the signal and background components. This additional information makes the $Z \rightarrow ee$ signal event determination more robust against statistical fluctuations. At high E_{T}, the statistical uncertainties on the template fit results are similar to those obtained with the cut-and-count method. This can be explained by the lower background yield at high E_{T}.

5.6.5 Results and Discussion

Section 5.6.2 showed that the template fit method is consistent with the conventional cut-and-count method and its validity was proven. Figures 5.31 and 5.32 illustrate scale factor results obtained by fitting templates to data in four and seven bins, respectively, and the template fit results are compared to the results of the cut-and-count method. The comparison indicates that the methods yield consistent results. At high E_{T}, very good agreement is observed, at lower E_{T}, a discrepancy of up to about 6% is observed. At low E_{T}, the template fit scale factor results are higher than those of the cut and count method. This discrepancy decreases very quickly with increasing electron E_{T} and becomes smaller than 1% for $E_{\text{T}} > 25$ GeV. In the following, the reason for this discrepancy is investigated.

As already explained in Section 5.6.2, the main difference issues from the absence of the probe isolation cut in the template fit method. Figure 5.33 illustrates the impact of the probe isolation cut on the template fit to four bins.

From Figure 5.33 can be extracted that the cut on the probe isolation decreases the scale factor at low E_{T}. Most of the difference between the results of the cut-and-count method and the template fit method can therefore be attributed to the cut on the probe isolation in the cut and count method (up to about 4%).

The remaining discrepancy of $< 2\%$ is caused by the intrinsic differences between the methods, namely the background template evaluation method which has been already discussed within the scope of the method validation in Section 5.6.2. The $Z \rightarrow ee$ signal yield is calculated as the difference between data and background yield. For identified electrons, the background yield is low, it amounts to about 0% to about 0.01% with respect to the total yield. No significant effects are expected to issue from differences in the background in identified electrons. At low E_{T}, the template fit method estimates a larger background yield in all probes than the cut-and-count method. Given the same MC efficiency after the application of a cut on the probe isolation, the scale factor results are higher in case of the template fit than for the cut-and-count method. The difference is less than 2% at $15 < E_{\text{T}} < 20$ GeV which quickly decreases to sub-percent level for $E_{\text{T}} > 20$ GeV.

At high E_{T}, the cut-and-count method generally estimates a higher background yield for all probes then the template fit method and the cut and count method therefore estimates higher scale factors. Differences are at sub-percent level, below 0.3% and therefore negligible due to the low background at high E_{T}.

A short qualitative check is now performed to see the behaviour of the dominant systematic uncertainty which arises from the background modelling and scaling. Figure 5.34

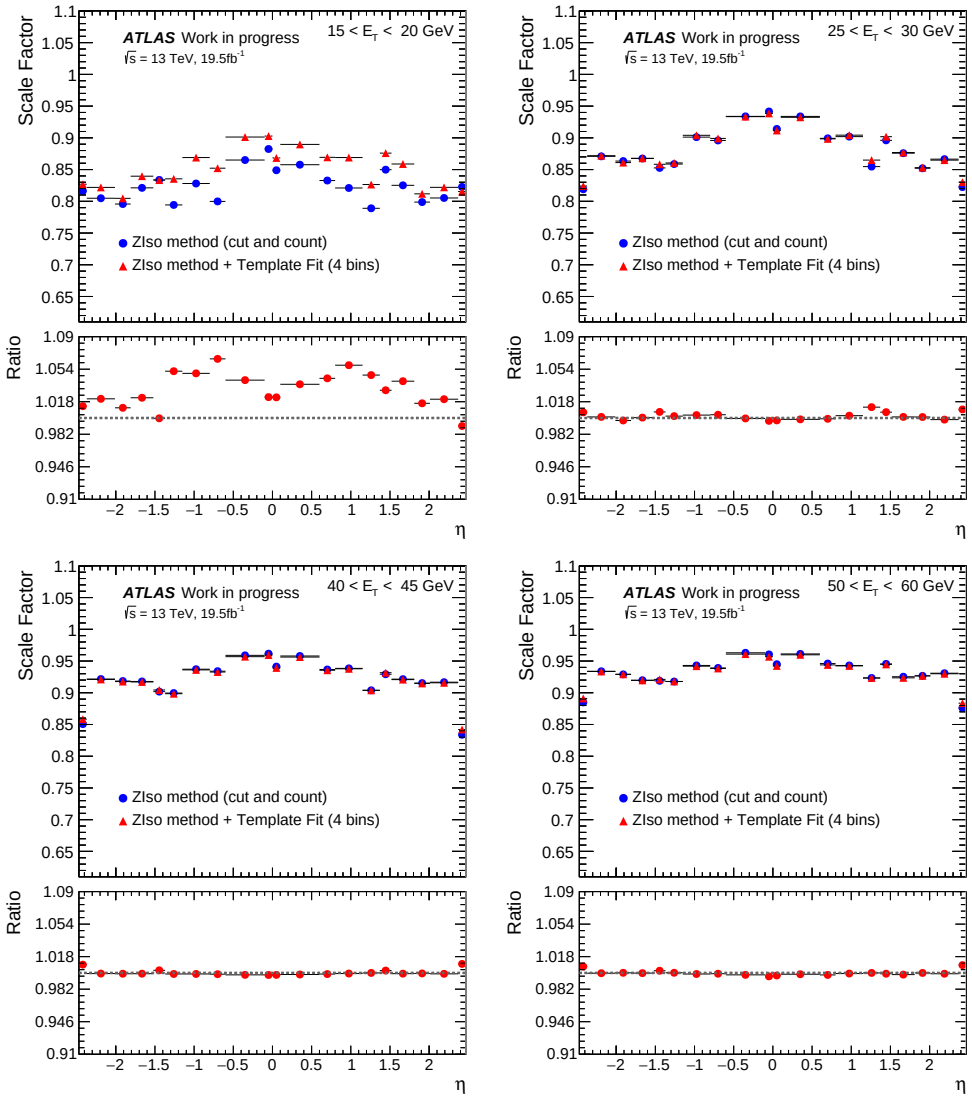

Figure 5.31 – *Scale factor results obtained with a template fit to the isolation distribution divided into four bins are indicated by the red triangles as a function of η for four bins in E_{T}. The results are compared to scale factor results obtained with the cut-and-count method (blue dots).*

shows the impact of a variation of the background model as defined in Section 5.3.2. On the left, the impact on the scale factor in case of the template fit to four bins is shown, and on the right, the impact in case of the cut-and-count method is shown for the two lowest E_{T} bins where the impact was observed to be largest for the cut-and-count method.

The impact of the variation of the background template on the scale factor result is lower for the template fit method. While the background estimation in the cut and count method relies only on the events in the background dominated tail of the probe electron isolation distribution, the template fit also takes into account the peak where the signal is accumulated. The discrepancy between the data and the MC signal model at low isolation is given more importance in the fit than the tail with lower statistics. This could lead to a more similar background yield comparing the three background models. The systematic uncertainty due to the background modelling could therefore be decreased with a template fit.

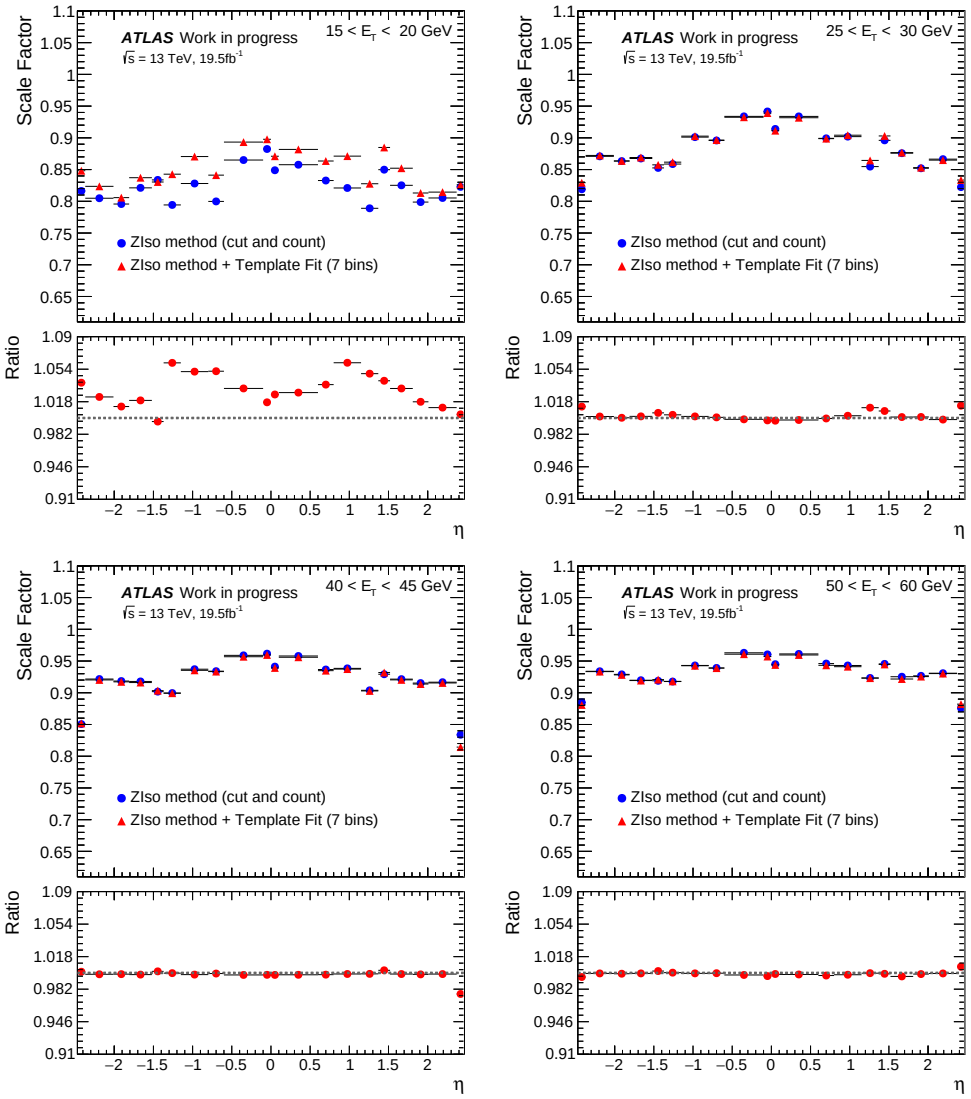

Figure 5.32 – *Scale factor results obtained with a template fit to the isolation distribution divided into seven bins are indicated by the red triangles as a function of η for four bins in E_{T}. The results are compared to scale factor results obtained with the cut-and-count method (blue dots).*

5.7 Outlook

In this chapter, the methodology to obtain electron identification scale factors with the Z_{iso} method was introduced. Within the scope of this thesis, scale factors were derived for the full 2015 data set and a large part of 2016 data using the cut-and-count method. These scale factors were applied in all ATLAS analyses using electrons in 2015 and 2016 data. Possible improvements of the method were also introduced: the replacement of the cut-and-count background template scaling procedure with a template fit.

In the template fit, the bias introduced by the application of the cut on the probe isolation, arising due to the correlation of the isolation variable and some variables included in the identification menu, would be eliminated. A template fit would furthermore provide a useful tool to rate the validity of possible background models by means of the goodness of fit. Studies on an improvement of the background modelling could therefore be more easily performed to reduce the systematics due to the background modelling. It has already been shown that only due to the different background scaling approach, the template fit

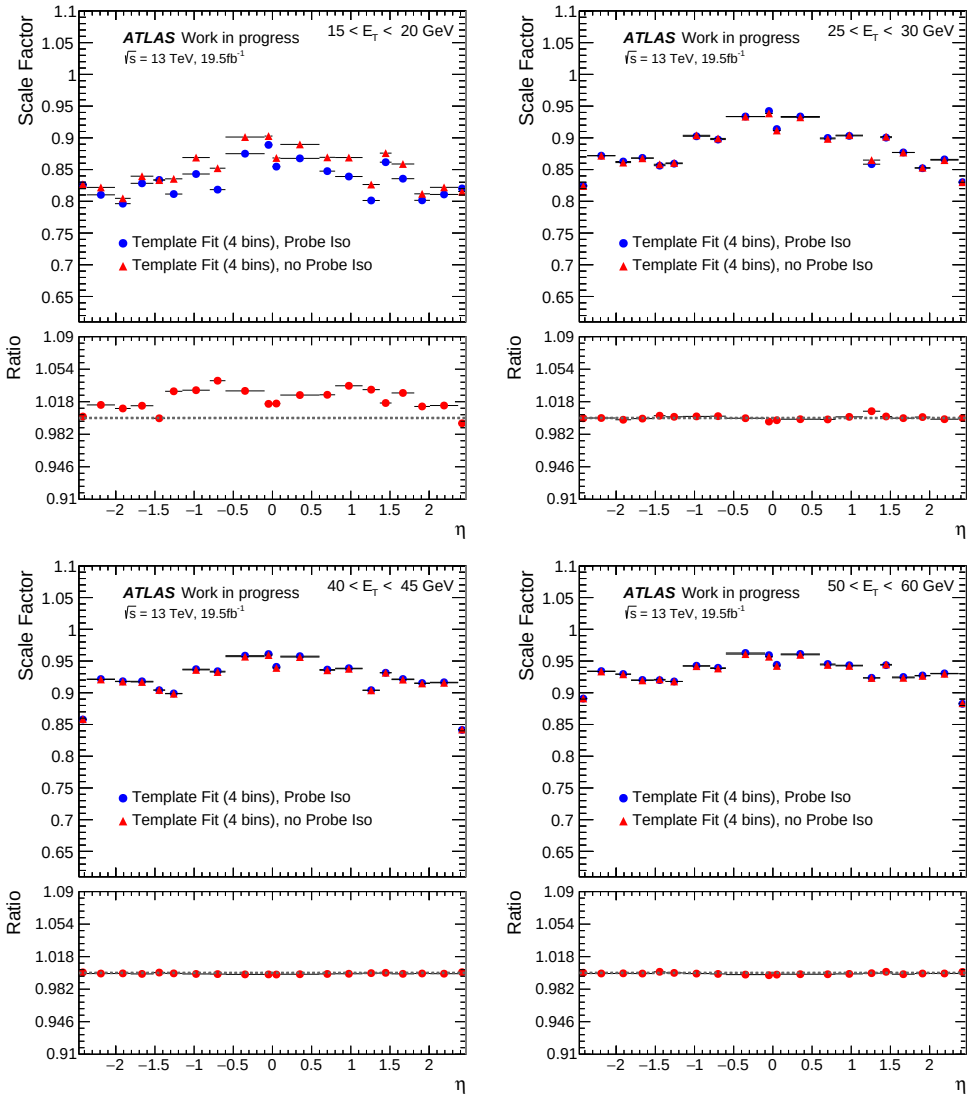

Figure 5.33 – *Comparison of template fit scale factor results of a fit to four bins with (blue dots) and without (red triangles) a cut on the probe isolation.*

could reduce the discrepancy between the background yield from the different background models and therefore also reduce the background modelling uncertainty which is the biggest uncertainty in the cut-and-count method. Including the shape information of the signal and background templates furthermore makes the result more robust against statistical fluctuations, it has been shown that a reduction of up to 40% on the statistical uncertainty can be achieved with the template fit.

In the Z_{mass} method, no cut on the probe isolation is applied. From a methodological point of view, the Z_{mass} and Z_{iso} method would approach if the probe isolation cut on the Z_{iso} method could be dropped. This could help to resolve some discrepancy between the methods, especially at low E_{T}.

In these first studies on the template fit, the validity of its application in the Tag and Probe electron identification efficiency measurement framework was proven. The method was shown to be stable, the results are consistent with the results of the cut-and-count method.

Within the scope of the method validation, a discrepancy of less than 0.4% has been observed, whereas a large part can be explained by the absence of a probe isolation cut

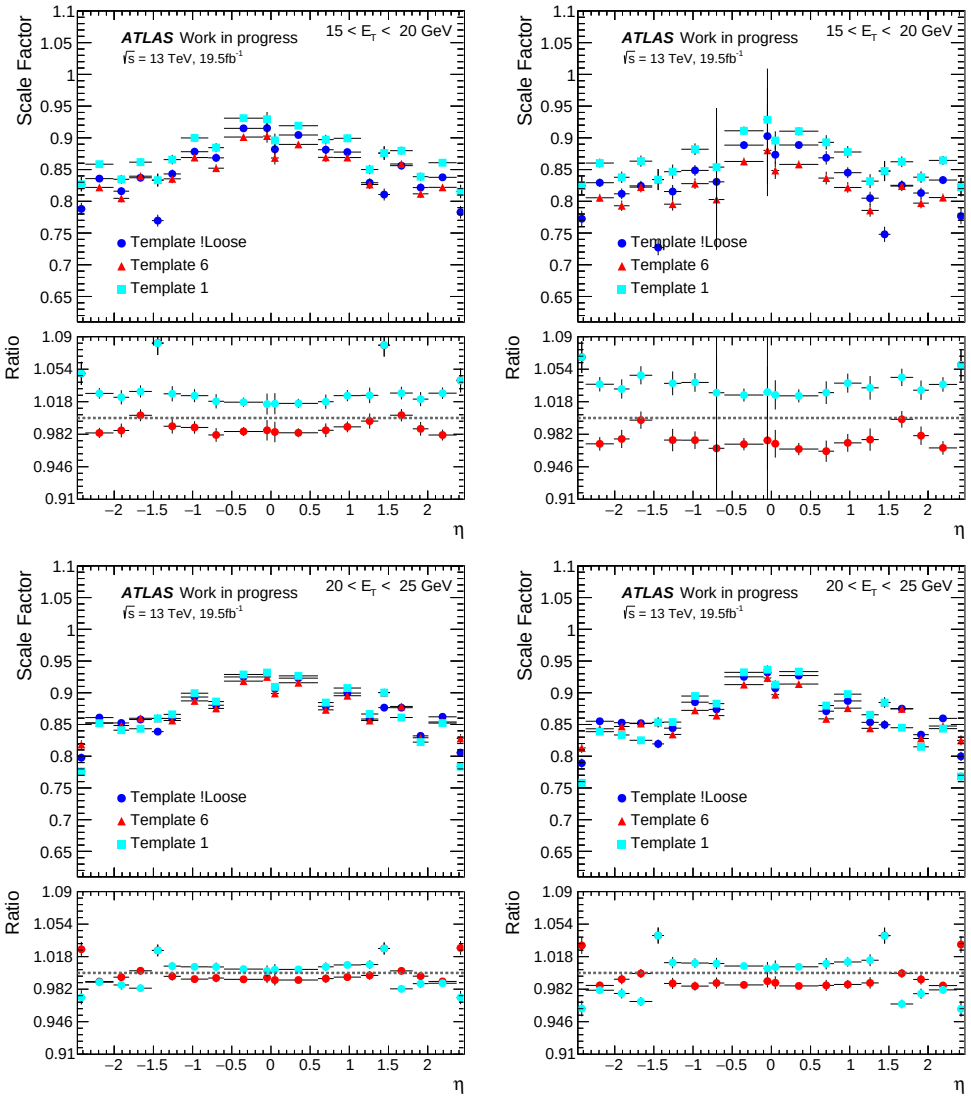

Figure 5.34 – *Impact of a variation of the background model in case of a template fit to four bins (left) and in case of the cut-and-count method (right) for the lowest E_{T} bin, $15 < E_{\mathrm{T}} < 20$ GeV (top), and for $20 < E_{\mathrm{T}} < 25$ GeV (bottom).*

in the template fit method, the remaining discrepancy by the different background yields issuing from the different background scaling methods and amounts to $< 0.2\%$. For a fit on more than two bins, at high E_{T}, the methods are in agreement and show a difference below 0.5%, at low E_{T}, differences by up to 6% can be observed. Again, these differences issue from the absence of the probe isolation cut and the different methods of the scaling of the background template which give slightly different background estimates. The differences are therefore well understood.

Statistical uncertainties are obtained directly from the fit, systematic uncertainties need to be redefined as different sources of uncertainty need to be considered. The uncertainty due to the background template, the definition of the isolation variable and due to the tag and probe invariant mass cut can still be applied, the scaling uncertainties and the probe isolation cut uncertainties can be dropped. Instead, an uncertainty on the probe isolation mis-modelling could be defined. Especially for electrons in the forward detector, the probe

isolation distributions are slightly shifted in MC with respect to data. Linear morphing of the expected probe isolation distributions can be applied to account for possible mismodelling effects. Consequently, the fit of the real electron contamination could be more stable and could be also added to the model. A restriction of the parameter range of the real electron contamination scale is recommended. Without some method to account for the MC mismodelling, including the real electron contamination of the background as a component of the fit will not be possible as otherwise, the real electron component would compensate for the MC signal mismodelling.

However, the whole procedure to evaluate the systematic uncertainty has to be changed, regardless of the method. The procedure of calculating the mean and RMS of the scale factor distribution consisting of all combination of variations was introduced in 2011 for the first electron efficiency measurements [113] and not changed ever since. Several issues were raised as discussed in Section 5.4.2 and it has been agreed to decide on one baseline variation and to evaluate the systematic uncertainties by taking the difference between the baseline result and the scale factor result for the variation. Furthermore, it has been decided to rely on systematic sources, for example on measurement on the electron p_{T}, the pile-up reweighting or the energy leakage from the isolation cone rather than variations of measurement parameters. This change in systematic uncertainty calculation is a compulsory next step in the calculation of the identification efficiency, regardless of whether the cut-and-count method or a template fit is applied.

Chapter 6

WZ analysis methodology

In this chapter, the main strategy to extract the WZ signal is presented. This main strategy consists of the selection of candidate WZ events and the estimation of non-WZ events passing this selection. These parts are the most crucial in the analysis: a careful selection of leptons and the definition of the event selection ensures low contamination of non-WZ events, denoted as background. Latter can never be avoided completely and has to be thoroughly and reliably estimated. Lepton and event selection are presented in Section 6.1 and 6.2, the background estimation is described in Section 6.3, the yield results in the signal region and the estimated background results are shown in Section 6.4.

The data analysed were collected by the ATLAS experiment during 2015 and 2016 LHC proton-proton collision runs at a center-of-mass energy of $\sqrt{s} = 13$ TeV, with a bunch-spacing of 25 ns.

In total, an integrated luminosity of $\mathcal{L} = 36.1$ fb^{-1} of data was included in the analysis, with an uncertainty on the integrated luminosity of 2.1% estimated using a method based on [114].

6.1 Lepton selection

As a first step in the selection of a WZ event candidate, a pool of events with leptons passing the signal requirements is identified, then, a dedicated selection exploiting the signal topology and kinematics is applied to assign the leptons to the bosons.

The lepton selection is a critical part of the analysis. Identification and isolation criteria can be used to reject background events from misidentified leptons or from processes with more than three leptons in the analysis, especially the ZZ process.

An outline of the lepton selection is presented in the following, a more detailed explanation and motivation of these choices will be given in Section 6.3.2.

The leptons selection is organized as a step-wise selection with three levels of tightness whereas the sets of leptons passing the tighter selections are a subset of the sets of leptons passing the looser selections. All signal leptons pass a loose selection, called baseline selection. Leptons assigned to the Z boson have to pass the so-called Z-lepton selection and W-lepton candidates have to pass the selection denoted as W-lepton selection. Most background is expected to enter through the W-lepton, therefore, a tighter selection is imposed on W-lepton candidates than on the Z-lepton candidates. The set of leptons passing the W-selection is a subset of the leptons passing the Z-lepton selection. W- and Z-leptons all pass the baseline selection.

A lepton selection imposing only loose requirements on the leptons is defined, it is denoted as **baseline-lepton selection** in the following. The main purpose of the baseline selection is to construct a veto requirement on events with more than three baseline lepton. This ensures less contamination from ZZ events which decay to four leptons. To maximize the rejection power of the veto, the leptons considered for the veto have to fulfill loose requirements:

- $p_{\mathrm{T}} > 5$ GeV
- Electrons and muons pass `Loose` identification requirements.
- Electrons have to be in the range where the tracker is available ($|\eta| < 2.5$[1]) and information from precision muon chambers has to be available ($|\eta| < 2.7$) in case of muons.
- The leptons have to be associated to the vertex, requirements on the transverse impact parameter ($d0$) significance and the longitudinal impact parameters ($z0$) have to be fulfilled. The transverse impact parameter is the distance of the track to the beam line in the transverse plane. Its significance $|\frac{d0}{\Delta d0}|$ has to be smaller than three for muons and smaller than five for electrons. The longitudinal impact parameter $z0$ is the difference in z between the point on the track at which $d0$ is defined and the z-coordinate of the primary vertex. For the track, the requirement $|z0{\cdot}\sin(\theta)| < 0.5$ mm has to be fulfilled for electrons and muons, where θ is the polar angle.
- Baseline muons pass an isolation selection requiring a calorimeter isolation of topoetcone20/pT < 0.2 and a track isolation of ptvarcone20/pT< 0.15, denoted `FixedCutLoose` menu.
- Baseline electrons fulfil the `LooseTrackOnly` isolation menu which includes only a cut on the track isolation aimed to have an electron selection efficiency of 99%.
- In order to avoid double-counting of electrons and muons, electrons sharing a track with a muon are removed, and in case of two overlapping electrons, the electron with sub-leading p_{T} is removed ("e-to-μ" and "e-to-e" overlap removal).

Note that calorimeter and track isolation were defined in Section 4.3. The requirements for baseline leptons above have been optimized to have a high ZZ rejection efficiency. The loose selection cuts (identification, isolation, lepton p_{T}) and the larger coverage in solid angle (inclusion of the crack region for electrons and the larger acceptance in η for muons) aim to detect more events with a fourth lepton and therefore increase the rejection power of the ZZ veto.

Based on this baseline selection, criteria on signal leptons possibly assigned to the W and the Z bosons are defined. Lepton selection optimization studies have shown that for the following requirements on the **Z-lepton** lead to a good background rejection and signal efficiency, details will be given in Section 6.3.2:

- Both Z-electrons and muons are required to pass the `Medium` identification.

[1] The $|\eta|$-cut on the electron candidate cluster is $|\eta^{\mathrm{cluster}}| < 2.47$.

- The `Gradient` isolation requirement is applied to the Z-electron. The `Gradient` isolation working point is aimed at providing a selection efficiency which follows a well-defined monotonically increasing function. The selection efficiency is defined to be 90% at a lepton p_{T} of 25 GeV and 99% at a lepton p_{T} of 60 GeV.
- Z-muons have to pass the `FixedCutLoose` isolation
- Jets misidentified as leptons or leptons reconstructed within a jet are further suppressed by removing leptons in the vicinity of hadronic jets. Electrons reconstructed within $0.2 < \Delta R < 0.4$ within a jet are removed ("e-to-jet overlap removal") and muons reconstructed within $\Delta R < 0.4$ of a jet with at least three tracks, are rejected ("μ-jet Overlap Removal").

Tighter selection criteria are imposed on top of the Z-lepton selection to define the **W-lepton selection**:

- W-electron and muon have to pass the `Tight` identification criteria and the `Gradient` isolation selection
- Electrons from photon conversion in general have a higher quality than electrons from hadron decays. In a way, they are real and isolated electrons, however, they don't issue from the collision vertex or a boson decay, therefore, they are considered as non-prompt, fake leptons in the analysis. Events from $Z + \gamma$ decay are an important source of misidentified lepton events in the analysis. To reduce fakes from photon conversion, ambiguous W-electrons also passing the photon reconstruction are removed.

Tighter transverse momentum cuts on the lepton with respect to baseline leptons are also targeted to decrease the fake lepton background. Fakes have predominantly low transverse momentum. A p_{T} cut of 15 GeV is imposed on Z-leptons which is increased to 20 GeV for W-leptons. The barrel-endcap transition region where the electron interacts with more detector material is excluded for electrons. To ensure good muon quality, information of the tracker has to be available for muons, restricting the possible detector range to $|\eta| < 2.5$.

The requirements used to define baseline, Z and W-lepton criteria are given in Table 6.1 for electrons and in Table 6.2 for muons.

6.2 WZ event selection

6.2.1 Neutrino reconstruction and definition of kinematic variables of the WZ system

In a true WZ event, the full kinematic information of the WZ event is not available due to the presence of the neutrino of the W decay. This concerns the total longitudinal momentum of the collision. Due to the constraint that the transverse momentum before the collision was zero, the total transverse momentum of the event can be inferred on. However, no such constraint is available for the longitudinal momentum of the proton constituents before the collision, the PDF only gives a probability distribution of the parton momenta in the proton. Using the invariant mass of the W, $m_W^2 = E_W^2 - \mathbf{p_W} \cdot \mathbf{p_W}$ with the W energy E_W and the momentum three-vectors $\mathbf{p}_W$, information on the longitudinal neutrino momentum can be extracted by plugging in kinematic information on the W-lepton and

Electron object selection			
Selection	Baseline selection	Z selection	W selection
$p_{\mathrm{T}} > 5$ GeV	✓	✓	✓
Electron object quality	✓	✓	✓
$\lvert\eta^{\mathrm{cluster}}\rvert < 2.47$, $\lvert\eta\rvert < 2.5$	✓	✓	✓
`Loose` identification	✓	✓	✓
$\lvert d_0^{\mathrm{BL}}/\sigma(d_0^{\mathrm{BL}})\rvert < 5$	✓	✓	✓
$\lvert\Delta z_0^{\mathrm{BL}} \sin\theta\rvert < 0.5$ mm	✓	✓	✓
`LooseTrackOnly` isolation	✓	✓	✓
e-to-μ and e-to-e overlap removal	✓	✓	✓
e-to-jets overlap removal		✓	✓
$p_{\mathrm{T}} > 15$ GeV		✓	✓
Exclude $1.37 < \lvert\eta^{\mathrm{cluster}}\rvert < 1.52$		✓	✓
`Medium` identification		✓	✓
`Gradient` isolation		✓	✓
$p_{\mathrm{T}} > 20$ GeV			✓
`Tight` identification			✓
Electron not reconstructed as photon			✓

Table 6.1 – *Three levels of electron object selection used in the analysis. Based on [82].*

Muon object selection			
Selection	Baseline selection	Z selection	W selection
$p_{\mathrm{T}} > 5$ GeV	✓	✓	✓
$\lvert\eta\rvert < 2.7$	✓	✓	✓
`Loose` quality	✓	✓	✓
$\lvert d_0^{\mathrm{BL}}/\sigma(d_0^{\mathrm{BL}})\rvert < 3$ *(for* $\lvert\eta\rvert < 2.5$ *only)*	✓	✓	✓
$\lvert\Delta z_0^{\mathrm{BL}} \sin\theta\rvert < 0.5$ mm *(for* $\lvert\eta\rvert < 2.5$ *only)*	✓	✓	✓
`FixedCutLoose` isolation	✓	✓	✓
μ-jet Overlap Removal		✓	✓
$p_{\mathrm{T}} > 15$ GeV		✓	✓
$\lvert\eta\rvert < 2.5$		✓	✓
`Medium` quality		✓	✓
$p_{\mathrm{T}} > 20$ GeV			✓
`Tight` quality			✓
`Gradient` isolation			✓

Table 6.2 – *Three levels of muon object selection used in the analysis. Based on [82].*

the missing transverse energy. But this is based on the assumption that all missing energy comes from the decay of one W-boson and therefore can be assigned to its neutrino.

Solving the quadratic equation for the longitudinal neutrino momentum, several cases are possible:

- Two values for the neutrino longitudinal momentum can solve the equation. In that case, the solution with the smaller absolute value is chosen.
- No real solution exists for the equation. This can happen due to mismeasurement of E_{T}^{miss} or the natural decay width of the W [115]. In that case, the real part of the complex solution is chosen.

Using the chosen solution for the neutrino longitudinal momentum, the W boson can be reconstructed.

The transverse mass of the W is an important kinematic variable used in the event selection. It is defined as:

$$m_{\mathrm{T}}^{W} = \sqrt{2p_{\mathrm{T}}^{\ell}E_{\mathrm{T}}^{\mathrm{miss}}\,(1-\cos\Delta\phi)}, \tag{6.1}$$

where p_{T}^{ℓ} denotes transverse momentum of the lepton assigned to the W and $\Delta\phi$ the angle between the direction of the lepton and the missing energy in the transverse plane.

The transverse mass of the WZ defined according to [16] as

$$m_{\mathrm{T}}^{WZ} = \sqrt{\Big(\sum_{\ell=1}^{3} p_{\mathrm{T}}^{\ell} + E_{\mathrm{T}}^{\mathrm{miss}}\Big)^{2} - \Big[\Big(\sum_{\ell=1}^{3} p_{x}^{\ell} + E_{x}^{\mathrm{miss}}\Big)^{2} + \Big(\sum_{\ell=1}^{3} p_{y}^{\ell} + E_{y}^{\mathrm{miss}}\Big)^{2}\Big)\Big]}. \tag{6.2}$$

6.2.2 Selection of WZ signal events

On the candidate event sample defined in Section 6.1, a selection targeting kinematic properties of WZ events is now applied and the leptons selected in Section 6.1 are assigned to W and Z boson candidates.

- Basic requirements on the **event cleaning** are imposed on the event. All detectors have to be fully operational, information from all sub-detectors has to be present. Events with at least one misidentified jet of non-collision origin are vetoed.
- Candidate events are selected with **a single-lepton trigger**: A dedicated trigger algorithm identifies electron and muon candidates. They have to fulfil a defined isolation requirement and pass a minimal energy: 20 GeV (24 GeV) for muons (electrons) in 2015. Due to the higher instantaneous luminosity in 2016, the trigger threshold was increased to 26 GeV.
- A WZ leptonic decay yields **exactly three leptons** in the final state, events with more than three baseline leptons are vetoed.
- Exactly **three leptons passing the Z-selection**, denoted Z-type leptons in the following, are required.
- One of these leptons has to be associated to the **trigger** element, which implies passing a certain transverse momentum threshold. For the leading lepton to be above the trigger efficiency turn-on curve, a minimum p_{T} of 25 GeV is required in 2015 and 27 GeV in 2016.

The intention in the following is to reconstruct a Z-boson candidate out of the three leptons in the event: **pairs of opposite-charge, same-flavour leptons** are built, if more than one pair is possible, the pair whose dilepton invariant mass $m_{\ell\ell}$ is closest to the Z-boson mass m_Z^{PDG} is assigned as the Z-boson candidate. This Z-boson candidate must have an **invariant mass within a window of 10 GeV** around the Z-mass. The third remaining lepton is required to **pass the W-lepton selection** and is associated with the W-boson candidate. **Missing transverse energy** E_{T}^{miss} is associated with the neutrino. To account for the neutrino in the selection, the **W-boson transverse mass**, m_{T}^{W}, as defined in equation (6.1), has to be larger than 30 GeV.

The most important criteria of the WZ event selection and lepton-to-boson assignment are summarized in Table 6.3.

Inclusive WZ event selection	
ZZ veto	< 4 baseline leptons
N leptons	$\equiv 3$ Z-type leptons
Leading lepton p_{T}	$p_{\mathrm{T}}^{\mathrm{lead}} > 25$ GeV (in 2015) or $p_{\mathrm{T}}^{\mathrm{lead}} > 27$ GeV (in 2016)
Z boson candidates	2 same flavor, oppositely charged Z-type leptons
Z boson invariant mass	$\lvert m_{\ell\ell} - m_Z^{PDG}\rvert < 10$ GeV
W-lepton	W-type lepton
W transverse mass	$m_{\mathrm{T}}^{W} > 30$ GeV

Table 6.3 – *Overview of the inclusive WZ event selection and lepton-to-boson assignment. Based on [82].*

6.3 Background estimation

Several processes can mimic the WZ signal and may bias measurements performed on WZ. A precise estimation is therefore vital to the measurement. These processes can be assigned to two groups: "irreducible background", which are processes with at least three real leptons in the final state, and "reducible background", processes which pass the signal selection due to an object in the final state which is mis-identified as lepton. Leptonic decays of ZZ events are the dominant contribution to irreducible background processes, decays of tri-boson events (VVV $V \in \{W, Z\}$), $t\bar{t}$ production in association with a W or a Z boson, and single top plus boson production tZ are subdominant irreducible background components. Z+jets, $t\bar{t}$ and $Z+\gamma$ events belong to the group of the reducible background. In the following, the estimation of these background components will be presented.

Monte Carlo simulations help to estimate the background. These will be presented in Section 6.3.1. A careful lepton selection can reject especially background from misidentified leptons. Studies to reduce the background have been performed and are presented in Section 6.3.2. Finally, Section 6.3.3 gives details on the estimation of the irreducible background and Section 6.3.4 on the estimation of the reducible background.

6.3.1 MC Background models

MC simulations are necessary to estimate the irreducible background yield and to study reducible background events. Background processes which fake a WZ signal event because they contain at least three real leptons in the final state, such as ZZ, VVV $V \in \{W, Z\}$,

Process	Generators	order in QCD	PDF	k-factor applied
$q\bar{q} \to ZZ \to \ell\ell\ell\ell / \ell\ell\nu\nu$	Sherpa 2.2.2	$ZZ + q$: NLO, $ZZ + 3q$: LO	NNPDF3.0nnlo	1.08
$gg \to \ell\ell\ell\ell$	Sherpa 2.1.1	LO	CT10	1.67·0.91
$Z \to \mu\mu, ee, \tau\tau$(+jets)	Sherpa 2.1	LO	NNPDF3.0nnlo	0.9751
$Z \to ee\gamma$, $\mu\mu\gamma$, $\tau\tau\gamma$	Sherpa 2.1	LO	NNPDF3.0nnlo	1.0
$t\bar{t}(\geqslant 1\ell)$	Powheg+Pythia8	NLO	NNPDF3.0nlo	1.1391
tZ (3ℓ)	MadGraph5_aMC@NLO +Pythia 6	LO	NNPDF2.3lo	1.0
$VVV \to a\ell b\nu$ $(a \in [2,6],\, b \in [0,4])$	Sherpa 2.1.1	LO	CT10	1.0
ttV	MadGraph5_aMC@NLO +Pythia 8	NLO	NNPDF3.0nlo	1.096
ttZ	MadGraph5_aMC@NLO +Pythia 8	NLO	NNPDF3.0nlo	1.12

Table 6.4 – *Summary of background MC simulations. Based on [82].*

$t\bar{t}$ production in association with a W or a Z boson and tZ, are modelled with MC. Events from $t\bar{t}$, Z+jets and $Z + \gamma$, which can enter the signal region due to one mis-identified lepton in the final state, are estimated with a data-driven technique. However, information on the origin of the mis-identified leptons is extracted from the truth information of these Monte Carlo simulations.

The main features of Monte Carlo simulation used to model background processes in the WZ analysis are listed in Table 6.4.

6.3.2 Event selection optimization studies

If the background contribution in the signal region is large, its uncertainty also will strongly impact the measured WZ signal yield. Besides having an estimation of the background which is as precise as possible, it is also advantageous to keep the background as low as possible. By carefully choosing the lepton selection criteria, the amount of background events in the signal region can be reduced.

The baseline lepton selection is optimized for an effective ZZ event veto. Baseline leptons have to fulfill loose requirements to be able to select as many events with four leptons as possible to have a high rejection power for ZZ events: the looser the lepton selection, the more powerful the veto. However, if the baseline lepton selection is too loose, misidentified leptons enter the selection and the veto could reject WZ signal events which are produced in association with another object. Especially, it is important to have a high acceptance for baseline leptons to reject also ZZ events with one lepton falling below the p_{T} threshold or outside the detector acceptance. Based on the studies done to optimize the selection, the p_{T} threshold for the leptons has been lowered to 5 GeV and the η-acceptance of the muon selection has been increased to $|\eta| < 2.7$.

The lepton selection, including cuts on identification and isolation variables, is an important tool to reject background from misidentified leptons. However, a balance has to be found between background rejection and signal efficiency: the tighter the cuts on identification and isolation variables, the lower the leptons efficiency and therefore also the signal efficiency. For instance, the decrease of the electron identification efficiency with the tightness of the identification working point has already been demonstrated in Section 5.5.

Selection optimization studies have been performed based on the significance $\frac{S}{\sqrt{S+B}}$ and the signal-to-background yield ratio $\frac{S}{B}$ where S is the signal yield and B the background yield. Figure 6.1 shows the WZ signal selection efficiency and the signal-to-background yield ratios $\frac{S}{B}$ for various options of electron (left) and muon (right) identification and isolation criteria. These studies were performed by applying different combinations of lepton identification and isolation selection criteria on MC signal and background events. For these studies, simulated events of all background processes entering the WZ signal

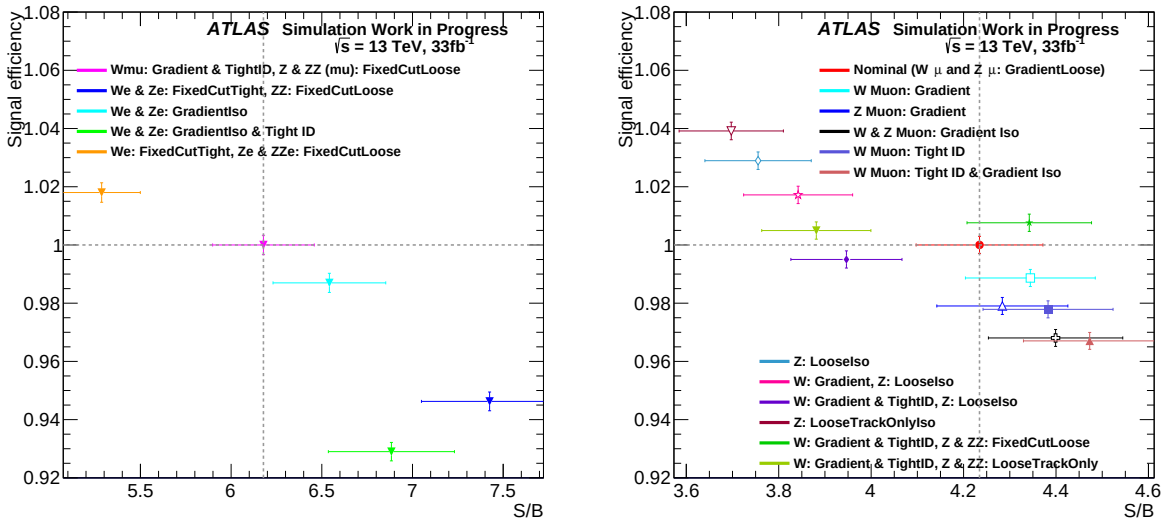

Figure 6.1 – *WZ signal selection efficiency and signal-to-background yield ration $\frac{S}{B}$ for different options for electron selection (left) and muon selection (right). These different options contain different combination of W and Z lepton identification and isolation criteria. All options are compared to the selection applied in [15, 16]. Note that the studies have been performed on MC signal and background events, uncertainties contain only statistical uncertainties on these samples. Background events contain reducible and irreducible background processes, tZ events have been excluded.*

region except for tZ events are included. The topology of tZ events is very signal-like and has therefore not been included in the background sample used for the background optimization studies. The reference selection in Figure 6.1 is the selection applied in previous analyses [15, 16].

Studies showed, that a tightening of the W-lepton selection rejects dominantly Z+jets events which constitute the most problematic fake background in the analysis: The large cross section of the Z production in association with hadrons and potential mis-measurement of the jet energy resulting into fake missing transverse energy makes Z+jets events prone to enter easily the signal region and makes Z+jets the largest source of misidentified lepton background. The W-type lepton is therefore required to pass strict identification and isolation criteria: both W-electron and muon have to pass the `Tight` identification criteria and the `Gradient` isolation selection.

Tightening the Z-lepton selection criteria dominantly effects $t\bar{t}$ background: $t\bar{t}$ background mostly enters the signal region through a heavy quark decaying into a non-isolated lepton. The isolation criteria on the Z-electron was therefore set to `Gradient` isolation. Both Z-electrons and muons are required to pass `Medium` identification. A tighter identification requirement was shown not to be beneficial and a tightening of the Z-lepton requirements is accompanied by a comparably high signal loss as two leptons are affected, as demonstrated for example by the green dot on the left plot in Figure 6.1 and the dark pink filled triangle on the right plot in Figure 6.1. An increase of `Medium` to `Tight` identification is a big increase in the tightness of the selection which would also decrease the signal loss by about 6% in case of electrons.

To increase the signal selection efficiency, the Z-muon isolation was set to `FixedCutLoose` isolation. Despite the rather loose isolation criteria, no significant increase of the back-

ZZ **control region selection:**
2 opposite-sign same-flavour Z-type leptons (ℓ)
$\lvert m_{\ell\ell} - m_Z^{PDG}\rvert < 10$ GeV
(if true for more than one pair, assign pair with $m_{\ell\ell}$ closest to m_Z^{PDG} to Z-boson)
additional W-type lepton, $p_{\mathrm{T}} > 15$ GeV
additional "baseline" lepton, $p_{\mathrm{T}} > 5$ GeV

Table 6.5 – *ZZ control region selection criteria.*

ground has been observed: the `FixedCut` isolation menus provide a constant cut over the lepton p_{T} while the efficiency-based menus are looser, the lower the p_{T} to guarantee the targeted selection efficiency despite the increased fake lepton yield at low p_{T}. The strict isolation at low p_{T} provides a good background rejecting as most fake leptons have low p_{T}, making up for the overall looser isolation selection with respect to other menus. Note that the `Gradient` isolation cut applied to the W-muon is always tighter than the `FixedCutLoose` menu in the p_{T} range in question to guarantee the validity of the stepwise lepton selection.

As a conclusion of these studies, the Z-electron identification was left at `Medium` identification but the isolation was tightened to `Gradient`, the W-electron identification was left at `Tight` and its isolation at `Gradient`. This option corresponds to the light blue option the right plot in Figure 6.1. The W-muon identification was set to `Tight` and `Gradient` isolation, the Z-muon selection was left at `Medium` identification but the isolation was loosened to `FixedCutLoose`. This corresponds to the dark green dot on the right plot of Figure 6.1.

6.3.3 Irreducible background

Irreducible background comes from processes with three or more leptons in the final state. In the following, the estimation of these backgrounds using Monte Carlo simulation is presented.

6.3.3.1 Estimation of the ZZ background

ZZ events are one of the dominant background contribution to the signal region. They enter the signal region because of either one lepton of the ZZ fully leptonic decay does not pass the signal lepton selection requirements or one of the leptons falls outside the acceptance region of the detector. By applying a veto on events with more than three leptons ("ZZ veto"), the contamination of ZZ events in the signal region is reduced. The remaining amount of ZZ events is estimated using Monte Carlo.

To verify the validity of the MC modelling of this dominant background, the MC is validated in a dedicated control region enriched in ZZ events. The ZZ veto is reverted. Instead, four leptons are required: in addition to the WZ signal leptons, a lepton fulfilling the criteria denoted as baseline criteria in Section 6.1 with $p_{\mathrm{T}} > 5$ GeV is selected. Table 6.5 lists the selection criteria of the ZZ control region.

According to the MC estimation of the event contributions to this control region, a high purity in ZZ events of 89% is achieved, a total number of 714 data events pass the control region selection. Based on the MC-data agreement in this control region, the ZZ events MC prediction is scaled by a global factor of 1.12 and a global normalisation uncertainty

of 12% is assigned to the ZZ yield estimated in the signal region. Figure 6.2 shows control distributions of the ZZ control region.

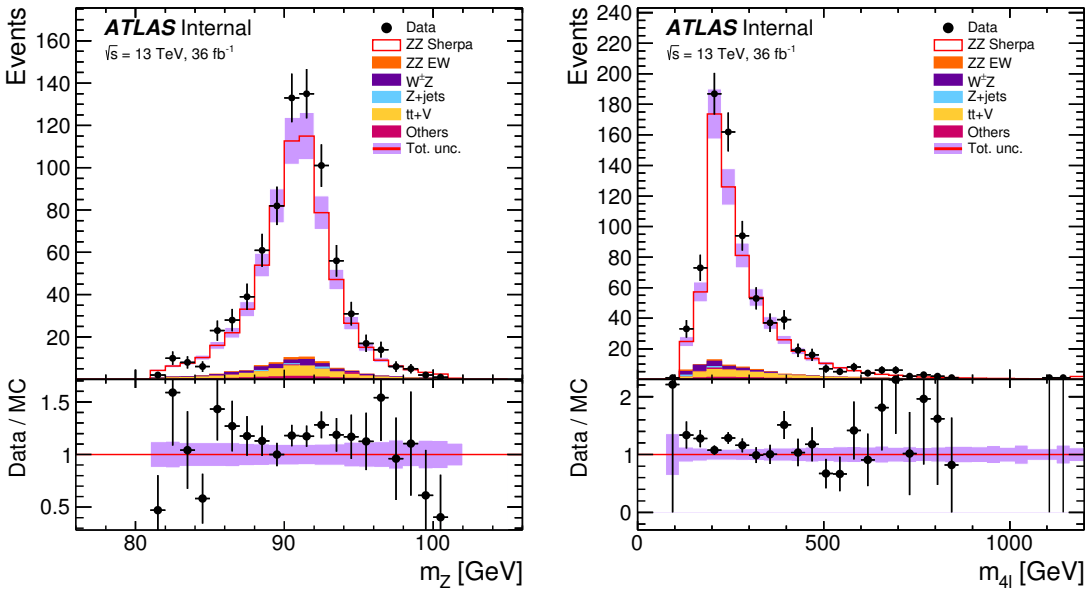

Figure 6.2 – *Control distributions in the ZZ control regions of the first Z boson invariant mass (left) and the invariant mass of the four leptons of the control region. The composition of the control region is estimated using MC, the violet band illustrates the systematic uncertainty on the MC including a global uncertainty on the MC normalization. From [82].*

6.3.3.2 Background from $t\bar{t}V$ events

To validate the MC modelling of $t\bar{t}V$ events, a dedicated control region is constructed. In addition to the nominal signal selection, two hadronic jets, assumed to come from the decay of a b-hadron, are selected. The tagging of those jets is based on a multivariate discriminant trained to recognize typical features of a b-hadron decay like secondary, displaced vertices [116]. The working point with a b-hadron identification efficiency of 85% is chosen. The selected events are dominated by $t\bar{t}V$ events, which contribute to the event yield in this control region with a fraction of 63%.

Based on the MC-data agreement in this control region, a rescaling factor of 1.30 is applied to the predictions of the $t\bar{t}V$ MC and an uncertainty of 30% is applied to the predicted $t\bar{t}V$ yield.

6.3.3.3 Other irreducible backgrounds

Minor contributions of irreducible background to the signal region issue from tri-boson production VVV $V \in \{W, Z\}$, single top plus boson production tZ and double-parton scattering. The amount of these events entering the signal region is estimated using MC prediction scaled to data luminosity. A global uncertainty of 20% uncertainty is assigned to the total yield of VVV events and of 15% to tZ events [82].

6.3.4 Reducible background

The fact that irreducible backgrounds are estimated using MC and optionally validated in data control region is based on the assumption that the the simulation describes well the identification and isolation selection criteria for real leptons. It has already been described in Section 5 that it is difficult to model the detector response of real leptons and that a discrepancy in the modelling of the detector response for real leptons is corrected with a scale factor. However, no such scale factor exists for other objects which pass the lepton identification and isolation criteria. Therefore, the prediction given by the simulation is not expected to give the correct results for the yield of mis-identified objects passing the signal selection. It is therefore best to derive their amount using data-driven techniques. In the framework of the WZ analysis, this component is estimated using the so-called Matrix Method.

6.3.4.1 The Matrix Method methodology

The concept of the fake background calculation using a Matrix Method was applied already in the WZ analysis with $\sqrt{s} = 8$ TeV ATLAS data [12]. Data are used to estimate the fake background in the WZ signal region. In data, the information whether the selected object is a real lepton from a boson decay or a fake lepton is not contained, the information has to be extracted using the information whether the lepton passes or fails identification and isolation requirements. The Matrix Method is based on the measurement of lepton misidentification efficiencies.

Within the scope of the Matrix Method, several types of leptons are defined:

- *Real* lepton (R): muon or electron from the decay of a W or Z bosons
- *Fake* lepton (F): object which is not a lepton but can pass the signal selection criteria: jets from hadrons, non-isolated leptons from the decay of heavy quarks and electrons from photon conversion
- *Tight* leptons (T): objects which pass the signal lepton criteria. Note that these are not necessary real leptons. They might also be hadronic jets or leptons from photon conversion. Thus, this class contains *Real* as well as *Fake* leptons. The *Tight* lepton selection criteria are listed in Table 6.6. The definition of *Tight* includes the W or Z electron or muon signal identification selection cuts and especially isolation criteria: the latter consist of track and calorimeter isolation as defined in Sections 4.3.1 and 4.3.2, and an isolation criterion to jets defined in Section 6.1 within the scope of the lepton to jets overlap removal.
- *Loose* leptons (L): Objects which fail the *Tight* criteria.

A 8×8 matrix relates the number of objects passing and failing the signal selection to the number of real and fake object in the sample. This matrix consists of the probabilities that a fake or real lepton passes the signal selection or not.

$$\begin{pmatrix} N_{TTT} \\ N_{TTL} \\ N_{TLT} \\ N_{LTT} \\ N_{TLL} \\ N_{LTL} \\ N_{LLT} \\ N_{LLL} \end{pmatrix} = \begin{pmatrix} e_1e_2e_3 & e_1e_2f_3 & e_1f_2e_3 & f_1e_2e_3 & e_1f_2f_3 & f_1e_2f_3 & f_1f_2e_3 & f_1f_2f_3 \\ e_1e_2\bar{e}_3 & e_1e_2\bar{f}_3 & e_1f_2\bar{e}_3 & f_1e_2\bar{e}_3 & e_1f_2\bar{f}_3 & f_1e_2\bar{f}_3 & f_1f_2\bar{e}_3 & f_1f_2\bar{f}_3 \\ e_1\bar{e}_2e_3 & e_1\bar{e}_2f_3 & e_1\bar{f}_2e_3 & f_1\bar{e}_2e_3 & e_1\bar{f}_2f_3 & f_1\bar{e}_2f_3 & f_1\bar{f}_2e_3 & f_1\bar{f}_2f_3 \\ \bar{e}_1e_2e_3 & \bar{e}_1e_2f_3 & \bar{e}_1f_2e_3 & \bar{f}_1e_2e_3 & \bar{e}_1f_2f_3 & \bar{f}_1e_2f_3 & \bar{f}_1f_2e_3 & \bar{f}_1f_2f_3 \\ e_1\bar{e}_2\bar{e}_3 & e_1\bar{e}_2\bar{f}_3 & e_1\bar{f}_2\bar{e}_3 & f_1\bar{e}_2\bar{e}_3 & e_1\bar{f}_2\bar{f}_3 & f_1\bar{e}_2\bar{f}_3 & f_1\bar{f}_2\bar{e}_3 & f_1\bar{f}_2\bar{f}_3 \\ \bar{e}_1e_2\bar{e}_3 & \bar{e}_1e_2\bar{f}_3 & \bar{e}_1f_2\bar{e}_3 & \bar{f}_1e_2\bar{e}_3 & \bar{e}_1f_2\bar{f}_3 & \bar{f}_1e_2\bar{f}_3 & \bar{f}_1f_2\bar{e}_3 & \bar{f}_1f_2\bar{f}_3 \\ \bar{e}_1\bar{e}_2e_3 & \bar{e}_1\bar{e}_2f_3 & \bar{e}_1\bar{f}_2e_3 & \bar{f}_1\bar{e}_2e_3 & \bar{e}_1\bar{f}_2f_3 & \bar{f}_1\bar{e}_2f_3 & \bar{f}_1\bar{f}_2e_3 & \bar{f}_1\bar{f}_2f_3 \\ \bar{e}_1\bar{e}_2\bar{e}_3 & \bar{e}_1\bar{e}_2\bar{f}_3 & \bar{e}_1\bar{f}_2\bar{e}_3 & \bar{f}_1\bar{e}_2\bar{e}_3 & \bar{e}_1\bar{f}_2\bar{f}_3 & \bar{f}_1\bar{e}_2\bar{f}_3 & \bar{f}_1\bar{f}_2\bar{e}_3 & \bar{f}_1\bar{f}_2\bar{f}_3 \end{pmatrix} \begin{pmatrix} N_{RRR} \\ N_{RRF} \\ N_{RFR} \\ N_{FRR} \\ N_{RFF} \\ N_{FRF} \\ N_{FFR} \\ N_{FFF} \end{pmatrix}. \quad (6.3)$$

	W	Z
Muons	•`Tight` ID • Isolation: + Track and Calo Iso + Isolation to jets	 • Isolation: + Track and Calo Iso + Isolation to jets
Electrons	•`Tight` ID • Isolation: + Track and Calo Iso + Isolation to jets not reconstructed as γ	 • Isolation: + Track and Calo Iso + Isolation to jets

Table 6.6 – *Definition of the Tight leptons.*

In the matrix of equation (6.3), the numbers $N_{i,j,k}$ with $i, j, k \in \{L, T\}$ denote the number of events whose set of three leptons fulfill a certain combination of *Loose* and *Tight* criteria, whereas i denotes the lepton from the W decay, j the leading lepton in p_{T} from the Z decay and k the sub-leading lepton from the Z decay: For instance, N_{TTT} is the number of events where all three leptons pass the *Tight* criteria, thus the number of data events in the signal region. N_{TTL} is the number of events where both the W-lepton and the leading Z lepton passes, but the sub-leading lepton fails the *Tight* criteria.

The numbers $N_{l,m,n}$ where $l, m, n \in \{R, F\}$ denote the amount of events with a combination of leptons assigned to the W- and Z-bosons being *Real* and *Fake*. N_{RRR} for instance represents the number of events with three real leptons from W or Z decays, N_{RRF} the number of events with a real lepton from a boson decay associated to the W-boson and a real lepton assigned as the highest-p_{T} lepton of the Z-candidate but the sub-leading lepton is a fake lepton from a hadronic jet or from photon conversion.

Latter numbers $N_{l,m,n}$ with $l, m, n \in \{R, F\}$ are unknown quantities which are estimated within the scope of this method. N_{RRR} is the number of real signal events from WZ in the selected signal sample, all other sub-samples $N_{l,m,n}$ with $l, m, n \in \{R, F\}$ are reducible background events with at least one fake, mis-identified object.

The matrix relating $N_{l,m,n}$ with $l, m, n \in \{R, F\}$ and $N_{i,j,k}$ with $i, j, k \in \{L, T\}$ contains probabilities f and e: f is the probability that a fake object F is mis-identified as a *Tight* lepton and e is the probability that a real lepton R is identified. The probabilities $\bar{f} = (1 - f)$ ($\bar{e} = (1 - e)$) are the probabilities that a fake (real) lepton fails the *Tight* requirements. The probabilities e are simply the lepton identification efficiencies. The probabilities f are measured in dedicated control regions enriched with fake objects.
Note that the matrix in equation (6.3) can be simplified: in past studies, it was shown that the probability of a mis-identification of three fake object as *Tight* signal leptons is negligible. The last column therefore can be eliminated such that the linear equation becomes an over-constrained 8×7 matrix. The last row giving the relation between *Real* and *Fake* leptons and the N_{LLL} term can also be eliminated by simply not considering the information in the method given by events with three *Loose* leptons.

6.3.4.2 Estimation of the reducible background in the signal region

Based on the matrix in equation (6.3) reduced to a 7×7 system, the expression for the fake background in the signal region can be obtained. In the terminology of equation (6.3), the expression for the amount of reducible background is given by the amount of events with three *Tight* leptons corrected by the number of events with three real leptons, the signal

events,

$$N_{fake} = N_{TTT} - e_1e_2e_3N_{RRR}. \tag{6.4}$$

The matrix in equation (6.3) can be rearranged by multiplying each row with a suitable term:

$$\begin{pmatrix} N_{TTT} \\ -N_{TTL}\frac{f_3}{\bar{f}_3} \\ -N_{TLT}\frac{f_2}{\bar{f}_2} \\ -N_{LTT}\frac{f_1}{\bar{f}_1} \\ N_{TLL}\frac{f_2}{\bar{f}_2}\frac{f_3}{\bar{f}_3} \\ N_{LTL}\frac{f_1}{\bar{f}_1}\frac{f_3}{\bar{f}_3} \\ N_{LLT}\frac{f_1}{\bar{f}_1}\frac{f_2}{\bar{f}_2} \end{pmatrix} = \begin{pmatrix} e_1e_2e_3 & e_1e_2f_3 & e_1f_2e_3 & f_1e_2e_3 & e_1f_2f_3 & f_1e_2f_3 & f_1f_2e_3 \\ -e_1e_2\bar{e}_3\frac{f_3}{\bar{f}_3} & -e_1e_2f_3 & -e_1f_2\bar{e}_3\frac{f_3}{\bar{f}_3} & -f_1e_2\bar{e}_3\frac{f_3}{\bar{f}_3} & -e_1f_2f_3 & -f_1e_2f_3 & -f_1f_2\bar{e}_3\frac{f_3}{\bar{f}_3} \\ -e_1\bar{e}_2e_3\frac{f_2}{\bar{f}_2} & -e_1\bar{e}_2f_3\frac{f_2}{\bar{f}_2} & -e_1f_2e_3 & -f_1\bar{e}_2e_3\frac{f_2}{\bar{f}_2} & -e_1f_2f_3 & -f_1\bar{e}_2f_3\frac{f_2}{\bar{f}_2} & -f_1f_2e_3 \\ -\bar{e}_1e_2e_3\frac{f_1}{\bar{f}_1} & -\bar{e}_1e_2f_3\frac{f_1}{\bar{f}_1} & -\bar{e}_1f_2e_3\frac{f_1}{\bar{f}_1} & -f_1e_2e_3 & -\bar{e}_1f_2f_3\frac{f_1}{\bar{f}_1} & -f_1e_2f_3 & -f_1f_2e_3 \\ e_1\bar{e}_2\bar{e}_3\frac{f_2}{\bar{f}_2}\frac{f_3}{\bar{f}_3} & e_1\bar{e}_2f_3\frac{f_2}{\bar{f}_2} & e_1f_2\bar{e}_3\frac{f_3}{\bar{f}_3} & f_1\bar{e}_2\bar{e}_3\frac{f_2}{\bar{f}_2}\frac{f_3}{\bar{f}_3} & e_1f_2f_3 & f_1\bar{e}_2f_3\frac{f_2}{\bar{f}_2} & f_1f_2\bar{e}_3\frac{f_3}{\bar{f}_3} \\ \bar{e}_1e_2\bar{e}_3\frac{f_1}{\bar{f}_1}\frac{f_3}{\bar{f}_3} & \bar{e}_1e_2f_3\frac{f_1}{\bar{f}_1} & \bar{e}_1f_2\bar{e}_3\frac{f_1}{\bar{f}_1}\frac{f_3}{\bar{f}_3} & f_1e_2\bar{e}_3\frac{f_3}{\bar{f}_3} & \bar{e}_1f_2f_3\frac{f_1}{\bar{f}_1} & f_1e_2f_3 & f_1f_2\bar{e}_3\frac{f_3}{\bar{f}_3} \\ \bar{e}_1\bar{e}_2e_3\frac{f_1}{\bar{f}_1}\frac{f_2}{\bar{f}_2} & \bar{e}_1\bar{e}_2f_3\frac{f_1}{\bar{f}_1}\frac{f_2}{\bar{f}_2} & \bar{e}_1f_2e_3\frac{f_1}{\bar{f}_1} & f_1\bar{e}_2e_3\frac{f_2}{\bar{f}_2} & \bar{e}_1f_2f_3\frac{f_1}{\bar{f}_1} & f_1\bar{e}_2f_3\frac{f_2}{\bar{f}_2} & f_1f_2e_3 \end{pmatrix} \begin{pmatrix} N_{RRR} \\ N_{RRF} \\ N_{RFR} \\ N_{FRR} \\ N_{RFF} \\ N_{FRF} \\ N_{FFR} \end{pmatrix}. \tag{6.5}$$

If adding rows 1,5,6,7 and subtracting 2,3,4 of the matrix in equation (6.5), the following expression is obtained:

$$N_{TTT} - N_{TTL}\frac{f_3}{\bar{f}_3} - N_{TLT}\frac{f_2}{\bar{f}_2} - N_{LTT}\frac{f_1}{\bar{f}_1} + N_{TLL}\frac{f_2}{\bar{f}_2}\frac{f_3}{\bar{f}_3} + N_{LTL}\frac{f_1}{\bar{f}_1}\frac{f_3}{\bar{f}_3} + N_{LLT}\frac{f_1}{\bar{f}_1}\frac{f_2}{\bar{f}_2} = \tag{6.6}$$

$$\left(e_1e_2e_3 - e_1e_2\bar{e}_3\frac{f_3}{\bar{f}_3} - e_1\bar{e}_2e_3\frac{f_2}{\bar{f}_2} - \bar{e}_1e_2e_3\frac{f_1}{\bar{f}_1} + e_1\bar{e}_2\bar{e}_3\frac{f_2}{\bar{f}_2}\frac{f_3}{\bar{f}_3} + \bar{e}_1e_2\bar{e}_3\frac{f_1}{\bar{f}_1}\frac{f_3}{\bar{f}_3} + \bar{e}_1\bar{e}_2e_3\frac{f_1}{\bar{f}_1}\frac{f_2}{\bar{f}_2}\right) N_{RRR} + \mathcal{O}(f^3).$$

Terms of the order of f^3 are neglected. Equation (6.6) can be rearranged to

$$N_{TTT} - e_1e_2e_3N_{RRR} = [N_{TTL} - e_1e_2\bar{e}_3N_{RRR}]\frac{f_3}{\bar{f}_3} + [N_{TLT} - e_1\bar{e}_2e_3N_{RRR}]\frac{f_2}{\bar{f}_2} + [N_{LTT} - \bar{e}_1e_2e_3N_{RRR}]\frac{f_1}{\bar{f}_1} \tag{6.7}$$

$$-[N_{TLL} - e_1\bar{e}_2\bar{e}_3N_{RRR}]\frac{f_2}{\bar{f}_2}\frac{f_3}{\bar{f}_3} - [N_{LTL} - \bar{e}_1e_2\bar{e}_3N_{RRR}]\frac{f_1}{\bar{f}_1}\frac{f_3}{\bar{f}_3} - [N_{LLT} - \bar{e}_1\bar{e}_2e_3N_{RRR}]\frac{f_1}{\bar{f}_1}\frac{f_2}{\bar{f}_2}.$$

The terms containing $a \cdot N_{RRR}$, where a is a product of e and $\bar{e}$, represent events where one or more real leptons fail the the tight signal selection. These events constitute irreducible background N^{irr}_{ijk} (for instance from WZ and ZZ events) in fake-enriched regions orthogonal to the signal region where one or two leptons fail the *Tight* signal criteria. Equation (6.7) therefore can be rewritten replacing the terms $a \cdot N_{RRR}$:

$$N_{fake} = N_{TTT} - e_1e_2e_3N_{RRR} = [N_{TTL} - N^{irr}_{TTL}]\frac{f_3}{\bar{f}_3} + [N_{TLT} - N^{irr}_{TLT}]\frac{f_2}{\bar{f}_2} + [N_{LTT} - N^{irr}_{LTT}]\frac{f_1}{\bar{f}_1} \tag{6.8}$$

$$-[N_{TLL} - N^{irr}_{TLL}]\frac{f_2}{\bar{f}_2}\frac{f_3}{\bar{f}_3} - [N_{LTL} - N^{irr}_{LTL}]\frac{f_1}{\bar{f}_1}\frac{f_3}{\bar{f}_3} - [N_{LLT} - N^{irr}_{LLT}]\frac{f_1}{\bar{f}_1}\frac{f_2}{\bar{f}_2}.$$

The expression

$$F_i = \frac{f_i}{\bar{f}_i}, \tag{6.9}$$

are ratios of the probabilities that a fake object passes to the probability that a fake object fails the *Tight* criteria, denoted as fake factor. Using the definition of the fake factor from equation (6.9), equation (6.8) can be rewritten as

$$N_{fake} = [N_{TTL} - N^{irr}_{TTL}]F_3 + [N_{TLT} - N^{irr}_{TLT}]F_2 + [N_{LTT} - N^{irr}_{LTT}]F_1 - [N_{TLL} - N^{irr}_{TLL}]F_2F_3 \tag{6.10}$$

$$-[N_{LTL} - N^{irr}_{LTL}]F_1F_2 - [N_{LTL} - N^{irr}_{LTL}]F_1F_2 - [N_{LLT} - N^{irr}_{LLT}]F_1F_2.$$

N^{red}_{ijk} is the number of events contained in a sample of events with the kinematic selection as in the signal region but with one or two objects failing the *Tight* signal selection. It consists of events containing one or two fake objects but also events with at least three *Real* leptons with one or two *Real* leptons failing the *Tight* signal criteria. With $N^{red}_{ijk} = N_{ijk} - N^{irr}_{ijk}$, equation (6.10) can be rewritten as

$$N_{fake} = N^{red}_{TTL}F_3 + N^{red}_{TLT}F_2 + N^{red}_{LTT}F_1 - N^{red}_{TLL}F_2F_3 - N^{red}_{LTL}F_1F_3 - N^{red}_{LTL}F_1F_3 - N^{red}_{LLT}F_1F_2. \tag{6.11}$$

The fake factors in equation (6.11) depend on the strictness of the identification and isolation criteria of the lepton selection. For both, leading and sub-leading Z-lepton, the selection criteria are the same, it makes sense to define only one fake factor for Z-leptons, F_Z. Plugging in F_Z and F_W, the fake factor for W-type leptons, equation (6.11) can be rewritten to

$$N_{fake} = N^{red}_{TTL}F_Z + N^{red}_{TLT}F_Z + N^{red}_{LTT}F_W - N^{red}_{TLL}F_ZF_Z - N^{red}_{LTL}F_WF_Z - N^{red}_{LTL}F_WF_Z - N^{red}_{LLT}F_WF_Z. \tag{6.12}$$

Also, the identification and isolation criteria are a function of the lepton-p_{T}. The fake factor has therefore to be calculated in bins of p_{T}. A different fake factor also has to be taken into account for electron and muon fakes.
The full Matrix Method equation giving the number of fake leptons in the signal region taking into account the dependence of the fake factor on p_{T} is

$$N_{fake} = \sum_i N^{red^i}{}_{TTL}F^i_Z + \sum_i N^{red^i}{}_{TLT}F^i_Z + \sum_i N^{red^i}{}_{LTT}F^i_W - \sum_i\sum_j N^{red^{ij}}{}_{TLL}F^i_ZF^j_Z \tag{6.13}$$

$$- \sum_i\sum_j N^{red^{ij}}{}_{LTL}F^i_WF^j_Z - \sum_i\sum_j N^{red^{ij}}{}_{LTL}F^i_WF^j_Z - \sum_i\sum_j N^{red^{ij}}{}_{LLT}F^i_WF^j_Z,$$

where i, j run over bins in fake lepton transverse momentum p_{T}. The procedure to obtain equation (6.13) is equivalent to the inversion of the matrix in equation (6.3).

The basic idea of the Matrix Method is to define a so-called Loose Signal region (LSR) constructed by requiring the same kinematic cuts as for the signal region except that one or two leptons fail the *Tight* lepton requirements. *Loose* leptons in the Loose Signal region pass only some basic selection criteria listed in Table 6.7, denoted "Matrix Method leptons" in the following, but fail the *Tight* lepton selection. Note that no isolation criteria are applied on Matrix Method leptons.

The N^{red}_{ijk} in equations (6.12) and (6.13) denote the yields in the Loose Signal region and the $F_i, i \in \{W, Z\}$ the fake factors calculated in separate control regions. By means of a fake factor, the yields in this Loose Signal region are extrapolated to the signal region which gives the estimation of the number of reducible background in the signal region N_{fake}.
Different kinematic selections are applied to define the control regions for the fake factor calculation. The control region is defined such that it is pure in fake objects and has as little contamination as possible from real leptons. All fake leptons in the control regions pass the same basic selection requirements as the leptons in the Loose Signal region, described in Table 6.7.

Electrons	Muons
$p_{\mathrm{T}} > 15$ GeV	$p_{\mathrm{T}} > 15$ GeV
$\lvert\eta\rvert$ <2.47	$\eta < 2.7$
!1.37 $< \lvert\eta\rvert < 1.52$	-
pass `Loose` LH ID	pass `Medium` LH ID
$z0$ <0.5	z0 <0.5 (if $\eta < 2.5$)
$d0$ significance < 5 (only LSR)	

Table 6.7 – *Selection of Matrix Method leptons.*

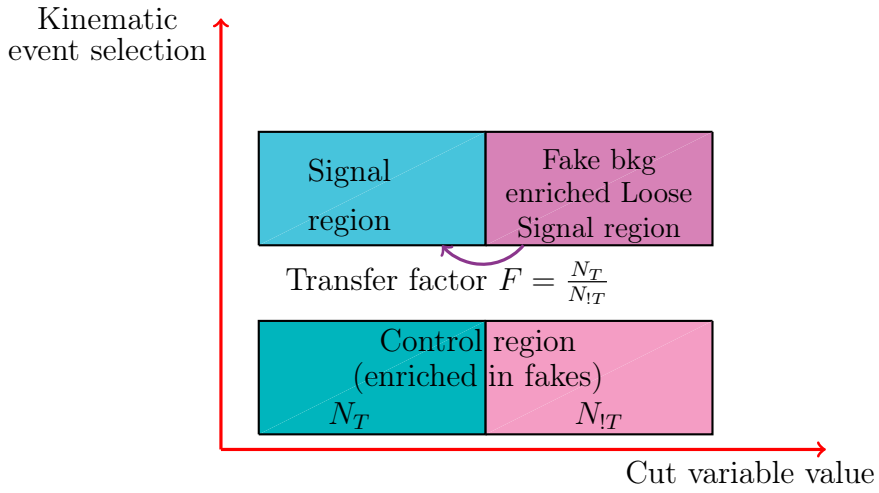

Figure 6.3 – *Illustration of the Matrix Method methodology.*

The fake factor definition in equation (6.9), $F_i = \frac{f_i}{\bar{f}_i}$, can be rewritten using the definition of f and $\bar{f}$. Given a fake lepton in a control region, f is the probability that this lepton is identified as a *Tight* lepton. In a pool of fake leptons, a *control region*, containing $N_{all,ctrl}$ events, f can be written as $f = \frac{N_T}{N_{all,ctrl}}$ and $\bar{f} = \frac{N_{!T}}{N_{all,ctrl}}$, whereas N_T is the number of events in that fake pool passing the *Tight* and $N_{!T}$ is the number of events failing the *Tight* requirements. Using this, equation (6.9) can be rewritten as

$$F = \frac{f}{\bar{f}} = \frac{N_T}{N_{!T}}. \tag{6.14}$$

The *Tight* signal requirements are applied on the pool of fake objects in the control region and the fake factor is calculated by taking the ratio of the number of events passing to the number of events failing the *Tight* requirements according to equation (6.14).
An illustration of the Matrix Method methodology is given in Figure 6.3.

Fake factors depend on the lepton selection criteria, implying cuts on identification and isolation variables. The tighter the criteria, the less fakes pass, the smaller the fake factor. The tightness of the selection criteria can depend on the lepton transverse momentum p_{T}. The fake factor is therefore a function of the transverse momentum of the fake. Studies also showed, that the fake factor also manifests a dependency on the detector region η where the fake is detected. The origin of the fake lepton, whether it is a lepton from a heavy quark decay, a mis-identified light hadron or an electron from photon conversion, also plays a role. For the fake factor to be applicable in the Loose Signal region, potential differences in the origin of the fake leptons between the control and the Loose Signal region have to be accounted for. A correction is derived within the scope of the Matrix Method

to correct for the differences in the relative contribution of the different sources of fake leptons between the control regions and the Loose Signal region.

6.3.4.3 Control regions for the fake factor calculation

The Matrix Method is based on the calculation of the probability that an object passes the *Tight* signal requirements given that it is a fake. Samples pure in fake leptons are needed, the so-called control regions of the Matrix Method. The clean event topology of a leptonic boson decay or the di-leptonic decay of a top quark is used to identify an event. An additional object passing the Matrix Method lepton selection as defined in Table 6.7 is required. This selected fake lepton is usually the Matrix Method lepton with the highest p_{T} which is not yet assigned to any of the object used to tag the event. It has to be verified though, that the fake is indeed not a real lepton, contamination of the fake sample with real leptons will bias the fake factor: real leptons have a higher probability to pass the signal lepton selection.

In fact, the methodology of the control region is in a way a tag and probe method: an object which can be easily identified due to its clean decay signature, such as a Z or W, is the tag, the additional Matrix Method lepton is the probe on which the measurement is performed in analogy to the method presented in Section 5.

Several control regions are defined. The Z+jets control region aims to select Z+jets events. A Z can be easily identified due to two isolated leptons having a defined invariant mass. Furthermore, the production of a Z along with a hadron has a large cross section. Moreover, it represents the topology of events which enter easily the WZ selection. An inversion of the cut on the transverse mass of the fake W constructed from the fake lepton transverse momentum and the fake missing transverse energy ensures orthogonality to the signal region.

Based on the Z+jets events selection, a photon conversion control region is defined. This control region represents the properties and fake factors of electrons from photon conversion. Note that this control region is only defined for fake electrons, the amount of photon conversion processes yielding muons is negligible. A Z decaying to Z-type muons is selected, however, the slightly different topology caused by the radiated photon from one of the leptons has to be considered: the final state radiation decreases the di-lepton invariant mass. Instead, the three object invariant mass from the two leptons and the fake should yield an invariant mass close to the Z mass.

A control region selection based on W+jets events exploits the high cross section of this process in order to create a control region with high statistics. The strict criteria of the W-type lepton selection and missing transverse energy are used to tag a W-boson. Only one additional Matrix Method lepton is allowed in the event, it should furthermore be opposite flavour and same-sign to reject real leptons coming from a Z or a top decay.

To probe the properties of fakes from heavy quark decay, a sample dominated by $t\bar{t}$ events is selected. The selection is based on the signature of a di-leptonic $t\bar{t}$ decay yielding an electron and a muon which are of opposite charge. To reject events from Z+jets, none of the two leptons tagged as the real lepton from the top decay, is allowed to form an opposite charge, same flavour pair with the object assigned as the fake, the remaining highest-p_{T} Matrix Method lepton.

Table 6.8 summarizes the basic features of the control region selections, the obtained event yield in data and the dominant contributions. Note that all control regions are orthogonal to both the signal and the Loose Signal region.

Events with more than two real leptons entering the control regions, for example ZZ and WZ events, might introduce a bias in the fake factor calculation: instead of selecting a fake, a real lepton could be selected. This contribution is estimated with Monte Carlo and subtracted from the data yield in the respective control regions.

6.3.4.4 Fake Factor results

In the following, results for the fake factors are given representational for the Z+jets and the $t\bar{t}$ selection to show the general features of the fake factors. Figures 6.4 and 6.5 show the fake factor as a function of the fake lepton transverse momentum p_{T} obtained in the Z+jets and $t\bar{t}$ control regions. On the left, fake factors for W-type leptons and on the right for Z-type leptons are displayed.

It is obvious that the MC does not describe well the fake factor. Fakes passing the lepton selection are not well modelled, this is why a data-driven approach for the fake background estimation is chosen.

Note that in case of data fake factors, a systematic uncertainty from the irreducible background subtraction is taken into account. An uncertainty on 15% is assumed on the cross section of the irreducible background processes which is correlated across p_{T} bins and for *Tight* and *Loose* leptons.

The tighter the lepton selection criteria, the smaller the fake factor. This can be observed in Figures 6.4 and 6.5: for Z-type leptons, larger fake factor results are obtained than for W-type leptons. The effect is most striking for fake electrons in the Z+jets control region. The same isolation criteria are applied on W and Z electrons, but on W-electrons, a tighter identification and a cut aimed at rejecting electrons from photon conversion are applied in addition. Theses cuts have a large impact on the fake factor. However, the fake factor obtained with the $t\bar{t}$ control region for fake electrons is much lower, especially for Z-electrons. Furthermore, the difference between W and Z electron fake factors is smaller in the $t\bar{t}$ than in the Z+jet control region. This can be explained as following: the Z+jets control region is expected to consist of fakes from hadrons and photon conversion, whereas the $t\bar{t}$ control region fakes are enriched with fakes from heavy quark decays. The cut rejecting ambiguous electrons reduces the amount of fakes from photon conversion which are expected to be present especially in the Z+jets control region but to be a negligible contribution in the $t\bar{t}$ control region. Non-prompt leptons from photon conversion therefore seem to have a larger fake factor than fakes from heavy quark decays. Electrons from photon conversion are real electrons, the probability that these pass the signal selection is higher. Muon fake factors are also lower than electron fake factors, these fakes are expected to issue mostly from heavy quark decays.

In conclusion, the W-lepton fake factors are lower than Z-lepton fake factor and the fake factor depends on the isolation and identification criteria. A large p_{T} dependence is observed. A dependence on the origin of the fake leptons is indicated. The rejection of electron from photon conversion has a large impact, electron from photon conversion seem to have a larger fake factor compared to leptons from heavy quark decays. The fake factor dependence on the fake lepton origin therefore has to be accounted for.

	Z+jets CR	Photon conversion CR	ℓ+jets	$t\bar{t}$
Object selection	• ≥ 2 Z-type leptons ℓ, same flavour, opposite charge • $\lvert m_{\ell\ell} - m_Z^{PDG}\rvert < 15$ GeV • Construct "fake W" from fake and E_T^{miss} • $m_{\mathrm{T}}^{\text{“}W''} < 30$ GeV • $E_T^{miss} < 30$ GeV (if fake electron) • $m_{ll} > 81$ GeV (if fake electron)	• ≥ 2 Z-type muons, opposite charge ($\mu^+\mu^-$) • $55 < m_{\mu\mu} < 85$ GeV • construct "fake W" from fake and E_T^{miss} • $m_{\mathrm{T}}^{\text{“}W''} < 30$ GeV • $E_T^{miss} < 30$ GeV • $m_{\mu^+\mu^-,\text{fake}} < 105$ GeV	• $\equiv$2 Matrix Method leptons, same charge • $\geq$1 W-type lepton • $\equiv$ 1 electron & $\equiv$1 muon • $E_T^{miss} > 25$ GeV • Construct W from W-lepton and E_T^{miss}	• $\geq 1Z$-type electron e_Z • $\geq 1Z$-type muon μ_Z • charge(μ_Z) $\cdot$ charge(e_Z) < 0 • lepton with different flavour than fake passes W-lepton requirements: l_W • charge(fake) $\cdot$ charge(l_W) > 0
Event Yield: **Electrons**: **Muons**:	 $6.5{\cdot}10^3$ $29{\cdot}10^3$	 $1.4{\cdot}10^3$ -	 $23.5{\cdot}10^3$ $98{\cdot}10^3$	 $2{\cdot}10^3$ $11{\cdot}10^3$
Main contributions	Z+jets	Z+jets $Z+\gamma$	$t\bar{t}$ W+jets	$t\bar{t}$

Table 6.8 – *Summary of the control regions selection. The data event yield for fake electrons and muons and the main contributions to the control region are also shown.*

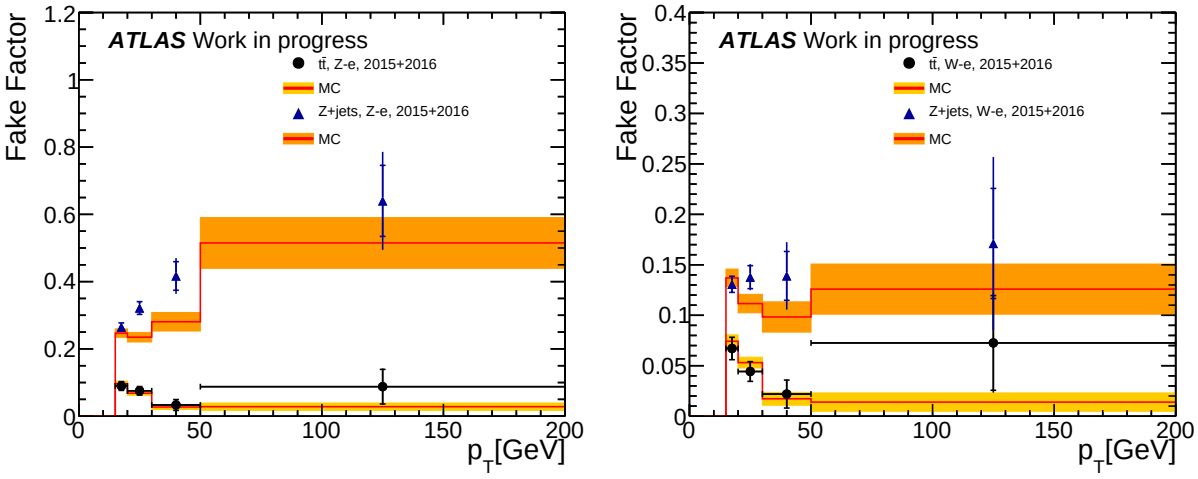

Figure 6.4 – *Fake factor results in the Z+jets (blue triangles) and $t\bar{t}$ control regions (black dots) as a function of p_{T} for fake electrons in data and MC (red histograms). In case of MC, uncertainties contain only the statistical uncertainty, the uncertainties on data contain both, statistical and systematic uncertainties. The uncertainty on the MC fake factor from the Z+jets control region is represented by the orange band, of the $t\bar{t}$ control region by the yellow band. Results for Z-type electrons are shown on the left, of W-type electrons on the right.*

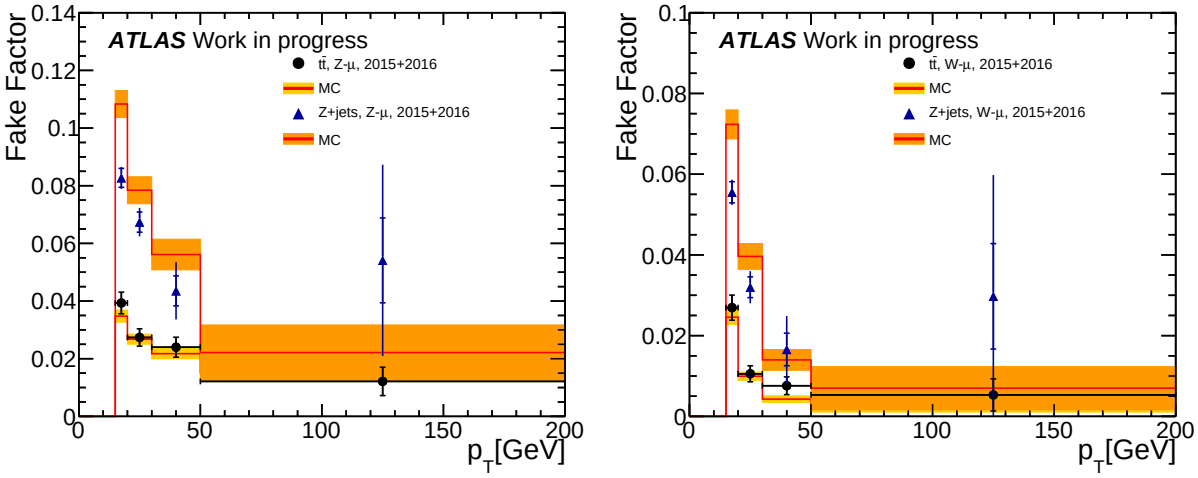

Figure 6.5 – *Fake factor results in the Z+jets (blue triangles) and $t\bar{t}$ control regions (black dots) as a function of p_{T} for fake muons in data and MC (red histograms). In case of MC, uncertainties contain only the statistical uncertainty, the uncertainties on data contain both, statistical and systematic uncertainties. The uncertainty on the MC fake factor from the Z+jets control region is represented by the orange band, of the $t\bar{t}$ control region by the yellow band. Results for Z-type muons are shown on the left, of W-type muons on the right.*

6.3.4.5 Derivation of a detector region correction of the fake factor

Studies showed that the fake factor is also dependent on the detector region were the fake lepton is reconstructed. However, the limited statistics in the control regions does not allow to calculate the fake factors in bins of p_{T} as well as η. An η-dependent correction is therefore derived. It has been found that the η-dependence is symmetric around $\eta = 0$, it

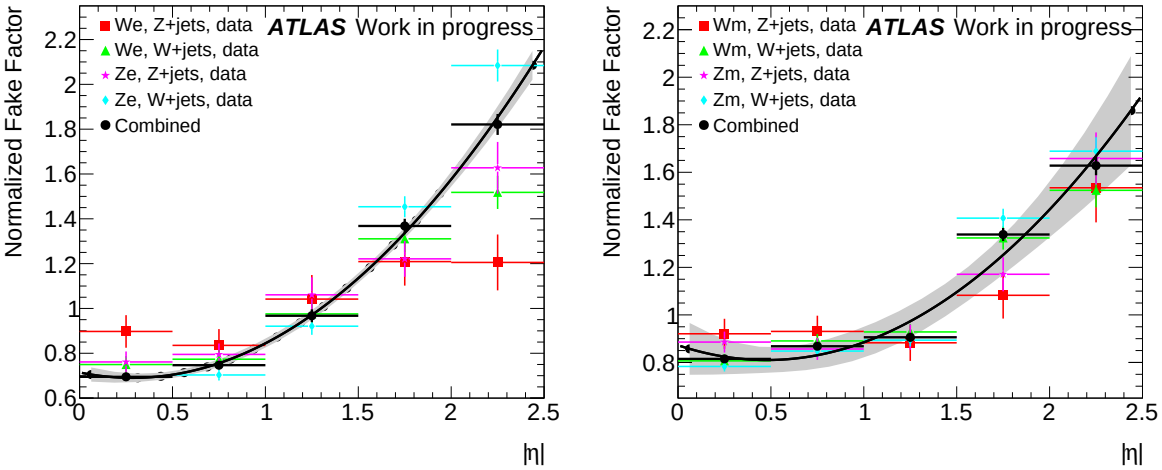

Figure 6.6 – *Fit of a parabolic function to the weighted mean of W- and Z-type lepton fake factor distributions $F_V(|\eta|)$ of the W+jets and Z+jets control regions (black dots). Electrons and muons are treated separately and displayed on the left and right, respectively. The shaded band around the fit result displays its 68% confidence interval. Full total uncertainties are displayed.*

is therefore enough to calculate the correction as a function of $|\eta|$. Studies were performed to investigate this η-dependence and its form. It has been shown that, once, the fake factor distribution as a function of $|\eta|$ is normalized by the mean fake factor of the control region, inclusive over p_{T} and η, the fake factors of all control regions show a very similar behaviour in $|\eta|$. Furthermore, the same correction can be applied on W- and Z-type leptons, however, a separate correction factor has to be derived for electrons and muons. The precision is best for fake factors calculated in the Z+jets and W+jets control regions. The weighted mean of the normalized W- and Z-type lepton fake factor distributions $F(|\eta|)$ obtained in the Z+jets and W+jets control regions is constructed taking into account their relative uncertainty. A parabolic function is fitted to this mean normalized fake factor as a function of $|\eta|$ and the resulting function evaluated at the fake lepton's $|\eta|$ is multiplied to the fake factor. The 68% confidence interval returned by the fit gives the uncertainty on the correction. Figure 6.6 shows the fit of the parabolic function. The 68% confidence interval from the fit is illustrated as a grey band.

6.3.4.6 Studies of the fake factor dependence on the fake lepton origin

Comparing the different fake factor results in Figures 6.4-6.5, it becomes obvious that the fake factor also depends on the type of the object which has been misidentified as a lepton: the probability that an object is misidentified as a lepton depends on its topology in the detector. Therefore, the fake factor is only applicable to the events in the Loose Signal region if the relative contribution of the different fake lepton sources in the Loose Signal region is reproduced in the control region. A separate correction accounts for the differences in the origins of the fake leptons between the Loose Signal region and the control regions.

The origin or source of fake leptons can be grouped in different categories according to their signal in the detector:

- Semi-leptonic heavy quark decays produce leptons which are reconstructed within a hadronic jet. They are denoted heavy flavour, "HF", in the following.

- Hadronic jets with origin light quark (light flavour, "LF") can be misidentified as

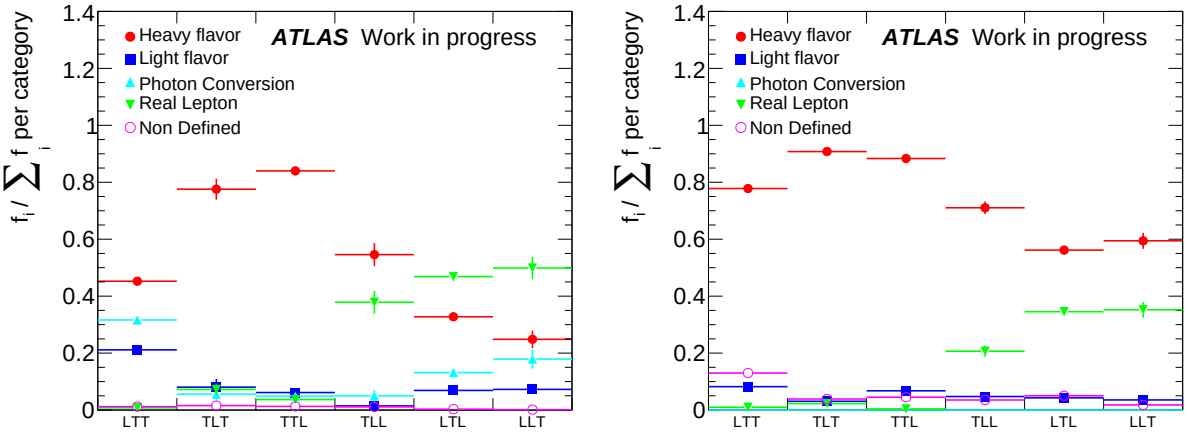

Figure 6.7 – *Relative contribution of each electron (left) and muon source (right) to the Loose Signal region. "L" denotes a Loose lepton and "T" denotes a tight lepton. The first position in the channel name is the W-lepton, followed by the leading and sub-leading Z-lepton.*

leptons in the detector.

- Photon conversion processes ("PC") produce real electrons which are largely isolated, however, they are counted as fakes as they do not originate from a boson decay.

- The samples can also contain real leptons from boson decays. Objects whose origin cannot be extracted for example because the truth information is missing, are denoted as origin "non defined".

Information on the origin of the fakes can be assessed using truth information in the MC sample.

Figure 6.7 shows the relative contribution of each *Loose* electron (left) and muon (right) source in the Loose Signal region. The Loose Signal region is divided in different channel defined by which lepton, the W-lepton, the Z-lepton leading or subleading in p_{T}, does not pass the *Tight* signal requirements. Note that this is the contribution of lepton sources in the Loose Signal region containing Z+jets, $t\bar{t}$ and $Z+\gamma$ processes which all contain two real leptons. To construct the Loose Signal region channels containing two *Loose* leptons ("TLL", "LTL", "LLT"), two *Loose* leptons are required in Z+jets, $t\bar{t}$ and $Z+\gamma$ events. It can occur that one real lepton does not pass the *Tight* signal requirements and is classified as *Loose* lepton, the categories containing two fakes therefore have a larger contamination from real leptons. These events are subtracted from the Loose Signal region.

Fake W-leptons suffer from a much larger content of photon conversion fakes than fake Z-leptons. To the latter class, especially fakes from heavy quark decays contribute. Objects with a good Z boson and an additional jet or photon enter the WZ signal selection due to the jet or photon mimicking the W-lepton. $t\bar{t}$ events enter the WZ signal selection due to the mis-identification of a non-prompt lepton, reconstructed inside a jet from a heavy quark decay, as a Z-lepton which is then combined with a lepton from a W-decay to a "fake Z". The remaining good lepton from the decay of the W originating from the other top quark is selected as the W-lepton by the WZ event reconstruction procedure. It is therefore not surprising that the Z-leptons get primarily contaminated by fakes from heavy quark decays.

Region	HF	LF	PC	Non Def
Z+jets	54.7 ± 0.8%	18.2 ± 0.6%	25.6 ± 0.7%	1.54± 0.17%
W+jets	59.8 ± 1.0%	11.4 ± 0.9%	27.1 ± 1.0%	1.7 ± 0.3%
$t\bar{t}$	92.2 ± 0.4%	3.1 ± 0.3%	3.3 ± 0.3%	1.4 ± 0.18%
$Z+\gamma$	5.5 ± 0.7%	5.0 ± 0.7%	88.9 ± 0.9%	0.49± 0.19%
Loose Signal region (W-lepton)	46.3 ± 1.2%	20.6 ± 1.0%	32.1 ± 1.1%	1.1 ± 0.3%
Loose Signal region (Z-lepton)	84.8 ± 1.2%	6.8 ± 1.0%	7.2 ± 0.8%	1.2 ± 0.3%

Table 6.9 – *Origin of fake electrons selected by the control regions selections introduced in Section 6.3.4.3 evaluated using truth information in the MC. Uncertainties contain statistical uncertainties of the MC samples. For comparison, the contribution of the different sources of the Loose leptons in the Loose Signal region are also shown.*

Region	HF	LF	PC	Non Def
Z+jets	86.1 ± 0.3%	7.1 ± 0.2%	0 ± 0%	6.81 ± 0.19%
W+jets	89.5 ± 0.4%	4.7 ± 0.3%	0 ± 0%	5.8 ± 0.3%
$t\bar{t}$	94.4 ± 0.2%	2.44 ± 0.10%	0 ± 0%	3.20 ± 0.11%
Loose Signal region (W-lepton)	79.8 ± 1.1%	8.0 ± 0.8%	0 ± 0%	12.3 ± 1.0%
Loose Signal region (Z-lepton)	89.2 ± 0.7%	6.2 ± 0.6%	0 ± 0%	4.7 ± 0.5%

Table 6.10 – *Origin of fake muons selected by the control regions selections introduced in Section 6.3.4.3 evaluated using truth information in the MC. Uncertainties contain statistical uncertainties of the MC samples. For comparison, the contribution of the different sources of the Loose leptons in the Loose Signal region are also shown.*

The composition in the non-prompt lepton sources in the Loose Signal region is now compared to the composition in the control regions. Table 6.9 shows the relative contribution of each fake electron source, the origin of fake muons is given in Table 6.10.

The relative contribution of the fake lepton sources in the control region varies as well as a function of the p_{T} of the fake lepton. This is exemplified by means of Figure 6.8 showing the fractions of each fake lepton source as a function of the fake object p_{T} in the Z+jets control region for fake electrons and fake muons.

Figures 6.9 and 6.10 show a comparison between fake factors of all control regions for one bin in p_{T} for Z- and W-type electrons and muons. Data and MC fake factors are displayed and in addition, the relative contribution of each fake lepton source is displayed. From these figures, the fake factor dependence on the origin of the fake lepton becomes obvious, especially the photon conversion content seems to have a high impact.

If the relative contribution of the different fake lepton sources in the control region and the Loose Signal region differ, the fake factor calculated in the control region is not valid any more for the Loose Signal region and the reducible background yield result might be biased. This is especially true for differences in the fraction of electrons from photon conversion which have a very different fake factor than electrons from other sources: photon conversion fakes are real electrons which are more or less isolated and therefore, the probability that these electrons pass the *Tight* signal selection is higher. Separate fake factors for fakes of origin photon conversion and non-photon conversion objects, that is hadrons, are therefore derived. This is only done in case of fake electrons, in case of fake

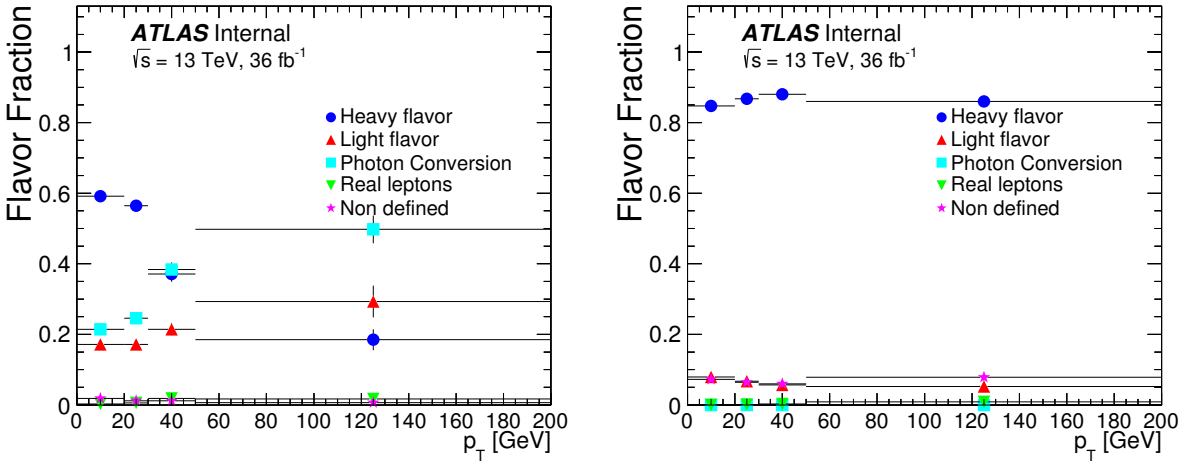

Figure 6.8 – *Relative contribution of each lepton source as a function of the fake lepton p_T selected by the Z+jets control region selection for fake electrons (left) and fake muons (right).*

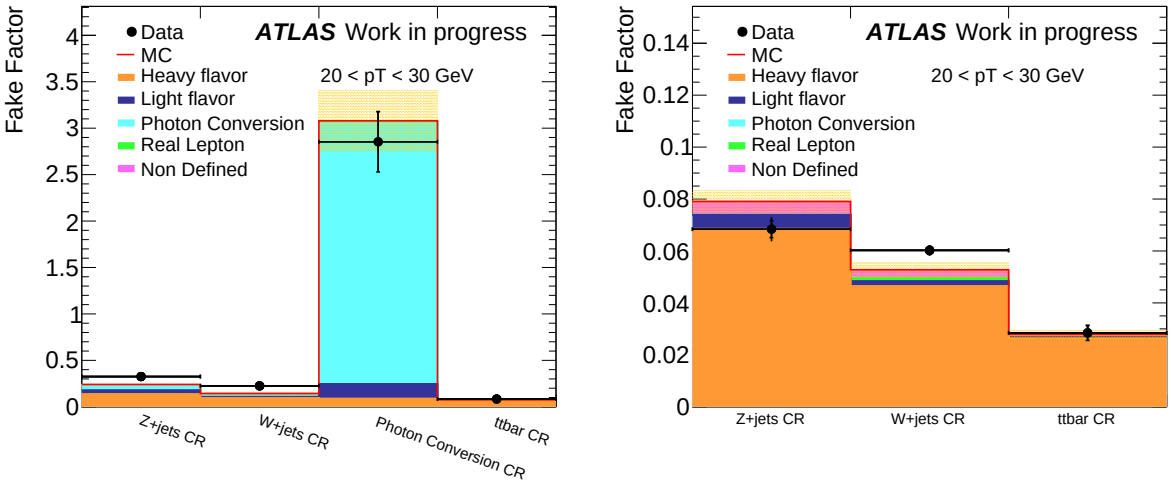

Figure 6.9 – *Fake factor results for fake Z-type electrons (left) and Z-type muons (right) from all control regions for $20 < p_{\mathrm{T}} < 30$ GeV. Data fake factors are illustrated as black dots, the red histogram represents the MC fake factors. The difference between those two is expected as the identification and isolation cuts are not well modelled in MC for fake leptons. The coloured bars show the relative contribution of each fake lepton source, it is represented as the MC fake factor times the fake lepton source's relative contribution.*

muons, the photon conversion content is negligible and no distinction is made between other fake lepton origins. In case of fake muons, the Z+jets control region fake factor from Figure 6.5 is applied.

6.3.4.7 Extraction of fake factors according to the origin of the fake

To extract fake factors for fakes from photon conversion and hadrons, all the information and statistics provided by the control regions defined in Section 6.3.4.3 is exploited. It has to be noted here that the Z+jets, photon conversion, W+jets and $t\bar{t}$ control region are statistically independent. A fit to the data fake factor distribution as a function of the photon conversion fraction can be performed. By means of the fit result, fake factors for

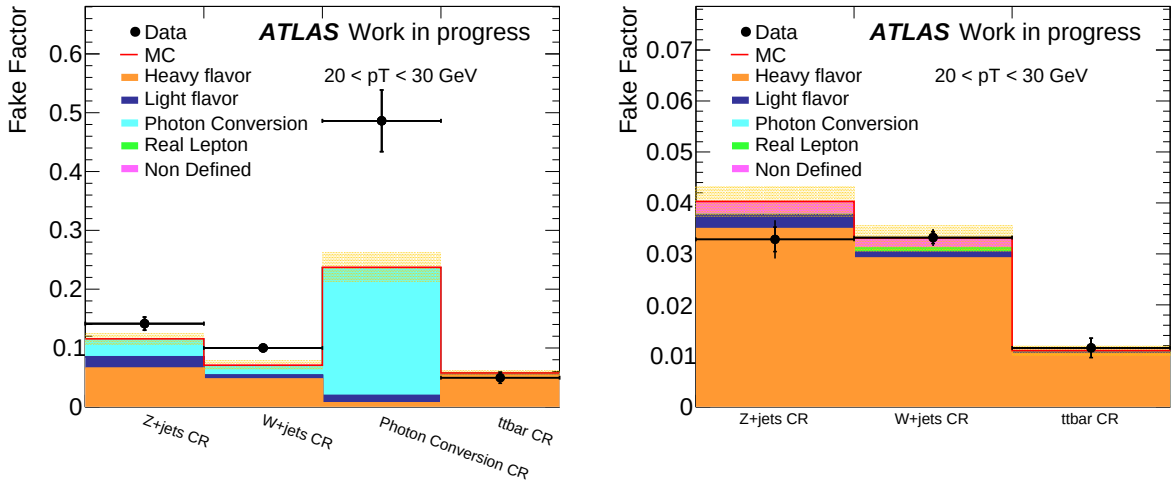

Figure 6.10 – *Fake factor results for W-type electrons (left) and W-type muons (right) from all control regions for $20 < p_{\mathrm{T}} < 30$ GeV. Data fake factors are illustrated as black dots, the red histogram represents the MC fake factors. The difference between those two is expected as the identification and isolation cuts are not well modelled in MC for fake leptons. The coloured bars show the relative contribution of each fake lepton source, it is represented as the MC fake factor times the fake lepton source's relative contribution.*

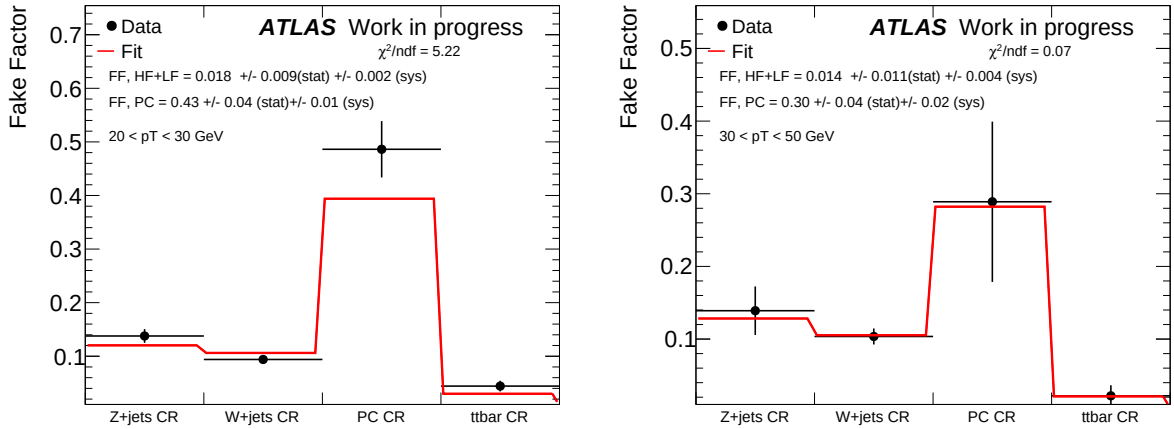

Figure 6.11 – *Fit to data fake factors using the relative fractions of the fake lepton sources in the each control region for $20 < p_T < 30$ GeV and for $30 < p_T < 50$ GeV for fake W-type leptons.*

photon conversion and non-photon conversion fake lepton objects can be extracted. Examples of the fit are shown in Figures 6.11 and 6.12 for W- and Z-type leptons in two bins in p_{T} respectively.

Photon-conversion and hadron fake factors are displayed in Figure 6.14 and 6.13 for Z- and W-type fakes, respectively. Uncertainties contain statistical uncertainties as well as systematic uncertainties from the subtraction of irreducible background. A fake factor corrected for the fake lepton origin composition is calculated according to the expected composition in the Loose Signal region. These fake factors are applied on the fake electrons in the Loose Signal region.

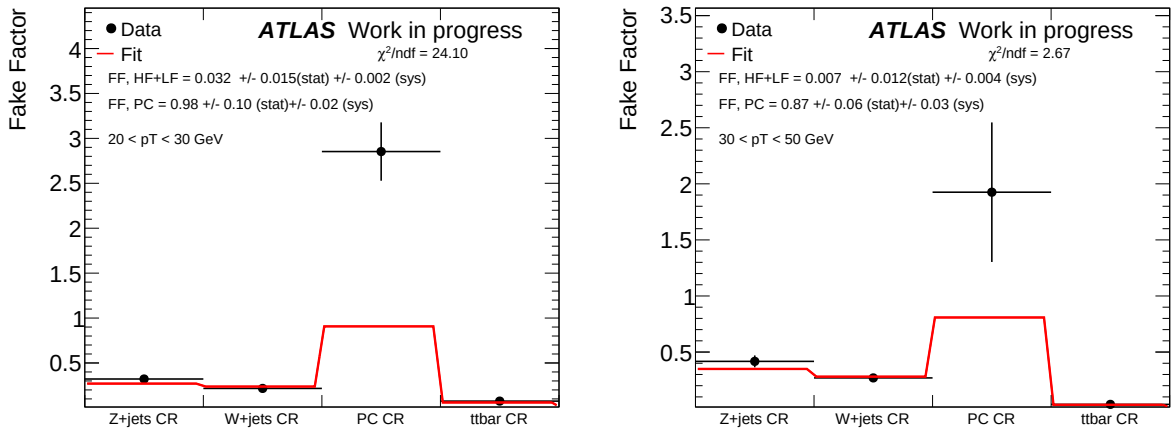

Figure 6.12 – *Fit to data fake factors using the relative fractions of the fake lepton sources in the each control region for* $20 < p_T < 30$ *GeV and for* $30 < p_T < 50$ *GeV for fake Z-type leptons.*

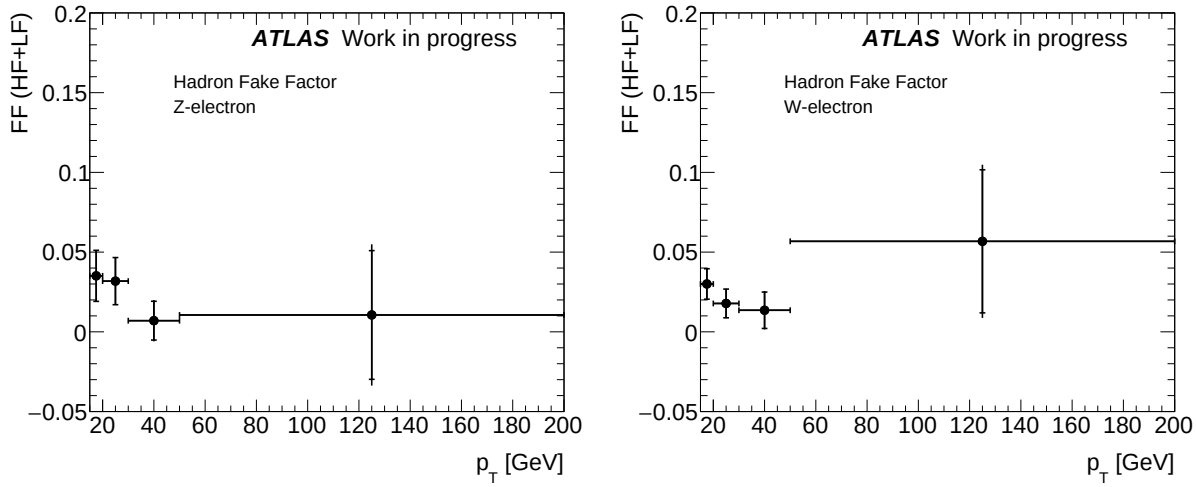

Figure 6.13 – *Hadron fake factor as a function of the fake electron transverse momentum for Z-electrons (left) and W-electrons (right). Total uncertainties are displayed, the inner uncertainties represent statistical uncertainties.*

6.3.4.8 Closure test of the matrix method

To proof the consistency of the Matrix Method procedure with all corrections, a closure test is performed. The presented procedure is applied on MC events and it is studied whether the results coincide with the MC prediction of reducible background events from Z+jets, $t\bar{t}$ and $Z+\gamma$ in the signal region. On fake muons in the Loose Signal region, the MC Z+jets control region fake factor is applied which is shown in Figure 6.5. On fake electrons, dedicated MC fake factors for fakes from photon conversion and from hadrons are applied. These fake factors are derived by applying the Z+jets control region selection on the Z+jets POWHEG+PYTHIA MC. To evaluate whether the fake lepton in the Z+jets control regions originates from a photon conversion process or a hadron, truth information in the MC is used. Table 6.11 shows that good closure is observed: the result of the Matrix Method applied on MC is very well in agreement with the MC prediction for the non-prompt background yield in the signal region for each row of the Matrix in equation (6.3). This shows the validity of the Matrix Method using dedicated fake factors according to the

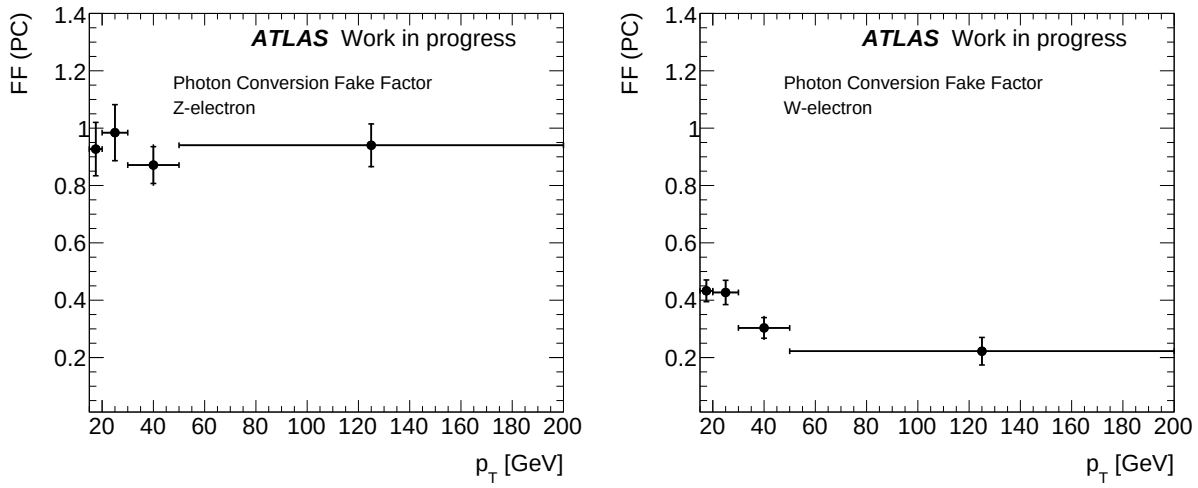

Figure 6.14 – *Photon conversion fake factor as a function of the fake electron transverse momentum for Z-electrons (left) and W-electrons (right). Total uncertainties are displayed, the inner uncertainties represent statistical uncertainties.*

origin of the fake.

Source	eee	μee	$e\mu\mu$	$\mu\mu\mu$	All
$N_{LTT} \cdot F_W$	71.2 ± 2.9	17.1 ± 0.8	89.2 ± 3.0	21.2 ± 0.9	198.8 ± 4.4
$N_{TLT} \cdot F_Z$	2.6 ± 0.3	1.8 ± 0.2	3.6 ± 0.3	5.0 ± 0.4	13.0 ± 0.6
$N_{TTL} \cdot F_Z$	25.2 ± 1.5	17.8 ± 0.8	22.7 ± 0.8	41.8 ± 1.7	107.4 ± 2.5
- 2 L Terms	-1.9 ± 0.1	-0.5 ± 0.0	-1.3 ± 0.1	-0.6 ± 0.0	-4.3 ± 0.2
Matrix Method result	$97.2 \pm 3.3 \pm 31.7$	$36.2 \pm 1.2 \pm 8.2$	$114.2 \pm 3.1 \pm 29.3$	$67.4 \pm 1.9 \pm 21.4$	$314.9 \pm 5.1 \pm 74.7$
($t\bar{t}$ + Z+jets + $Z\gamma$) MC	102.6 ± 10.7	40.5 ± 5.1	113.1 ± 8.3	57.9 ± 6.0	314.0 ± 15.7
N_{FRR}	65.5 ± 7.1	20.1 ± 5.0	87.8 ± 8.9	23.2 ± 4.6	196.6 ± 13.2
N_{RFR}	3.7 ± 0.9	2.6 ± 0.9	3.1 ± 1.1	4.7 ± 1.7	14.0 ± 2.4
N_{RRF}	29.4 ± 10.8	19.2 ± 3.1	21.8 ± 3.6	33.0 ± 4.6	103.4 ± 12.6
N_{RFF}	1.2 ± 0.6	0.0 ± 0.0	0.0 ± 0.0	0.0 ± 0.0	1.2 ± 0.6
N_{FRF}	0.0 ± 0.0	0.0 ± 0.0	0.0 ± 0.0	0.0 ± 0.0	0.0 ± 0.0
N_{FFR}	0.1 ± 0.0	0.0 ± 0.0	0.0 ± 0.0	0.0 ± 0.0	0.1 ± 0.0
N_{FFF}	0.0 ± 0.0	0.0 ± 0.0	0.0 ± 0.0	0.0 ± 0.0	0.0 ± 0.0

Table 6.11 – *Output of the MC closure test using the procedure described in the text. The N_{ijk} with $i, j, k \in R, F$ denote the predicted yields of Z+jets, $t\bar{t}$ and $Z + \gamma$ events in the signal region, the N_{lmn} with $l, m, m \in L, T$ the yields in the loose signal region which are extrapolated to the signal region by means of the fake factors F_V.*

6.3.4.9 Estimation of the uncertainties on the fake background

Several sources of uncertainties limit the precision of the fake background estimate:

- Limited statistics in the control regions and the Loose Signal region
- The uncertainty on the irreducible background cross section, namely of WZ and ZZ
- Uncertainty on the fake origin composition and due to the merging of fake factors of fakes from heavy and light quark decays
- Uncertainty on the $|\eta|$-correction of the fake factor

The two sources of statistical uncertainty, the statistical uncertainty on the fake factors and on the yield in the Loose Signal region, are treated as uncorrelated.

Source	eee	μee	$e\mu\mu$	$\mu\mu\mu$	All
Relative uncertainties [%]					
F_W muon	0.0	4.6	0.0	3.5	1.0
F_Z muon	0.0	0.0	0.6	2.7	0.7
F_W electron	7.7	0.0	8.0	0.0	5.9
F_Z electron	2.1	6.4	0.0	0.0	1.3
Correlated Irr. subtraction	8.0	23.2	8.0	18.7	10.6
Correlated η correction (e)	2.6	1.0	2.2	0.0	1.9
Correlated η correction (μ)	0.0	5.1	1.0	8.2	2.1
Correlated flavour unc. (e)	31.4	12.0	26.9	0.0	23.2
Correlated flavour unc. (μ)	0.0	19.0	3.8	31.0	7.8
Total sys.	33.3	33.1	29.2	37.5	27.4
Stat.	3.4	4.9	2.8	3.1	1.8
Total	33.5	33.5	29.3	37.6	27.5
Absolute uncertainties					
Total	46.3	11.4	56.6	26.9	120.1

Table 6.12 – *Matrix Method systematics and statistical uncertainties. The table shows the correlation between channels. The four first lines corresponds to the statistical uncertainties on the fake factors. The first correlated uncertainty corresponds to the subtraction of the irreducible backgrounds in the loose signal regions, as well as in the calculation of the fake factors. The correlated uncertainties arising from the η dependence correction on the fake factors are shown in lines* 6-7*. The correlated uncertainties arising from the effect of flavour composition on the fake factors are shown in lines* 8-9*.*

An uncertainty of 15% is assumed on the cross sections of irreducible background processes which are present in the control regions as well as in the Loose Signal region, like ZZ and WZ. This component is treated fully correlated across control regions, the Loose Signal region, across p_{T} bins and the yield in *Loose* and *Tight* leptons.

An additional uncertainty of 30% is assigned on the fake factor due to the uncertainty on the fake origin composition and the merging of the fake factor for fake leptons from origin light and heavy quarks. The 30% uncertainty is treated uncorrelated between electron and muon fake factors but fully correlated between W- and Z-type fake factors because of the statistical overlap between the corresponding control region samples.

The precision of the $|\eta|$-correction is accounted for by means of the 68% confidence band of the fit described in Section 6.3.4.5. A different correction has been derived for electrons and muons, therefore, this correction is treated as uncorrelated between electrons and muons. However, as the same correction is used for W- and Z-type leptons, the correction is treated as fully correlated between W- and Z-type leptons.

All the above mentioned sources of systematic uncertainty are treated as uncorrelated among each other. Uncertainties on the fake factor are propagated to the signal region.

Table 6.12 shows the fake background uncertainty result and lists the impact of the different uncertainty contributions. In total, the precision of the fake background yield is 27.5%, the largest uncertainty contributions issue from the irreducible background subtraction and the uncertainty on the fake factor due to the fake lepton origin.

6.3.4.10 Fake background results

Table 6.13 shows the fake background yield obtained with the Matrix Method compared to the MC prediction of Z+jets, $t\bar{t}$ and $Z+\gamma$ events in the signal region. It can clearly be

Source	eee	μee	$e\mu\mu$	$\mu\mu\mu$	All
$N_{LTT} \cdot F_W$	120.3 ± 4.4	21.3 ± 0.9	171.6 ± 5.2	26.8 ± 1.0	339.9 ± 7.0
$N_{TLT} \cdot F_Z$	3.4 ± 0.7	3.0 ± 0.7	3.3 ± 0.6	6.1 ± 0.7	15.8 ± 1.3
$N_{TTL} \cdot F_Z$	16.6 ± 1.4	10.2 ± 1.2	19.7 ± 1.3	39.3 ± 1.8	85.7 ± 2.9
- 2 L Terms	-2.1 ± 0.2	-0.4 ± 0.0	-1.6 ± 0.1	-0.8 ± 0.1	-4.9 ± 0.2
Matrix Method result	$138.1 \pm 4.7 \pm 46.1$	$34.1 \pm 1.7 \pm 11.3$	$193.0 \pm 5.4 \pm 56.4$	$71.4 \pm 2.2 \pm 26.8$	$436.7 \pm 7.7 \pm 119.8$
($t\bar{t}$ + Z+jets + $Z\gamma$) MC	102.6 ± 10.7	40.5 ± 5.1	113.1 ± 8.3	57.9 ± 6.0	314.0 ± 15.7
N_{FRR}	65.5 ± 7.1	20.1 ± 5.0	87.8 ± 8.9	23.2 ± 4.6	196.6 ± 13.2
N_{RFR}	3.7 ± 0.9	2.6 ± 0.9	3.1 ± 1.1	4.7 ± 1.7	14.0 ± 2.4
N_{RRF}	29.4 ± 10.8	19.2 ± 3.1	21.8 ± 3.6	33.0 ± 4.6	103.4 ± 12.6
N_{RFF}	1.2 ± 0.6	0.0 ± 0.0	0.0 ± 0.0	0.0 ± 0.0	1.2 ± 0.6
N_{FRF}	0.0 ± 0.0	0.0 ± 0.0	0.0 ± 0.0	0.0 ± 0.0	0.0 ± 0.0
N_{FFR}	0.1 ± 0.0	0.0 ± 0.0	0.0 ± 0.0	0.0 ± 0.0	0.1 ± 0.0
N_{FFF}	0.0 ± 0.0	0.0 ± 0.0	0.0 ± 0.0	0.0 ± 0.0	0.0 ± 0.0

Table 6.13 – *Comparison of the data-driven background estimate (top, lines labelled with $N_{lmn} \times F_V$ with $l, m, m \in L, T$) and the MC estimate in the signal region (bottom, lines labeled with $N_{ijk} \in R, F$).*

seen that the MC prediction underestimates the fake background yield with respect to the Matrix Method result in overall by about 30%. The MC prediction includes the statistical uncertainties only, the uncertainty on the Matrix Method results contains both, statistical and systematic uncertainties. It can be also pointed out from Table 6.13, that the fake background result obtained with the Matrix Method has a better statistical precision than the prediction from MC. Figure 6.15 shows plots comparing the fake background results predicted by MC and obtained with the Matrix Method. The shape of the fake background distribution is similar for the Matrix Method result and MC prediction. The leading lepton p_{T} spectrum of reducible background events is slightly softer in data than predicted.

6.3.5 Conclusion on the reducible background estimation

To confirm the fake background estimation with the Matrix method, another method was developed for cross-checks. Events in reducible background MC are weighted with a scale factor to correct for the mismodelling of the probability that a fake lepton passes the identification and isolation criteria. For every reducible background component, a dedicated control region as pure as possible in a certain reducible background is defined to derive a MC-to-data scale factor. The control region definition follows largely the one in Table 6.8. However, the lepton denoted as Matrix Method lepton has to pass either the W or the Z-lepton selection. A simultaneous fit is applied to the three control regions for electrons and the two for muons and scaling factors for each fake background contribution, for fake electrons and muon separately and for each lepton type (W- or Z-type lepton) are derived. Additionally, a distinction is made whether less or at least two jets are in the event to account for mis-modelling of the number of jets in the Monte Carlo. The resulting scale factors range from 0.5 to 2.9. MC events of Z+jets, $t\bar{t}$ and $Z + \gamma$ are weighted by the corresponding MC-to-data scale factor. Figure 6.16 compares two resulting distributions with results from the Matrix Method and the unweighted MC prediction. The yields obtained with the Matrix method and the "MC scaling method" agree within 3.3% the shapes of the distributions agree within 40%.

Good agreement is therefore found between the two complementary background estimates.

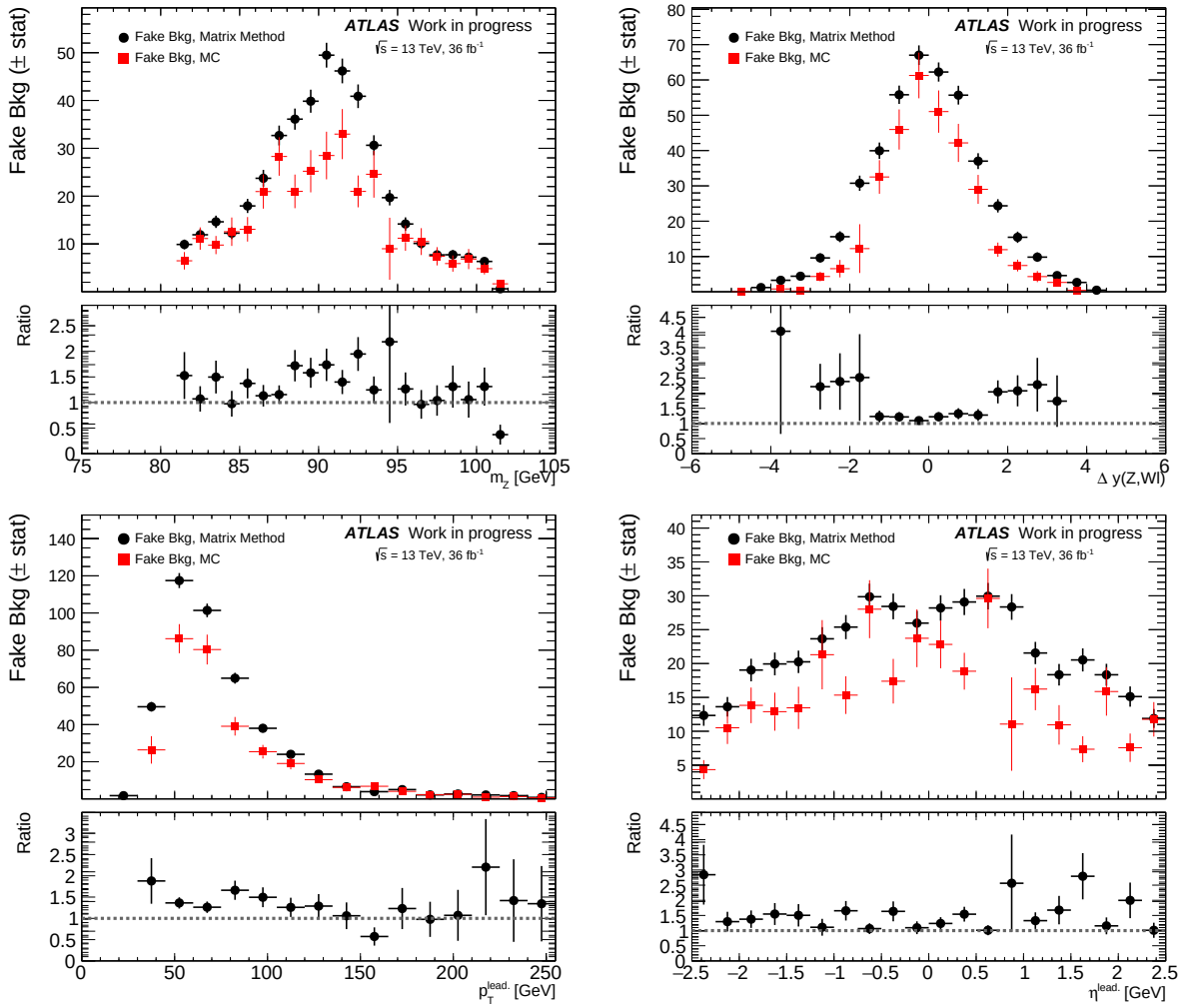

Figure 6.15 – *Fake background di-lepton invariant mass of the leptons assigned to the Z (top left), the rapidity difference distribution of the Z and the W-lepton (top right), the p_T (bottom left) and the η distribution (bottom right) of the leading lepton obtained with the Matrix Method (black dots) and as predicted by MC (red dots). The uncertainties only contain statistical uncertainties.*

6.4 WZ signal yield results

Table 6.14 shows the overall result of the event yield in the WZ signal region following the event selection described in Section 6.1- 6.2 and the estimation of reducible and irreducible backgrounds according to Section 6.3.

Considering the reducible background and the expected irreducible background and signal yields, an overall signal-to-background ratio of 3.95 is reached.

Figure 6.17 shows control plots of the agreement between data and signal expectation and estimated background in the signal region. In overall good agreement is observed between the data and the sum of the background yield estimate and predicted signal.

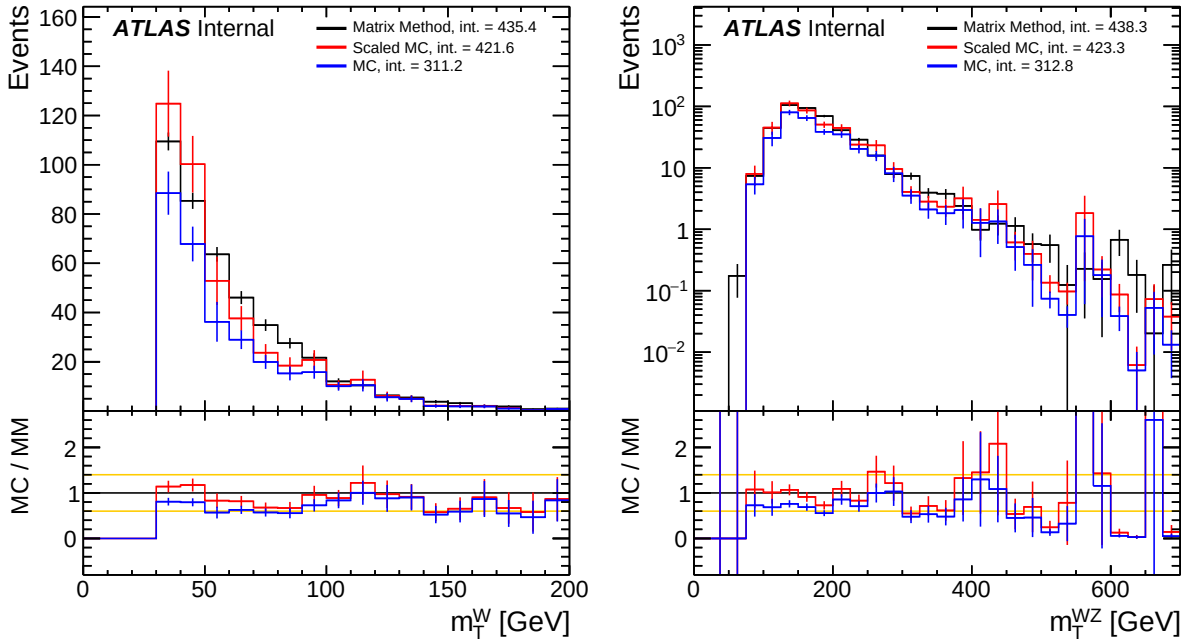

Figure 6.16 – *Comparison of the fake background distribution obtained with the Matrix method (black), the unweighted MC prediction (blue) and with the "MC scaling method" (red). The transverse mass of the W is shown on the left, the transverse mass of the WZ on the right. The uncertainties only contain statistical uncertainties. The yellow lines in the ratio indicates a 40% uncertainty band. From [82].*

Channel	eee	μee	$e\mu\mu$	$\mu\mu\mu$	All
Data	1279	1281	1671	1929	6160
Total Expected	1221 ± 7	1281 ± 6	1653 ± 8	1830 ± 7	5986 ± 14
WZ	922 ± 5	1077 ± 6	1256 ± 6	1523 ± 7	4778 ± 12
Misid. leptons	138 ± 5	34 ± 2	193 ± 5	71 ± 2	436 ± 8
ZZ	86 ± 1	89 ± 1	117 ± 1	135 ± 1	426 ± 3
$t\bar{t}$+V	50.0 ± 0.7	54 ± 0.7	56.1 ± 0.7	63.8 ± 0.8	225 ± 1
tZ	23.1 ± 0.4	24.8 ± 0.4	28.8 ± 0.4	33.5 ± 0.5	110 ± 1
VVV	2.5 ± 0.1	2.8 ± 0.1	3.2 ± 0.1	3.6 ± 0.1	12.0 ± 0.2
$\frac{S}{B}$	3.08	5.26	3.15	4.96	3.95

Table 6.14 – *Expected and measured yield in the $W^{\pm}Z$ signal region. The yields area also splitted according to channel, the first lepton in abb, $a, b \in \{e, \mu\}$ denotes the W-lepton, the second and third lepton the Z-leptons. Uncertainties only include statistical uncertainties. From [82].*

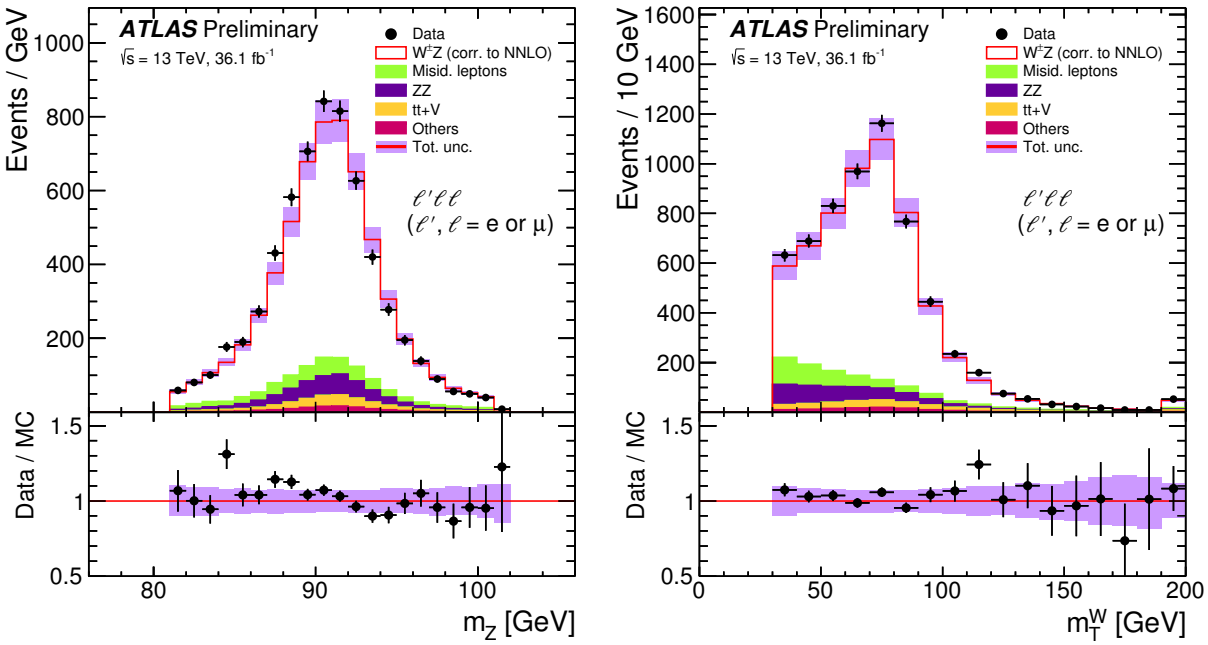

Figure 6.17 – *Control distributions of the data-MC agreement in the signal region illustrating the contributions of all backgrounds and the signal. On the left, the invariant mass of the Z-boson candidate leptons is shown, on the right, the transverse mass of the W-candidate. The black dots show the data, the red line the estimated signal consisting of the predictions of the signal MC, irreducible background components from MC and fake background estimate obtained with a data-driven method. All MC predictions are scaled to the integrated luminosity of data. The purple error band on the MC predictions represents the quadrature sum of all systematic uncertainties on the total MC expectations and an uncertainty of 2.1% for the integrated luminosity in data. From [82].*

Chapter 7

WZ cross section measurement

Based on the event reconstruction and selection and the background estimation presented in Section 6, the cross-section measurement can now be performed. The fiducial cross section will be calculated and an extrapolation will be performed to calculate the total cross section in Section 7.2. The phase space in which these cross sections are defined is presented in Section 7.1.1. The methodology of the cross-section calculation is introduced in Section 7.1.

7.1 Methodology of cross section measurements

7.1.1 Definition of the measurement phase space

Measurements of the cross section are performed in the fiducial phase space. The fiducial phase space is defined to be close to the measurement phase space given by the detector acceptance and the selection cuts to minimize extrapolation uncertainties. An extrapolation to the total phase space is also implemented, whereas the total phase space is defined as the total production cross section of the WZ with the bosons decaying to all possible final states in the complete solid angle. However, only decays of resonant Z-bosons are considered, the decay products of the Z have to fulfil the condition on the invariant mass $66 < m_{\ell^+\ell^-} < 116$ GeV. Table 7.1 lists the requirements on the fiducial and total phase spaces.

Figure 7.1 illustrates the phase spaces used for the measurement: the total phase phase which includes all WZ events in the complete solid angle and all decays, the fiducial phase-space which is a subset of the total phase space and comprises the WZ events generated in the solid angle accessible with the detector and with the measurement cuts applied. The fiducial phase space also considers only decays of the WZ pair to a single, fully leptonic decay channel. The measurement of the fiducial cross section is only performed using

Variable	Total	Fiducial inclusive
Lepton $\lvert\eta\rvert$	—	< 2.5
p_{T} of ℓ_Z, of ℓ_W [GeV]	—	> 15, > 20
m_Z range [GeV]	$66 - 116$	$\lvert m_Z - m_Z^{\mathrm{PDG}}\rvert < 10$
m_{T}^W [GeV]	—	> 30
$\Delta R(\ell_Z^-, \ell_Z^+)$, $\Delta R(\ell_Z, \ell_W)$	—	> 0.2, > 0.3

Table 7.1 – *Definition of the fiducial and total phase-spaces. From [82].*

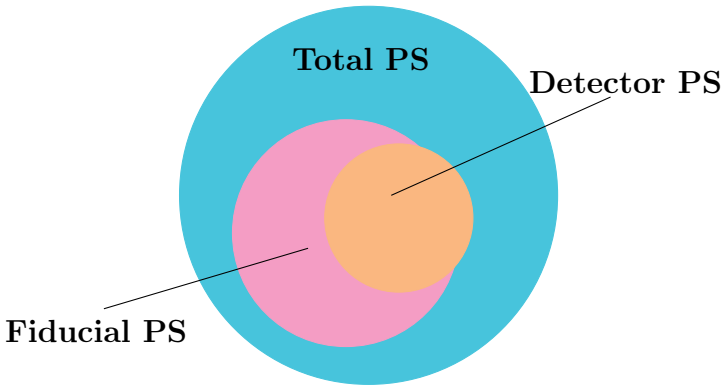

Figure 7.1 – *Illustration of the different phase spaces (PS) defined in the text. Note that this illustration is not to scale.*

decays to electrons and/or muons. Due to the kinematic selection cuts and the restricted solid angle in the definition of the fiducial phase space, about 35% of events of the total phase space decaying to one fully leptonic decay channel to electrons and/or muons are contained in the fiducial phase space. These cuts and the low branching ratio of a single leptonic decay channel explain why the fiducial phase space contains only about one per mille of the events of the total phase space.

Finally, the detector phase space includes events which are reconstructed in the detector. As not all generated WZ events are reconstructed in the detector, the fiducial phase space is larger than the detector phase space. However, it is not a subset as events which are generated outside the fiducial phase space can be reconstructed inside the detector.

The predicted cross sections, extrapolation and correction factors are estimated with MC at generator level using truth particles, i.e. before the simulation of the detector. The event reconstruction a truth level follows a different algorithm than that defined for the reconstruction of data events in Section 6.2. This so-called "resonant-shape algorithm" [12] is independent on MC generators: MC generators do not necessarily follow the same mother to daughter particle assignment algorithm or the structure or the level of information contained in the MC is not necessarily the same. Therefore, the resonant-shape algorithm provides a reliable truth event reconstruction which is uniform for all generators. Note that this algorithm, though being more efficient than the detector-level reconstruction in Section 6.2, cannot be applied to reconstructed events as the full information about the neutrino kinematics is not available at detector level. The resonant-shape algorithm reconstructs the events according to the kinematic properties of the WZ, namely information on the invariant masses of the bosons and their decay width. The combination of assignments of truth particles to the bosons is chosen which maximize the following estimator:

$$P = \left| \frac{1}{m^2_{(\ell^+,\ell^-)} - \left(m_Z^{\mathrm{PDG}}\right)^2 + i\,\Gamma_Z^{\mathrm{PDG}}\,m_Z^{\mathrm{PDG}}} \right|^2 \times \left| \frac{1}{m^2_{(\ell',\nu_{\ell'})} - \left(m_W^{\mathrm{PDG}}\right)^2 + i\,\Gamma_W^{\mathrm{PDG}}\,m_W^{\mathrm{PDG}}} \right|^2 , \tag{7.1}$$

where m_W^{PDG} and m_Z^{PDG} are the W and Z invariant masses and Γ_Z^{PDG} and Γ_W^{PDG} the total decay widths of Z and W bosons respectively, corresponding to the world average as listed by the Particle Data Group [33].

The assignment maximizing equation (7.1) is the assignment which is supposed to be most compatible with the WZ decay kinematics.

The possible bias of the lepton-to-boson assignment algorithm of equation (7.1) has been

investigated within the scope of [15]. In the same flavour channels containing only either electrons or muons, the assignment of the leptons to the W and the Z boson is ambiguous as there can be more than one possibility of assignment, while the assignment is clear if the event contains both, electrons and muons. The assignment resulting from the resonant-shape algorithm has been compared to the assignment provided by the truth information contained in the MC sample in the same flavour channels. Using truth information, the truth lepton can be unambiguously traced back to the mother particle. It has been shown, that the agreement between the resonant-shape algorithm and the assignment done using MC truth information is within 0.5%.

The measurement is unfolded to "dressed leptons". Final state radiation of photons (QED FSR) is collected within a cone of $\Delta R < 0.1$ around the "bare" lepton. Bare leptons are leptons after final state radiation. Dressed leptons correspond most to the reality of the measurement: In the detector, the photons around the electrons are clustered along with the lepton, therefore, dressed leptons are closer to the lepton topology as measured in the detector. All leptons at truth level therefore are dressed.

7.1.2 Fiducial cross-section

The cross section of the WZ production and decay to leptons is calculated using the following equation:

$$\sigma^{\text{fid}}_{WZ\to\ell\nu\ell\ell} = \frac{N_{\text{obs}} - N_{\text{bkg}}}{\mathcal{L}\cdot C_{WZ}} \times \left(1 - \frac{N^{\tau}_{\text{MC,rec}}}{N^{\text{all}}_{\text{MC,rec}}}\right). \tag{7.2}$$

The fiducial cross section in equation (7.2) is defined as the WZ production cross section with subsequent decay to a channel containing only leptons. This includes all lepton flavours, electrons, muons and taus. The measurement is designed for a selection of electrons and muons, however, also some WZ events with at least one boson decaying to a τ lepton pass the event selection. The factor in brackets corrects for this contribution of τ leptons. The so-called τ-factor

$$f_{\tau} = \frac{N^{\tau}_{\text{MC,rec}}}{N^{\text{all}}_{\text{MC,rec}}}, \tag{7.3}$$

is estimated using MC. It is calculated as the fraction of all MC events at reconstruction level in the detector phase space with at least one τ-lepton in the final state with respect to all reconstructed leptonic WZ decays in the measurement phase space.

N_{obs} is the number of observed data events passing the event selection and reconstruction presented in Sections 6.1 and 6.2, and N_{bkg} are the estimated reducible and irreducible background events from Sections 6.3.3 and 6.3.4. $\mathcal{L}$ is the integrated luminosity of 2015 and 2016 data which amounts to 36.1 ± 0.8 fb^{-1}.

The factor C_{WZ} accounts for detector inefficiencies, namely trigger, reconstruction and identification efficiencies. This factor is estimated with MC separately for each decay channel and represent the ratio of events reconstructed at detector level $N_{\text{MC,rec,cuts}}$ with all cuts applied to the generated number of events in the fiducial phase-space $N_{\text{MC,gen,fid}}$,

$$C_{WZ} = \frac{N_{\text{MC,rec,cuts}}}{N_{\text{MC,gen,fid}}}. \tag{7.4}$$

The C_{WZ} factor is the efficiency that a WZ event is detected in the fiducial phase space. Several effects can lead to the non-detection of a WZ event:

Channel	C_{WZ}	f_τ
eee	0.389 ± 0.002	0.041 ± 0.001
μee	0.462 ± 0.002	0.037 ± 0.001
$e\mu\mu$	0.537 ± 0.002	0.038 ± 0.001
$\mu\mu\mu$	0.652 ± 0.003	0.037 ± 0.001

Table 7.2 – *C_{WZ} and τ-factors for the inclusive WZ measurement in each decay channel containing exclusively electrons and/or muons. The uncertainties only contain the statistical precision obtained with the MC sample. From [82].*

- The efficiency of the event reconstruction: restricted knowledge of the event kinematics due to the neutrinos limits the information which can be used in the reconstruction.

- The efficiency of the detector: regions excluded in the detector but considered in the fiducial PS count to that category. This would for example be the crack region $1.37 < |\eta| < 1.52$ excluded in case of electrons. Also, the lepton selection has a limited efficiency. It was already shown in Section 5 at the example of electrons that, depending on the selection tightness, the lepton p_{T} and η, a small fraction of real leptons are rejected by the selection.

- Events from inside the fiducial phase space can be rejected due to mis-measurements, for example of the lepton p_{T}. On the other hand, events from outside the fiducial phase space can migrate inside the measurement phase space. They are also considered in the C_{WZ} factor.

To estimate the number of events generated in the fiducial phase space, WZ events are reconstructed using the resonant-shape algorithm on dressed leptons. To estimate the number of reconstructed leptons in the detector phase-space, simulated WZ events pass through the detector simulation, mis-modelling of the lepton efficiencies is corrected with the scale factors to be as close as possible to the real measurement. Contributions from decays to τ-leptons are subtracted.

The resulting C_{WZ} factors per channel are shown in Table 7.2 along with the results for the τ-factors f_τ per channel. The table presents only the statistical uncertainties from the MC sample with which the calculation has been performed. Mis-modelling uncertainties for example of lepton reconstruction, identification, the energy resolution also affect the C_{WZ} and the τ-factor. Their impact on the cross-section measurement result will be given later.

7.1.3 Total cross section

The total cross section indicates the total production cross section of the WZ pair, taking into account all decays, leptonic decays as well as hadronic decays. The branching ratios of the leptonic decays of the W boson, $\mathrm{BR}_{W\to\ell\nu}$, and the Z boson, $\mathrm{BR}_{Z\to\ell\ell}$, therefore have to be considered in the extrapolation as well as the so-called A_{WZ} factor which extrapolates the cross section in the fiducial phase space to the total phase space:

$$\sigma^{\mathrm{tot}}_{WZ} = \frac{\sigma^{\mathrm{fid}}_{WZ\to\ell\nu\ell\ell}}{\mathrm{BR}_{W\to\ell\nu}\cdot\mathrm{BR}_{Z\to\ell\ell}\cdot A_{WZ}}. \tag{7.5}$$

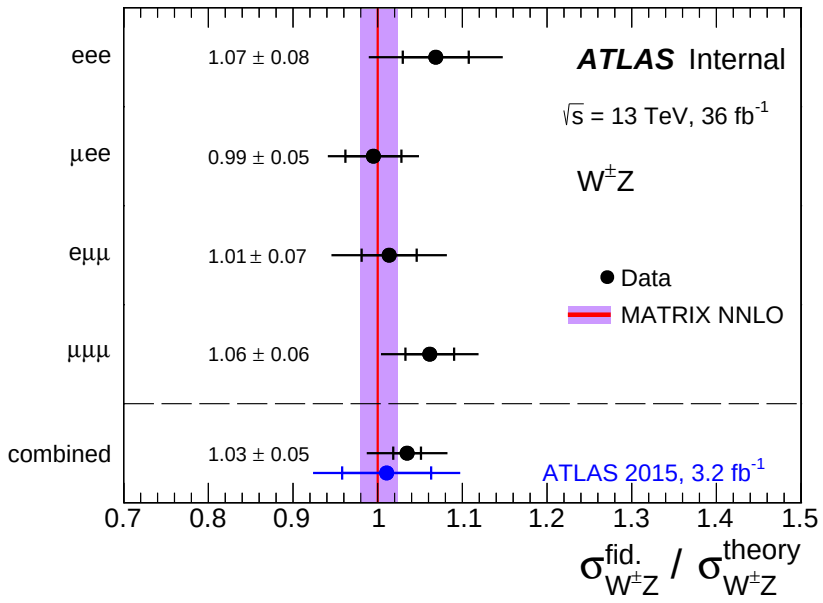

Figure 7.2 – *Fiducial cross section results normalized by the theory prediction at NNLO obtained with* MATRIX *corrected to dressed leptons. Results are shown for the different measurement channels and their combination. The result obtained with 3.2* fb^{-1} *of* $\sqrt{s} = 13$ *TeV data is displayed for comparison (blue dot). From [82].*

$\sigma^{\text{fid}}_{WZ\to\ell\nu\ell\ell}$ denotes the fiducial cross section as presented in Section 7.1.2 and A_{WZ} is estimated by the following relation:

$$A_{WZ} = \frac{N_{\text{MC,gen,fid}}}{N_{\text{MC,gen}}}. \tag{7.6}$$

All generated events in the fiducial phase space are represented by $N_{\text{MC,gen,fid}}$ in equation (7.6) and $N_{\text{MC,gen}}$ denotes the number of generated events in the total phase space. These numbers are estimated with MC and only leptonic decays are included in the calculation, however, with the Z-lepton invariant mass $m_{\ell^+\ell^-}$ in $66 < m_{\ell^+\ell^-} < 116$ GeV. As for the fiducial cross-section measurement, all leptons at truth level are dressed.

The leptonic branching fractions of the W and Z decays, $\text{BR}_{W\to\ell\nu}$ and $\text{BR}_{Z\to\ell\ell}$ respectively, amount to $\text{BR}_{W\to\ell\nu} = 10.86 \pm 0.09$ % and $\text{BR}_{Z\to\ell\ell} = 3.3658 \pm 0.0023$ % [33].

7.2 Cross-section measurement results

Cross-section results are obtained with equation (7.2) using the C_{WZ} factors quoted in Section 7.1.2. The cross section is calculated separately for each measurement channel. These are then combined to an inclusive cross section using a χ^2 minimization method, this procedure is for example described in [117]. All uncertainties and their correlations across different channels are taken into account.

Figure 7.2 displays the results for the fiducial cross section separately for each measurement channel and their combination. The results are compared to the prediction at NNLO precision in QCD and the result obtained with 3.2 fb^{-1} of $\sqrt{s} = 13$ TeV data [15] is displayed for comparison.

Different sources of uncertainties affect the cross section result. The uncertainty on the reducible background has been discussed in Section 6.3.4, the uncertainty on the irreducible

	eee	μee	$e\mu\mu$	$\mu\mu\mu$	combined
Relative uncertainties [%]					
e energy scale	0.2	0.1	0.1	< 0.1	0.1
e id. efficiency	2.8	1.8	1.0	< 0.1	1.1
μ momentum scale	< 0.1	< 0.1	< 0.1	< 0.1	< 0.1
μ id. efficiency	< 0.1	1.3	1.6	2.8	1.5
$E_{\mathrm{T}}^{\mathrm{miss}}$ and jets	0.2	0.2	0.3	0.5	0.3
Trigger	< 0.1	< 0.1	0.2	0.3	0.2
Pileup	1.0	1.5	1.2	1.5	1.3
Misid. leptons background	4.7	1.1	4.5	1.6	1.9
ZZ background	1.0	1.0	1.1	1.0	1.0
Other backgrounds	1.6	1.5	1.4	1.2	1.4
Uncorrelated	0.7	0.6	0.7	0.5	0.3
Total systematics	6.0	3.5	5.4	4.1	3.6
Luminosity	2.4	2.4	2.4	2.4	2.4
Theory	0.5	0.5	0.5	0.5	0.5
Statistics	3.6	3.3	3.2	2.7	1.6
Total	7.4	5.4	6.7	5.4	4.6

Table 7.3 – *Relative uncertainties on the measured WZ fiducial cross section in the different channels as well as the uncertainty on the combination. The impact of the different sources of uncertainties and the total relative uncertainties are listed. From [82].*

background yield has been presented in Section 6.3.3. C_{WZ}, τ-factors and the irreducible background are also affected by the object uncertainties correcting for MC mismodelling of the detector response. The effect of the parton shower modelling on the C_{WZ} factor has been estimated by calculating the C_{WZ} factor also with the POWHEG+HERWIG simulated sample and by comparing the result to the nominal POWHEG+PYTHIA result. The effect of the parton shower modelling on the C_{WZ} is estimated to 0.5% after eliminating the effect of the MC sample statistics. It is denoted as "theory uncertainty" in the uncertainty table in this section. The luminosity enters in several places: directly in the calculation of the cross section but also indirectly through the normalization of the irreducible background. The uncertainty on the luminosity has been measured to 2.1% in [118]. The impact of the different sources of uncertainty on the cross-section measurements in the different channels can be seen in Table 7.3 along with the combined uncertainties and the total uncertainty on the cross-section measurement.

The result for the measured fiducial cross section for collisions with a center-of-mass energy of $\sqrt{s} = 13$ TeV and an integrated luminosity of 36.1 fb^{-1} is

$$\begin{aligned} \sigma^{\text{fid.PS}}_{W^{\pm}Z\to\ell'\nu\ell\ell} &= 63.7 \pm 1.0\,(\text{stat.}) \pm 2.3\,(\text{syst.}) \pm 0.3\,(\text{mod.}) \pm 1.5\,(\text{lumi})\ \text{fb}, \\ \sigma^{\text{fid.PS}}_{W^{\pm}Z\to\ell'\nu\ell\ell} &= 63.7 \pm 2.9\ \text{fb}. \end{aligned} \tag{7.7}$$

When comparing the measurement result to the prediction provided by MATRIX, it has to be taken into account that this prediction has been obtained at Born level, which are leptons before QED final state radiation. However, the measured cross section has been extracted using dressed leptons. A correction factor has to be applied on the MATRIX cross section prediction to account for the fact that the measurement is performed on dressed leptons. The effect of this dressing is evaluated by comparing the cross section

at Born level with the cross section with dressed leptons using the POWHEG+PYTHIA MC. This factor is around 1.04 and has been calculated separately for each measurement channel, it ranges from 1.038 to 1.044. Performing this extrapolation, the MATRIX cross section prediction becomes

$$\sigma^{\text{fid.,MATRIX}}_{W^\pm Z\to\ell'\nu\ell\ell} = 61.5^{1.4}_{1.3}\ \text{fb}. \tag{7.8}$$

A comparison of the measured to the predicted cross section yields a ratio of measurement to prediction of 1.03 ± 0.05. The NNLO prediction therefore agrees with the measurement within the uncertainty.

The measurement with an integrated luminosity of 36.1 fb^{-1} agrees within the uncertainty with the WZ cross section obtained with 3.2 fb^{-1} at a center-of-mass energy of $\sqrt{s} = 13$ TeV [15],

$$\sigma^{\text{fid.,3.2fb}^{-1}}_{W^\pm Z\to\ell'\nu\ell\ell} = 63.2\ \pm\ 3.2\,(\text{stat.})\ \pm\ 2.6\,(\text{sys.})\ \pm 1.5\,(\text{lumi.})\ \text{fb}. \tag{7.9}$$

The total precision on the measured cross section is 4.6% and is therefore competitive to the measurement precision obtained with the currently most precise measurement of the WZ cross section done at $\sqrt{s} = 8$ TeV on ATLAS data [12] where a precision of 4.2% was achieved. Dominant contributions to the uncertainty issue from the uncertainty on the reducible background, the pile-up and the lepton identification efficiencies. A detailed discussion is given below in Section 7.3.1.

By means of equation (7.5), the measured fiducial cross section is extrapolated to the total phase space, resulting into a measured total cross section of

$$\begin{aligned}\sigma^{\text{tot.PS}}_{W^\pm Z} &= 51.0 \pm 0.8\,(\text{stat.}) \pm 1.8\,(\text{sys.}) \pm 0.9\,(\text{mod.}) \pm 1.2\,(\text{lumi.})\,\text{pb} \\ &= 51.0 \pm 2.5\,(\text{tot.})\,\text{pb}.\end{aligned} \tag{7.10}$$

This result agrees with the theory prediction on the total cross section calculated using dressed leptons which is $49.1^{+1.1}_{-1.0}$pb. Note that a correction factor of 0.99 is applied to the MATRIX prediction to take into account QED final state radiation: It has to be considered that the measurement is unfolded to dressed leptons, the MATRIX predictions, however, yield cross section result taking into account leptons at Born level.

A summary plot of all WZ total cross-section results to date compared to predictions is shown in Figure 7.3. It includes measurements done at CDF and D0 at the Tevatron particle collider at Fermilab, by CMS and ATLAS. Note that, comparing to Figure 3.5, the dot representing the ATLAS measurement at $\sqrt{s} = 13$ TeV has been replaced with the new measurement presented in this thesis. The latest CMS measurement on 35.9 fb^{-1} of $\sqrt{s} = 13$ TeV collision data [119] is not included yet in this plot, it has been published after this plot has been created.

7.3 Comparison of the results to previous ATLAS results and to results from CMS

7.3.1 Comparison to the WZ measurement result obtained with collision data at $\sqrt{s} = 8$ TeV with ATLAS

Up to now, the cross-section measurement performed with proton-proton collision data from the ATLAS experiment at a center-of-mass energy of $\sqrt{s} = 8$ TeV is the most precise measurement with a precision of 4.2%.

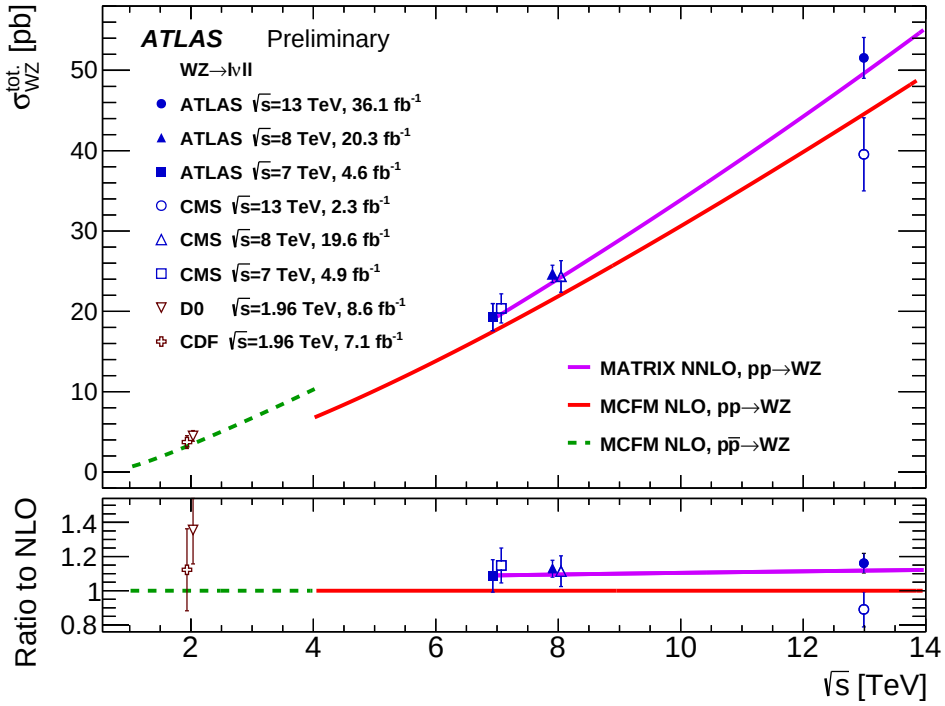

Figure 7.3 – *Comparison of to date measurements of the WZ total cross section with predictions at NLO and NNLO including measurements from CDF, D0, CMS and ATLAS. This plot is an updated version of Figure 3.5 which includes the measurement presented in this thesis. From [82].*

Using the available 36.1 fb^{-1} of data at $\sqrt{s} = 13$ TeV, a higher statistical precision is obtained due to the larger integrated luminosity and the higher WZ cross section at the higher center-of-mass energy: In [15], the 13-to-8 TeV cross section ratio was measured to $\frac{\sigma^{\text{fid.,13 TeV}}_{W^\pm Z\to\ell'\nu\ell\ell}}{\sigma^{\text{fid.,8 TeV}}_{W^\pm Z\to\ell'\nu\ell\ell}} = 1.8$. A tighter lepton selection at 13 TeV decreases slightly the WZ event selection efficiency with respect to 8 TeV. A statistical measurement precision of 1.6% was obtained in overall at $\sqrt{s} = 13$ TeV, compared to a statistical precision of 2.7% at $\sqrt{s} = 8$ TeV.

The measurement at $\sqrt{s} = 13$ TeV is dominated by systematic uncertainties: while the systematic uncertainty at $\sqrt{s} = 8$ TeV with 2.4% was a subdominant uncertainty compared to the statistical uncertainty, it dominates now the measurement precision. The systematic uncertainty amounts to 3.6% with $\sqrt{s} = 13$ TeV data.

The largest increase is due to the larger contribution of the pile-up uncertainty: it increased from 0.2% ($\sqrt{s} = 8$ TeV) to 1.3% ($\sqrt{s} = 13$ TeV). The collisions at $\sqrt{s} = 13$ TeV indeed suffer from more pile-up due to the higher instantaneous luminosity.

Following the data-MC agreement in the ZZ control region, an uncertainty on the ZZ irreducible background yield of 12% has been assigned on the measurement presented in this thesis, while at $\sqrt{s} = 8$ TeV, due to the better data-MC agreement in the control region, only an uncertainty of 7% has been assigned. The $\frac{S}{B}$ ratio for the ZZ background is similar for both measurements despite of the increase of the ZZ cross section with higher collision center-of-mass energy, therefore, the impact of the ZZ uncertainty is expected to approximately double: the impact of the ZZ background yield uncertainty impacts with 1.0% while its contribution was 0.5% on the $\sqrt{s} = 8$ TeV measurement.

The impact on the relative uncertainties of the other irreducible backgrounds, like $t\bar{t}V$

$p_{\mathrm{T}}^{\ell_{Z1}}$	>25 GeV	p_{T} of leading Z-lepton
$p_{\mathrm{T}}^{\ell_{Z2}}$	>10 GeV	p_{T} of sub-leading Z-lepton
$p_{\mathrm{T}}^{\ell_W}$	>25 GeV	p_{T} of W-lepton
$\lvert m_{\ell_{Z1}\ell_{Z2}} - m_Z^{PDG}\rvert$	<15 GeV	invariant mass of Z-leptons
$p_{\mathrm{T}}^{\mathrm{miss}}$	>30 GeV	missing transverse momentum
$n_{b\text{-jet}}$	0	number of b-tagged jets in event
$m_{\ell_{Z1}\ell_{Z2}\ell_W}$	> 100 GeV	three-lepton invariant mass
n_ℓ	3	number of leptons in event
$m_{\ell\ell'}$	> 4 GeV	invariant mass of any lepton pair

Table 7.4 – *Selection cuts applied in the WZ cross-section measurement performed by the CMS collaboration.*

and tZ also increased from 0.7% to 1.4%. This is attributed to the increased cross section of these processes at $\sqrt{s} = 13$ TeV.

The contribution of the reducible background uncertainty has also increased from 1.3% for the $\sqrt{s} = 8$ TeV measurement to 1.9% for the measurement at $\sqrt{s} = 13$ TeV. At $\sqrt{s} = 8$ TeV, cut-based lepton identification menus were used which had a smaller fake rejection efficiency with respect to the likelihood-based identification menus. The loose Matrix Method selection let in more fakes, the contribution from irreducible background processes was smaller. Indeed, the irreducible background subtraction is a dominant uncertainty to the reducible background estimate. The present measurement also assumes a higher contribution due to the fake lepton origin. At $\sqrt{s} = 8$ TeV, fake factors calculated using the Z+jets and W+jets control region were applied for the nominal fake background estimate and the fake factors derived according to the fake lepton origin were only used to estimate the systematic uncertainty. Whereas, in the $\sqrt{s} = 13$ TeV measurement, fake factors according to the fake lepton origin are applied to the nominal measurement and an uncertainty of 30% is assumed in the fake factor as systematic uncertainty due to the estimation of the composition of the control region which adds up to a larger uncertainty. There is also no correction for the $|\eta|$-dependence of the fake factor at $\sqrt{s} = 8$ TeV.

7.3.2 Comparison to the cross-section measurement results obtained with CMS

At the same time as the ATLAS analysis on the WZ cross-section measurement was published, the corresponding CMS measurement results became public [119]. The measurement was performed on $\sqrt{s} = 13$ TeV collision data using 35.9 fb^{-1} of data taken in 2016 by the CMS experiment. As in the measurement presented in this thesis, only final states containing electrons, muons and neutrinos are considered. Different reconstruction algorithms are used and the identification and isolation working points are different in CMS, but otherwise, the analyses are similar. To reconstruct the WZ events in data, pairs of opposite-sign, same-flavour leptons are matched among the three leading leptons, the pair whose invariant mass is closest to the Z mass is assigned to the Z bosons, the remaining lepton to the W boson. Selection cuts are listed in Table 7.4.

The most prominent difference is the veto on jets from b-hadrons.

Reducible background from Z+jets and $t\bar{t}$ is estimated with a data-driven method similar to the Matrix Method. The estimation of the irreducible background from ZZ, $t\bar{t}Z$ and tZ is based on simulation and validated in dedicated control regions. However,

unlike in the ATLAS measurement, background from $Z+\gamma$ is not included in the reducible background estimate, it is estimated using MC and validated in a dedicated control region.

The measurement is performed using a maximum likelihood fit to the total yields in the four different signal regions corresponding to the four different WZ decay channels considered. The parameter of interest in this fit is the WZ signal strength, systematic uncertainties are modeled as nuisance parameters.

As in the ATLAS cross section measurement, the cross section is unfolded to dressed leptons.

The final total cross-section result is

$$\sigma^{tot.}_{WZ,CMS} = 48.09^{+1.00}_{-0.96}\,(\text{stat.})^{+2.39}_{-2.17}\,(\text{syst.})^{+0.44}_{-0.37}\,(\text{theo.}) \pm 1.39\,(\text{lumi})\ \text{pb},$$
$$\sigma^{tot.}_{WZ,CMS} = 48.09^{+2.98}_{-2.78}\ \text{pb}. \qquad (7.11)$$

The total phase space differs slightly from the one defined in the ATLAS analysis: the Z-boson invariant mass is required to be within $60 < |m_Z| < 120$ GeV, whereas in ATLAS, the corresponding requirement is $66 < |m_Z| < 116$ GeV. Therefore, also the MATRIX prediction at NNLO is slightly larger, it has been calculated to $\sigma^{tot.}_{WZ,MATRIX,NNLO} = 49.98^{+2.2\%}_{-2.0\%}$. The prediction slightly overestimates the measurement result, the ratio $\frac{\sigma^{tot.}_{WZ,CMS}}{\sigma^{tot.}_{WZ,MATRIX,NNLO}}$ is $0.96\pm^{0.07}_{0.06}$. It is slightly smaller than the ATLAS result. However, the prediction at NNLO precision in QCD agrees well with the measurement.

The measurement precision is about 6%. Dominant contributions to the uncertainty are lepton and trigger efficiencies, uncertainty from the b-tagging and the non-prompt lepton background estimation.

Chapter 8

WZ polarisation measurement

Within the scope of this thesis, the first measurement of diboson polarisation with hadronic collision data could be performed. A measurement of the diboson polarisation is sensitive to aTGCs and diboson production mechanism: New particles decaying to a WZ pair or modified couplings could lead to different polarisation fractions than predicted. This measurement is also a first step towards measuring the boson polarisation in vector boson scattering. At high energies, the Higgs cancels a singularity in the scattering of two longitudinal bosons. Any deviation in this fragile cancellation would become visible.

Special focus is laid on the measurement or evidence of longitudinal polarisation. In Section 8.1, the methodology of the measurement will be introduced, the predictions will be presented in Section 8.2, optimization studies are discussed in Section 8.3. The measurement is affected by several uncertainties, these will be quantified in Section 8.4, the resulting expected significance for longitudinal boson polarisation in diboson events will be given in Section 8.5. Finally, the polarisation results will be presented in Section 8.6 for the fiducial phase space.

8.1 Methodology of the polarisation measurement

8.1.1 Introduction on the measurement method

The polarisation measurement relies on the different kinematic properties of the decay products of polarised bosons. Especially, angular variables of the decay products are sensitive to boson polarisation and the shape of the angular distributions are therefore good discriminating variables. This is in particular true for the $\cos(\theta^*)$ distribution which has already been introduced in Sections 3.3.2 and 3.3.4. Note that equations (3.11) and (3.13) describing the behaviour of the $\cos(\theta^*)$ distribution as a function of the polarisation fractions, are only valid in the total phase space. However, a measurement cannot be performed in the complete solid angle and in the full kinematic ranges, a fit with the expression in equations (3.11) and (3.13) cannot be applied to reconstructed data. Also, the functions do not consider reconstruction effects. In Section 3.3.5, the generation of samples containing only a single polarisation state has been discussed. By means of these samples, the properties and distribution shapes of polarised bosons can be assessed. In particular, fiducial cuts and the event reconstruction effects can be propagated.

The fiducial phase space follows the definition given in Section 7.1.1. Note that for this analysis, the leptons at truth level are assigned to the bosons using the truth information contained in the Monte Carlo sample. The leptons and the neutrino can therefore be

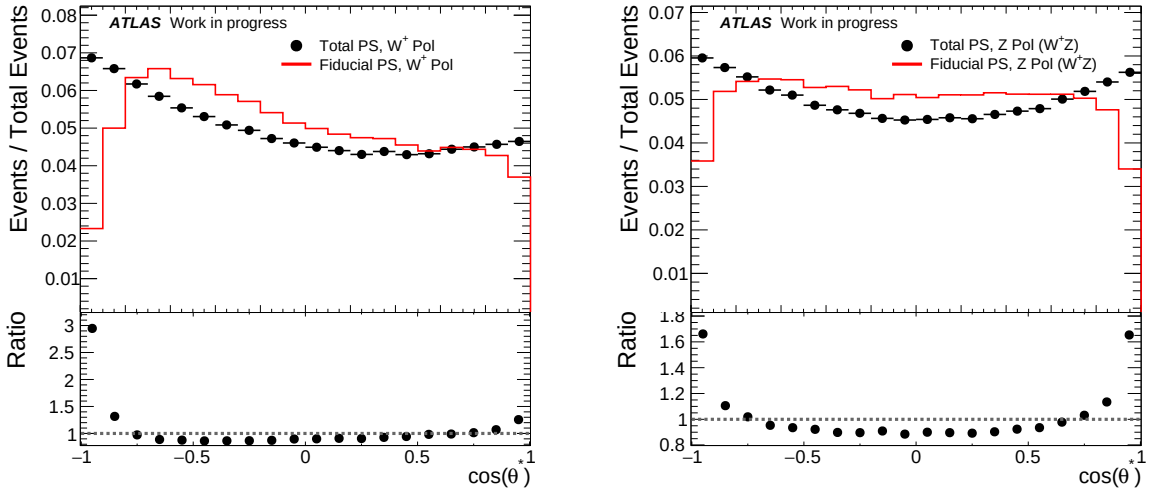

Figure 8.1 – *Distribution of the* $\cos(\theta^*)$ *in the total (black) and in the fiducial (red) phase space. On the left, the distribution is shown for the charged lepton of the* W *decay, on the right, for the negatively charged lepton from the* Z *decay in* W^+Z *events. Note that the distributions are normalized by their integral to allow for a comparison of the distribution shapes.*

unambiguously assigned to the mother bosons. Hence, the truth assignment is different with respect to the cross-section measurement where the leptons are assigned to the mother bosons via the resonant-shape algorithm.

The polarisation measurement is unfolded to leptons at Born level which are leptons before any QED final state radiation. Therefore, the truth lepton definition differs from the definition used in the cross-section measurement where dressed leptons are used.

Closure studies proved the validity of the reweighting method: the templates obtained with the reweighting process in Section 3.3.5 are fit to the $\cos(\theta^*)$ distribution in the total phase space. The polarisation fractions obtained by fitting these templates are consistent with those extracted from the analytic fit as shown in Table 8.1.

Fiducial cuts alter the polarisation fractions. Some kinematic regions are discarded by the fiducial cuts, however, the polarisation is strongly correlated with the decay kinematics. Effects of the fiducial cuts on the polarisation fractions have been studies for example in [85].

The p_{T} cuts on the leptons from the boson decay distort the $\cos(\theta^*)$ distribution: cutting on low p_{T} will reject those events where one lepton from the boson decay carries away very little of the boson energy and is emitted in an angle of close to 180° with respect to the boson. This will reject events with $\cos(\theta^*)$ around +1 or -1. No cut on E_{T}^{miss} is applied as it has been shown that it strongly distorts the $\cos(\theta^*)$ distribution of the W lepton around +1. Lepton identification and isolation cuts are often stricter the lower the lepton p_{T}, consequently, the selection efficiency is lower at low p_{T}. This also distorts the $\cos(\theta^*)$ distribution around +1 or -1. Figure 8.1 compares the expected $\cos(\theta^*)$ distribution in the total and in the fiducial phase space. The distortion around $\cos(\theta^*) = \pm 1$ is clearly visible.

In Table 8.1 polarisation results obtained with MC in the fiducial phase space are listed and they can be directly compared to the results obtained in the total phase space. The polarisation fractions is altered by kinematic cuts with respect to the total phase space due to the fact that the lepton kinematics and the polarisation are correlated.

Due to their different production modes and different kinematics of the initial state partons, the polarisation fractions differ for W^+ and W^- bosons. From equations (3.11)

W boson polarisation in WZ events				
	W^+Z		W^-Z	
Total PS Analytical Fit	f_0	0.209 ± 0.0017	f_0	0.218 ± 0.0022
	f_L	0.472 ± 0.0011	f_L	0.342 ± 0.0013
	f_R	0.319 ± 0.0010	f_R	0.440 ± 0.0014
Total PS Template Fit	f_0	0.209 ± 0.0021	f_0	0.217 ± 0.0027
	f_L	0.472 ± 0.0013	f_L	0.343 ± 0.0016
	f_R	0.319 ± 0.0013	f_R	0.441 ± 0.0017
Fiducial PS Template fit	f_0	0.230 ± 0.0042	f_0	0.245 ± 0.0053
	f_L	0.427 ± 0.0026	f_L	0.347 ± 0.0028
	f_R	0.343 ± 0.0023	f_R	0.409 ± 0.0033
Z boson polarisation in WZ events				
	W^+Z		W^-Z	
Total PS Analytical Fit	f_0	0.209 ± 0.0017	f_0	0.208 ± 0.0022
	f_L	0.310 ± 0.0045	f_L	0.513 ± 0.0058
	f_R	0.481 ± 0.0046	f_R	0.279 ± 0.0058
Total PS Template Fit	f_0	0.208 ± 0.0021	f_0	0.207 ± 0.0025
	f_L	0.310 ± 0.0056	f_L	0.513 ± 0.0069
	f_R	0.481 ± 0.0056	f_R	0.280 ± 0.0069
Fiducial PS Template fit	f_0	0.227 ± 0.0039	f_0	0.233 ± 0.0047
	f_L	0.231 ± 0.0098	f_L	0.432 ± 0.0117
	f_R	0.542 ± 0.0101	f_R	0.335 ± 0.0117

Table 8.1 – *Results of the polarisation fractions in MC extracted with the analytical fit and the template fit in the total phase space and the result of the fit in the fiducial phase space. The analytical and template fit results in the total phase space are in agreement which is a closure test of the reweighting method. The polarisation fractions in the total and the fiducial phase space are not in agreement due to the correlation between kinematics and polarisation, kinematic cuts alter the boson polarisation. From [82].*

and (3.14), it becomes obvious that the template shape for transverse W polarisation is dependent on the W charge by a sign on $\cos(\theta^*)$. W^+ and W^- polarisation are measured separately. To increase the sensitivity on longitudinal W polarisation however, the inclusive $W^\pm$ polarisation is also measured. In that case, the $\cos(\theta^*)$ distribution is combined but the different sign of the $\cos(\theta^*)$ value for W^+ and W^- for left- and right-handed polarised W bosons is considered. Using that parametrization, the distinct shapes of the templates for left- and right-handed polarisation are conserved. In case of a Z polarisation measurement, W^+Z and W^-Z events are summarized without further modifications. It is interesting to measure also separately the Z polarisation in W^+Z and W^-Z events. Different polarisation fractions are predicted for Z bosons in W^+Z and W^-Z events due to different production modes of the Z in W^+Z and W^-Z events: in case of a W^+Z event, the Z is produced from a $u\bar{u}$ quark pair, in case of a W^-Z event, the Z is produced from a $d\bar{d}$ quark pair. Different polarisation fractions arise due to the different right- and left-handed couplings of the Z to u and d quarks [85].
To reconstruct the W and WZ restframes, the longitudinal momentum of the neutrino has to be calculated. To avoid the reconstruction of the neutrino, the variable $\cos(\theta^*_{2D})$ can be used as a discriminating variable, it has been defined in Section 3.3.2. Studies on

pseudodata are performed to evaluate which variable, $\cos(\theta^*_{2D})$ or $\cos(\theta^*)$, yields the largest significance for longitudinal polarisation in W bosons.
To measure the polarisation, a template fit is performed to the angular distribution in data using templates representing the angular variable distributions of the pure polarisation states. The fit yields which linear combination of polarisation templates describe the data best. The measurement concept will be introduced in the following section.

8.1.2 Polarisation measurement concept

In the following, it will be described how the measurement is performed on data: The parametrization of the fit is presented in Section 8.1.2.1, the correction for reconstruction effects in Section 8.1.2.2 and the technical implementation of the fit in Section 8.1.2.3.

8.1.2.1 Parametrization of the fit

In the measurement, the templates representing the angular distribution of the polarised boson decay products are fit to the $\cos(\theta^*)$ distribution in data. The samples representing the properties of polarised bosons have to pass through the detector simulation and the WZ events are reconstructed the same way as the data.

As the three polarisation fractions sum up to one, only two fractions are independent and therefore, only the longitudinal polarisation fraction f_0 and the difference between the left- and right-handed polarisation fractions, $f_L - f_R$, are left floating in the fit. The polarisation fractions f_0, f_L and f_R as defined in equations (3.11) and (3.13) are normalized by the total cross section. A third fit parameter has to be defined, the normalization N_{tot} which corresponds to the number of WZ signal events. N_{tot} is therefore proportional to the WZ cross section.

The fit is parametrized such that the polarisation fraction and their uncertainties can be extracted directly from the fit. The fit scales the polarisation templates with the integral N_i^{Template} by the scaling factor μ_i, where $i \in \{0, L, R\}$. The factor $f_i \times N_{\text{tot}}$ corresponds to the number WZ events where the boson has a certain polarisation i. Expressing μ_i in terms of the polarisation fractions f_i and the normalization N_{tot} and using the relation $f_0 + f_L + f_R = 1$, one obtains equations (8.1)- (8.3), the parametrization of the fit:

$$\mu_0 = \frac{f_0 \times N_{\text{tot}}^{\text{fit}}}{N_0^{\text{Template}}}, \tag{8.1}$$

$$\mu_R = \frac{(1 - f_0 - (f_L - f_R)) \times N_{\text{tot}}^{\text{fit}}}{2 \times N_R^{\text{Template}}}, \tag{8.2}$$

$$\mu_L = \frac{(1 - f_0 + (f_L - f_R)) \times N_{\text{tot}}^{\text{fit}}}{2 \times N_L^{\text{Template}}}. \tag{8.3}$$

The data contains also decays of WZ to τ leptons. These are treated as background in the measurement. However, its magnitude depends strongly on the cross section of WZ, it therefore has to be treated as dependent on the normalization parameter N_{tot} in the fit. A normalization factor μ_τ correlates the magnitude of the background of WZ decays to τ leptons to N_{tot}. The factor μ_τ is defined as

$$\mu_\tau = \frac{N_{\text{tot}} \cdot C_{WZ} \cdot \frac{f_\tau}{1-f_\tau}}{N_\tau^{\text{Template}}}, \tag{8.4}$$

where f_τ is the τ-factor introduced in equation (7.3) and N_τ^{Template} is the integral over the template representing events with WZ boson decays to τ leptons at reconstruction level passing the data selection. The C_{WZ}-factor was introduced in equation (7.4). In the extraction of the polarisation in the total phase space, the A_{WZ}-factor of equation (7.6) is multiplied to equation 8.4.

Although the polarisation depends on p_{T} and the rapidity, the measurement is performed inclusively over both variables. It is from the statistical point of view not reasonable to split the sample, otherwise the goal to provide evidence of longitudinal polarisation cannot be attained. A larger sample will be necessary to also capture the evolution of the polarisation with p_{T} and the rapidity, however, this is left for future measurements on a larger dataset.

8.1.2.2 Template reconstruction efficiency

Using equations (8.1)-(8.3) to extract the polarisation will lead to a small bias in the polarisation fraction from reconstruction effects. The event reconstruction can have the following effects:

- The template shape can be distorted due to migration among the bins in the measurement phase space.
- Events from outside the fiducial phase space can migrate in the measurement phase space.
- Not all events which are produced in the fiducial phase space are reconstructed. The WZ event reconstruction efficiency is a function of $\cos(\theta^*)$.

Shape effects on the template caused by event migration among the bins in the measurement phase space and from outside the fiducial phase space are taken into account by passing the templates with generated events in the total phase space through the detector simulation and by reconstructing them in the same way as the data. All shape distortions should therefore be propagated to the template if the modelling of the detector response is correct. This has been checked by independent measurements done by the ATLAS combined detector performance groups. Scale and correction factors make sure that the simulation describes well the data.

Each polarisation template populates a different kinematic region, the leptons have different kinematic distributions depending on their polarisation. Leptons from different kinematic regions are affected differently by reconstruction effects, for example detector and lepton efficiencies. The goal is to measure the boson polarisation in the fiducial phase space, the fractions have to be corrected by the WZ event reconstruction efficiency. In analogy to the fiducial cross-section measurement, a C_{WZ}^{fi} factor is applied to equations (8.1)- (8.3). This polarisation template C_{WZ}^{fi} factor is derived and applied for each polarisation template separately. Figure 8.2 shows this C_{WZ}^{fi} factor for each of the three templates.

The integral of the polarisation templates N_i^{Template} is divided by the respective C_{WZ}^{fi} factor, where $i \in \{0, L, R\}$. This corresponds to a correction of the measured polarisation fractions at reconstruction level $f_i^{rec.}$ by

$$f_i^{fid} = \frac{C_{WZ}}{C_{WZ}^{fi}} \times f_i^{rec.}, \tag{8.5}$$

where C_{WZ} is the correction factor for the inclusive WZ event reconstruction efficiency and has been defined in equation (7.4). In the implementation of the fit in equations (8.1)-(8.3), the integral over the detector-level polarisation templates N_i^{Template} is replaced by

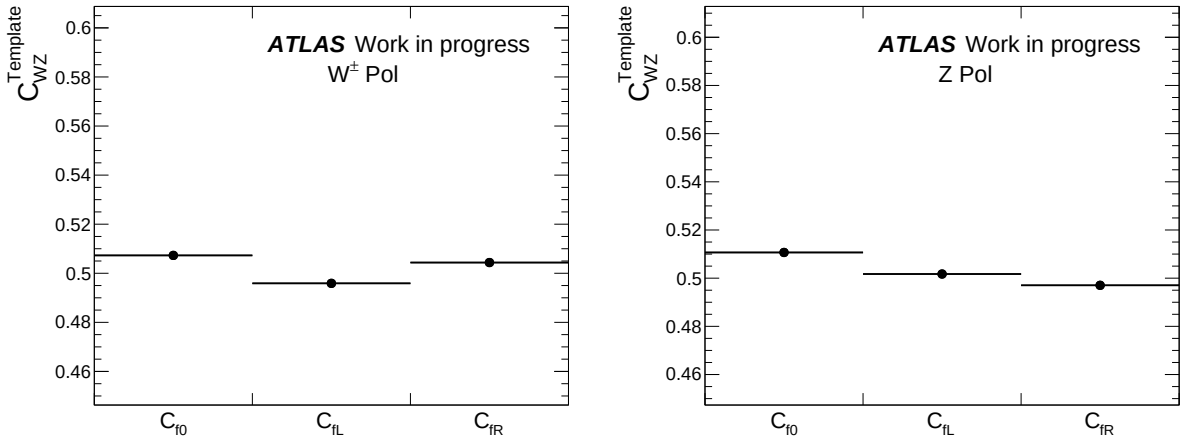

Figure 8.2 – *Template C_{WZ} factor to correct the polarisation fraction from the detector to the fiducial phase space for the $W^{\pm}$ polarisation measurement (left) and the Z polarisation measurement in $W^{\pm}Z$ events (right). The uncertainties contain the statistical uncertainties on the MC sample theory uncertainties from the QCD scale and the PDF.*

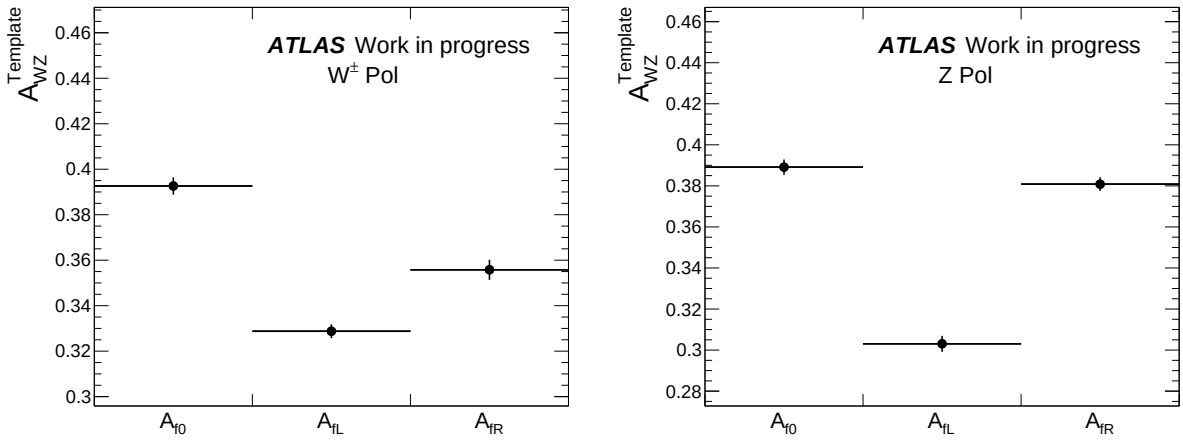

Figure 8.3 – *Template A_{WZ}^{fi} factor to correct the polarisation fraction from the fiducial to the total phase space for the $W^{\pm}$ polarisation measurement (left) and the Z polarisation measurement in $W^{\pm}Z$ events (right). The uncertainties contain statistical uncertainties on the MC sample and theory uncertainties from the QCD scale and the PDF.*

the integral over the templates at fiducial level before the detector simulation.

In analogy to the polarisation template C_{WZ}^{fi} factor to extrapolate from the measurement to the fiducial phase space, a template A_{WZ}^{fi} can be derived to extrapolate from the fiducial to the total phase space. The concept of the A_{WZ} factor has already been introduced in Section 7.1.3 and equation (7.6). The template A_{WZ}^{fi} factor is calculated as the fraction of events in the polarisation template in the total phase space which survive the fiducial cuts. Examples for the A_{WZ}^{fi} for the $W^{\pm}$ polarisation measurement and the Z polarisation measurement in $W^{\pm}Z$ events are shown in Figure 8.3.

To extrapolate the polarisation measurement result to the total phase space, the polarisation template integral in equations (8.1-8.2) is weighted by the inverse of the corresponding template $A_{WZ}^{fi} \times C_{WZ}^{fi}$ factor. This means that the denominator in equations (8.1-8.3) is replaced by the integral over the polarisation template at truth level in the total phase space. Therefore, the fit is the same as in the fiducial phase space, the only difference is the parametrization of the template normalization factors $\mu_i, i \in \{0, L, R\}$. For the polarisation fraction results in the total phase space f_i^{totPS} therefore applies

$$f_i^{\text{totPS}} = \frac{A_{WZ}}{A_{WZ}^{fi}} \times f_i^{fid}, \tag{8.6}$$

where A_{WZ} is the interpolation factor from the fiducial phase space in the total phase space for all polarisations and A_{WZ}^{fi} is the template A_{WZ}-factor.

To check the consistency of the method and the fit parametrization, a closure test has been performed. A new $\cos(\theta^*)$ distribution in MC has been created out of the sum of the polarisation templates, however, with modified relative integrals and therefore polarisation fractions. A fit was performed on this new modified $\cos(\theta^*)$ MC distribution and it was verified that the fractions extracted from the fit corresponded to the modified input fractions. The level of non-closure is about 0.005-1.5% in the fiducial phase space.

Kinematic cuts can introduce a bias in the polarisation templates due to the limited number of bins of the polarisation weights in p_{T} and the pseudorapidity, the statistical precision of the analytic fit or a dependence of the polarisation weights on other variables apart from the boson p_{T} and pseudorapidity. The sum of the polarisation templates and the simulated $\cos(\theta^*)$ distribution would differ as a consequence. At truth level, the difference is negligible, at reconstruction level, a difference of 1% can be observed. To evaluate the impact of this bias, the polarisation fractions are extracted at truth and reconstruction level and compared. The observed difference is within the statistical uncertainty.

8.1.2.3 Technical implementation

The fit is performed using the `HistFactory` Tool [120]. The tool provides a correct treatment of all statistical and systematic uncertainties. A Likelihood $L(\vec{\mu}, \vec{\theta}|N_{obs})$ is built out of all input variables and templates, nuisance parameters $\vec{\theta}$, constraints $G(\theta_k^{obs}; \theta_k; 1)$ and the set of parameters of interest $\vec{\mu}$, given the observed data N_{obs} [121]

$$L(\vec{\mu}, \vec{\theta}|N_{obs}) = \prod_{j=1}^{N} \frac{(\vec{\mu} \circ \vec{s_j}(\vec{\theta}) + B_j(\vec{\theta}))^{n_j}}{n_j!} \exp(-(\vec{\mu}\vec{s_j}(\vec{\theta}) + B_j(\vec{\theta}))) \prod_{k=1}^{n_{sys}} G(\theta_k^{obs}; \theta_k; 1), \tag{8.7}$$

where B_j is the number of background events in bin j, $\vec{s_j}$ are the signal templates in bin j, which are each multiplied by one parameter of interest, n_j is the number of entries in each bin and n_{sys} runs over the number of nuisance parameters. The fit yields the solution which maximizes the likelihood function given the observed data N_{obs}.

`HistFactory` is capable of incorporating shape and normalization uncertainties on the fit components and the statistical uncertainties as nuisance parameters. Statistical uncertainties on the data are taken into account with bin-to-bin variations. Statistical uncertainties on the fit components, the polarisation and background templates are treated using an approximative method which summarizes the statistical uncertainty of all components in one bin to one nuisance parameter.

A binned fit of the distributions in the discriminating variable $\cos(\theta^*)$ is performed. Signal templates representing the angular distributions of the boson decay products of polarised bosons are fitted to the data considering their yield and shape and the given background distributions. Note that the normalization of the background template is not estimated in the fit but given as an external constraint: the magnitude of the reducible background was estimated in Section 6.3.4 and of the irreducible background in Section 6.3.3. Overall systematic uncertainties are implemented affecting the rate of the background contributions.

Systematic uncertainties affecting the polarisation templates are considered by implementing alternative polarisation templates along with the nominal templates obtained by varying a parameter by its $\pm 1\sigma$ uncertainty. This allows to treat systematic uncertainties affecting the shape and normalization of the templates.

The ratio between two Likelihoods λ can be used as a discriminant between two hypotheses, where λ is defined as

$$\lambda(f_0) = \frac{L(\mu_0 = 0, \hat{\hat{\mu_L}}|_{\mu_0=0}, \hat{\hat{\mu_R}}|_{\mu_0=0}, \hat{\hat{\vec{\theta}}}|_{\mu_0=0})}{L(\hat{\mu_0}, \hat{\mu_L}, \hat{\mu_R}, \hat{\vec{\theta}})}, \tag{8.8}$$

where $\hat{\mu_L}$, $\hat{\mu_R}$, $\hat{\mu_0}$ and $\hat{\vec{\theta}}$ are the results of the parameters of interest and the nuisance parameters in the unconditional fit and $\hat{\hat{\vec{\theta}}}|_{\mu_0=0}$, $\hat{\hat{\mu_L}}|_{\mu_0=0}$ and $\hat{\hat{\mu_R}}|_{\mu_0=0}$ are the best-fit values of the conditional fit if fixing μ_0 to $\mu_0 = 0$.

In this measurement, the goal is to give evidence for the existence of the longitudinal polarisation in WZ diboson events. The two hypotheses are therefore $f_0 = 0$ and $f_0 > 0$ which correspond to $\mu_0 = 0$ and $\mu_0 > 0$. A test statistics, the one-sided profile likelihood ratio q_0, can be defined as

$$q_0 = \begin{cases} -2\ln\left(\frac{L(\mu_0=0, \hat{\hat{\mu_L}}|_{\mu_0=0}, \hat{\hat{\mu_R}}|_{\mu_0=0}, \hat{\hat{\vec{\theta}}}|_{\mu_0=0})}{L(\hat{\mu_0}, \hat{\mu_L}, \hat{\mu_R}, \hat{\vec{\theta}})}\right) & \mu_0 \geq 0 \\ 0 & \mu_0 < 0. \end{cases} \tag{8.9}$$

The distribution $f(q_0|\mu_0)$ for a given hypothesis for f_0 is a χ^2 distribution for one degree of freedom if the entries in the binned histogram follow a Gaussian probability distribution which is the true for the amount of statistics available in this measurement.

The level of agreement of data with an hypothesis H_0 can be expressed with the p-value. It is defined as the area under the distribution $f(q_0|\mu_0)$, given by the hypothesis H_0 (for instance $\mu_0^{H_0} = 0$, corresponding to the background-only hypothesis), above the observed value for q_0^{obs},

$$p = \int_{q_0^{obs}}^{\infty} f(q_0|\mu_0^{H_0}) dq_0. \tag{8.10}$$

The p-value can also be interpreted as the area under the normalized Gaussian distribution of the parameter of interest μ_0 given by hypothesis H_0 above some value $\tilde{\mu_0}$ which is the measured value or the value given my another model H_1.

Another estimator for the level of agreement between the data and a given hypothesis H_0, which is frequently used in High Energy Physics, is the significance Z. It is defined by means of the p-value:

$$Z = \Phi^{-1}(1 - p), \tag{8.11}$$

where Φ^{-1} is the inverse of the cumulative distribution of the standard Gaussian. Illustratively, the significance is the number of standard deviations of a value $\tilde{f}_0 \neq 0$ above the assumed value for f_0, for instance $f_0 = 0$.

For a data sample which is large enough to assume that the number of entries in bins follows a Gaussian distribution, the significance can be written as $Z = \sqrt{q_0}$, thus

$$Z = \sqrt{-2\ln\left(\frac{L(\mu_0 = 0, \hat{\hat{\mu}}_L|_{\mu_0=0}, \hat{\hat{\mu}}_R|_{\mu_0=0}, \hat{\hat{\vec{\theta}}}|_{\mu_0=0})}{\mathrm{L}(\hat{\mu}_0, \hat{\mu}_L, \hat{\mu}_R, \hat{\vec{\theta}})}\right)}. \tag{8.12}$$

8.2 Predictions on the polarisation fractions

Prediction on the polarisation fractions in the fiducial (total) phase space are obtained by fitting the polarisation templates to the $\cos(\theta^*)$ distribution at truth level in the fiducial (total) phase space. The fit in the total phase space can either be performed using the polarisation templates or the analytical expressions in equation (3.11) or (3.13). The predictions are affected by statistical uncertainties of the MC sample and by modelling uncertainties. Statistical uncertainties are taken care of by `HistFactory`.

Modelling uncertainties due to missing higher orders in QCD and due to the modelling of the PDF are estimated by fitting the $\cos(\theta^*)$ distribution obtained with the up or down variation by the 1σ PDF uncertainty or QCD scale variation.

The analytic functions are not valid in the fiducial phase space. The polarisation templates obtained by reweighting the MC to pure polarisation states are fit to the modified $\cos(\theta^*)$ distribution. To be fully correct, the polarisation templates would need to be recreated: the polarisation template can change if the PDF or the QCD scales have been changed. This means that the polarisation fractions would need to be re-extracted and a new polarised boson MC sample would have to be created by reweighting by the newly extracted fractions. However, for reasons of simplicity, the nominal Powheg+Pythia templates are used as approximation in the fiducial phase space. This approximation is validated first by comparing the theory uncertainties extracted in the total phase space using the approximation of the template fit of the nominal templates, with those extracted using the analytic fit, which corresponds to the exact procedure. The two procedures yield very similar results for the uncertainties. QCD scale and PDF uncertainties on the predictions are combined by linear addition following the procedure in [122].

A complementary model is provided by MATRIX. MATRIX is able to calculate differential cross sections up to NNLO in QCD and therefore provides an estimate for the impact of higher orders on the polarisation prediction. In MATRIX, also different QCD scales and a different PDF are implemented. However, the MATRIX framework returns histograms and, in contrast to Powheg+Pythia, does not produce single events. Therefore, the reweighting procedure to obtain the polarisation templates is not applicable to MATRIX. Instead, the $\cos(\theta^*)$ distribution is fitted with Powheg+Pythia templates. Uncertainties from QCD scale variations are also extracted.

In both, the MATRIX and the Powheg+Pythia models, the G_μ electroweak scheme is implemented, the electroweak parameters are related to the precisely measured values of the W and Z boson masses m_W and m_Z and the Fermi coupling G_F. For the polarisation measurement, impact is especially expected from the weak mixing angle $\sin^2(\theta_W)$, which determines the mixing of the B boson of $U(1)_Y$ and the third component of the W^3-field

	$f_L - f_R$		$G_\mu \to$ Eff
	$\sin^2(\theta_W^{Eff})$	$\sin^2(\theta_W^{G_\mu})$	$f_L - f_R$
W^+ in W^+Z	0.0952	0.0867	0.008
W^- in W^-Z	-0.0677	-0.0653	-0.002
$W^\pm$ in $W^\pm Z$	0.0292	0.0251	0.004
Z in W^+Z	-0.255	-0.268	0.014
Z in W^-Z	0.0478	0.0992	-0.05
Z in $W^\pm Z$	-0.132	-0.120	-0.012

Table 8.2 – *Fit results of the template fit in the fiducial phase space to* $\cos(\theta^*)$ *distributions simulated using the* MCFM *MC with two different weak mixing angles,* $\sin^2(\theta_W^{G_\mu}) = 0.2229$ *("*G_μ*") and* $\sin^2(\theta_W^{Eff}) = 0.23152$ *("Eff"), implemented.*

of $SU(2)_L$. This impacts the coupling of the Z to left- and right-handed fermions. In the G_μ scheme, a value of $\sin^2(\theta_W) = 1 - \frac{m_W^2}{m_Z^2} = 0.2229$ has been implemented, the measured value is $\sin^2(\theta_W) = 0.23129$ [33].

The implemented value of the weak mixing angle is expected to have an impact on the prediction of $f_L - f_R$. To evaluate its impact and correct the MATRIX and POWHEG+PYTHIA predictions, studies with the parton-level Monte-Carlo program MCFM are performed [123, 124]. In MCFM, the value of the weak mixing angle can be changed while leaving all other parameters unchanged. Table 8.2 shows the change in the value of $f_L - f_R$ if going from a weak mixing angle of $\sin^2(\theta_W^{G_\mu}) = 0.2229$ to $\sin^2(\theta_W^{Eff}) = 0.23152$. The latter is denoted as "effective scheme" ("Eff") in the Table 8.2. These values are added to the MATRIX and POWHEG+PYTHIA predictions for $f_L - f_R$. However, the correction does not have a large impact.

The uncertainties on the theory predictions from POWHEG+PYTHIA are shown in Table 8.3 on the predictions in the fiducial phase space. The impact of the theory uncertainties from the QCD scale and the PDF on the predictions are small, the impact of the total theory uncertainty from the QCD scales and the PDF is smaller or of the same magnitude than the MC statistical uncertainty. The QCD scale uncertainty is in most cases the dominant theory uncertainty. In almost all cases, the impact of the MC statistics is the dominant uncertainty on the prediction. On f_0, the total relative uncertainties are of the order of 1-2% in the fiducial phase space. On $f_L - f_R$, total relative uncertainties on the predictions range between 3.9-44% in the fiducial phase space, depending on the boson polarisation measured. Note that the central value of $f_L - f_R$ varies much among the measurements of the different boson polarisations and due to the fact that it is the difference between two fractions, it can also become quite small which makes the relative uncertainty seem very large. The order of magnitude of the absolute uncertainties is however similar as can be seen in Table 8.3.

The predictions provided by MATRIX and their uncertainties are shown in Table 8.4. For MATRIX, the dominant uncertainty is the QCD scale uncertainty. Note that, however, the statistical uncertainty is about 6-7 times smaller on the MATRIX prediction than on the POWHEG+PYTHIA prediction.

In Table 8.5, the predictions for the polarisation fractions in the fiducial phase space by POWHEG+PYTHIA and MATRIX are compared. Total uncertainties are given on both predictions: QCD scale, PDF and MC statistical uncertainties on the POWHEG+PYTHIA

	Absolute Uncertainties						prediction
	QCD	PDF	Theory, total	Stat.	Total unc.	Total unc. [%]	Powheg+Pythia
W^+, f_0	0.0008	0.00022	0.0010	0.004	0.004	1.8	0.233 ± 0.004
W^+, $f_L - f_R$	0.0018	0.0004	0.0022	0.0028	0.004	3.9	0.091 ± 0.004
W^-, f_0	0.0008	0.00032	0.0011	0.005	0.005	2.0	0.245 ± 0.005
W^-, $f_L - f_R$	0.0030	0.0015	0.004	0.0034	0.006	8.9	-0.063 ± 0.006
Z (in W^+Z), f_0	0.0008	0.0005	0.0014	0.004	0.004	1.8	0.225 ± 0.004
Z (in W^+Z), $f_L - f_R$	0.008	0.0014	0.010	0.019	0.021	7.2	-0.297 ± 0.021
Z (in W^-Z), f_0	0.0008	0.0004	0.0012	0.005	0.005	2.1	0.235 ± 0.005
Z (in W^-Z), $f_L - f_R$	0.0010	0.00009	0.0011	0.023	0.023	44	0.052 ± 0.023
$W^\pm$ (in $W^\pm Z$), f_0	0.00041	0.000011	0.0004	0.0031	0.0031	1.3	0.2376 ± 0.0031
$W^\pm$ (in $W^\pm Z$), $f_L - f_R$	0.00006	0.0005	0.0005	0.0022	0.0022	7.7	0.0289 ± 0.0022
Z (in $W^\pm Z$), f_0	0.0008	0.0005	0.0013	0.0030	0.0033	1.4	0.2294 ± 0.0033
Z (in $W^\pm Z$), $f_L - f_R$	0.005	0.0010	0.006	0.015	0.016	10	-0.156 ± 0.016

Table 8.3 – *Contributions of statistical and modelling uncertainties on the predicted polarisation fractions in the fiducial phase space obtained with* Powheg+Pythia. *On the prediction in the last column, total uncertainties, consisting of the theory and statistical uncertainties are given, the predicted central value of $f_L - f_R$ has been shifted by the values given in Table 8.2 to correct for the implemented value of the weak mixing angle which is given in the G_μ scheme in* Powheg+Pythia.

	f_0 MATRIX prediction	$f_L - f_R$ MATRIX prediction
W^+	0.2448 ± 0.0006 (stat.) ± 0.0008 (QCD)	0.0868 ± 0.0004 (stat.) ± 0.0013 (QCD)
W^-	0.2651 ± 0.0006 (stat.) ± 0.0014 (QCD)	-0.0342 ± 0.0004 (stat.) ± 0.004 (QCD)
$W^\pm$	0.2506 ± 0.0004 (stat.) ± 0.0005 (QCD)	0.03747 ± 0.00031 (stat.) ± 0.0010 (QCD)
Z in W^+Z	0.2401 ± 0.0006 (stat.) ± 0.0012 (QCD)	-0.2624 ± 0.0031 (stat.) ± 0.008 (QCD)
Z in W^-Z	0.2389 ± 0.0006 (stat.) ± 0.0014 (QCD)	0.0468 ± 0.0028 (stat.) ± 0.0020 (QCD)
Z in $W^\pm Z$	0.2398 ± 0.0004 (stat.) ± 0.0013 (QCD)	-0.1354 ± 0.0021 (stat.) ± 0.006 (QCD)

Table 8.4 – *Prediction for the polarisation fractions provided by* MATRIX. *The contributions from QCD scale uncertainties and MC statistical uncertainties are shown separately. Note that the predicted polarisation fractions have been shifted by the values given in Table 8.2 to correct for the difference between the measured weak mixing angle and the one implemented in* MATRIX.

prediction and QCD scale and MC statistical uncertainties on the MATRIX prediction. Powheg+Pythia and MATRIX yield very similar predictions for both polarisation fractions, f_0 and $f_L - f_R$. The discrepancy is largest for W^- polarisation. The difference between the predictions is mostly attributed to the different precision in QCD of the two simulations: the MATRIX prediction is calculated up to NNLO while the Powheg+Pythia prediction includes only calculations up to NLO. It can be assumed from the comparison between the two simulations that missing higher orders in QCD do not seem to have a high impact on the polarisation fractions.

	f_0		$f_L - f_R$	
	Powheg+Pythia	MATRIX	Powheg+Pythia	MATRIX
W^+	0.233 ± 0.004	0.2448 ± 0.0010	0.091 ± 0.004	0.0868 ± 0.0014
W^-	0.245 ± 0.005	0.2651 ± 0.0015	-0.063 ± 0.006	-0.034 ± 0.004
$W^\pm$	0.2376 ± 0.0031	0.2506 ± 0.0006	0.0289 ± 0.0022	0.0375 ± 0.0011
Z in W^+Z	0.225 ± 0.004	0.2401 ± 0.0014	-0.297 ± 0.021	-0.262 ± 0.009
Z in W^-Z	0.235 ± 0.005	0.2389 ± 0.0015	0.052 ± 0.023	0.0468 ± 0.0034
Z in $W^\pm Z$	0.2294 ± 0.0033	0.2398 ± 0.0014	-0.156 ± 0.016	-0.135 ± 0.006

Table 8.5 – *Summary of the predictions provided by* POWHEG+PYTHIA *and* MATRIX *in the fiducial phase space. Uncertainties on* POWHEG+PYTHIA *contain statistical uncertainties from the MC sample statistics and theory uncertainties from the PDF and QCD scale, uncertainties on the* MATRIX *prediction contain statistical uncertainties and QCD scale uncertainties. Note that the predicted central value of $f_L - f_R$ has been shifted by the value given in Table 8.2 to correct for the implemented value of the weak mixing angle which is given in the G_μ scheme in both simulations.*

8.3 Measurement optimization studies

8.3.1 Studies on the histogram binning

Shape information help the fit to discriminate between the different polarisation templates and background. In case of finer binning, more shape information is available which could lead to a larger discriminating power of the templates. However, the templates statistics have to be taken into account, they are a limiting factor for finer binning.

The goal of the measurements is to proof that longitudinal boson polarisation exists in diboson events, $f_0 > 0$. Studies on the histogram binning are therefore performed to optimize the significance for $f_0 > 0$ given the data available.

Asimov datasets with different histogram binnings are created from simulated WZ signal events with the expected statistical precision in data, the MC predictions for irreducible background and the data-driven reducible background estimate. A fit to these Asimov datasets are performed taking into account uncertainties on the background normalization, the statistical uncertainties of the dataset and all fit components, templates and background predictions. The fact that object and theory uncertainties only have a minor impact on the overall uncertainties is anticipated here, proof is given later.

Several binning options are implemented: The $\cos(\theta^*)$ distributions are divided in 5, 10, 15 and 20 bins of equal width. These options are shown in Figure 8.4 for W^+ polarisation. Options with variable bin width are also tested, a finer binning in regions which are more sensitive to polarisation effects could lead to a better discrimination between the components. Two variable bin width options test a finer binning around $\cos(\theta^*) = \pm 1$, a region which is expected to be very sensitive to polarisation effects, another options tries whether a gain in sensitivity for longitudinal polarisation can be obtained by implementing a finer binning around $\cos(\theta^*) = 0$. Figure 8.5 illustrates these options with variable bin width for the W^+ polarisation measurement.

Table 8.6 lists the expected significances for longitudinally polarised W^+ bosons and for longitudinally polarised Z bosons in W^+Z events for the different binning options.

bin option	significiance of $f_0 > 0$ in W^+	significiance of $f_0 > 0$ in Z (in $W^+Z events$)
5 bins	2.71	4.31
10 bins	2.93	4.59
15 bins	2.96	4.65
20 bins	2.98	4.66
binvar 1	2.97	4.63
binvar 2	2.93	4.60
binvar 3	2.98	4.64

Table 8.6 – *Expected significance for longitudinal boson polarisation for the different binning options. In the first column, the expected significances for W^+ polarisation are shown, in the second column, the significances for Z polarisation in W^+Z events are displayed.*

Following conclusions can be drawn from Table 8.6:

- No gain in significance is expected if the $\cos(\theta^*)$ distribution is divided into bins with variable width. The significances are all comparable to the significances obtained by fitting bins with equal width, only the number of bins seem to matter. Although the option "binvar 2" with finer binning around $\cos(\theta^*) = 0$ has less sensitivity than

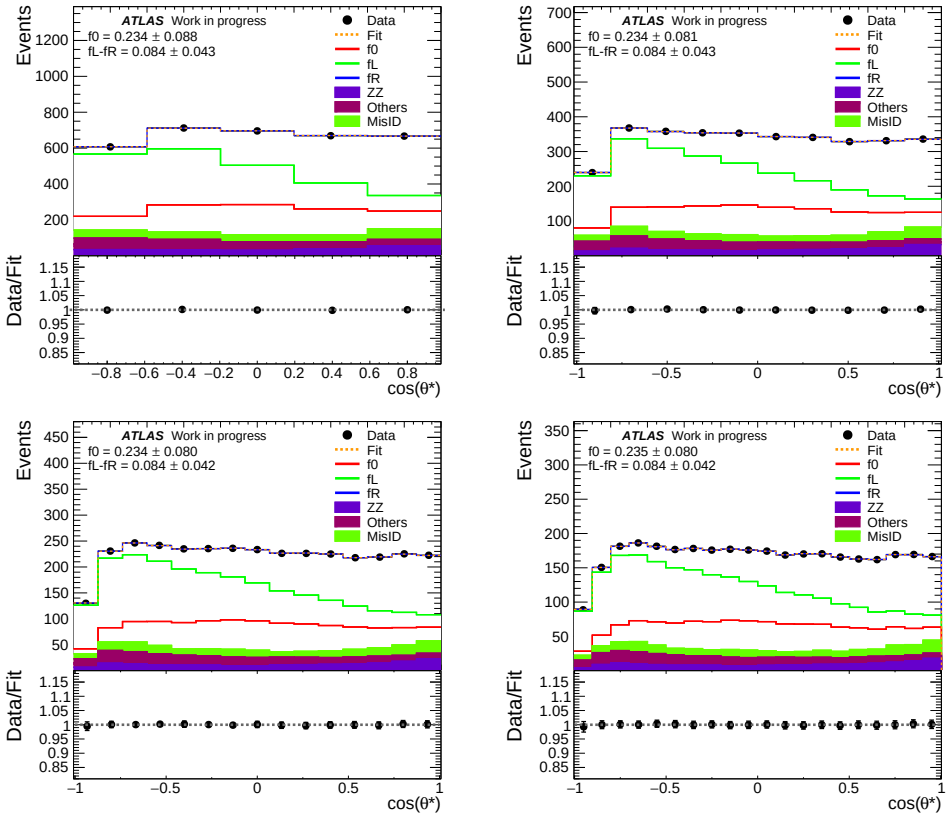

Figure 8.4 – *Fits to* $\cos(\theta^*)$ *distribution for the* W^+ *with different number of bins of equal width. Note that the distribution labelled as "Data" shows the expected* WZ *signal with all background components added. The figures from top to bottom, left to right display the following binning options: 5 bins, 10 bins, 15 bins and 20 bins.*

the option "binvar 1" with the same number of bins than "binvar2" but finer binning around $\cos(\theta^*) = \pm 1$, differences in sensitivity in certain regions of the $\cos(\theta^*)$ can at this stage not be confirmed with absolute certainty.

- In case of equal bin width, one can state that the higher the number of bins, the higher the expected significance for $f_0 > 0$.
- The option with 20 bins of equal width yields the highest expected significance for $f_0 > 0$.
- Going from 15 to 20 bins does not increase the expected significance by much. Options with more bins are therefore not tested as the increase in sensitivity is not expected to be of any importance. Furthermore, the limited template statistics might impact the result at some point.

According to Table 8.6, the highest significance can be achieved by dividing the $\cos(\theta^*)$ distribution in 20 bins of equal width.

The impact of object systematics and theory uncertainties is also tested. The $\cos(\theta^*)$ distribution divided in 10 and 20 bins is fitted with all object systematic and theory and modelling uncertainties included. The expected significance for $f_0 > 0$ is calculated to check whether the conclusion from Table 8.6 still holds. The result is shown in Table 8.7.

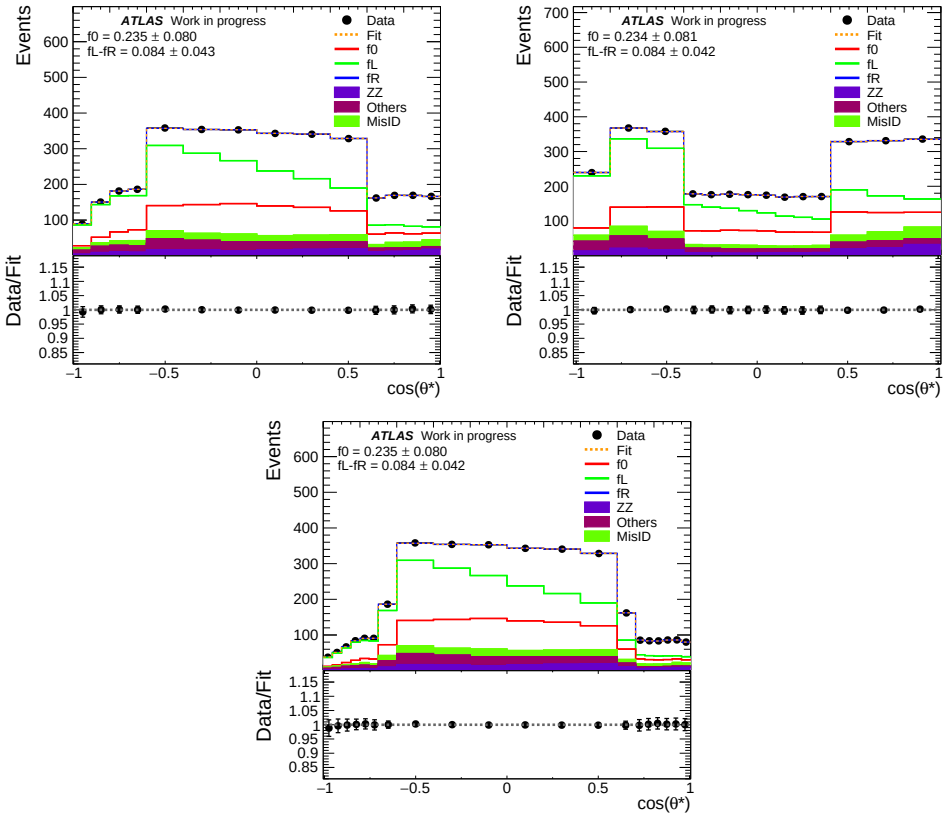

Figure 8.5 – *Fits to* $\cos(\theta^*)$ *distribution for the* W^+ *with different number of bins of variable width. Note that the distribution labeled as "Data" shows the expected* WZ *signal with all background components added. The figures on the top left and on the bottom show options with finer binning around* $\cos(\theta*) = \pm 1$ *with 14 and 20 bins, respectively. The distribution on the top right is binned more finely around* $\cos(\theta^*) = 0$ *and has 14 bins.*

Comparing the results in Table 8.7 with the expected significance results for 10 and 20 bins in Table 8.6, the conclusion that the object uncertainties indeed have a small impact on the uncertainty can be drawn.

bin option	significance of $f_0 > 0$ in W^+	significance of $f_0 > 0$ in Z (in W^+Z)	significance of $f_0 > 0$ in $W^\pm$
10 bins	2.93	4.51	3.75
20 bins	2.96	4.56	3.80

Table 8.7 – *Expected significances for the longitudinal boson polarisation obtained with the 10 and 20 bin options calculated considering the full systematics. In the first column, the expected significances for longitudinal* W^+ *polarisation are shown, in the second column, the significances for longitudinal* Z *polarisation in* W^+Z *events and in the third column, the expected results for* W *longitudinal polarisation in* $W^\pm Z$ *events.*

The fit is performed on 20 bins of equal width in the following.

8.3.2 Discriminating variable for W polarisation measurement

It will now be checked whether the sensitivity for longitudinal W polarisation can be improved by performing the measurement in the transverse plane only. The reconstruction of the longitudinal neutrino momentum can be avoided by projecting the angle $\cos(\theta^*)$ in the transverse plane. The variable $\cos(\theta^*_{2D})$ has already been introduced in Section 8.1.1. The expected significances for W^+ polarisation obtained by fitting on $\cos(\theta^*_{2D})$ and $\cos(\theta^*)$ considering the full set of systematics except for theory and modelling uncertainties, are shown in Table 8.8. In case of 20 bins, the fit to $\cos(\theta^*)$ yields a higher significance. It has been decided to continue using $\cos(\theta^*)$ as a discriminating variable.

bin option	W^+ Polarisation, 3D	W^+ Polarisation, 2D
10 bins	2.91	2.24
20 bins	2.96	2.26

Table 8.8 – *Expected significance for longitudinal boson polarisation for the 10 and 20 bin options calculated considering the full systematics. In the first column, the expected significances for W^+ polarisation taking into account transverse and η coordinates are shown, the second column lists the significances for W^+ polarisation considering only the information in the transverse plane ($\cos(\theta^*_{2D})$).*

8.4 Uncertainties on the polarisation measurement

Several sources of uncertainties affect the polarisation measurement. Statistical uncertainties from the limited data, polarisation template and background statistics are implemented as described in Section 8.1.2.3.

Overall systematic uncertainties are implemented affecting the rate of the background contributions. These uncertainties are given as an external constraint, their magnitude is extracted elsewhere: The estimation of the uncertainties on the irreducible background has been presented in Section 6.3.3. A 40% uncertainty is assumed on the reducible background considering the shape agreement of the results of the two complementary reducible background estimation methods described in Section 6.4.

Independent auxiliary measurements constrain object systematics like for example on the electron identification efficiency scale factor measurement presented in Section 5, an uncertainty on the pile-up reweighting, object calibration and energy scales, to name a few. These measurements are provided externally by the ATLAS combined performance groups. These so-called object uncertainties affect the templates and can distort their shapes as well as their normalization. The nominal template together with the templates representing the $\pm 1\sigma$ variations of a particular object uncertainty are passed to `HistFactory`. That way, the impact of the dominant object uncertainties is assessed. A set of object uncertainties which are expected to have a small impact as a single uncertainty, could sum up and have a large impact. Therefore, the remaining subdominant object uncertainties are not neglected but merged. Object uncertainties affecting the same object, either electrons, muons, jets or E/γ clusters, are grouped, and for each group, a combined $\pm 1\sigma$ template variation is created in the following way: In each polarisation template bin, the differences between the nominal template and the up or down variations caused by each merged source of systematics are

evaluated. The square root of the squared sum of all these differences is added to the nominal bin content of the templates to obtain the $+1\sigma$ template or subtracted to obtain the -1σ template. That way, the merged uncertainties are treated fully correlated. This approach is conservative but allows for a simplification of the fit.

The decision of which object uncertainty is treated separately or merged is based on an estimator. This estimator is the relative difference between the integral of the nominal histogram and the integral of the templates of the up or down variations with respect to the integral of the nominal template. All variations which have an impact of larger than 0.05% on the template integral are taken into account as single uncertainties in the fit, all others are merged. In total, twenty-three object uncertainties are treated as single uncertainties, the remaining subdominant seventy-five uncertainties are merged.

The polarisation templates are modelled with MC. Higher-order effects and uncertainties due to the limited knowledge of the PDF can distort the shape of these templates. Higher order effects are estimated by evaluating the impact of up and down variations of renormalization and factorization scale. Polarisation templates representing the impact of QCD scale variations by ± 1 σ are passed to the fit as template variations. Alternative templates are created by varying the PDF according to the description in Section 3.2.3. The alternative templates representing variations of the QCD scale and the PDF are scaled to the same truth level cross section at fiducial level as the nominal template to account for shape as well as acceptance differences.

A common polarisation template modelling uncertainty can be evaluated by implementing an alternative model for the template as systematic variation. This alternative model is provided by MC@NLO. The MC@NLO model differs to POWHEG+PYTHIA especially in the following respects: In MC@NLO, a value of $\sin^2(\theta_W) = 0.2311$ is implemented which is much closer to the measured value of $\sin^2(\theta_W) = 0.23129$ [33] than the weak mixing angle implemented in the G_μ scheme. The MC@NLO prediction does not include the Z/γ^* interference term in contrast to POWHEG+PYTHIA [125]. The polarisation is different for the γ^* and its interference with the Z. As a consequence, the polarisation fractions f_L and f_R are a function of the invariant mass of the two leptons $m_{\ell\ell}$ assigned to the Z in POWHEG+PYTHIA, whereas in MC@NLO, f_L and f_R are constant in $m_{\ell\ell}$. This would impact especially the prediction in the total phase space due to the larger $m_{\ell\ell}$ window of $66 < m_{\ell\ell} < 116$ GeV. Furthermore, the two MC generators provide different models for the parton shower and hadronization and a different QCD scale is implemented.

The same Monte Carlo reweighting procedure is applied as described in Section 3.3.5 on MC@NLO and new templates representing polarised bosons are created.

To implement this systematics, the difference between the nominal POWHEG+PYTHIA template is evaluated and added and subtracted from the nominal template in order to symmetrize the uncertainty on the modelling. The MC@NLO has been scaled to the same truth level cross section at fiducial level as the nominal POWHEG+PYTHIA template to account for shape and acceptance differences. The comparisons of the three POWHEG+PYTHIA and MC@NLO polarisation templates for the $W^\pm$ inclusive polarisation measurement are shown in Figure 8.6 in the fiducial phase space at reconstruction level. Note that the statistical uncertainty is larger in case of the MC@NLO sample. However, the statistical uncertainties on the systematic template variations are not considered in the fit, therefore, statistical fluctuations of the templates would be taken into account in the systematic uncertainty. To eliminate the effect of the statistical uncertainty, the contribution of the statistical uncertainty to the absolute difference between the

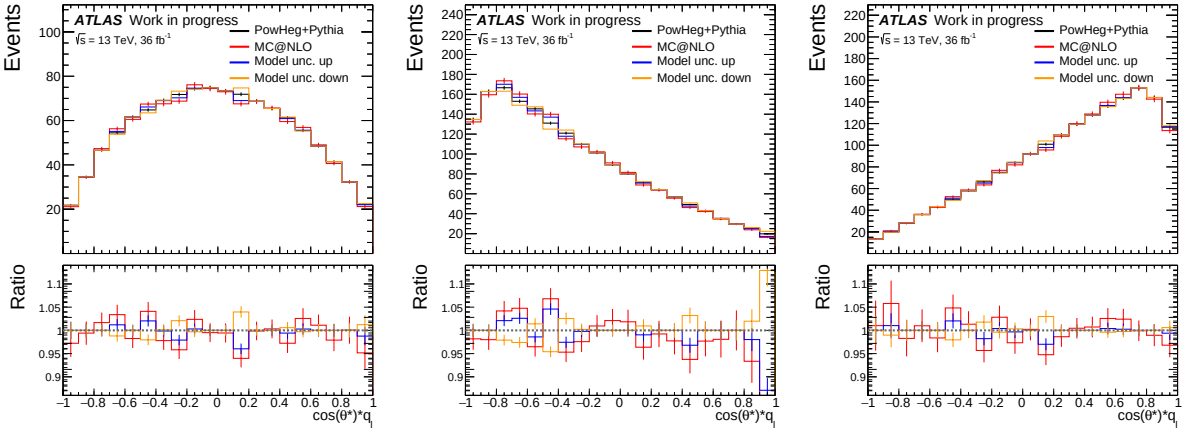

Figure 8.6 – *Comparison of the polarisation templates provided by* Powheg+Pythia *(black) and* MC@NLO *(red) in the fiducial phase space at reconstruction level. Note that the* MC@NLO *and* Powheg+Pythia *templates have been normalized to the same fiducial truth level cross section. The effect of the MC statistical uncertainties has been subtracted from the difference between the* Powheg+Pythia *and the* MC@NLO *polarisation templates (see text) and symmetrized (orange and blue histograms). On the left, the template representing longitudinal polarised $W^{\pm}$ bosons is shown, in the center, the template for left-handed and on the right, the template for right-handed polarised W bosons.*

Powheg+Pythia and the MC@NLO polarisation templates is subtracted from each bin. The content in each bin of the systematic templates representing the modelling uncertainty is calculated as follows:

$$e_{sys,i}^{\text{model},\pm} = \begin{cases} e_i^{\text{nominal}} \pm sgn(e_i^{diff}) \cdot (\sqrt{(e_i^{diff})^2 - \text{stat}_i^2}) & \text{if } e_i^{diff} \geq \text{stat}_i \\ e_i^{\text{nominal}} & \text{else,} \end{cases}$$

(8.13)

where stat_i is the statistical uncertainty in bin i, e_i^{nominal} is the bin content of the nominal Powheg+Pythia template and e_i^{diff} is the difference between the bin contents of the Powheg+Pythia and MC@NLO templates. The difference between the template is either added or subtracted to the nominal template to symmetrize the systematic variation. This is expressed by the $\pm$ sign in equation 8.13.

The expected impact of each source of uncertainty in the fit to Asimov pseudo-data and its contribution to the total uncertainty is evaluated. Table 8.9 shows the expected contribution of the absolute uncertainties to the $W^{\pm}$ polarisation measurement uncertainty on the left and the expected contribution of the absolute uncertainties to the total uncertainty on the Z inclusive polarisation measurement on the right in the fiducial phase space. From these tables, it becomes clear that the measurement precision of the polarisation fractions f_0 and $f_L - f_R$ will be dominated by statistics. N_{tot}, the normalization parameter, is dominated by systematics. The normalization parameter gives a complementary estimate of the W^+Z, W^-Z or the inclusive fiducial cross section. Therefore, the impact of the object uncertainty contributions should largely correspond to those of the inclusive measurement. The parameter N_{tot} seems to largely "absorb" the systematic uncertainties in

the measurement. Object systematics are of minor importance for f_0 and $f_L - f_R$ which can be explained by the fact that the polarisation fractions f_0 and $f_L - f_R$ correspond to cross-section ratios and a cancellation of uncertainties in the ratios is therefore possible. Also, the uncertainty on the luminosity is expected to cancel in a cross section ratio.

Dominant contribution to the systematic uncertainty on the longitudinal polarisation fraction f_0 and N_{tot} are expected to issue from the fake background. On $f_L - f_R$, the modelling uncertainty is expected to be the dominant systematic uncertainty in case of the $W^{\pm}$ polarisation measurement and the fake background normalization in case of the Z polarisation measurement in $W^{\pm}Z$ events.

	f_0	f_{LR}	σ_{fid}
Absolute Uncertainties			
Electrons	0.0024	0.0005	120
Muons	0.0017	0.0018	140
Jets	0.0027	0.0009	50
Pileup	0.005	0.0002	110
Misid. lepton background	0.031	0.0022	340
ZZ background	0.009	0.00022	100
Other backgrounds	0.0008	0.0007	130
QCD scale	< 0.0001	0.0014	< 1
PDF	< 0.0001	0.0009	< 1
Modelling	0.004	0.007	3
Total systematics	0.034	0.008	440
Luminosity	0.0015	< 0.0001	220
Statistics	0.06	0.032	150
Total	0.07	0.033	500
Total [rel.]	28	130	5.4

	f_0	f_{LR}	σ_{fid}
Absolute Uncertainties			
Electrons	0.005	0.0022	110
Muons	0.0009	0.004	140
Jets	0.0009	0.004	40
Pileup	0.0018	0.008	120
Misid. lepton background	0.007	0.01	340
ZZ background	0.0005	0.0011	100
Other backgrounds	0.0022	0.0016	130
QCD scale	< 0.0001	0.008	< 1
PDF	< 0.0001	< 0.0001	< 1
Modelling	0.00032	0.005	17
Total systematics	0.009	0.017	440
Luminosity	< 0.0001	< 0.0001	220
Statistics	0.04	0.16	150
Total	0.04	0.16	510
Total [rel.]	16	110	5.6

Table 8.9 – *Summary of the expected impact of statistical, object, theory, modelling and background uncertainties on the $W^{\pm}$ polarisation measurement (left) and the Z polarisation measurement in $W^{\pm}Z$ events (right) on each parameter of interest in the fit to Asimov pseudo-data. In the last line, the expected total relative uncertainty is given, the single contributions are given as absolute uncertainties.*

8.5 Expected significance for the measurement of W and Z longitudinal polarisation

All expected significances for $f_0 > 0$ evaluated with Asimov pseudo-data along with the expected statistical and systematic uncertainties are listed in Table 8.10. To calculate the expected significances in Table 8.10, all uncertainties are considered.

In a hadron collider, W^+Z events are expected to have a higher cross section than W^-Z events, while the contribution of the fake background is similar. It is therefore not surprising to have a larger significance for boson polarisation in W^+ events. A significance of close to 3 σ is expected for longitudinal polarisation in W^+ events. The expected significance to measure longitudinal Z polarisation exceeds 3 σ in W^+Z as well as in W^-Z events. The significance of former is even expected to be close to 5 σ.
For the inclusive W and Z polarisation measurement in $W^{\pm}$ events, evidence for longitudinal polarisation is expected for the W and a measurement is expected for longitudinal Z polarisation.

Measurement	significance for $f_0 > 0$	$\pm\Delta f_0^{stat.}$ $\pm\Delta f_0^{sys.}$	Δf_0^{tot}
W^+ Pol.	2.96	$\pm$ 0.076 (stat.) $\pm$ 0.028 (sys.)	0.08
W^- Pol.	2.69	$\pm$ 0.086 (stat.) $\pm$ 0.040 (sys.)	0.09
$W^\pm$ Pol.	3.80	$\pm$ 0.058 (stat.) $\pm$ 0.034 (sys.)	0.07
Z Pol. (in W^+Z)	4.56	$\pm$ 0.049 (stat.) $\pm$ 0.0088 (sys.)	0.05
Z Pol. (in W^-Z)	4.10	$\pm$ 0.057 (stat.) $\pm$ 0.011 (sys.)	0.06
Z Pol.	6.07	$\pm$ 0.037 (stat.) $\pm$ 0.0088 (sys.)	0.04

Table 8.10 – *Expected significances of the boson polarisation measurements and the expected absolute statistical, systematic and total uncertainties.*

The second column of Table 8.10 shows the expected statistical and systematic uncertainties. It becomes clear that the measurement result of f_0 will be dominated by statistical uncertainties.

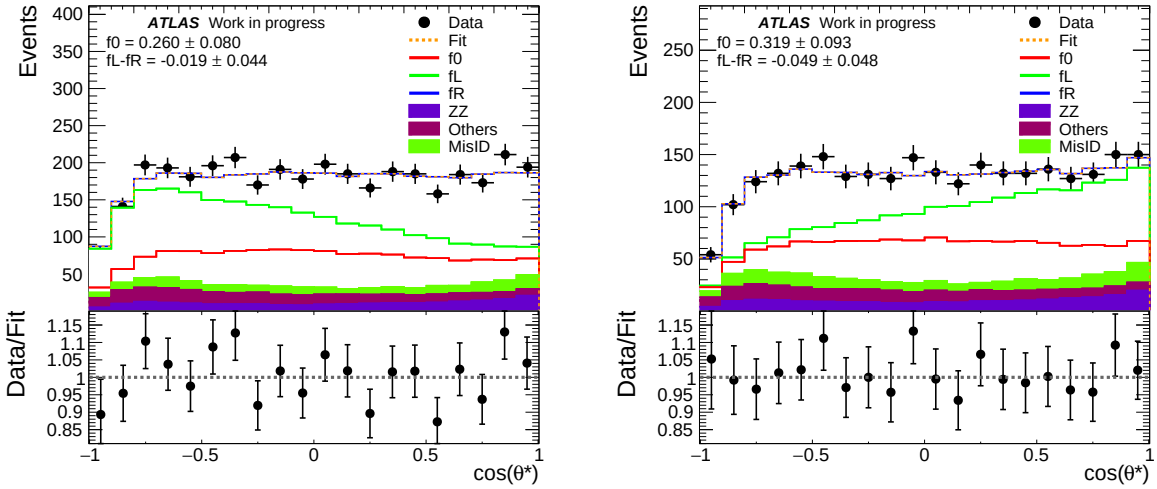

Figure 8.7 – *Fit to the* $\cos(\theta^*)$ *distribution in data to extract the W-polarisation (W^+-polarisation: left, W^--polarisation: right). The resulting polarisation fractions* f_0 *and* $f_L - f_R$ *along with their total uncertainties are displayed on the figure. All background distributions and fitted polarisation templates are stacked in the plot. The ratio plot illustrates the agreement of the fit with data.*

8.6 Polarisation measurement results

8.6.1 Polarisation fit and uncertainties

The fit is performed on the $\cos(\theta^*)$ distribution in data on 20 bins of equal width inclusively over p_{T} and the pseudorapidity. Polarisation results are obtained for W^+ and W^- bosons, the corresponding fits are shown in Figure 8.7. The Z boson polarisation is measured separately in W^+Z and W^-Z events, the fits are displayed in Figure 8.8. To gain in sensitivity, a combined measurement of the $W^\pm$ polarisation is performed as described in Section 8.1.1. The inclusive Z polarisation is also extracted. Both fits are shown in Figure 8.9.

The uncertainties on the results of the $W^\pm$ and the Z polarisation in $W^\pm$ events are shown in Table 8.11. They correspond well with the expected uncertainties presented in Section 8.4. The difference in relative uncertainties on $f_L - f_R$ can be explained by the different central values on $f_L - f_R$ in the measurements with respect to the predictions. However, the expected absolute uncertainties on the measured value of $f_L - f_R$ corresponds well with the predicted absolute uncertainty. Note that, as $f_L - f_R$ is a difference between two polarisation fractions, it can become small if the right- and left-handed polarisation fractions are similar.

The relative uncertainties on N_{tot} agree well with the uncertainties on the measured cross section in Table 7.3. The statistical and the luminosity uncertainties agree quite well. The overall systematic uncertainty is larger. Object uncertainties and the irreducible background uncertainties are of a similar order of magnitude, however, the uncertainty on the reducible background is larger on N_{tot} in the polarisation measurement: its contribution to the cross section measurement is 1.9% whereas it is 3.5% and 3.6% in case of the W and Z polarisation measurement. This has two reasons: first, the uncertainty on the reducible background assumed for the fit is more conservative than in the cross section measurement as possible shape discrepancies are taken into account. Instead of the 30% uncertainty

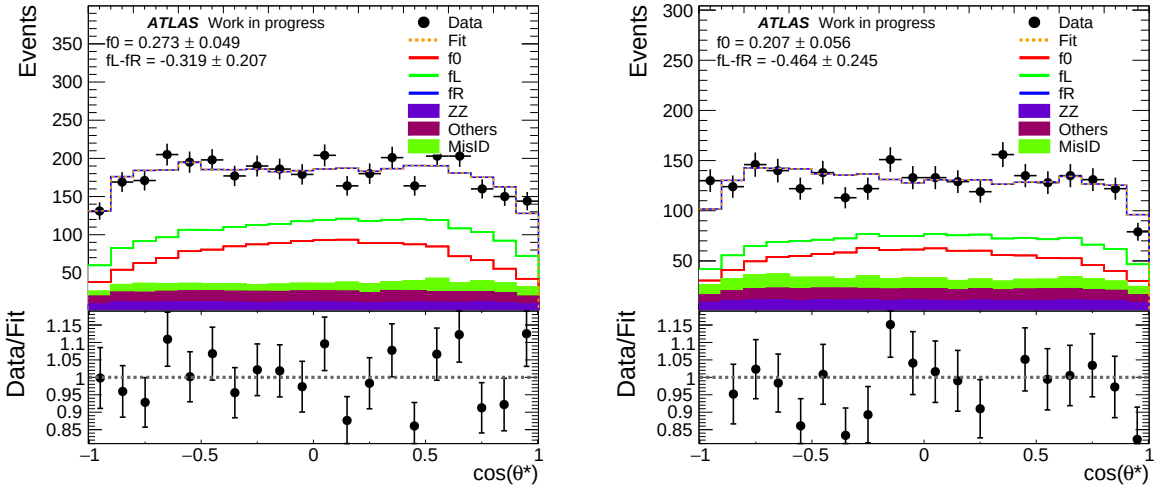

Figure 8.8 – *Fit to the* $\cos(\theta^*)$ *distribution in data to extract the* Z*-polarisation (in* W^+Z *events: left, in* W^-Z *events: right). The resulting polarisation fractions* f_0 *and* $f_L - f_R$ *are displayed on the figure along with their total uncertainties. All background distributions and fitted polarisation templates are stacked in the plot. The ratio plot illustrates the agreement of the fit with data.*

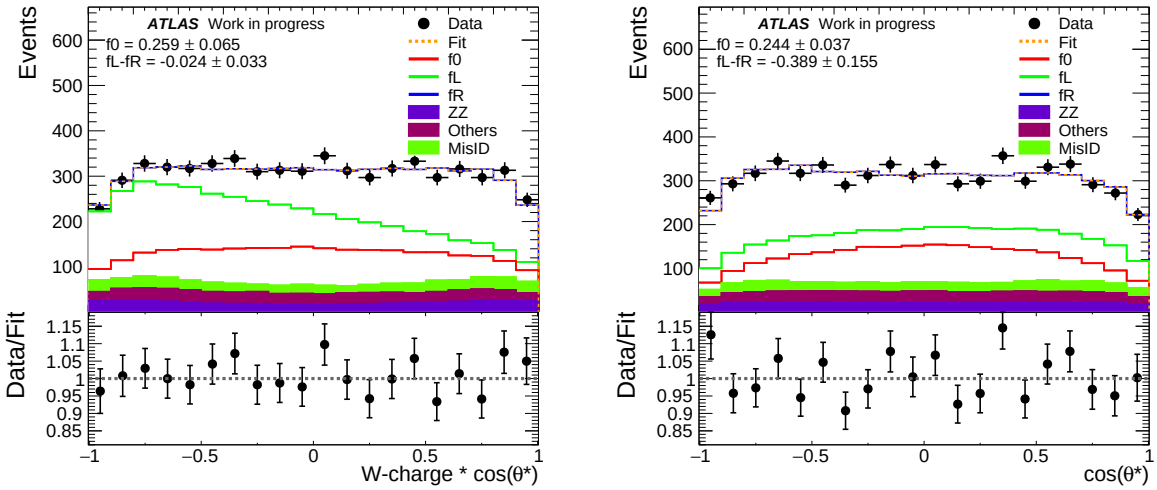

Figure 8.9 – *Fit to the* $\cos(\theta^*)$ *distribution in* $W^\pm Z$ *events in data to extract the* W*-polarisation (left) and the* Z*-polarisation (right). The resulting polarisation fractions* f_0 *and* $f_L - f_R$ *are displayed on the figure along with their total uncertainties. All background distributions and fitted polarisation templates are stacked in the plot. The ratio plot illustrates the agreement of the fit with data.*

on the background derived with the Matrix Method, a conservative 40% uncertainty is assumed according to the shape agreement between the Matrix Method and the MC Scale method. Further, in the cross section measurement, the four decay channels, $WZ \to e\nu_e ee$, $WZ \to e\nu_e \mu\mu$, $WZ \to \mu\nu_\mu ee$ and $WZ \to \mu\nu_\mu \mu\mu$, are combined using a χ^2 fit. That way, the uncertainty on the reducible background can be constrained.

8.6.2 Studies on the consistency of the fit

Nuisance parameters taking into account systematic variations of the fit components could also compensate for mismodelling of a signal or background template. In that case, the value of the nuisance parameter which minimizes the likelihood could differ from that

	f_0	f_{LR}	σ_{fid}
Absolute Uncertainties			
Electrons	0.0024	0.0004	120
Muons	0.0013	0.0027	150
Jets	0.0024	0.001	50
Pileup	0.005	0.0001	100
Misid. lepton background	0.031	< 0.0001	330
ZZ background	0.009	0.0004	100
Other backgrounds	0.0012	0.0005	140
QCD scale	0.0008	0.0013	1.5
PDF	0.0011	0.0009	1.9
Modelling	0.004	0.007	2.2
Total systematics	0.033	0.008	440
Luminosity	0.0015	< 0.0001	230
Statistics	0.057	0.032	150
Total	0.07	0.033	500
Total [rel., %]	25	130	5.3

	f_0	f_{LR}	σ_{fid}
Absolute Uncertainties			
Electrons	0.005	0.0021	120
Muons	0.0018	0.008	150
Jets	0.0017	0.005	40
Pileup	0.0014	0.005	100
Misid. lepton background	0.007	0.019	340
ZZ background	0.0007	0.0012	100
Other backgrounds	0.0018	0.005	130
QCD scale	0.0004	0.008	1.0
PDF	< 0.0001	< 0.0001	0.8
Modelling	0.0015	0.0028	20
Total systematics	0.009	0.024	440
Luminosity	< 0.0001	0.0008	230
Statistics	0.04	0.15	150
Total	0.04	0.16	520
Total [rel., %]	15	40	5.5

Table 8.11 – *Summary of the impact of statistical, object and background uncertainties on the $W^{\pm}$ (left) and Z polarisation measurement (right) in $W^{\pm}Z$ events on each parameter of interest in the fit. In the last line, the total relative uncertainty is given, the single contribution are given as absolute uncertainties.*

expected. The behaviour of the nuisance parameter is checked by means of the pull which is defined as

$$\text{Pull} = \frac{\theta_{\text{fit}} - \theta_0}{\Delta\theta}, \tag{8.14}$$

where θ_{fit} is the value of the nuisance parameter which minimizes the likelihood, θ_0 is its predicted value and $\Delta\theta$ its 1σ variation. The pull value is close to zero in case the value for the nuisance parameter minimizing the likelihood is compatible with its prediction provided by an external measurement. Non-zero pulls therefore might indicate a compensation of the mismodelling of another nuisance parameter, polarisation or background template. Strong correlations between two parameters could also indicate possible absorption of template mismodelling by a nuisance parameter. In case of a strong correlation between two parameters, it needs to be checked whether this correlation makes sense.
However, no suspicious correlations have been observed, especially, no large correlations are observed between the fit parameters describing the polarisation fractions, f_0 and $f_L - f_R$.

Figures 8.10 and 8.11 show the pulls for the $W^{\pm}$ polarisation measurement and the Z polarisation measurement in $W^{\pm}Z$ events, respectively. No problematic pulls are observed. The pull values deviating most from zero are the pulls of the pile-up energy subtraction term in the jet energy calculation in case of the W polarisation measurement ("JET_Pileup_RhoTolology") and the modelling of the templates in case of the Z polarisation measurement. However, there is no strong correlation between the polarisation fractions and these nuisance parameters, therefore, this is expected to cause no problems.

8.6.3 Results of the measurement in the fiducial phase space

The results of the boson polarisation in data extracted from the fit and the corresponding predictions from POWHEG+PYTHIA and MATRIX are displayed in Figure 8.12 for W^+ (left) and W^- (right) and for Z polarisation in W^+Z events and W^-Z in Figure 8.13. The results of the inclusive polarisation measurements on W and Z bosons are visualized

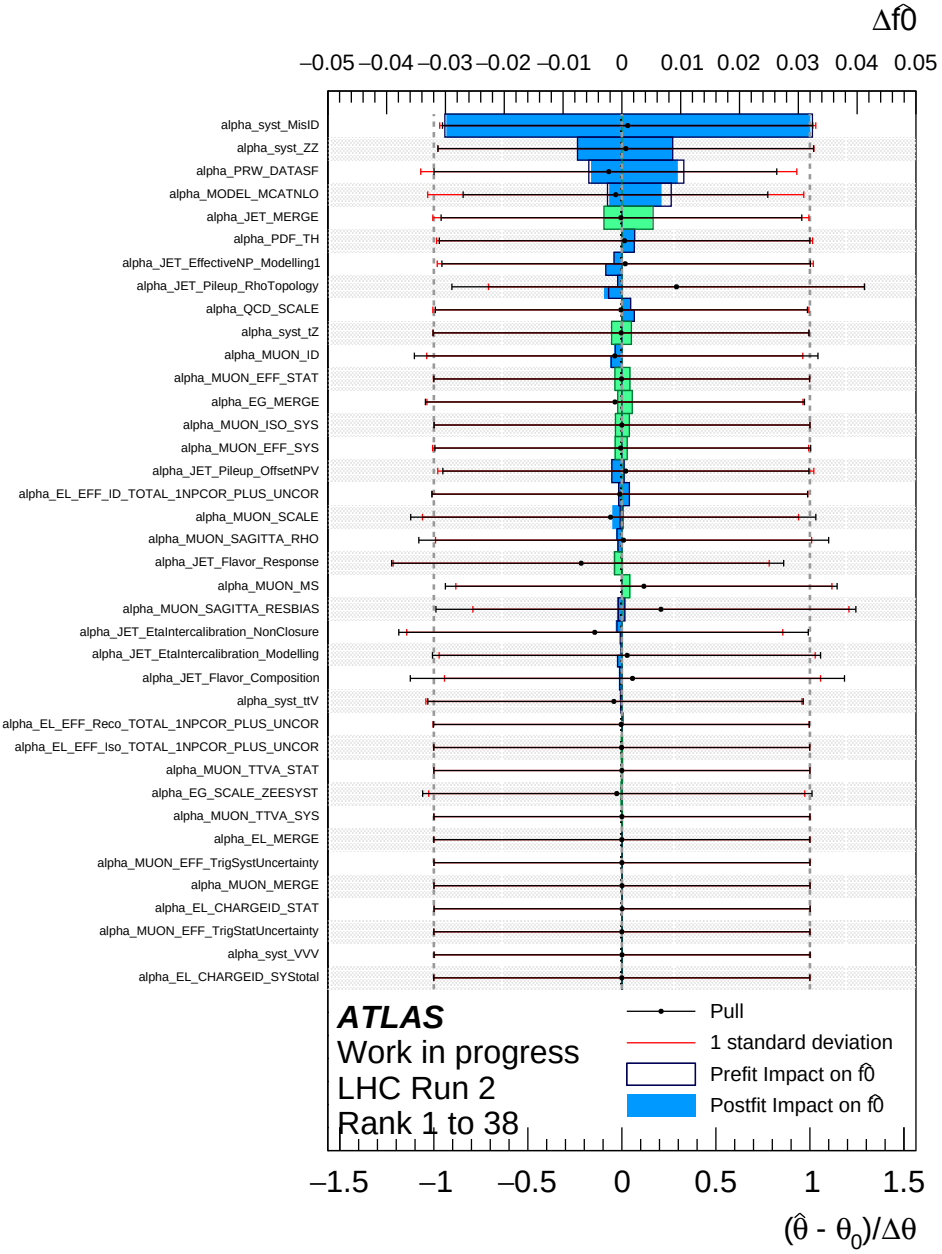

Figure 8.10 – *Pull of the fit to measure the $W^{\pm}$ polarisation and the ranking of the single uncertainty contributions to the longitudinal polarisation measurement.*

in Figure 8.14. The combination is profitable in terms of smaller uncertainties on the polarisation fractions. Figures 8.12-8.14 also display the correlations between the fractions f_0 and $f_L - f_R$ from the fit in data. Its absolute value is, depending on the measurement, in most cases below 5% but for all measurements below 10%. All measurement results are listed also in Table 8.12 and are compared to the predictions by POWHEG+PYTHIA and MATRIX.

The existence of longitudinal polarisation in W bosons in WZ diboson events has been determined with a significance of 4.2 σ, for an expected significance of 3.8 σ. The presence of longitudinal Z polarisation has been observed with a significance of 6.5 σ for an expected significance of 6.1 σ.

Overall, the agreement with the predictions at NLO and NNLO in QCD is good for

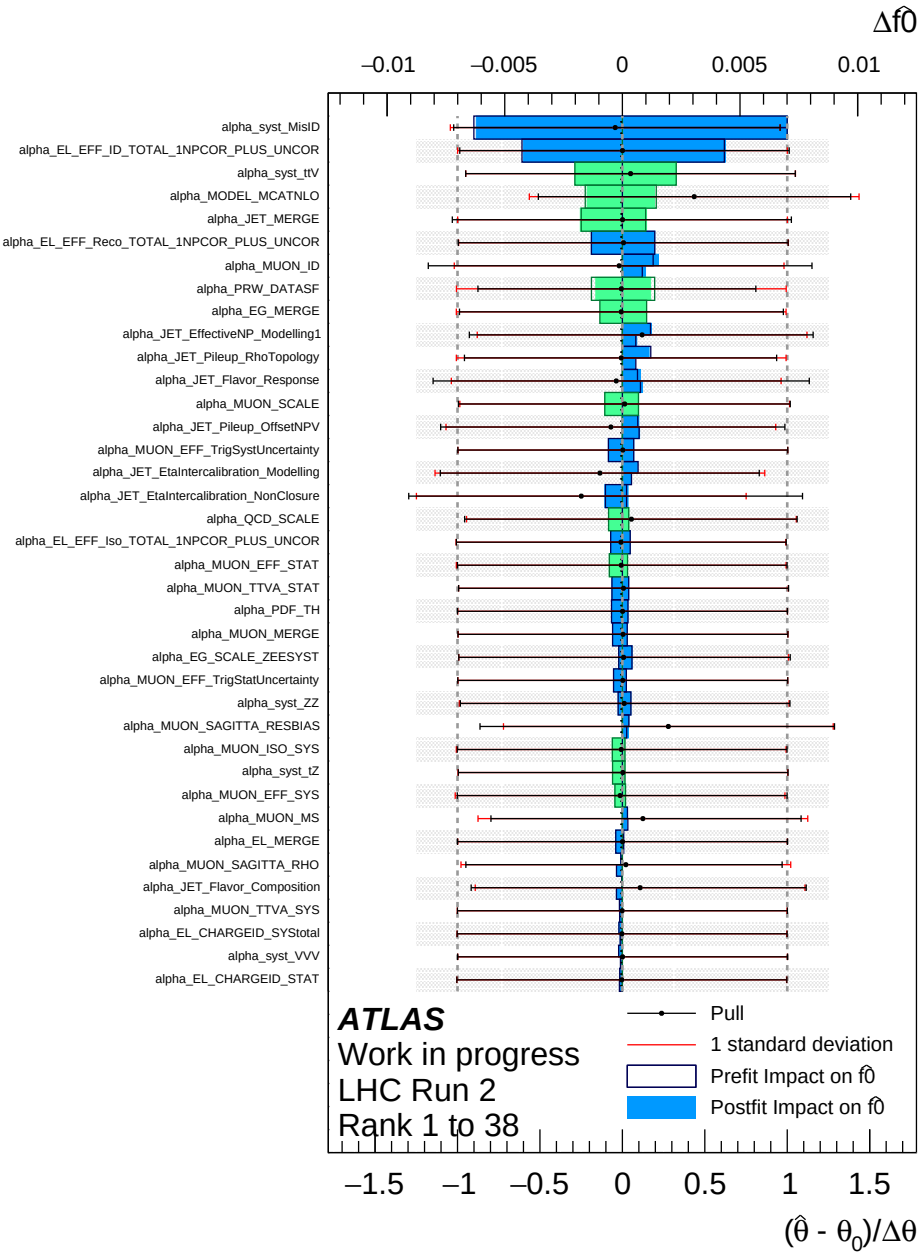

Figure 8.11 – *Pull of the fit to measure the inclusive Z polarisation and the ranking of the single uncertainty contributions to the longitudinal polarisation measurement.*

the longitudinal polarisation: for both models, the predicted value for the longitudinal polarisation fraction agrees with the measurement within 1 σ. For $f_L - f_R$, measurement and predictions often do not agree within their uncertainties, the measured value is lower than the prediction. However, in most cases and in overall, for $f_L - f_R$ in $W^{\pm}$ and for Z bosons in $W^{\pm}Z$ events, the agreement is within 2 σ, the agreement is even within 1 σ for W^- polarisation and Z polarisation in W^+Z events for both models. An agreement of worse than 2 σ is observed for W^+ polarisation and for Z polarisation in W^-Z events.

One possible explanation for the discrepancy in $f_L - f_R$ could be missing higher-order electroweak corrections in the simulation which are at leading order precision only. NLO EW corrections introduce a new production mode, the photon-quark-induced WZ production presented in Section 3.2.2.2. As the polarisation is very sensitive to the production

	f_0			$f_L - f_R$		
	data	Powheg+Pythia	MATRIX	data	Powheg+Pythia	MATRIX
W^+	0.26 ± 0.08	0.233 ± 0.004	0.2448 ± 0.0010	-0.02± 0.04	0.091 ± 0.004	0.0868 ± 0.0014
W^-	0.32 ± 0.09	0.245 ± 0.005	0.2651 ± 0.0015	-0.05± 0.05	-0.063 ± 0.006	-0.034 ± 0.004
$W^\pm$	0.26 ± 0.06	0.2376 ± 0.0031	0.2506 ± 0.0006	-0.024± 0.033	0.0289 ± 0.0022	0.0375 ± 0.0011
Z in W^+Z	0.27 ± 0.05	0.225 ± 0.004	0.2401 ± 0.0014	-0.32 ± 0.21	-0.297 ± 0.021	-0.262 ± 0.009
Z in W^-Z	0.21 ± 0.06	0.235 ± 0.005	0.2389 ± 0.0015	-0.46± 0.25	0.052 ± 0.023	0.0468 ± 0.0034
Z in $W^\pm Z$	0.24 ± 0.04	0.2294 ± 0.0033	0.2398 ± 0.0014	-0.39± 0.16	-0.156 ± 0.016	-0.135 ± 0.006

Table 8.12 – *Results for the polarisation fractions in the fiducial phase space with Born level leptons: the columns labelled "data" display the measurement results, they are compared to the predictions from* Powheg+Pythia *and* MATRIX *corrected to* $\sin^2\theta_W^{\text{eff}} = 0.23152$. *The uncertainties on data contain the total uncertainty. The uncertainties on the predictions contain statistical uncertainties and theory uncertainties, the uncertainties on the* Powheg+Pythia *prediction include QCD scale and PDF uncertainties, the uncertainties on the* MATRIX *prediction include QCD scale uncertainties.*

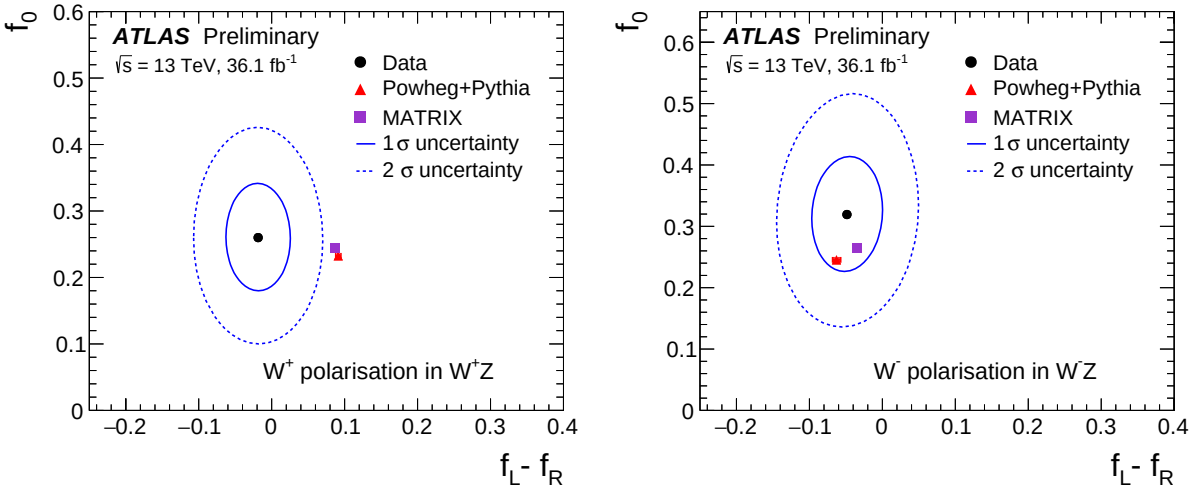

Figure 8.12 – *Visualization of the measurement results for the* W^+ *polarisation (left) and the* W^- *polarisation (right). The prediction obtained with a fit to truth distributions in the fiducial phase space with* Powheg+Pythia *(red dot) and* MATRIX *(purple square) are also shown. The* Powheg+Pythia *and* MATRIX *predictions are corrected to* $\sin^2\theta_W^{\text{eff}} = 0.23152$. *The 1 σ and 2 σ total uncertainty ellipses (full and dashed blue lines) drawn around the data points also indicate the correlation between* f_0 *and* $f_L - f_R$. *The* Powheg+Pythia *prediction contains statistical uncertainties (inner error bars) and theory uncertainties from QCD scale and PDF uncertainties, the uncertainties on the* MATRIX *prediction contain statistical uncertainties and QCD scale uncertainties. The uncertainties on the predictions are of the same size than the marker.*

mode of the WZ, this could have an impact on the result. However, confirmation on the size and the direction of the impact can only be given when the NLO EW correction become available.

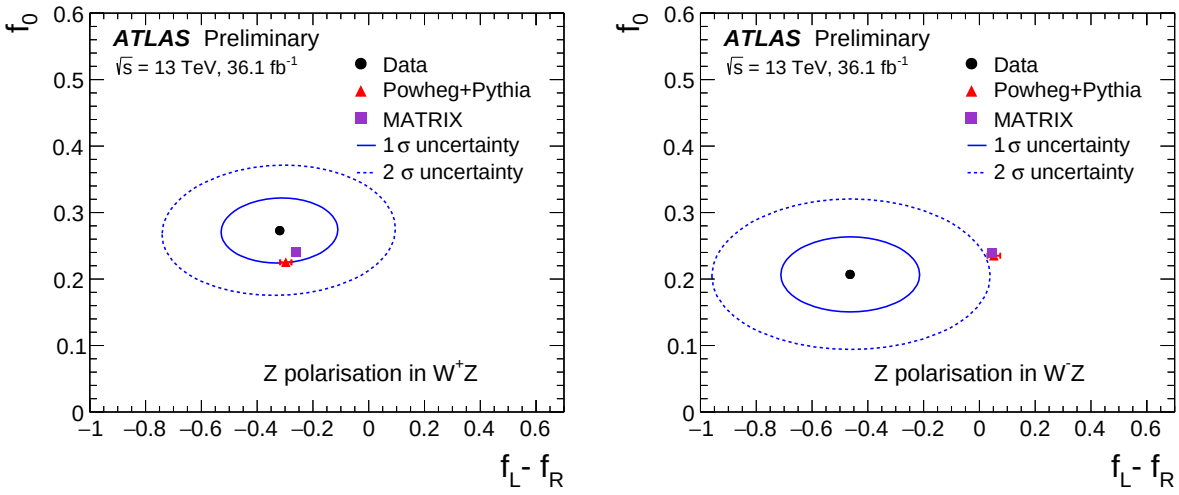

Figure 8.13 – *Visualization of the measurement results for the Z polarisation in W^+Z events (left) and in W^-Z events (right). The prediction obtained with a fit to truth distributions in the fiducial phase space with* Powheg+Pythia *(red dot) and* MATRIX *(purple square) are also shown. The* Powheg+Pythia *and* MATRIX *predictions are corrected to* $\sin^2\theta_W^{\text{eff}} = 0.23152$. *The 1 σ and 2 σ total uncertainty ellipses (full and dashed blue lines) drawn around the data points also indicate the correlation between* f_0 *and* $f_L - f_R$. *The* Powheg+Pythia *prediction contains statistical uncertainties (inner error bars) and theory uncertainties from QCD scale and PDF uncertainties, the uncertainties on the* MATRIX *prediction contain statistical uncertainties and QCD scale uncertainties. The uncertainties on the predictions are of the same size than the marker.*

8.7 Conclusion of the polarisation studies

This measurement provides the first results of boson polarisation in a diboson system in hadronic collisions. The longitudinal polarisation fraction f_0 and the transverse polarisation fraction difference $f_L - f_R$ has been extracted in the fiducial and the total phase space. A precision of 15% can be obtained on the longitudinal Z polarisation, which is the most precise measurement of the longitudinal polarisation fraction. A precision of 30% can be obtained on the measured longitudinal polarisation fractions of the W boson separated by charge and of 25% on the longitudinal W polarisation in $W^\pm Z$ events. The dominant contribution is the statistical uncertainty. The dominant systematic source on the longitudinal polarisation is the uncertainty on the reducible background which contributes with 12% to the total uncertainty in the $W^\pm$ polarisation measurement and with 3% in the Z longitudinal polarisation measurement in $W^\pm Z$ events.

Two models are available for comparison with the measurement: Powheg+Pythia and MATRIX which provide results at NLO and NNLO precision in QCD, respectively. Both models provide a similar level of agreement with the measurement, whereas the prediction describes the longitudinal polarisation f_0 in data within 1 σ. The predictions describe the longitudinal polarisation fraction better than the transverse polarisation difference $f_L - f_R$, which in overall agrees with the measurement within 2 σ.

Consistency checks confirm the stability of method. Another consistency check is presented here as a conclusion: a cross section measurement can be performed with the nor-

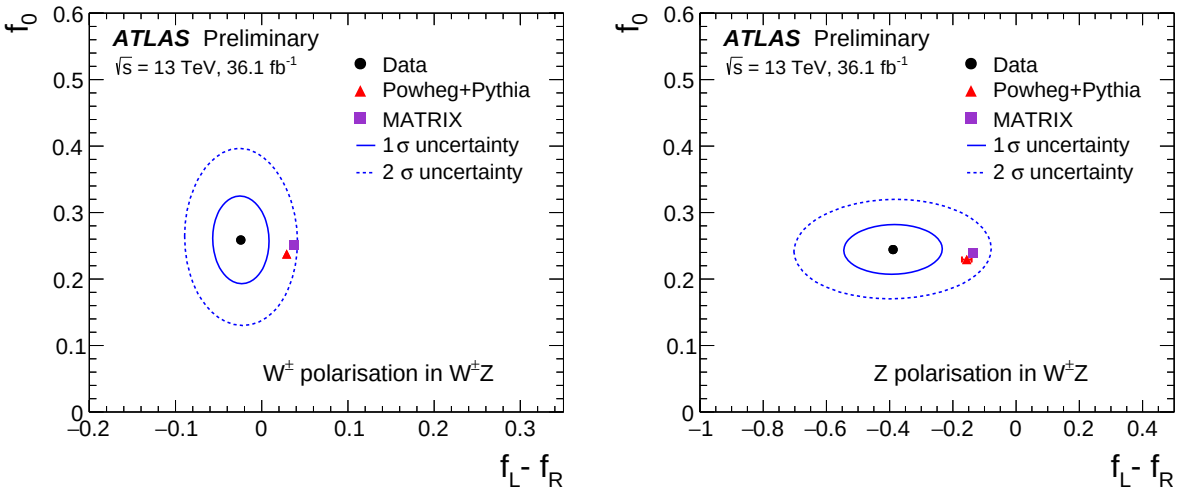

Figure 8.14 – *Visualization of the measurement results for the W inclusive polarisation (left) and the Z inclusive polarisation (right) taking into account all $W^{\pm}Z$ events in data. The prediction obtained with a fit to truth distributions in the fiducial phase space with* Powheg+Pythia *(red dot) and* MATRIX *(purple square) are also shown. The* Powheg+Pythia *and* MATRIX *predictions are corrected to* $\sin^2\theta_{\mathrm{W}}^{\mathrm{eff}} = 0.23152$. *The 1 σ and 2 σ total uncertainty ellipses (full and dashed blue lines) drawn around the data points also indicate the correlation between f_0 and $f_L - f_R$. The* Powheg+Pythia *prediction contains statistical uncertainties (inner error bars) and theory uncertainties from QCD scale and PDF uncertainties, the uncertainties on the* MATRIX *prediction contain statistical uncertainties and QCD scale uncertainties. The uncertainties on the predictions are of the same size than the marker.*

malization parameter N_{tot} extracted from the fit. N_{tot} should be equal to the WZ signal yield extrapolated to the fiducial phase space, either by charge or inclusively, depending on the measurement. It is already corrected by the τ contribution. Dividing N_{tot} by the integrated luminosity $\mathcal{L} = 36.1$ fb^{-1} and by the number of decay channels, which is four, should yield a comparable result to equation (7.7).

Here, a measurement of the fiducial cross section inclusively over the W charge is presented. The parameter N_{tot} therefore has to be taken either from the inclusive W or Z polarisation measurement. Table 8.13 lists the extracted values of N_{tot} in the inclusive W and Z polarisation measurement and the calculated fiducial cross section per channel obtained by dividing by the luminosity $\mathcal{L} = 36.1$ fb^{-1} and the decay channel number. Note that all uncertainties, including statistical, systematic and luminosity uncertainty, are already considered in the measurement of N_{tot} and the relative uncertainty on σ_{WZ} is equal to the relative uncertainty on N_{tot}. The order of magnitude of the uncertainty contributions obtained on N_{tot} from the fit are also similar to those of the inclusive cross-section measurement. Only the reducible background contribution is larger leading to a larger total uncertainty on the cross section of 5% with respect to the 4.3% obtained with the cross section measurement.

Table 8.13 shows that the N_{tot} value obtained with the W and Z polarisation measurements are both consistent, they yield a value for N_{tot} which agrees on the per mil level. The cross section extracted with the polarisation measurement has to be compared to the prediction by MATRIX at Born level from equation (3.3), stating a value of $\sigma^{\mathrm{fid.PS}}_{W^{\pm}Z,\,\mathrm{MATRIX}} = 64.0 \pm 0.02\,(\mathrm{stat.})^{+1.5}_{-1.3}\,(\mathrm{scale})$ fb. The cross section obtained with the fit

	W	Z
N_{tot}	9477	9514
σ_{WZ} [fb]	65.6	65.9
$\Delta\sigma_{WZ}$ [%]	5.3	5.5
$\Delta\sigma_{WZ}$, [fb]	3.5	3.6

Table 8.13 – *Inclusive fiducial cross section results obtained from the inclusive W and Z polarisation measurement.*

of the event yield in the polarisation measurement is therefore 2.5-3.0% higher than the cross section predicted by MATRIX at NNLO . Considering the 5% uncertainty on the measurement and also the uncertainty on the prediction, it is very well compatible with the MATRIX prediction. Considering that the polarisation measurement is unfolded to Born level and the cross section measurement in Section 7.2 is unfolded to dressed leptons, the cross-section result obtained with the polarisation fit is slightly lower. The difference in the cross section measurement results can be explained by the channel combination method: in the standard cross section measurement, the cross section measurement is performed separately in each measurement channel and the channels are combined using a χ^2 fit while in this measurement, the cross section is measured inclusively and the cross section per channel is a simple average.

Chapter 9

Conclusion

Within the scope of this thesis, the WZ cross section measurement was presented and the polarisation was measured for the first time in diboson events produced in hadronic collisions. The data were collected with the ATLAS experiment at the LHC in 2015 and 2016 at a center-of-mass energy of $\sqrt{s} = 13$ TeV and an integrated luminosity of 36.1 fb^{-1}. On the cross-section measurement, a precision of 4.6% was obtained, this is competitive to the precision of 4.2% obtained in the $\sqrt{s} = 8$ TeV measurement. The measurement is now dominated by systematic uncertainty and not any more by statistical uncertainties. The main systematic uncertainties in the cross-section measurement issue from the reducible background, the pile-up reweighting, the ZZ irreducible background, the muon and the electron identification. Within the scope of this thesis, detailed studies on the electron identification efficiency and the reducible background were performed.

The electron identification efficiency was calculated for 2015 and 2016 data using the probe isolation to discriminate signal against background. The agreement with MC simulation was studied and scale factors were extracted to correct for mis-modelling. These were combined with a complementary electron identification efficiency measurement and provided to the ATLAS collaboration. The precision of the scale factor results is of the order of 3-5% at low transverse energy but becomes better at higher transverse energy where a precision at the sub-percent level is reached. The main uncertainty contribution issues from the background in the measurement. This precision on the electron identification scale factors translates to an uncertainty contribution of 1.1% in the WZ cross section measurement. A suggestion to improve the method to extract the electron identification scale factors has also been given in this thesis.

As in the $\sqrt{s} = 8$ TeV measurement, the reducible background is the dominant source of uncertainty in the WZ cross section measurement. The reducible background is the biggest background contribution. Studies on the lepton selection were performed to keep this component as low as possible. In total, a signal-to-background ratio of 4.0 can be obtained.

The remaining contribution of the reducible background was determined with the data-driven Matrix Method. A precision of 30% on this component is achieved. A correction due to the composition of the origins of the fake lepton, the control region statistics and contamination from real leptons limit the precision of this background estimate. The reducible background was also evaluated with another, complementary method which provides an independent cross check of the Matrix Method estimate. Both method are in good agreement within 3.3%. The estimate of irreducible background is based on MC estimates.

Using these results, the WZ cross section can be extracted in each of the measurement

channels and combined. The measured cross section result is

$$\sigma^{\text{fid.PS}}_{W^\pm Z} = 63.7 \pm 2.9 \text{ fb}.$$

which is compared to the NNLO prediction provided by MATRIX of

$$\sigma^{\text{fid.,MATRIX}}_{W^\pm Z \to \ell' \nu \ell \ell} = 61.5^{1.4}_{1.3} \text{ fb}.$$

The cross-section result has been found to exceed the predictions by MATRIX at NNLO by about 3% and is compatible with the MATRIX prediction within the uncertainties. The measurement is further in good agreement with the measurement results obtained with 3.2 fb^{-1} of 2015 data at $\sqrt{s} = 13$ TeV. Also, the total cross section has been extracted.

Within the scope of this thesis, the first polarisation measurement of WZ pairs and in diboson events produced in hadronic collisions has been performed. Angular distributions are very sensitive to polarisation effects, this has been exploited in this measurement. Templates have been created from samples representing the properties of polarised boson which were fit to the data angular distribution. The longitudinal polarisation fraction and transverse polarisation fraction differences are extracted from a maximum Likelihood fit. A fraction of 26% of longitudinally polarised W and of 24% of longitudinally polarised Z bosons with uncertainties on the fractions of 6% and 4%, respectively, are measured in data in the fiducial phase space. A precision on the longitudinal polarisation fraction of 17-31% can be obtained, whereas the measurement of the polarisation fraction is nearly entirely dominated by statistical uncertainties. The dominant systematic source on the longitudinal polarisation fraction is the estimation of the reducible background.

The polarisation measurement results are compared to two models provided by Powheg+Pythia, a simulation with a precision of NLO in QCD and MATRIX, which is NNLO in QCD. Both models give a similar degree of agreement with the data, the longitudinal polarisation fraction is description better in overall than the left- and right-handed transverse polarisation difference. The predicted longitudinal polarisation agrees with the data within 1 σ, the overall level of agreement for the left- and right-handed transverse polarisation difference is about 1-2 σ.

It will be very interesting to perform these measurements again with a larger dataset. In particular by adding data collected by ATLAS in 2017 and 2018 to the data collected in 2015 and 2016. Although being not any more statistically dominated, the WZ cross-section measurement could profit from a larger data sample: part of the systematic uncertainties come from statistical uncertainties for example from the control regions and the Matrix Method extrapolation region. Differential cross section measurement could profit from a larger dataset, especially in kinematic regions sensitive to high partonic center-of-mass energy where these measurements are still dominated by statistical uncertainties. Also, more precise measurements of the cross section of irreducible background components, for example ZZ could help to get a better constraint on the irreducible background and the irreducible background contamination in the Matrix Method control regions.

A larger precision could be obtained on the polarisation measurement with the full Run 2 dataset, this measurement is statistically dominated. It has been shown that the polarisation is sensitive to aTGCs also. However, the effect is beyond the precision that can be obtained in the measurement. More collision events with a high partonic center-of-mass energy would be necessary where larger impact from aTGCs is expected. This could be achieved with a larger collider center-of-mass energy or a larger integrated luminosity.

Ultimately, it will be very interesting to measure the polarisation in vector boson scattering events, especially the longitudinal component which is very sensitive to new physics in vector boson scattering. With 2015 and 2016 data, electroweak production of WZ has been observed for the first time with a significance of 5.6 standard deviations [23], the extraction of the polarisation in these events is however a rather distant prospect yet. Even with full Run 2 data, this measurement will not be feasible.

Acknowledgments

Last but not least, I would like to take the opportunity to thank some people with whom I could work together during the three years of my PhD and who contributed to the success of this work. I was very lucky to meet and to collaborate with a lot of kind and competent people, some of them are mentioned in the following.

First, I would like to thank my thesis supervisor Emmanuel Sauvan. I appreciate very much the constructive discussions, his effort and engagement and all the time he took for the supervision and the fact that his office doors were always open in case of questions. Thanks to him, I could learn so much on experimental particle physics during my PhD.

I would also like to express my thanks to Lucia Di Ciaccio with whom I worked on the WZ analysis. She was always available to answer my questions, especially on all MC-truth related topics.

Elena Yatsenko was a Postdoctoral Researcher at LAPP working with me on the WZ analysis and on polarisation truth studies. I would like to thank her for the nice and fruitful collaboration, especially on the polarisation. I enjoyed working together with her.

Special thanks to the ATLAS group at LAPP for their warm welcome. I enjoyed the great working atmosphere in the group and was lucky to be welcomed by a team with so many kind and competent researchers. It was a great pleasure to be a part of your team!

I want to thank at this point also Nicolas Berger who was available to answer all my statistics-related questions, Narei Lorenzo and Louis Portales for their support with the HistFactory framework.

During my first year of my PhD, I was working on the electron identification efficiency measurement. I would like to express my thanks to Joseph Reichert, Eleonora Benhar Noccioli, Cristinel Diaconu, Christos Anastopoulos, Philip Sommer and Kristin Lohwasser from the E/γ team for their input and suggestions.

I would like to take the opportunity to thank at this point the members of my PhD jury: Claude Charlot and Prof. Elzbieta Richter-Was were the Rapporteurs of my jury. Thanks a lot for agreeing to read my thesis, for the discussions and for all your useful suggestions. I would also like to thank Prof. Elzbieta Richter-Was for inviting me to the Jagiellonian University to give seminars and for the very detailed discussion about my thesis.

Thanks a lot to my Examinateurs Pascal Pralavorio, Jan Kretzschmar and Giovanni Lamanna with who I was also able to discuss in detail about my work and who also provided me with constructive input. During all the discussions with my Jury members, I was able to learn a lot. I would like to thank them for their interest in my work and the time they took for discussions.

I would like to express my thanks to the LAPP institute for the opportunity to do my PhD thesis at this research institute and for the warm welcome.

Thanks a lot also to the administration of LAPP for their quick, uncomplicated and efficient help with all the paperworks that accumulates during the PhD.

Within the scope of my teaching activity, I was able to work together with Isabelle Debonis. I would like to thank her for accepting to supervise me during my teaching activity and for her support. She was very engaged and always made sure that everything worked well in the classes.

Thanks to my colleagues Olympia Dartsi, Saskia and Peter Falke, Sergii Raspopov, Louis Portales, Francesco Constanza and Oleh Kivernyk, the coffee and lunch breaks became a nice diversion from the daily work routine. Thanks for all the good time I could spend together with you!

Thanks to Sergii Raspopov with whom I shared the office during the three years of my PhD for the nice working atmosphere in the office and all the chocolate!

Further I would like to thank all the PhD students at LAPP for the good time I could spend together with you at LAPP and in Annecy!

Thanks to Prof. Dr. Otmar Biebel, Francesco Constanza and Nicolas Berger for having agreed to look through some parts of my thesis.

Thanks to my parents Christl and Norbert for all their love and continuous support, not only during my time as a PhD student.

Résumé

I. Introduction

Cette thèse présente la mesure de la section efficace de la production par paire de bosons WZ et la polarisation des bosons W et Z lors de leur production par paire. Des données de collisions protons-protons enregistrées par le détecteur ATLAS en 2015 et 2016 avec une énergie dans le centre de masse de $\sqrt{s} = 13$ TeV sont analysées. Un des modes de production WZ contient le couplage tri-boson WWZ qui est prédit par le Modèle Standard de la Physique de Particules. Ce mode de production étant rare, il n'y a pas encore de constraintes strictes sur la force de ces couplages. Les mesures de la section efficace et des autres propriétés sont donc sensibles à la nouvelle physique.

Les mesures des couplages tri-bosons sont une partie importante du programme de physique du LHC. La section efficace WZ a été également mesurée avec des données du détecteur ATLAS avec une énergie de $\sqrt{s} = 7$ TeV, $\sqrt{s} = 8$ TeV et avec des données enregistrées en 2015 à $\sqrt{s} = 13$ TeV.

Par rapport à des études avec les données enregistrées en 2015, cette nouvelle mesure utilise aussi les données enregistrées en 2016, donc, pour cette mesure, dix fois plus de statistique est disponible, avec un total de 36 fb^{-1}. Récemment, les mesures peuvent être comparées avec des calculs théoriques avec une précision au next-to-next-to leading order.

Pour la première fois en collisions hadroniques, une étude sur la polarisation des bosons produits par paire a été menée. Auparavant, la polarisation des bosons produits par paire a été mesuré seulement lors de la production de WW avec des données produits par le collisionneur électron-positron LEP.

Les événements WZ sont identifiés lors de leur désintégration en leptons, en électrons, muons et neutrinos. L'identification des électrons et son efficacité joue donc un rôle important dans les mesures de production WZ. La mesure de l'efficacité d'identification des électrons dans les données et dans la simulation est également présentée.

Les thèmes centraux de cette thèse sont l'optimisation de la sélection des leptons pour les mesures WZ, l'estimation du bruit de fond des objects identifiés à tort comme des leptons et la mesure de la polarisation. La mesure de l'efficacité d'identification des électrons a été aussi effectuée dans le cadre de cette thèse.

Le chapitre 2 donne un bref aperçu de la théorie fondamentale, le Modèle Standard, le chapitre 3 explique les mécanismes de production de paires WZ et leur description théorique, ainsi que la paramétrisation de la polarisation des bosons. Le chapitre 4 résume les caractéristiques les plus importantes du détecteur ATLAS et la reconstruction des particules. Le chapitre 5 présente la mesure de l'efficacité d'identification des électrons. Le chapitre 6 donne la méthode des études du WZ, la selection et reconstruction des événements et l'estimation du bruit de fond, et le chapitre 7 présente la mesure de la section

efficace de la production par paire WZ. Dans le chapitre 8, la mesure de la polarisation des bosons est presentée et une brève conclusion est donnée dans le chapitre 9.

II. Elements du Modèle Standard de la physique des particules

La production par paire des bosons WZ est décrite par le Modèle Standard (MS) qui est le modèle théorique de la dynamique des particules élémentaires. Le MS est décrit dans le cadre de la théorie quantique des champs basée sur les principes de la mécanique quantique et la théorie de la relativité. Il s'agit d'une théorie de gauge, par conséquence, le Lagrangien doit être invariant sous des transformations locales de gauge.

Le contenu en particules du MS peut être groupé en deux classes de particules : des bosons et des fermions. Les fermions sont les constituants de la matière, les bosons, dont les bosons W et Z, transmettent les interactions entre les particules élémentaires.

Le MS est basé sur le groupe de symétrie $SU(3)_C \times SU(2)_L \times U(1)_Y$. La théorie de Chromodynamique quantique décrit les interactions entre les quarks qui est mediée par les gluons. Elle est formulée dans le groupe de symétrie $SU(3)_C$. L'interaction électrofaible est décrite dans le groupe de symétrie $SU(2)_L \times U(1)_Y$. Quatre bosons sont associés à cette interaction, trois bosons $\mathbf{W}_\mu = (W^1_\mu, W^2_\mu, W^3_\mu)$ associé au groupe $SU(2)_L$ et le boson B_μ associé au groupe $U(1)_Y$. A basse énergie, la symétrie est brisée par un champs scalaire qui couple les champs de gauge. Le potentiel introduit par le champs scalaire a une symétrie continue et les états en énergie les plus bas ne partagent pas la symétrie du Lagrangien. Le système choisis un état de base, donc, la symétrie est brisée. L'état de base est choisi tel que le groupe $U(1)_{\mathrm{QED}}$ du électromagnétisme, est l'état de base du vide. Cette brisure de symétrie crée les bosons $W^\pm$, Z et le photon. Selon le théorème de Goldstone, trois bosons de Goldstone sans masse sont crées. Ces derniers sont absorbés par les bosons de gauge W et Z et deviennent leurs polarisations longitudinales et ils obtiennent une masse. L'existence de la polarisation longitudinale est donc connectée avec le mécanisme de brisure spontanée de symétrie.

Les couplages entre les bosons W et Z sont rendus possibles grâce à la propriété non-Abelian du groupe $SU(2)_L \times U(1)_Y$. La force de ces couplages est donnée par le MS et le mécanisme de brisure spontanée de symétrie. Une mesure de la production par paire des bosons WZ donc test la force du couplage entres bosons W et Z et est donc un test du MS.

III. Production par paire des bosons WZ dans les collisions proton-proton et polarisation des bosons vecteurs

Ce chapitre est un exposé du cadre théorique de la production par paire des bosons WZ et la polarisation des bosons. Parmi les trois canaux de productions des bosons par paire incluant des bosons W et/ou Z, la production par paire WZ est un bon compromis entre une section efficace de production assez élevée et un bruit de fond bas. Uniquement les désintégrations des bosons W et Z en électrons, muons et neutrinos sont prises en compte, résultant en quatre états finals considérés.

Pour pouvoir comparer les mesures avec la théorie, il faut des calculs théoriques précis et près de la réalité. Le calcul de la production WZ est effectué en plusieurs ordres en la théorie de perturbation. En premier ordre ("Leading Order", LO), les pairs WZ sont

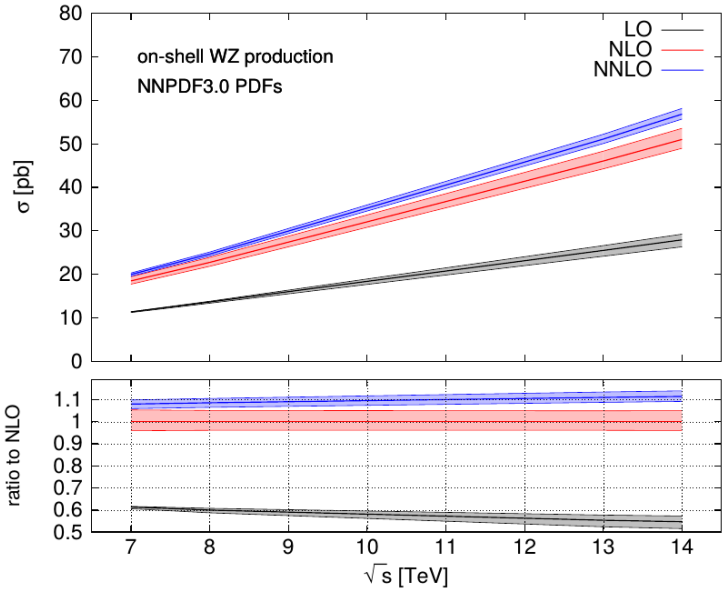

Figure III.1 *Résultat du calcul théorique de la section efficace de la production par paire des bosons WZ au premier ordre et les corrections introduites par le calcul de deux ordres supérieurs, NLO et NNLO.*

produits par la diffusion d'un quark et d'un antiquark et par l'annilihation d'un paire quark–anti-quark. Ce dernier mode contient un vertex de couplage WWZ.

Pour prendre en compte des ordres supérieurs, des corrections virtuelles avec des gluons et quark dans des boucles et des radiations réeles de quark et gluons sont introduits. Egalement, au next-to-leading order ("NLO"), un nouveau mode de production, la fusion d'un quark et d'un gluon, est introduit.

Négliger les ordres supérieurs résulte en une sous-estimation de la section efficace. Les corrections NLO augmentent l'estimation de la section efficace de la production W^+Z (W^-Z) par 79.0% (83.1%), les corrections NNLO augmentent la section efficace de la production W^+Z (W^-Z) par 10.9% (11.0%), par rapport à la prédiction au NLO.

Les prédictions théoriques récentes mettent à disposition les calculs jusqu'à un ordre "next-to-next-to leading order" (NNLO). La Figure III.1 montre la section efficace au premier ordre et la contribution des ordres supérieurs, NLO et NNLO.

Plusieurs calculs sont disponibles pour simuler la section efficace de la production par paire des bosons WZ et leurs proprietés. La simulation MATRIX génère des distributions cinématiques au NNLO et Powheg+Pythia génère des événements au NLO et contient aussi une simulation de la réponse du détecteur.

Pour les bosons massifs, il y a trois modes de polarisation : transverse, droite et gauche, et longitudinale. La polarisation dépend du système de référence.

Les observables angulaires sont très sensibles aux effets de la polarisation. La variable discriminante utilisée dans cette étude est le cosinus de l'angle θ^* qui est l'angle entre les leptons de la désintégration du boson dans le référentiel du boson au repos et la diréction du boson. Cette dernière est donnée dans le référentiel au repos du système WZ. Dans le cas d'une mesure de la polarisation du boson Z, le lepton négativement chargé est utilisé dans la mesure et le lepton chargé pour la mesure de la polarisation du boson W. La définition de l'angle θ^* est illustrée dans la Figure III.2.

En supposant une symétrie autour l'axe du boson, la section efficace différentielle en $\cos(\theta^*)$ est exprimée en fonction des états de polarisation. L'équation (III.1) montre cette

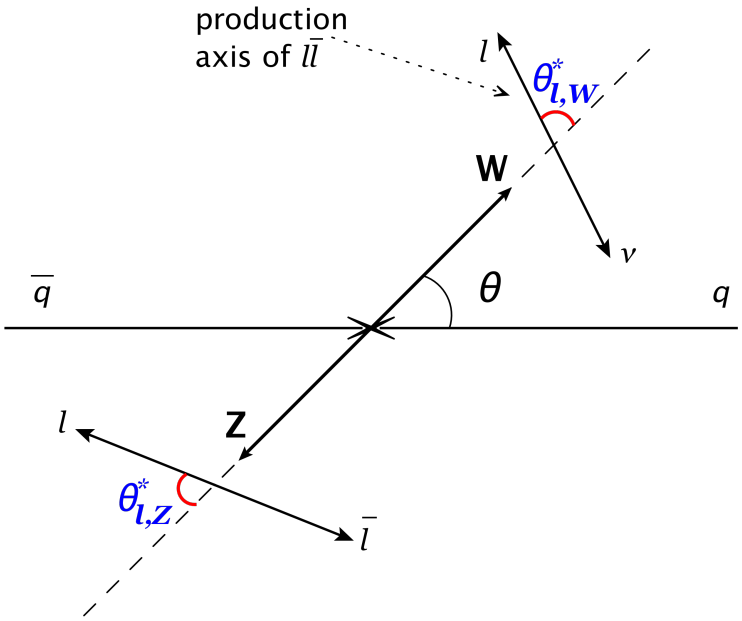

Figure III.2 *Définition de l'angle θ^*. La définition du système de référence est donnée dans le texte.*

expression pour le boson W :

$$\frac{1}{\sigma^{\mathrm{U+L}}}\frac{d\sigma}{d\cos(\theta^*)} = \frac{3}{8}f_L(1\mp\cos(\theta^*))^2) + \frac{3}{8}f_R(1\pm\cos(\theta^*))^2 + \frac{3}{4}f_0\sin^2(\theta^*), \tag{III.1}$$

et l'équation (III.2) pour le boson Z,

$$\begin{aligned}\frac{1}{\sigma^{\mathrm{U+L}}}\frac{d\sigma}{d\cos(\theta^*)} = \frac{3}{8}f_L(1+\cos(\theta^*)^2 - 2\cdot\frac{2\cdot c_v c_a}{c_v^2+c_a^2}\cos(\theta^*)) + \frac{3}{8}f_R(1+\cos(\theta^*)^2 \\ +2\cdot\frac{2\cdot c_v c_a}{c_v^2+c_a^2}\cos(\theta^*)) + \frac{3}{4}f_0\sin^2(\theta^*).\end{aligned} \tag{III.2}$$

Les fractions de polarisation f_0 (longitudinale), f_L (transverse gauche) et f_R (transverse droite) sont normalisées par la section efficace. Ces équations sont valables exclusivement pour l'espace de phase total mais pas pour des événements reconstruits. Pour avoir une modèle du comportement des bosons polarisés, on doit pondérer les événements dans la simulations. Les poids sont calculés à l'aide des équations (III.1) et (III.2).

IV. Le grand collisionneur de hadrons LHC et le détecteur ATLAS

Le LHC est un collisionneur circulaire de particules. Le synchrotron accélère des protons, qui circulent en sens opposé dans l'anneau, jusqu'à une énergie dans le centre de masse de $\sqrt{s} = 13$ TeV. Les protons entrent en collision en quatre points de l'anneau, là où des détecteurs sont situés.

Les données utilisées pour cette étude ont été enrégistrées par le détecteur ATLAS, un détecteur polyvalent. Les particules provenant des collisions inélastiques des protons sont

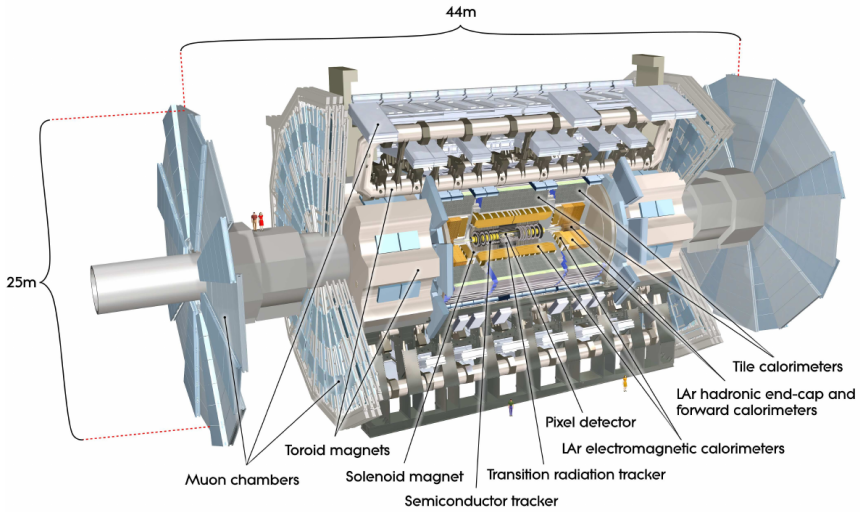

Figure IV.1 *Illustration du détecteur ATLAS.*

réconstruites, identifiées et leurs energies, impulsions, charges électriques et leurs positions sont mesurées. Le détecteur a une forme cylindrique et couvre presque tout l'angle solide. Il est arrangé symétriquement autour du point de collision.

Le système de coordonnées d'ATLAS est droitier et son origine est située au point d'interaction. L'axe z est aligné avec la direction du faiseau, l'angle azimuthal ϕ donne l'angle dans le plan transverse, le plan décrit par les coordonnées x et y. L'angle polaire θ est l'angle avec l'axe z, cet angle est souvent converti en une grandeur dénommée pseudorapidité qui est calculée pour des objets sans masse avec la formule $\eta = -ln(\tan(\frac{\theta}{2}))$.

ATLAS est composé de trois sous-détecteurs, chaque sous-détecteur donne des informations complémentaires sur l'événement, toutes les informations sont assemblées pour obtenir une vue globale de l'événement. Une illustration du détecteur ATLAS est montrée en Figure IV.1.

Le détecteur intérieur ("Inner Detector", ID) est consisté de détecteurs à semiconducteurs et d'un détecteur gazeux qui produisent un signal quand une particule chargée les transverse. A l'aide d'un champ magnétique, la charge et l'impulsion des particules peuvent être mesurées. La trajectoire de la particule et le point d'interaction sont reconstruits.

Les calorimètres sont composés d'un calorimètre électromagnétique (ECAL) et d'un calorimètre hadronique (HCAL). Le ECAL mesure l'énergie des électrons et des photons profitant des interactions électromagnétiques de ces paticules avec le milieu et le HCAL mesure l'énergie des hadrons à l'aide des interactions hadroniques.

Les détecteurs de muons sont des détecteurs gazeux. Des interactions avec des muons ionisent le gaz et les électrons d'ionisation sont collectés par une cathode. L'impulsion du muon est mesurée grâce à la courbure de sa trajectoire dans un champ magnétique.

Un trigger reconnaît les signatures typiques des particules et des événements intéressants et décide dans un instant très court si l'événement est enrégistré ou pas. Grâce au trigger, le numéro des événements entrégistrés par seconde est réduit de $40{\cdot}10^6$ à 1000.

Pour la reconstruction des particules, des algorithmes cherchent des signatures typiques dans les sous-détecteurs et connectent aussi des informations de sous-détecteurs différents. De cette façons, des candidates d'électrons, muons et des jets hadroniques sont reconstruits. Des algorithmes d'identifications et des critères d'isolation de sévérités différentes, réduisent le bruit de fond. Les neutrinos sont reconstruits en reconstituant la balance d'impulsion dans l'événement et leur énergie est associée avec l'énergie manquante dans le plan

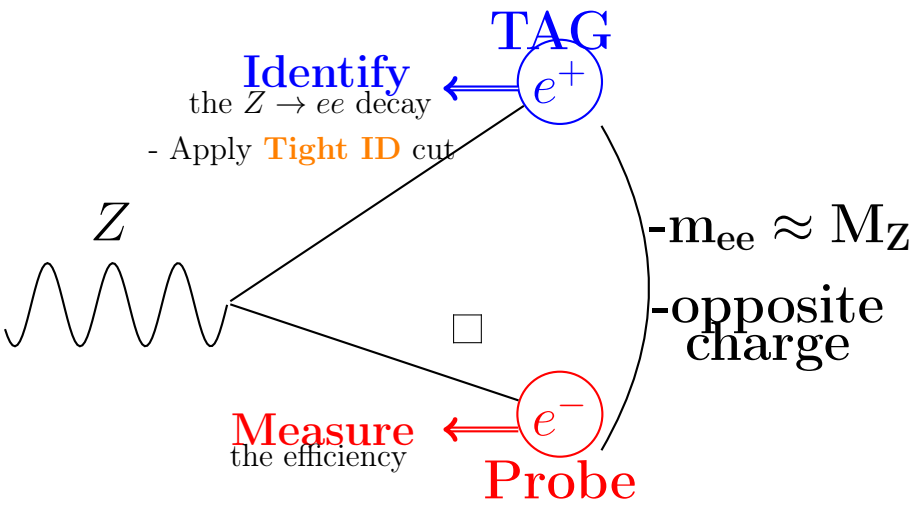

Figure V.1 *Illustration de la méthode "Tag and Probe".*

transverse.

V. Mesure de l'efficacité d'identification des électrons utilisant ses proprietés d'isolation et la méthode "Tag and Probe" basée sur la désintégration $Z \to ee$

Pour identifier des électrons, les analyses appliquent des critères d'identification avec des niveaux de sévérité différents : `Loose`, `Medium` et `Tight`. Il est important pour les analyses de connaître l'efficacité d'identification des électrons dans le détecteur ATLAS et la qualité de la modélisation de cette efficacité par la simulation. Des différences en efficacité d'identification entre la simulation et les données sont corrigées par un facteur de correction. Ce dernier est calculé en prenant le rapport entre l'efficacité mesurée dans les données et prédite par la simulation.

Pour pouvoir calculer l'efficacité d'identification des électrons, un échantillon d'électrons pur et non-biaisé est nécessaire. Cet échantillon est sélectionné avec la méthode "Tag and Probe" basée sur la désintégration $Z \to ee$. La désintégration d'un boson Z donne deux électrons dont, à un électron dénommé "Tag", des critères d'identification stricts sont appliqués. A l'autre électron, dénommé "Probe", aucun critère d'identification n'est appliqué mais le Probe est identifié indirectement à l'aide de l'électron Tag et en profitant de la signature de la désintégration $Z \to ee$: la masse invariante et la charge électrique opposée des deux électrons. Le schéma de la Figure V.1 montre le principe de la méthode Tag and Probe.

La méthode Tag and Probe donne déjà un échantillon d'électrons réels très pur. Le bruit de fond restant est estimé avec une méthode qui s'appuie sur les données. Le signal est séparé du bruit de fond grâce à des propriétés d'isolation des électrons probes : des électrons réels provenant de la désintégration du boson Z sont isolés contrairement à la plupart des objets du bruit de fond de la mesure. Un discriminant qui utilise l'énergie transverse dans un cône autour de l'électron est construit, tandis que l'énergie transverse associée à l'électron n'est pas inclue dans le calcul.

Un modèle de la forme de la distribution de ce discriminant de l'isolation des électron est crée pour les événements de bruit de fond en inversant certains des critères de la sélection. Ce modèle est renormalisé à la quantité de données observées à l'aide d'un échantillon

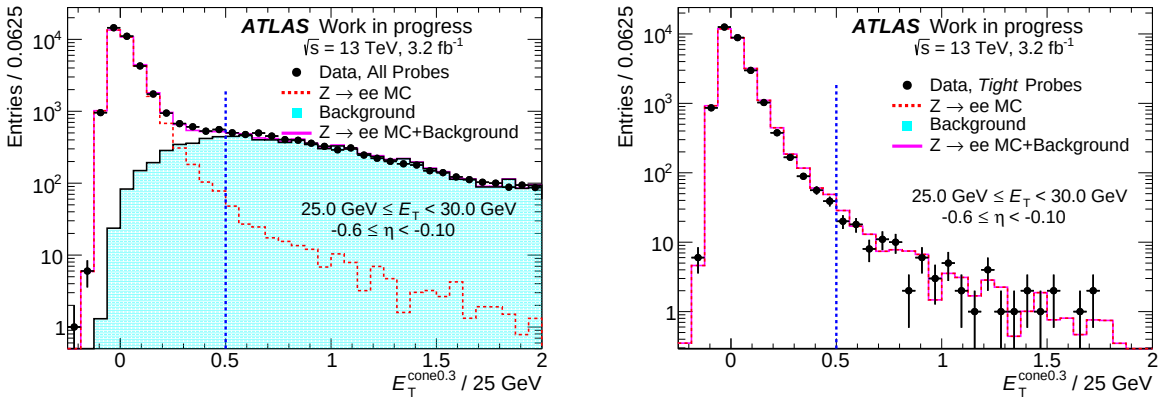

Figure V.2 *Distribution d'isolation des électrons en données (noir), pour le bruit de fond (bleu clair) et en simulation (rouge hachuré). À gauche, la distribution d'isolation des probes reconstruits est montrée, à gauche, pour des probes identifiés. La ligne bleu foncée hachurée indique la définition d'échantillon du signal et de contrôle.*

de contrôle contenant des électrons non-isolés. Cet échantillon contient en majorité des object du bruit de fond. Des exemples de la distribution d'isolation des électrons probe sont montrés dans la Figure V.2.

Des effets systématiques réduisent la précision de la mesure. Les incertitudes systématiques sont estimées en variant des critères de sélection et les paramètres de l'analyse. La systèmatique la plus importante correspond à la modélisation du bruit de fond qui contribue avec une incertitude rélative d'environ 3-5% sur le calcul du facteur de correction pour les électrons de basse énergie. La précision totale des facteurs de correction a été estimée à environ 3-5% pour une énergie transverse des électrons de $15 < E_{\mathrm{T}} < 20$ GeV et devient inférieures au pourcent pour des énergies plus hautes.

Deux mesures de l'efficacité d'identification des électrons et du facteur de correction sont combinées et la combinaison est mise à la disposition de la collaboration ATLAS. Le facteur de correction est calculé pour le détecteur intérieur pour un spectre d'énergie de $15 < E_{\mathrm{T}} < 200$ GeV. Les résultats de la combinaison sont montrés en Figure V.3. Les deux méthodes donnent des résultats compatibles, avec une légère tension aux basses énergies.

VI. Sélection des événements WZ

La sélection et l'analyse des événements WZ est présentée dans ce chapitre. Elle se décompose en : sélection des leptons, reconstruction des événements WZ et estimation du bruit de fond.

La sélection des leptons est optimisée afin de réduire le bruit de fond. Les critères de sélection des leptons, les critères d'identification et d'isolation des électrons et des muons, sont optimisés afin d'obtenir un bas niveau de bruit de fond tout en gardant une grand efficacité de sélection du signal.

L'énergie transverse manquante est associée au neutrino, et à l'aide de la masse du bosons W, l'impulsion longitudinale du neutrino est réconstruite. Des critères sur la cinématique de l'événement et sur le nombre de leptons reconstruits donne un échantillon de candidats d'événements WZ. Selon ses signatures typiques, des événements WZ sont reconstruits : un événement WZ contient exactement trois leptons dont deux leptons de la même sorte avec charge opposée et une masse invariante proche de la masse du boson

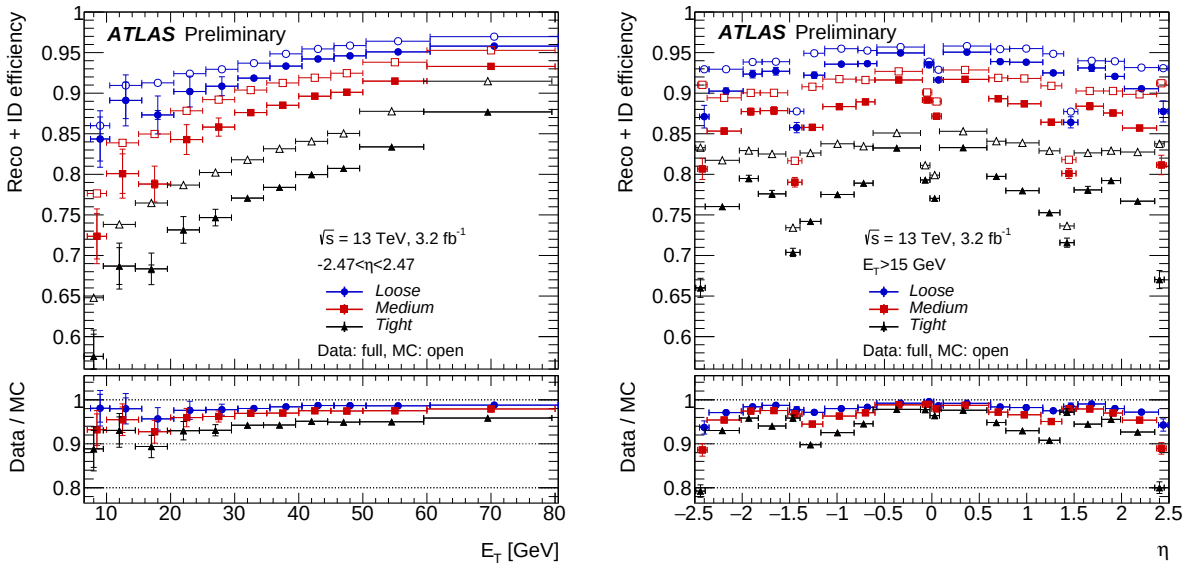

Figure V.3 *Les résultats de la combinaison des deux méthodes de la mesure d'efficacité d'identification des électrons. La méthode qui s'appuie sur l'isolation des électrons contribue à ces résultats pour des énergies de* $15 < E_T < 200$ *GeV. Les efficacités pour des énergies plus basses sont calculés avec une autre méthode basée sur la désintégration du* J/ψ *en deux électrons. Les efficacités sont montrés sur les tableaux en haut, les facteurs de correction sur les tableaux en bas.*

Z. Le troisième lepton et le neutrino doivent être cohérents de provenir d'un boson W.

Le bruit de fond doit être précisément estimé. Les événements de bruit de fond peuvent être regroupés en deux classes : le bruit de fond réductible et irréductible. Le groupe du bruit de fond irréductible rassemble tous les processus qui donnent trois leptons ou plus. C'est le cas pour les événements ZZ, $t\bar{t}W$, $t\bar{t}Z$, tZ et tri-bosons. Le bruit de fond irréducible est estimé à l'aide des simulations. Les simulations modélisant les événements ZZ et $t\bar{t}V$ ($V = W$, Z) sont validées dans des regions de contrôle dédiées.

Par contre, le bruit de fond réductible est estimé avec une méthode qui s'appuie sur les données. Le bruit de fond réductible rassemble des événements avec moins de trois vrai leptons et qui contiennent des objets identifiés à tort comme des leptons, par exemple, les événements Z+jets, $t\bar{t}$ et $Z + \gamma$. La méthode pour estimer le bruit de fond réductible, dénommée "Matrix Method", est basée sur l'inversion d'une matrice qui contient des efficacités et des probabilités de fausse identification des leptons prompts et non-prompts. La méthode est basée sur des critères d'identification et d'isolation et sur la probabilité qu'un objet soit faussement identifié comme un lepton. Cette dernière est estimée dans des échantillons composés d'objets non-leptoniques. Ces probabilités sont dépendantes de l'impulsion transverse p_{T}, de la pseudorapidité η et du type d'objet qui a été sujet à une fausse identification. Les probabilités de fausse identification sont calculées en fonction du p_{T} du lepton et des corrections ont été derivées pour prendre en compte la dépendance en η et du type d'objet. La précision obtenue par cette méthode sur l'estimation du bruit de fond est de 27.5%.

La figure VI.1 montre des distributions cinématiques des événements WZ sélectionés et la Table VI.1 montre les résultats de la sélection des événements et de l'estimation du bruit de fond.

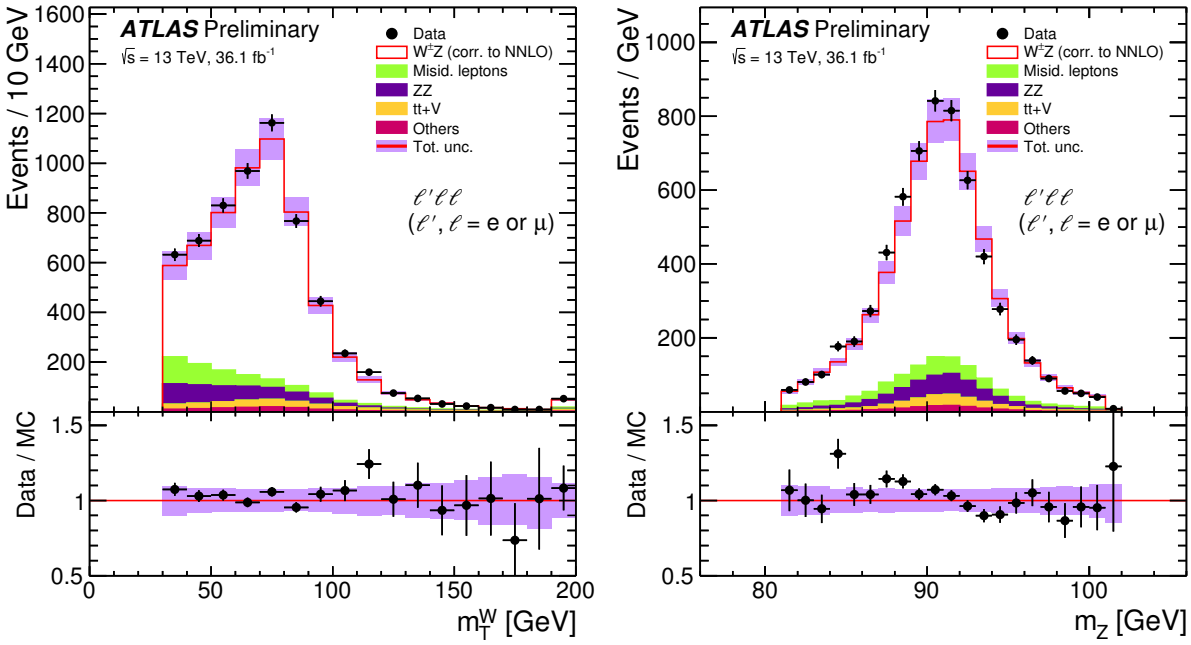

Figure VI.1 *Distributions cinématiques du signal (blanc) et du bruit de fond (coloré). Les points noirs répresentent les données. A gauche, la masse transverse du boson W est montrée et à droite, la masse invariante du boson Z.*

Channel	eee	μee	$e\mu\mu$	$\mu\mu\mu$	All
Data	1279	1281	1671	1929	6160
Total Expected	1221 ± 7	1281 ± 6	1653 ± 8	1830 ± 7	5986 ± 14
WZ	922 ± 5	1077 ± 6	1256 ± 6	1523 ± 7	4778 ± 12
Misid. leptons	138 ± 5	34 ± 2	193 ± 5	71 ± 2	436 ± 8
ZZ	86 ± 1	89 ± 1	117 ± 1	135 ± 1	426 ± 3
$t\bar{t}$+V	50.0 ± 0.7	54 ± 0.7	56.1 ± 0.7	63.8 ± 0.8	225 ± 1
tZ	23.1 ± 0.4	24.8 ± 0.4	28.8 ± 0.4	33.5 ± 0.5	110 ± 1
VVV	2.5 ± 0.1	2.8 ± 0.1	3.2 ± 0.1	3.6 ± 0.1	12.0 ± 0.2
$\frac{S}{B}$	3.08	5.26	3.15	4.96	3.95

Table VI.1 *Résultat de la sélection d'événements WZ : signal attendu et mesuré et le bruit de fond estimé.*

VII. Mesure de la section efficace de la production WZ

La section efficace est mesurée dans un espace de phase défini par l'acceptance du détecteur et par la sélection des événements, espace de phase appelé fiduciel. Elle est ensuite extrapolée dans un espace de phase plus grand, dit total. La définition des leptons prend en compte les radiations électromagnétique dans l'état final.

La section efficace est calculée en utilisant l'équation

$$\sigma^{\text{fid}}_{WZ\to\ell\nu\ell\ell} = \frac{N_{\text{obs}} - N_{\text{bkg}}}{\mathcal{L} \cdot C_{WZ}} \times \left(1 - \frac{N^{\tau}_{\text{MC,rec}}}{N^{\text{all}}_{\text{MC,rec}}}\right), \tag{VII.1}$$

où N_{obs} est le nombre d'événements sélectionnés, N_{bkg} le bruit de fond estimé et $\mathcal{L}$ est

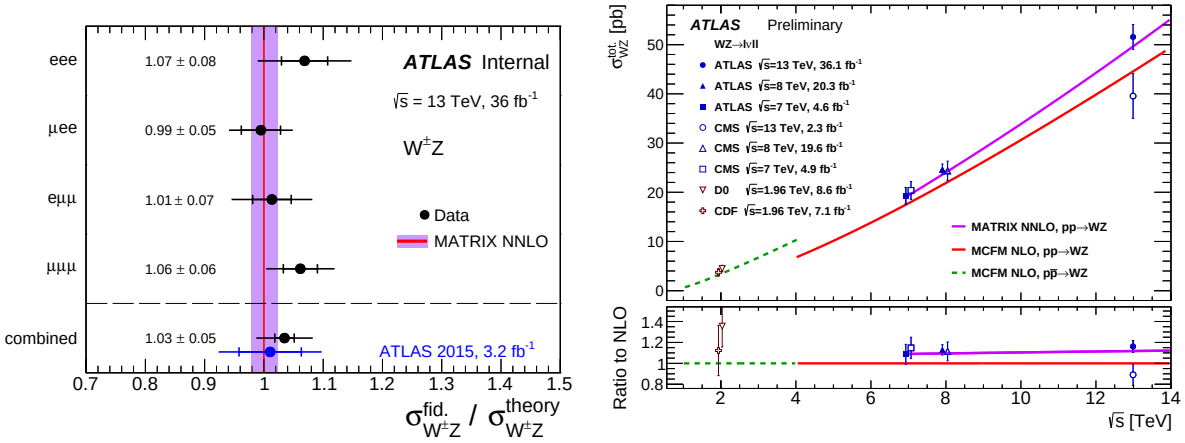

Figure VII.1 *Mesures de la section efficace de la production WZ dans l'espace de phase fiduciel (gauche) et mesures de la section efficace dans l'espace de phase total comparées aux autres mesures existantes et aux prédictions théoriques au NLO et NNLO (droite).*

la luminosité integrée des données enregistrés en 2015 et 2016, soit au total 36.1 ± 0.8 fb^{-1}. C_{WZ} est l'efficacité de la reconstruction d'un événement WZ dans le détecteur ATLAS et l'expression entre parenthèses corrige pour la contribution des événements WZ qui se désintègres en au moins un lepton τ. Cette contribution ainsi que C_{WZ} sont estimés par la simulation. Le résultat de la section efficace pour un canal de désintégration entièrement leptonique est

$$\sigma^{\text{fid.PS}}_{W^{\pm}Z\to\ell'\nu\ell\ell} = 63.7 \pm 2.9 \text{ fb}. \tag{VII.2}$$

La Figure VII.1 (gauche) montre la séction efficace mesurée comparée aux calculs théoriques pour les quatre canaux de désintégration considerés et le résultat final, la combinaison. Les résultats sont en accord avec les calculs théoriques obtenus avec le programme MATRIX avec une précision au NNLO.

La précision de la mesure est 4.6%, elle est dominée par l'incertitude systématique. Les incertitudes de mesure les plus importantes proviennent de l'estimation du bruit de fond réductible, du pile-up et de l'efficacité d'identification des leptons.

La section efficace est également extrapolée dans l'espace de phase total qui inclus tous les modes de désintégration et tout l'angle solide. Il n'y a pas de coupures cinématiques hormis sur la masse invariante des leptons associés au boson Z, $m_{\ell\ell}$, qui doit satisfaire $66 < m_{\ell\ell} < 116$ GeV. Le résultat de la section efficace en l'espace de phase total est

$$\sigma^{\text{tot.PS}}_{W^{\pm}Z} = 51.0 \pm 2.5\,(\text{tot.})\,\text{pb}, \tag{VII.3}$$

qui est en accord avec le calcul théorique NNLO qui prédit $49.1^{+1.1}_{-1.0}$pb.

La figure VII.1 (droite) montre le résultat de la section efficace totale comparé à toutes les mesures faites avec les données d'ATLAS et du Tevatron et avec les calculs théoriques d'une précision NLO et NNLO.

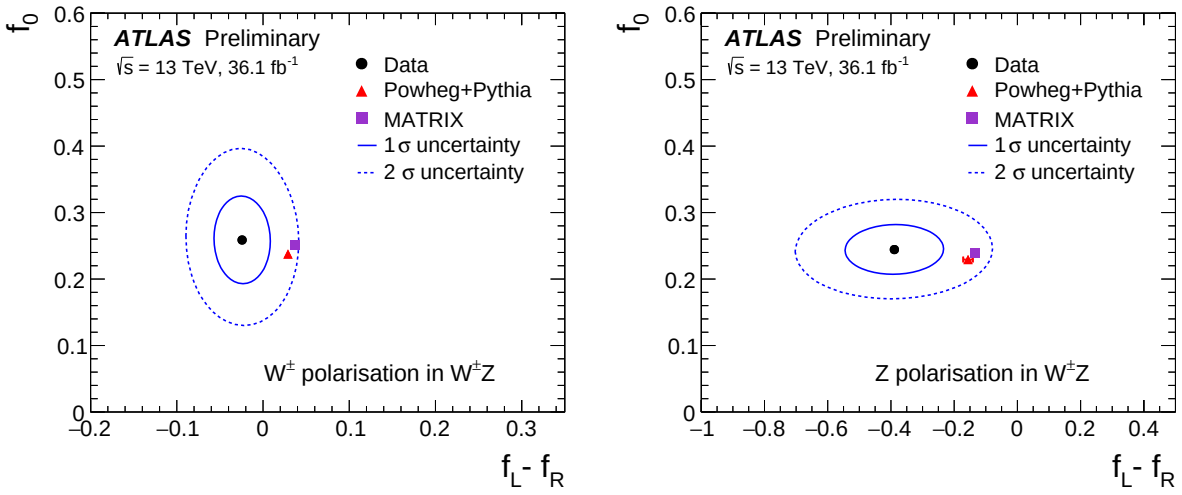

Figure VIII.1 *Résultats de la mesure de la polarisation des boson W (gauche) et Z (droit) dans des événements $W^{\pm}Z$ et leurs incertitudes. Les résultats sont comparés avec les prédictions de* Powheg+Pythia *et* Matrix

VIII. La mesure de la polarisation des bosons WZ lors de leur production par paire

Ce chapitre présente la mesure de la polarisation des bosons produits dans les événements WZ. Pour discriminer les différents modes de polarisation, une variable angulaire est utilisée, le cosinus de l'angle θ^*. Les taux de polarisation sont normalisés, donc, seulement deux taux sont indépendants et la polarisation longitudinale f_0 et la différence entre les polarisations transverses gauche et droite, $f_L - f_R$, sont extraites. La méthode est basée sur un ajustement statistique de maximum de vraisemblance de modèles de distributions angulaires des bosons polarisés à la distribution angulaire des données.

L'étude s'intéresse plus particulièrement à la mesure de la polarisation longitudinale. Par conséquence, la mesure est optimisée, utilisant des échantillons d'Asimov, pour maximiser la significance de la mésure de la polarisation longitudinale.

Un taux de bosons W (Z) longitudinalement polarisés de 26±6% (24±4%) a été mesuré. Une significance de 4.2 σ a été trouvée pour l'existence de bosons W avec une polarisation longitudinale, la significance attendue correspondante était de 3.8 σ. L'existence des bosons Z longitudinalement polarisés a été mesurée avec une significance de 6.5 σ, tandis que la significance attendue était de 6.1 σ.

Les mesures sont comparées avec les calculs de Powheg+Pythia et Matrix. Les deux simulations arrivent à bien décrire la polarisation longitudinale. Pour la mesure de $f_L - f_R$, l'accord entre les prédictions théoriques et la mesure est de l'ordre de 1-2 σ.

Les résultats de la mesure de la polarisation des bosons W et Z dans des événements $W^{\pm}Z$ sont montrés dans la Figure VIII.1 et comparés aux prédictions de Powheg+Pythia et Matrix.

IX. Conclusion

Dans le cadre de cette thèse, la mesure de la section efficace de la production par paire WZ et de la polarisation des bosons ont été présentés. Les données des collisions proton-proton avec une énergie dans le centre de masse de $\sqrt{s} = 13$ TeV, utilisées pour cette mesure, ont été enregistrées par le détecteur ATLAS en 2015 et 2016. Au total, des données avec

luminosité intégrée de 36.1 fb^{-1} étaient disponibles. La section efficace a été mesurée dans un espace de phase défini par l'acceptance du détecteur et les critères de selection. Le résultat de la section efficace dans cet espace de phase fiduciel a une précision de 4.6% qui est dominée par les incertitudes systématiques. Cette section efficace a été également extrapolée dans l'espace de phase total. Tous les résultats sont bien en accord avec les prédictions théoriques qui ont une précision au NNLO en QCD.

La première mesure de la polarisation des bosons vecteurs lors de leur production par paire en collisions hadroniques a été effectuée. Un taux de 26% (24%) de bosons W (Z) longitudinalement polarisés a été observé avec une significance de 4.2 σ (6.5 σ). L'incertitude est dominée par l'incertitude statistique. Le calcul théorique MATRIX avec une précision au NNLO en QCD décrit bien la polarisation longitudinale mesurée.

La mesure de l'efficacité d'identification des éléctrons a été également effectuée, pour les données enrégistrées en 2015 et 2015 et en simulation. Un facteur de correction pour corriger l'efficacité d'identification prédite par la simulation est calculé. La méthode "Tag and Probe" a été utilisée pour créer un échantillon pur et non-biaisé. Pour discriminer le signal du bruit de fond, les propriétés d'isolation des électron ont été utilisées. Une précision de 3-5% pour des énergies transverses de 15-20 GeV a été obtenue, la précision devient meilleure que le pourcent quand l'énergie des électrons augmente.

Bibliography

[1] The ATLAS collaboration, *Measurement of total and differential W^+W^- production cross sections in proton-proton collisions at $\sqrt{s} = 8$ TeV with the ATLAS detector and limits on anomalous triple-gauge-boson couplings*, JHEP **09** (2016) p. 029, arXiv: 1603.01702 [hep-ex].

[2] The ATLAS collaboration, *Measurement of W^+W^- production in association with one jet in proton–proton collisions at $\sqrt{s} = 8$ TeV with the ATLAS detector*, Phys. Lett. B **763** (2016) p. 114, arXiv: 1608.03086 [hep-ex].

[3] The ATLAS collaboration, *Measurement of the W^+W^- production cross section in pp collisions at a centre-of-mass energy of $\sqrt{s} = 13$ TeV with the ATLAS experiment*, Phys. Lett. B **773** (2017) p. 354, arXiv: 1702.04519 [hep-ex].

[4] The CMS collaboration, *Measurement of the $\mathrm{W^+W^-}$ cross section in pp collisions at $\sqrt{s} = 8$ TeV and limits on anomalous gauge couplings*, Eur. Phys. J. C **76** (2016) p. 401, arXiv: 1507.03268 [hep-ex].

[5] The CMS collaboration, "Measurement of the WW cross section pp collisions at $\sqrt{s}$=13 TeV", tech. rep. CMS-PAS-SMP-16-006, CERN, 2016, URL: https://cds.cern.ch/record/2160868.

[6] The ATLAS collaboration, *$ZZ \to \ell^+\ell^-\ell'^+\ell'^-$ cross-section measurements and search for anomalous triple gauge couplings in 13 TeV pp collisions with the ATLAS detector*, Phys. Rev. D **97** (2018) p. 032005, arXiv: 1709.07703 [hep-ex].

[7] The ALTAS collaboration, *Measurement of the ZZ production cross section in proton-proton collisions at $\sqrt{s} = 8$ TeV using the $ZZ \to \ell^-\ell^+\ell'^-\ell'^+$ and $ZZ \to \ell^-\ell^+\nu\bar{\nu}$ channels with the ATLAS detector*, JHEP **01** (2017) p. 099, arXiv: 1610.07585 [hep-ex].

[8] The ATLAS collaboration, *Measurement of the ZZ Production Cross Section in pp Collisions at $\sqrt{s} = 13$ TeV with the ATLAS Detector*, Phys. Rev. Lett. **116** (2016) p. 101801, arXiv: 1512.05314 [hep-ex].

[9] The CMS collaboration, *Measurement of the $pp \to ZZ$ production cross section and constraints on anomalous triple gauge couplings in four-lepton final states at $\sqrt{s}$ =8 TeV*, Phys. Lett. B **740** (2015) p. 250, arXiv: 1406.0113 [hep-ex].

[10] The CMS collaboration, *Measurements of the $\mathrm{pp} \to \mathrm{ZZ}$ production cross section and the $\mathrm{Z} \to 4\ell$ branching fraction, and constraints on anomalous triple gauge couplings at $\sqrt{s} = 13$ TeV*, Eur. Phys. J. C **78** (2018) p. 165, arXiv: 1709.08601 [hep-ex].

[11] The ATLAS collaboration, *Measurement of the $W^{\pm}Z$ production cross section and limits on anomalous triple gauge couplings in proton-proton collisions at $\sqrt{s} = 7$ TeV with the ATLAS detector*, Phys. Lett. B **709** (2012) p. 341, arXiv: 1111.5570 [hep-ex].

[12] The ATLAS collaboration, *Measurements of $W^{\pm}Z$ production cross sections in pp collisions at $\sqrt{s} = 8$ TeV with the ATLAS detector and limits on anomalous gauge boson self-couplings*, Phys. Rev. D **93** (2016) p. 092004, arXiv: 1603.02151 [hep-ex].

[13] The CMS collaboration, *Measurement of the WZ production cross section in pp collisions at $\sqrt{s} = 7$ and 8 TeV and search for anomalous triple gauge couplings at $\sqrt{s} = 8$ TeV*, Eur. Phys. J. C **77** (2017) p. 236, arXiv: 1609.05721 [hep-ex].

[14] The CMS collaboration, *Measurement of the WZ production cross section in pp collisions at $\sqrt{(s)} = 13$ TeV*, Phys. Lett. B **766** (2017) p. 268, arXiv: 1607.06943 [hep-ex].

[15] The ATLAS collaboration, *Measurement of the $W^{\pm}Z$ boson pair-production cross section in pp collisions at $\sqrt{s} = 13$ TeV with the ATLAS Detector*, Phys. Lett. B **762** (2016) p. 1, arXiv: 1606.04017 [hep-ex].

[16] The ATLAS collaboration, "Measurement of $W^{\pm}Z$ boson pair-production in pp collisions at $\sqrt{s} = 13$ TeV with the ATLAS Detector and confidence intervals for anomalous triple gauge boson couplings", tech. rep. ATLAS-CONF-2016-043, CERN, 2016, URL: https://cds.cern.ch/record/2206093.

[17] The ATLAS collaboration, *Measurement of $WW/WZ \to \ell\nu qq'$ production with the hadronically decaying boson reconstructed as one or two jets in pp collisions at $\sqrt{s} = 8$ TeV with ATLAS, and constraints on anomalous gauge couplings*, Eur. Phys. J. C **77** (2017) p. 563, arXiv: 1706.01702 [hep-ex].

[18] The CMS collaboration, *Search for anomalous couplings in boosted $\mathrm{WW/WZ} \to \ell\nu\mathrm{q\bar{q}}$ production in proton-proton collisions at $\sqrt{s} = 8$ TeV*, Phys. Lett. B **772** (2017) p. 21, arXiv: 1703.06095 [hep-ex].

[19] L. Randall and R. Sundrum, *A Large mass hierarchy from a small extra dimension*, Phys. Rev. Lett. **83** (1999) p. 3370, arXiv: hep-ph/9905221 [hep-ph].

[20] I. P. Ivanov, *Building and testing models with extended Higgs sectors*, Prog. Part. Nucl. Phys. **95** (2017) p. 160, arXiv: 1702.03776 [hep-ph].

[21] The CMS collaboration, *Search for massive resonances decaying into WW, WZ or ZZ bosons in proton-proton collisions at $\sqrt{s} = 13$ TeV*, JHEP **03** (2017) p. 162, arXiv: 1612.09159 [hep-ex].

[22] The ATLAS collaboration, *Search for resonant WZ production in the fully leptonic final state in proton-proton collisions at $\sqrt{s} = 13$ TeV with the ATLAS detector*, (2018), arXiv: 1806.01532 [hep-ex].

[23] The ATLAS collaboration, "Observation of electroweak $W^{\pm}Z$ boson pair production in association with two jets in pp collisions at $\sqrt{s} = 13$TeV with the ATLAS Detector", tech. rep. ATLAS-CONF-2018-033, CERN, 2018, URL: https://cds.cern.ch/record/2630183.

[24] A. Ballestrero, E. Maina, and G. Pelliccioli,
W boson polarization in vector boson scattering at the LHC,
JHEP **03** (2018) p. 170, arXiv: 1710.09339 [hep-ph].

[25] The ATLAS collaboration,
Measurement of the polarisation of W bosons produced with large transverse momentum in pp collisions at $\sqrt{s} = 7$ TeV with the ATLAS experiment,
Eur. Phys. J. C **72** (2012) p. 2001, arXiv: 1203.2165 [hep-ex].

[26] The CMS collaboration, *Measurement of the Polarization of W Bosons with Large Transverse Momenta in W+Jets Events at the LHC*,
Phys. Rev. Lett. **107** (2011) p. 021802, arXiv: 1104.3829 [hep-ex].

[27] The ATLAS collaboration,
Measurement of the angular coefficients in Z-boson events using electron and muon pairs from data taken at $\sqrt{s} = 8$ TeV with the ATLAS detector,
JHEP **08** (2016) p. 159, arXiv: 1606.00689 [hep-ex].

[28] The CMS collaboration,
Angular coefficients of Z bosons produced in pp collisions at $\sqrt{s} = 8$ TeV and decaying to $\mu^+\mu^-$ as a function of transverse momentum and rapidity,
Phys. Lett. C **750** (2015) p. 154, arXiv: 1504.03512 [hep-ex].

[29] The L3 Collaboration, *Measurement of W polarisation at LEP*,
Phys. Lett. B **557** (2003) p. 147, arXiv: hep-ex/0301027 [hep-ex].

[30] The OPAL Collaboration, *W boson polarization at LEP2*,
Phys. Lett. B **585** (2004) p. 223, arXiv: hep-ex/0312047 [hep-ex].

[31] D. J. Griffiths, *Introduction to Elementary Particles, Second Edition*,
TextBook Physics, Wiley-VCH Verlag GmbH Co. KGaA, 2008.

[32] T. Plehn, *Lectures on LHC physics. An LHC lecture*, Lecture notes in physics,
Springer, 2012, URL: https://cds.cern.ch/record/1405414.

[33] C. Patrignani et al. (Particle Data Group), *2017 Review of Particle Physics*,
Chin. Phys. C **40** (2016, 2017) p. 100001.

[34] C.S. Wu et al., *Experimental Test of Parity Conservation in Beta Decay*,
Phys. Rev. (1957).

[35] C. N. Yang and R. L. Mills,
Conservation of Isotopic Spin and Isotopic Gauge Invariance,
Physical Review **96** (1954) p. 191.

[36] D. H. Perkins, *Introduction to high-energy physics; 4th ed.*
Cambridge Univ. Press, 2000, URL: https://cds.cern.ch/record/396126.

[37] A. Pich, "The Standard Model of Electroweak Interactions",
Proceedings, High-energy Physics. Proceedings, 18th European School (ESHEP 2010): Raseborg, Finland, June 20 - July 3, 2010, 2012 p. 1,
arXiv: 1201.0537 [hep-ph],
URL: https://inspirehep.net/record/1083304/files/arXiv:1201.0537.pdf.

[38] S. Dawson, "Introduction to electroweak symmetry breaking",
Proceedings, Summer School in High-energy physics and cosmology: Trieste, Italy, June 29-July 17, 1998, 1998 p. 1, arXiv: hep-ph/9901280 [hep-ph].

[39] P. W. Higgs, *Broken Symmetries and the Masses of Gauge Bosons*, Phys. Rev. Lett. **13** (16 1964) p. 508, URL: https://link.aps.org/doi/10.1103/PhysRevLett.13.508.

[40] P. W. Higgs, *Spontaneous Symmetry Breakdown without Massless Bosons*, Phys. Rev. **145** (4 1966) p. 1156, URL: https://link.aps.org/doi/10.1103/PhysRev.145.1156.

[41] F. Englert and R. Brout, *Broken Symmetry and the Mass of Gauge Vector Mesons*, Phys. Rev. Lett. **13** (9 1964) p. 321, URL: https://link.aps.org/doi/10.1103/PhysRevLett.13.321.

[42] G. S. Guralnik, C. R. Hagen, and T. W. B. Kibble, *Global Conservation Laws and Massless Particles*, Phys. Rev. Lett. **13** (20 1964) p. 585, URL: https://link.aps.org/doi/10.1103/PhysRevLett.13.585.

[43] T. W. B. Kibble, *Symmetry Breaking in Non-Abelian Gauge Theories*, Phys. Rev. **155** (5 1967) p. 1554, URL: https://link.aps.org/doi/10.1103/PhysRev.155.1554.

[44] The ATLAS collaboration, *A particle consistent with the Higgs Boson observed with the ATLAS Detector at the Large Hadron Collider*, Science **338** (2012) p. 1576.

[45] The CMS collaboration, *Observation of a new boson with mass near 125 GeV in pp collisions at $\sqrt{s}$ = 7 and 8 TeV*, JHEP **06** (2013) p. 081, arXiv: 1303.4571 [hep-ex].

[46] The CMS Collaboration, "Determination of the strong coupling constant from the measurement of inclusive multijet event cross sections in pp collisions at $\sqrt{s} = 8$ TeV", tech. rep. CMS-PAS-SMP-16-008, CERN, 2017, URL: http://cds.cern.ch/record/2253091.

[47] S. Wahrmund, A. Straessner, and D. Stöckinger, "Underlying event studies using calorimeter jets with the ATLAS detector at LHC", 2010, URL: https://cds.cern.ch/record/1324558.

[48] G. Zanderighi, "Lecture on Precision QCD, within the scope of the 2016 EUROPEAN SCHOOL OF HIGH-ENERGY PHYSICS", https://indico.cern.ch/event/467465/contributions/1975117/attachments/1293328/1927250/QCD-2.pdf.

[49] J. M. Campbell, J. W. Huston, and W. J. Stirling, *Hard Interactions of Quarks and Gluons: A Primer for LHC Physics*, Rept. Prog. Phys. **70** (2007) p. 89, arXiv: hep-ph/0611148 [hep-ph].

[50] H.-L. Lai et al., *New parton distributions for collider physics*, Phys. Rev. D **82** (2010) p. 074024, arXiv: 1007.2241 [hep-ph].

[51] M. Schott and M. Dunford, *Review of single vector boson production in pp collisions at $\sqrt{s} = 7$ TeV*, Eur. Phys. J. C **74** (2014) p. 2916, arXiv: 1405.1160 [hep-ex].

[52] S. Höche, "Introduction to parton-shower event generators", *Proceedings, Theoretical Advanced Study Institute in Elementary Particle Physics: Journeys Through the Precision Frontier: Amplitudes for Colliders (TASI 2014): Boulder, Colorado, June 2-27, 2014*, 2015 p. 235, arXiv: 1411.4085 [hep-ph], URL: https://inspirehep.net/record/1328513/files/arXiv:1411.4085.pdf.

[53] S. Frixione and B. R. Webber, *Matching NLO QCD computations and parton shower simulations*, JHEP **06** (2002) p. 029, arXiv: hep-ph/0204244 [hep-ph].

[54] B. Webber, *A QCD model for jet fragmentation including soft gluon interference*, Nuclear Physics B **238** (1984) p. 492 , URL: http://www.sciencedirect.com/science/article/pii/055032138490333X.

[55] B. Andersson et al., *Parton fragmentation and string dynamics*, Physics Reports **97** (1983) p. 31 , URL: http://www.sciencedirect.com/science/article/pii/0370157383900807.

[56] R. D. Field, *The Underlying event in hard scattering processes*, eConf **C010630** (2001) P501, arXiv: hep-ph/0201192 [hep-ph].

[57] The ATLAS collaboration, "Summary plot of Standard Model Production Cross Section Measurements", https://atlas.web.cern.ch/Atlas/GROUPS/PHYSICS/CombinedSummaryPlots/SM/ATLAS_b_SMSummary_FiducialXsect/ATLAS_b_SMSummary_FiducialXsect.pdf, 2018.

[58] U. Baur, T. Han, and J. Ohnemus, *WZ production at hadron colliders: Effects of nonstandard WWZ couplings and QCD corrections*, Phys. Rev. D **51** (1995) p. 3381, arXiv: hep-ph/9410266 [hep-ph].

[59] M. Grazzini et al., *$W^{\pm}Z$ production at the LHC: fiducial cross sections and distributions in NNLO QCD*, JHEP **05** (2017) p. 139, arXiv: 1703.09065 [hep-ph].

[60] F. Campanario and S. Sapeta, *WZ production beyond NLO for high-pT observables*, Phys. Lett. B **718** (2012) p. 100, arXiv: 1209.4595 [hep-ph].

[61] U. Baur, T. Han, and J. Ohnemus, *Amplitude zeros in W+- Z production*, Phys. Rev. Lett. **72** (1994) p. 3941, arXiv: hep-ph/9403248 [hep-ph].

[62] M. Grazzini et al., *$W^{\pm}Z$ production at hadron colliders in NNLO QCD*, Phys. Lett. **B761** (2016) p. 179, arXiv: 1604.08576 [hep-ph].

[63] A. Bierweiler, T. Kasprzik, and J. H. Kühn, *Vector-boson pair production at the LHC to $\mathcal{O}(\alpha^3)$ accuracy*, JHEP **12** (2013) p. 071, arXiv: 1305.5402 [hep-ph].

[64] E. Accomando and A. Kaiser, *Electroweak corrections and anomalous triple gauge-boson couplings in W^+W^- and $W^{\pm}Z$ production at the LHC*, Phys. Rev. D **73** (2006) p. 093006, arXiv: hep-ph/0511088 [hep-ph].

[65] J. Baglio, L. D. Ninh, and M. M. Weber, *Massive gauge boson pair production at the LHC: a next-to-leading order story*, Phys. Rev. D **88** (2013) p. 113005, arXiv: 1307.4331 [hep-ph].

[66] B. Biedermann, A. Denner, and L. Hofer,
Next-to-leading-order electroweak corrections to the production of three charged leptons plus missing energy at the LHC, JHEP **10** (2017) p. 043, arXiv: 1708.06938 [hep-ph].

[67] R. S. Thorne, "The Role of uncertainties in parton distribution functions", *Statistical issues for LHC physics. Proceedings, Workshop, PHYSTAT-LHC, Geneva, Switzerland, June 27-29, 2007*, 2007 p. 141, arXiv: 0711.2986 [hep-ph], URL: http://cds.cern.ch/record/1070235/files/p141.pdf.

[68] R. D. Ball et al., *Parton distributions for the LHC Run II*, JHEP **04** (2015) p. 040, arXiv: 1410.8849 [hep-ph].

[69] J. Butterworth et al., *PDF4LHC recommendations for LHC Run II*, J. Phys. G **43** (2016) p. 023001, arXiv: 1510.03865 [hep-ph].

[70] J. A. et al., *Recent developments in Geant4*, Nuclear Instruments and Methods in Physics Research Section A: Accelerators, Spectrometers, Detectors and Associated Equipment **835** (2016) p. 186 , URL: http://www.sciencedirect.com/science/article/pii/S0168900216306957.

[71] S. Alioli et al., *A general framework for implementing NLO calculations in shower Monte Carlo programs: the POWHEG BOX*, JHEP **06** (2010) p. 043, arXiv: 1002.2581 [hep-ph].

[72] T. Sjostrand, S. Mrenna, and P. Z. Skands, *A Brief Introduction to PYTHIA 8.1*, Comput. Phys. Commun. **178** (2008) p. 852, arXiv: 0710.3820 [hep-ph].

[73] G. Corcella et al., *HERWIG 6: An Event generator for hadron emission reactions with interfering gluons (including supersymmetric processes)*, JHEP **01** (2001) p. 010, arXiv: hep-ph/0011363 [hep-ph].

[74] T. Gleisberg et al., *Event generation with SHERPA 1.1*, JHEP **02** (2009) p. 007, arXiv: 0811.4622 [hep-ph].

[75] T. Gleisberg and S. Hoeche, *Comix, a new matrix element generator*, JHEP **12** (2008) p. 039, arXiv: 0808.3674 [hep-ph].

[76] S. Schumann and F. Krauss,
A Parton shower algorithm based on Catani-Seymour dipole factorisation, JHEP **03** (2008) p. 038, arXiv: 0709.1027 [hep-ph].

[77] S. Catani et al., *QCD matrix elements + parton showers*, JHEP **11** (2001) p. 063, arXiv: hep-ph/0109231 [hep-ph].

[78] S. Hoeche et al., *QCD matrix elements and truncated showers*, JHEP **05** (2009) p. 053, arXiv: 0903.1219 [hep-ph].

[79] S. Hoeche et al., *QCD matrix elements + parton showers: The NLO case*, JHEP **04** (2013) p. 027, arXiv: 1207.5030 [hep-ph].

[80] J.-C. Winter, F. Krauss, and G. Soff, *A Modified cluster hadronization model*, Eur. Phys. J. C **36** (2004) p. 381, arXiv: hep-ph/0311085 [hep-ph].

[81] M. Schonherr and F. Krauss,
Soft Photon Radiation in Particle Decays in SHERPA, JHEP **12** (2008) p. 018, arXiv: 0810.5071 [hep-ph].

[82] The ATLAS collaboration,
"Measurement of $W^{\pm}Z$ production cross sections and gauge boson polarisation in pp collisions at $\sqrt{s} = 13$ TeV with the ATLAS detector",
tech. rep. ATLAS-CONF-2018-034, CERN, 2018,
URL: https://cds.cern.ch/record/2630187.

[83] A. Azatov et al.,
Novel measurements of anomalous triple gauge couplings for the LHC,
JHEP **10** (2017) p. 027, arXiv: 1707.08060 [hep-ph].

[84] G. Panico, F. Riva, and A. Wulzer, *Diboson Interference Resurrection*,
Phys. Lett. B **776** (2018) p. 473, arXiv: 1708.07823 [hep-ph].

[85] W. J. Stirling and E. Vryonidou, *Electroweak gauge boson polarisation at the LHC*,
JHEP **07** (2012) p. 124, arXiv: 1204.6427 [hep-ph].

[86] E. Mirkes and J. Ohnemus, *W and Z polarization effects in hadronic collisions*,
Phys. Rev. D **50** (1994) p. 5692, arXiv: hep-ph/9406381 [hep-ph].

[87] E. Mirkes, *Angular decay distribution of leptons from W bosons at NLO in hadronic collisions*, Nucl. Phys. B **387** (1992) p. 3.

[88] C. Degrande et al.,
Effective Field Theory: A Modern Approach to Anomalous Couplings,
Annals Phys. **335** (2013) p. 21, arXiv: 1205.4231 [hep-ph].

[89] Lucio Rossi, "The longest journey: the LHC dipoles arrive on time",
Published in the CERN Courier; http://cerncourier.com/cws/article/cern/29723, 2006.

[90] L. Evans and P. Bryant, *LHC Machine*, JINST **3** (2008) S08001.

[91] Picture taken from http://lhc-beam-beam.web.cern.ch/lhc-beam-beam/bb-meeting/CAS/CAS2014_Chavannes/0606052-A4-at-144-dpi.jpg; January 2015.

[92] R. Bruce et al., "LHC Run 2: Results and Challenges",
tech. rep. CERN-ACC-2016-0103, CERN, 2016,
URL: https://cds.cern.ch/record/2201447.

[93] S. Pandolfi,
CERN Press release: LHC Report: end of 2016 proton-proton operation, 2016,
URL: https://home.cern/cern-people/updates/2016/10/lhc-report-end-2016-proton-proton-operation.

[94] The ATLAS collaboration, "ATLAS public plot: Number of Interactions per Crossing, combined 13 TeV data from 2015 and 2016",
https://twiki.cern.ch/twiki/bin/view/AtlasPublic/LuminosityPublicResultsRun2.

[95] Z. Marshall, *Simulation of Pile-up in the ATLAS Experiment*,
J. Phys. Conf. Ser. **513** (2014) p. 022024.

[96] The ATLAS collaboration,
The ATLAS Experiment at the CERN Large Hadron Collider,
JINST **3** (2008) S08003.

[97] A. La Rosa, *The ATLAS Insertable B-Layer: from construction to operation*,
JINST **11** (2016) p. C12036, arXiv: 1610.01994 [physics.ins-det].

[98] Luciano Musa, "Advanced Detector Technology 3/3",
https://indico.cern.ch/event/598530/contributions/2547230/attachments/1517510/2368905/HCP2017_LMusa_L3.pdf,
Lecture on advanced detector technology in the framework of the CERN-Fermilab hadron collider physics summer school, 28 August 2017 to 6 September 2017, 2017.

[99] A. Ruiz-Martinez and ATLAS Collaboration,
"The Run-2 ATLAS Trigger System", tech. rep. ATL-DAQ-PROC-2016-003, CERN, 2016, URL: https://cds.cern.ch/record/2133909.

[100] M. zur Nedden,
"The Run-2 ATLAS Trigger System: Design, Performance and Plan",
tech. rep. ATL-DAQ-PROC-2016-039, CERN, 2016,
URL: https://cds.cern.ch/record/2238679.

[101] The ATLAS Collaboration, "Electron efficiency measurements with the ATLAS detector using the 2015 LHC proton-proton collision data",
tech. rep. ATLAS-CONF-2016-024, CERN, 2016,
URL: https://cds.cern.ch/record/2157687.

[102] The ATLAS collaboration, "Electron and photon energy calibration with the ATLAS detector using data collected in 2015 at $\sqrt{s} = 13$ TeV",
tech. rep. ATL-PHYS-PUB-2016-015, CERN, 2016,
URL: https://cds.cern.ch/record/2203514.

[103] The ATLAS collaboration, *Electron efficiency measurements with the ATLAS detector using 2012 LHC proton–proton collision data*,
Eur. Phys. J. C **77** (2017) p. 195, arXiv: 1612.01456 [hep-ex].

[104] The ATLAS collaboration, *Muon reconstruction performance of the ATLAS detector in proton–proton collision data at* $\sqrt{s}$ *=13 TeV*,
Eur. Phys. J. C **76** (2016) p. 292, arXiv: 1603.05598 [hep-ex].

[105] The ATLAS collaboration,
Jet energy scale measurements and their systematic uncertainties in proton-proton collisions at $\sqrt{s} = 13$ *TeV with the ATLAS detector*,
Phys. Rev. D **96** (2017) p. 072002, arXiv: 1703.09665 [hep-ex].

[106] M. Cacciari, G. P. Salam, and G. Soyez, *The Anti-k(t) jet clustering algorithm*,
JHEP **04** (2008) p. 063, arXiv: 0802.1189 [hep-ph].

[107] The ATLAS collaboration, "Jet Calibration and Systematic Uncertainties for Jets Reconstructed in the ATLAS Detector at $\sqrt{s} = 13$ TeV",
tech. rep. ATL-PHYS-PUB-2015-015, CERN, 2015,
URL: https://cds.cern.ch/record/2037613.

[108] The ATLAS collaboration, *Performance of pile-up mitigation techniques for jets in pp collisions at* $\sqrt{s} = 8$ *TeV using the ATLAS detector.*,
Eur. Phys. J. C **76** (2015) 581. 54 p, URL: http://cds.cern.ch/record/2058295.

[109] The ATLAS collaboration,
"Performance of missing transverse momentum reconstruction for the ATLAS detector in the first proton-proton collisions at at $\sqrt{s}$= 13 TeV",
tech. rep. ATL-PHYS-PUB-2015-027, CERN, 2015,
URL: http://cds.cern.ch/record/2037904.

[110] The ATLAS collaboration, "Topological cell clustering in the ATLAS calorimeters and its performance in LHC Run 1", tech. rep. arXiv:1603.02934. CERN-PH-EP-2015-304, CERN, 2016, URL: https://cds.cern.ch/record/2138166.

[111] S. Laplace, "Twelve years in ATLAS: selected topics", Habilitation à diriger des recherches, https://lpnhe.in2p3.fr/spip.php?article1245, 2015.

[112] Craig Blocker, "Uncertainties on Efficiencies", http://www-cdf.fnal.gov/physics/statistics/notes/cdf7168_eff_uncertainties.ps, 2004.

[113] The ATLAS collaboration, *Electron reconstruction and identification efficiency measurements with the ATLAS detector using the 2011 LHC proton-proton collision data*, Eur. Phys. J. C **74** (2014) p. 2941, arXiv: 1404.2240 [hep-ex].

[114] The ATLAS collaboration, *Luminosity determination in pp collisions at $\sqrt{s} = 8$ TeV using the ATLAS detector at the LHC*, Eur. Phys. J. C **76** (2016) p. 653, arXiv: 1608.03953 [hep-ex].

[115] M. U. Mozer, *Electroweak Physics at the LHC*, Springer Tracts Mod. Phys. **267** (2016) p. 1.

[116] The ATLAS collaboration, *Measurements of b-jet tagging efficiency with the ATLAS detector using $t\bar{t}$ events at $\sqrt{s} = 13$ TeV*, JHEP **08** (2018) p. 089, arXiv: 1805.01845 [hep-ex].

[117] F. D. Aaron et al., *Measurement of the Inclusive ep Scattering Cross Section at Low Q^2 and x at HERA*, Eur. Phys. J. C **63** (2009) p. 625, arXiv: 0904.0929 [hep-ex].

[118] The ATLAS collaboration, *Improved luminosity determination in pp collisions at sqrt(s) = 7 TeV using the ATLAS detector at the LHC*, Eur. Phys. J. C **73** (2013) p. 2518, arXiv: 1302.4393 [hep-ex].

[119] The CMS collaboration, "Measurements of the pp → WZ inclusive and differential production cross section and constraints on charged anomalous triple gauge couplings at $\sqrt{s} = 13$ TeV.", tech. rep. CMS-PAS-SMP-18-002, CERN, 2018, URL: https://cds.cern.ch/record/2628761.

[120] K. Cranmer et al., "HistFactory: A tool for creating statistical models for use with RooFit and RooStats", tech. rep. CERN-OPEN-2012-016, New York U., 2012, URL: http://cds.cern.ch/record/1456844.

[121] G. Cowan et al., *Asymptotic formulae for likelihood-based tests of new physics*, Eur. Phys. J. C **71** (2011) p. 1554, arXiv: 1007.1727 [physics.data-an].

[122] S. Dittmaier et al., *Handbook of LHC Higgs Cross Sections: 1. Inclusive Observables*, (2011), arXiv: 1101.0593 [hep-ph].

[123] J. M. Campbell, R. K. Ellis, and W. T. Giele, *A Multi-Threaded Version of MCFM*, Eur. Phys. J. C **75** (2015) p. 246, arXiv: 1503.06182 [physics.comp-ph].

[124] J. M. Campbell, R. K. Ellis, and C. Williams,
Vector boson pair production at the LHC, JHEP **07** (2011) p. 018,
arXiv: 1105.0020 [hep-ph].

[125] S. Frixione et al., *The MCaNLO 4.0 Event Generator*, (2010),
arXiv: 1010.0819 [hep-ph].

Abstract The measurements presented in this thesis use proton-proton collision data from 2015 and 2016 recorded by the ATLAS experiment at the Large Hadron Collider. The data-taking period was successful and data with an integrated luminosity of 36.1 fb^{-1} has been collected. The knowledge of the efficiency of electron identification in the ATLAS detector is very important for ATLAS analyses. The electron identification efficiency has been measured in data and simulation and correction factors to the simulation have been derived. These correction factors are applied to all ATLAS analyses using electrons in 2015 and 2016. Focus is laid on studies of potential biases and a possible improvement of the method is presented. The electron identification efficiency and its uncertainty is also an important input to the measurement of WZ production using fully leptonic decays to electrons, muons and a neutrino. Measurements of the WZ production are sensitive to the WWZ vector boson coupling. An important difficulty of the measurement is the determination of the background from misidentified leptons. It is the dominant background and also the dominant source of systematic uncertainty. It is determined using a data-driven method, with a precision of 30% which contributes with a relative uncertainty of 1.9% to the WZ production cross-section measurement. The latter has a total precision of 4.6% and the result is well compatible with predictions at next-to-leading order in QCD. Finally, the first polarisation measurement of pair-produced bosons in hadronic collisions has been presented. The measurement is a first step of the characterization of the polarisation in vector boson scattering events. The longitudinal polarisation is directly related to the Electroweak Symmetry breaking mechanism. A fraction of longitudinally polarised W (Z) bosons of 26% (24%) is observed with an observed significance of 4.2 σ (6.5 σ). The uncertainty is dominated by the statistical uncertainty.

Résumé Dans le travail presenté dans cette thèse, l'ensemble des données enregistrées par l'expérience ATLAS au LHC dans les années 2015 et 2016 est utilisé. La campagne de prise de données a été un succès avec une luminosité integrée de 36.1 fb^{-1} accumulée. Il est très important pour les analyses de connaître l'efficacité d'identification des électrons dans le détecteur ATLAS. Cette efficacité a été mesurée dans les données et les simulations. Des facteurs de correction pour la simulation ont été calculés. Ces facteurs de correction sont utilisés pour les analyses des données ATLAS utilisant des électrons en 2015 et 2016. Une étude des bias éventuels de ces mesures d'efficacité et une amélioration de la méthode est également presentée. L'efficacité d'identification des électrons et son incertitude est aussi un aspect important de l'étude de la production de paire de dibosons WZ et leurs désintégrations en électrons, muons et un neutrino. La mesure de la production de WZ par paire est sensible aux couplages à trois bosons WWZ des bosons. Une partie importante de l'analyse est la détermination du bruit de fond réductible. C'est le bruit du fond le plus important et aussi la source d'incertitude syst´matique la plus grande. Il est déterminé avec une précision de 30% par une méthode qui s'appuie sur les données. Il impacte par une incertitude relative de 1.9% la mesure de la section efficace. Cette dernière est déterminée avec une précision de 4.6% et est compatible avec les prédictions théoriques ayant une précision à l'ordre NNLO. Finalement, une première étude de la polarisation des bosons produits par paire en collisions hadroniques est presentée. Cette mesure est un premier pas vers la caractérisation de la polarisation dans les événements de diffusion de bosons vecteurs. La polarisation longitudinale est reliée au mécanisme de brisure de symétry électrofaible. Un taux de 26% (24%) des bosons W (Z) longitudinalement polarisés a été observé avec une significance de 4.2 σ (6.5 σ). L'incertitude est dominée par l'incertitude statistique.